

Formation and Evolution of Beach Cusps

Anurak Sriariyawat, MEng.

GEORGE GREEN LIBRARY OF
SCIENCE AND ENGINEERING[↑]

Thesis submitted to The University of Nottingham
for the degree of Doctor of Philosophy

December 2009

Abstract

Beach cusps are swash zone morphological patterns that have been of interest to many scientists and engineers. This study aims to improve understanding of the formation and long-term evolution of beach cusps by numerical simulation using a 2D process-based morphodynamic model, solving the coupled NLSW equations and sediment conservation equation simultaneously. A numerical implementation is applied building on the model of Dodd et al. (2008), which succeeds in simulating the occurrence of beach cusps. The numerical scheme improves the accuracy and stability of the swash zone computation. Results from a comparison between different numerical implementations concludes that the most suitable numerical scheme is the Roe-averaged scheme of Castro Diaz et al. (2008) with Minmod flux-limiter using the Harten and Hyman (1983) entropy fix method and the Hubbard and Dodd (2002) approach for the shoreline boundary condition.

Before simulating the 2D beach cusps, the sensitivity of the model parameters and two different types of incoming waves are tested in the 1D bed change. The sensitivity test results show that there is a convergence of the results when the

minimum computational depth ($d_{tol} \leq 1$ mm). Also the relationship between the bed profile and beach cusp parameters is that a greater maximum tip position ($x_{s,max}$) is achieved, and more erosion in the tip region occurs when the bed friction coefficient (f_w), the hydraulic conductivity (K), and d_{tol} are smaller. On the other hand, the effect of scaling the sediment transport coefficient (A) is to scale the rate of change of the bed level, and appears not to lead to qualitative differences. Moreover, the incoming sine wave creates three components of 1D beach profile (long-shore bar, trough, and swash berm) in the computational domain, while the incoming sawtooth wave creates a wider equivalent region, because of wave simply breaking farther offshore.

The 2D simulations give approximately the same beach cusp formation as those of Dodd et al. (2008); however, the geometrical parameters (f) from the self-organisation theory are still high when compared with previous field observation and numerical simulations. The evolution of the beach cusps is investigated by Fourier and global analyses (Garnier et al., 2006), and can be divided into three stages: 1D development in the cross-shore profile, 2D small cusp spacing pattern, and 2D final bigger cusp spacing pattern, caused by the coalescing of two small bays and subsequent rearrangement to an equal spacing. However, an unphysical behaviour is found during cusp evolution, which is the reversing behaviour between horn and embayment. It appears that this reversible behaviour is caused by deposition at the embayment head, created from high infiltration and the usage of the velocity-only type of sediment transport equation in the model.

Acknowledgements

I would like to thank my supervisor Professor Nicholas Dodd for his continual guidance and support during my PhD. He provided a constant supply of ideas, motivation and all essential to the successful completion of this thesis.

I would also like to acknowledge the help and support of my colleagues at the Environmental Fluid Mechanics research group both past and present; in particular Dr. David Kelly, Dr. Roland Garnier, Dr. Riccardo Briganti, Mr. Meinard Tiessen, Dr. Haider Hasen, and Mr. Diego Pedrozo-Acuña. Additionally, I would like to thank my friends at the Coates building room C11, postgraduate research office; Dr. Sebastian Skatulla, Dr. Omar Amoudi, Miss Julia Revuz, Mr. Karwan Fendi, Mr. Bruce Kakimpa, and Dr. Jean-francois Ferellec for making the office a better place and teaching me the multi-cultural experiences.

I wish to give a special thank to my parents for their supports all time of my life. My brothers, Tae and Top, and my family for their best wishes to me. Lastly, I wish to thank my beautiful girlfriend, Nice, for getting me through the tough times.

Throughout the course of this research, I was in receipt of a generous grant from the Royal Thai Government and my department, Department of Water Resources Engineering, Faculty of Engineering, Chulalongkorn University for the funding my Ph.D. tuition fee and my living expense in UK.

Notation

[*] Denotes units of the parameter or variable

A [m^{-1}s^2]	Sediment transport coefficient
\tilde{A} [-]	Roe-averaged Jacobian matrix of cross-shore direction $\frac{\partial \vec{F}}{\partial \vec{W}}$
$\tilde{\mathcal{A}}$ [-]	Roe-averaged Castro-Diaz Jacobian matrix of cross-shore direction
b [m]	Bed change from initial beach profile
$ b $ [m]	Global bed change
$ b - \langle b \rangle $ [m]	Global bed change with alongshore averaged subtraction
$\langle b \rangle$ [m]	average of bed change in alongshore direction
B [m]	Bed level
B_t [ms^{-1}]	Rate of bed change
$B_{t,max}$ [ms^{-1}]	Maximum value of rate of bed change
$B_{t,norm}$ [ms^{-1}]	Normalised value of rate of bed change $\frac{B_t}{ B_{t,max} }$
$B_B(x)$ [m]	Cross-shore profile of embayment section
$B_H(x)$ [m]	Cross-shore profile of horn section

$\tilde{\mathbf{B}}$ [-]	Roe-averaged Jacobian matrix of alongshore direction $\frac{\partial \vec{G}}{\partial \vec{W}}$
$\tilde{\mathcal{B}}$ [-]	Roe-averaged Castro-Diaz Jacobian matrix of alongshore direction
B [-]	Nonlinear flux limiter function
c [ms^{-1}]	Wave celerity
c_0 [ms^{-1}]	Initial wave celerity
C [-]	Diffusion coefficient
d [m]	Total water depth
d_0 [m]	Initial water depth
d_i [m]	Undisturbed water depth
d_{tol} [m]	Minimum computation depth
\hat{d} [-]	Dimensionless total water depth
D_{50} [m]	Sediment grain size diameter
\tilde{D} [-]	Roe-averaged term corresponding to the sediment transport equation
\vec{e}_k [-]	Right eigenvectors of the Roe-averaged Jacobian matrix
\tilde{E} [-]	Roe-averaged term corresponding to the sediment transport equation
f [-]	Geometrical parameter
f_w [-]	Bed friction coefficient
\vec{F} [-]	Vector of interface fluxes for cross-shore direction
g [ms^{-2}]	Gravity acceleration
\vec{G} [-]	Vector of interface fluxes for alongshore direction

h_0 [m]	Initial water depth at offshore boundary
h_b [m]	Uniform bore height
H_h [m]	Hydraulic head
\mathcal{H} [m]	Fourier coefficient of the topographic signal
K [ms ⁻¹]	Hydraulic conductivity
L_x [m]	Length of computation domain in cross-shore direction
L_y [m]	Length of computation domain in alongshore direction
M [m]	Averaged cross-shore profile between horn and embayment
N_x [-]	Number of computation cell in cross-shore direction
N_y [-]	Number of computation cell in alongshore direction
p [-]	Porosity of the beach material
\vec{q} [m ² s ⁻¹]	Sediment transport rate
\vec{q}^* [m ² s ⁻¹]	Modified sediment flux vector
q_u [m ² s ⁻¹]	Cross-shore sediment transport rate
q_v [m ² s ⁻¹]	Alongshore sediment transport rate
Q_c [m ² s ⁻¹]	Discharge of channel flow
\tilde{r}_k [-]	Ratio of upwind wave strength to the local wave strength
Re [-]	Reynolds number
\mathcal{R} [-]	Right eigenvector matrix
S_e [m]	Swash excursion
S_s [m ⁻¹]	Specific yield
\vec{S} [-]	Vector of source terms
t [s]	Time

t_{res} [s]	Residual time of the number of wave period
t_{swash} [s]	Swash period
T [s]	Wave period
u [ms ⁻¹]	Cross-shore velocity
U [ms ⁻¹]	Cross-shore depth-averaged velocity
$\langle U \rangle$ [ms ⁻¹]	Cross-shore velocity averaged over alongshore section
U_b^* [ms ⁻¹]	Bore velocity at the initial shoreline position
U_{cr} [ms ⁻¹]	Critical velocity for sediment movement
U_s [ms ⁻¹]	Tip speed
\vec{U} [ms ⁻¹]	Vector of horizontal depth-averaged velocity
v [ms ⁻¹]	Alongshore velocity
\tilde{v}_k [-]	Courant number
V [ms ⁻¹]	Alongshore depth-averaged velocity
V_b [m ³]	Net volume of the bed change
w [ms ⁻¹]	Vertical flow velocity in the porous media
\vec{W} [-]	Vector of conserved variables
x [m]	Cross-shore co-ordinate
x_0 [m]	Initial co-ordinate
x_s [m]	Shoreline position or tip position
$x_{s,max}$ [m]	Maximum tip position
$x'_{s,max}$ [m]	Maximum tip position of SM63 analytical solution
y [m]	Alongshore co-ordinate
z [m]	Vertical co-ordinate

$\tilde{\alpha}_k$ [-]	Roe-averaged wave strength
$\tilde{\beta}_k$ [-]	Roe-averaged source term decomposition coefficient
$\tan \beta$ [-]	Beach slope
γ_s [-]	Specific gravity of sediment $\frac{\rho_s}{\rho}$
δ_k [ms ⁻¹]	Entropy fix parameter
Δt [s]	Time step
Δx [m]	Cross-shore grid spacing
Δy [m]	Alongshore grid spacing
ϵ [-]	Computation error in each cell and equation
ϵ_c [-]	Idealised beach cusp parameter
ϵ_p [m]	Perturbed elevation
ϵ_{rms} [-]	Root mean square error of the computational cells
ζ [m]	Free surface elevation in the porous media
η [m]	Free surface elevation
ζ_0 [m]	Unperturbed surface elevation
λ_c [m]	Cusp spacing
λ_m [m]	Cusp dominant wavelength from Fourier analysis
$\tilde{\lambda}_k$ [ms ⁻¹]	Eigenvalues of the Roe averaged Jacobian matrix (characteristic speed)
ν [m ² s ⁻¹]	Kinematic viscosity
ξ [-]	Bed porosity parameter $\frac{1}{1-p}$
ρ [kgm ⁻³]	Density of water
ρ_s [kgm ⁻³]	Density of sediment

σ [s^{-1}]	Linear growth rate
ϕ [-]	Angle of repose of sediment

Subscripts:

a	Denotes Roe-averaged Jacobian matrix component number
b	Denotes Roe-averaged Jacobian matrix component number
i	Cell number in cross-shore direction
j	Cell number in alongshore direction
k	Denotes Roe-averaged Jacobian matrix component number
L	Denotes left component of computational cell
n	Denotes number of equation
P	Denotes Primitive variables
R	Denotes right component of computational cell

Superscripts:

F	Denote that variable is associated with \vec{F}
G	Denote that variable is associated with \vec{G}
L	Denotes left edge of the rarefraction wave
R	Denotes right edge of the rarefraction wave
n	Time level
\wedge	Denotes non-dimensional variable
\sim	Denotes Roe-averaged variable

Contents

1	Introduction	1
2	Literature Review	8
2.1	Swash Zone Processes	8
2.1.1	Swash Infiltration	11
2.1.2	Swash Sediment Transport	14
2.2	Beach Cusps	15
2.2.1	Standing Edge Wave Theory	18
2.2.2	Self-Organisation Theory	20
2.2.3	Physical Mechanisms	21
2.3	Numerical Model in Swash Zone	21
2.3.1	Non-Linear Shallow Water Equations	22
2.3.2	Morphodynamic Models	26

3	Morphodynamic Model	32
3.1	Governing Equations	33
3.2	Sediment Transport Rate	35
3.3	Bed Diffusion	37
3.4	Infiltration	38
3.5	Roe's Scheme	41
3.5.1	Source Terms	45
4	Model Development	46
4.1	Entropy Fix	47
4.1.1	Harten and Hyman Entropy Fix	49
4.1.2	Hubbard and Dodd Entropy Fix	49
4.2	Castro-Diaz Scheme	50
4.3	Time Operator Splitting Scheme	60
4.4	Shoreline Boundary Condition	63
4.4.1	Wetting/Drying Algorithm	63
4.4.2	Fluxes via Hubbard and Dodd Approach	64
4.4.3	Primitive Form BC	65

4.5	Test Cases	74
4.5.1	Dam-break Problem	75
4.5.2	Shen and Meyer Solution	76
4.5.3	Hibberd and Peregrine Solution	78
4.6	Test Results	79
4.6.1	Comparing the Entropy Fixes	81
4.6.2	Results from Test Cases	85
4.6.3	Comparing Testing Case Results with Previous Works . .	90
5	1D Swash Zone Simulation	99
5.1	1D Long-term Evolution of Beach Profile	99
5.2	Sensitivity Test of Numerical Parameters	101
5.2.1	Variation in Minimum Depth	102
5.3	Sensitivity Test for Physical Parameters	104
5.3.1	Variation in Bed Friction	104
5.3.2	Variation in Hydraulic Conductivity	106
5.3.3	Variation in Sediment Transport Coefficient	106
5.4	Variation in Incoming Wave Types	108

5.5	Discussion	110
6	Formation and Evolution of Beach Cusps	115
6.1	2D Cusp Simulation	116
6.1.1	Perturbations in the model	117
6.1.2	Comparison of Wave Perturbation and Bed Perturbation .	119
6.1.3	Comparison in Positions and Elevation of Bed Perturbation	122
6.2	Cusps Parameters	124
6.2.1	Growth rate	124
6.3	Beach Cusp Formation	128
6.4	Beach Cusp Evolution	131
6.5	Global Analysis	137
6.6	Simulation of Initial Curved beach	140
6.6.1	Cusp Formation of Initial Curved beach	142
6.6.2	Evolution of Initial Curved beach	145
6.7	Discussion	147
6.7.1	Sensitivity Test of Bed Diffusion Coefficient	147
6.7.2	Reversible Behaviour	149

6.7.3	The Effect of Domain size	150
6.7.4	Grid Convergence	151
6.7.5	Numerical Problems in the model	153
7	Beach Permeability	154
7.1	Sensitivity Test of Hydraulic Conductivity in 2D Simulations . . .	155
7.2	Infiltration in One Swash Period	159
7.3	Variation in Infiltration Calculation	162
7.4	Discussion	168
8	Testing Sediment Transport Equations	174
8.1	Sediment Transport in One Swash Period	175
8.2	Dean and Maurmeyer Beach Cusps	180
8.3	Variation in Sediment Transport Equations	182
8.4	Discussion	186
9	Conclusions and Recommendations	192
9.1	Review and Conclusions	192
9.2	Recommendations for future research	197

References

200

List of Figures

- 2.1 Types of swash flow circulation associated with beach cusp morphology (Masselink and Pattiaratchi, 1998). 17
- 2.2 Shallow water flow with a surface under gravity in 1D. 23
- 2.3 Flowchart of the morphodynamic model (from Horikawa (1988)). 28
- 3.1 Computation domain and boundary conditions. 36
- 3.2 Run-up on initially dry beach. 39
- 3.3 Grid system used to solve the numerical scheme within *OTT2dm*.
 (*) is cell centre, (x) cell interface (edge). 42
- 4.1 Entropy fix for left transonic rarefaction wave. The single jump $U_{*L} - U_L$ travelling with speed $\tilde{\lambda}_k$ is split into the two jumps $U_{SL} - U_L$ and $U_{*L} - U_{SL}$ travelling with speeds λ_k^L and λ_k^R ; where U_{SL} is a transonic state. 48

4.2	Water depth results of the classical dambreak problem simulated by Dodd et al. (2008) model where a) $B = 0$ m case and b) $B = 1$ m case.	52
4.3	The wetting/drying procedure illustrated in 1D.	65
4.4	Applying the primitive and normal Roe-averaged fluxes to cells illustrated in 1D	66
4.5	Initial conditions of dambreak test case	76
4.6	Initial conditions of SM63 test case	77
4.7	Notation and initial bathymetry for a uniform bore approaching a plane sloping beach	79
4.8	Water depth results of the dambreak problem simulated by first order upwind Castro-Diaz scheme where a) $B = 0$ m case and b) $B = 1$ m case.	80
4.9	Results of dambreak problem using a) no entropy fix, b) Harten and Hyman entropy fix, and c) Hubbard and Dodd entropy fix.	82
4.10	Results of SM63 problem using a) no entropy fix, b) Harten and Hyman entropy fix, and c) Hubbard and Dodd entropy fix.	83
4.11	Results of HP79 problem using a) no entropy fix, b) Harten and Hyman entropy fix, and c) Hubbard and Dodd entropy fix.	84
4.12	Examples of strange behaviours that occur in the test cases.	88

4.13	Comparing the model result (colour lines) with Ritter solution (dashed black lines) for rigid bed dambreak problem when $f_w = 0$, $d_{tol} = 0.0001$ m, $A = 1 \times 10^{-8}$ s ² /m.	92
4.14	Comparing the model result (colour lines) with numerical solution of Kelly and Dodd (2009) (dashed black lines) for mobile bed dambreak problem when $f_w = 0$, $d_{tol} = 0.0001$ m, $A = 0.004$ s ² /m.	93
4.15	Comparing the model result (colour lines) with analytical solution (dashed black lines) for SM63 case when $f_w = 0$, $d_{tol} = 0.0001$ m, $A = 0.004$ s ² /m.	94
4.16	Comparing tip result of SM63 case between analytical solution and the model result.	95
4.17	Comparing the model result with approximate solution for HS03 case at $t = 230,000$ s.	98
5.1	1D simulation initial condition.	100
5.2	Bed change result of 1D beach profile evolution for the reference case.	101
5.3	Bed change results of sensitivity test of minimum depth, d_{tol} , from $t = 0 - 20,000$ s. a) $d_{tol} = 0.5$ mm, b) $d_{tol} = 1.0$ mm, c) $d_{tol} = 2.0$ mm, d) $d_{tol} = 5.0$ mm.	103

5.4	Bed change results of sensitivity test of bed friction, f_w from $t = 0 - 20,000$ s. a) $f_w = 0.005$, b) $f_w = 0.02$, c) $f_w = 0.05$, d) $f_w = 0.1$	105
5.5	Bed change results of sensitivity test of hydraulic conductivity, K from $t = 0 - 20,000$ s. a) $K = 0.001$ m/s, b) $K = 0.01$ m/s, c) $K = 0.04$ m/s.	107
5.6	Bed change results of sensitivity test of sediment transport coefficient, A from $t = 0 - 20,000$ s. a) $A = 0.001$ s ² /m, b) $A = 0.004$ s ² /m.	108
5.7	Bed change results of sensitivity test of sediment transport coefficient, A from $t = 0 - 20,000$ s. a) $A = 0.001$ s ² /m, b) $A = 0.004$ s ² /m.	110
5.8	Bed change results of $A = 0.04$ s ² /m during $t = 60-63$ s.	113
6.1	Change in bed level (m) relative to a plane beach (colours) after 20, 100, 200, 300, and 400 periods, and velocity vectors averaged over preceeding period for the wave perturbation reference case.	120
6.2	Change in bed level (m) relative to a plane beach (colours) after 20, 100, 200, 300, and 400 periods, and velocity vectors averaged over preceeding period for the bed perturbation at (5,25) with $\epsilon_p = 1$ mm, and other parameters as same as reference case.	121

6.3 Change in bed level (m) relative to a plane beach (colours) after 400 periods, and velocity vectors averaged over preceeding period for the bed perturbation at a) (3,25) with $\epsilon_p = 1$ mm, b) (5,25) with $\epsilon_p = 1$ mm, c) (7,25) with $\epsilon_p = 1$ mm, and d) (5,25) with $\epsilon_p = 5$ mm. 123

6.4 Definition of beach cusp spacing and swash excursion. 125

6.5 Linear growth rate computation using discrete Fourier analysis for the reference case ($T = 5$ s) at section $x = 7.2$ and 5.1 m. a) Series of the $x = 7.2$ m section in time, b) Discrete Fourier analysis of the section $x = 7.2$ m, c) Logarithmic value of the amplitude of the dominant wavelength for section $x = 7.2$ m, d) Series of the $x = 5.1$ m section in time, e) Discrete Fourier analysis of the section $x = 5.1$ m, f) Logarithmic value of the amplitude of the dominant wavelength for section $x = 5.1$ m. 127

6.6 Changing in bed level (m) relative to a plane beach (colours), and velocity vectors averaged over preceeding period after 400 periods of $T = 3, 4, 5, 6, 7$, and 8 s cases. 129

6.7 Change in bed level (m) relative to a plane beach (colours) and velocity vectors averaged over preceeding period for the reference case from $t = 100$ -500 s. 132

6.8	Change in bed level (m) relative to a plane beach (colours) and velocity vectors averaged over preceeding period for the reference case from $t = 600$ - $1,000$ s.	133
6.9	Change in bed level (m) relative to a plane beach (colours) and velocity vectors averaged over preceeding period for the reference case from $t = 1,100$ - $1,500$ s.	134
6.10	Change in bed level (m) relative to a plane beach (colours) and velocity vectors averaged over preceeding period for the reference case from $t = 1,600$ - $2,000$ s.	135
6.11	Comparison of a) the global bed change ($ b $), b) the global bed change with alongshore averaged subtraction ($ b - \langle b \rangle $), and c) the Fourier analysis of section $x = 7.2$ m for the reference case. . .	138
6.12	Comparison of the global bed change with alongshore averaged subtraction in time for different d_{tol} values of the $T = 3, 4, 5, 6, 7$, and 8 s case. Solid line: $d_{tol} = 0.5$ mm; dot-dashed line: $d_{tol} = 1$ mm; dashed line: $d_{tol} = 2$ mm; thick solid line: $d_{tol} = 5$ mm. . . .	141
6.13	Differences of $ b - \langle b \rangle $ between $d_{tol} = 0.5$ and 1.0 mm over h_0 of $T = 3, 4, 5, 6, 7$, and 8 s cases.	143
6.14	Comparison of averaged beach profile between the initial plane sloping beach and the initial curved beach for $T = 4$ s cases at $t = 400$ periods.	145

6.15 The global bed change with alongshore averaged subtraction in
time of initial curved beach, $T = 5$ s case. 146

6.16 Change in bed level (m) relative to a plane beach (colours) after
20, 100, 200, 300, and 400 periods, and velocity vectors averaged
over preceeding period for sensitivity test of bed diffusion, $C =$
2.0, when other parameters as same as reference. 148

6.17 The global bed change with alongshore averaged subtraction in
time for expansion in y -direction to 60 m case when other param-
eters as same as reference. 151

6.18 Grid convergence test result. 153

7.1 Change in bed level (m) relative to a plane beach (colours) after
20, 100, 200, 300, and 400 periods, and velocity vectors averaged
over preceding period for $K = 0.001$ m/s, and other parameters
as same as reference. 156

7.2 Change in bed level (m) relative to a plane beach (colours) after
20, 100, 200, 300, and 400 periods, and velocity vectors averaged
over preceding period for $K = 0.005$ m/s, and other parameters
as same as reference. 157

- 7.3 Change in bed level (m) relative to a plane beach (colours) after 20, 100, 200, 300, and 400 periods, and velocity vectors averaged over preceding period for $K = 0.02$ m/s, and other parameters as same as reference. 158
- 7.4 Instantaneous infiltration velocity, w , (m/s) and depth averaged velocity vectors over one wave period ($t = 503$ - 508 s) for the reference case. 160
- 7.5 Accumulated infiltration volume (m^3) over one swash period ($t = 503$ - 508 s) and average velocity vectors at $t = 508$ s for the reference case. 161
- 7.6 Difference in sediment sizes along the beach cusps at Barton on Sea, UK provided by Guthrie, J.G.L. 164
- 7.7 Change in bed level (m) relative to a plane beach (colours) after 20, 100, 200, 300, and 400 periods, and velocity vectors averaged over preceding period for Alternative 1). 165
- 7.8 Change in bed level (m) relative to a plane beach (colours) after 20, 100, 200, 300, and 400 periods, and velocity vectors averaged over preceding period for Alternative 3). 166
- 7.9 Change in bed level (m) relative to a plane beach (colours) after 20, 100, 200, 300, and 400 periods, and velocity vectors averaged over preceding period for Alternative 4). 167

7.10	Instantaneous infiltration velocity, w , (m/s) and depth averaged velocity vectors over one wave period ($t = 503\text{-}508$ s) for Alternative 3).	170
7.11	Instantaneous infiltration velocity, w , (m/s) and depth averaged velocity vectors over one wave period ($t = 503\text{-}508$ s) for Alternative 4).	171
7.12	Accumulated infiltration volume (m^3) over one swash period ($t = 503\text{-}508$ s) and average velocity vectors at $t = 508$ s for the infiltration only uprush phase case.	172
7.13	Accumulated infiltration volume (m^3) over one swash period ($t = 503\text{-}508$ s) and average velocity vectors at $t = 508$ s for the linear variation of K case.	172
8.1	Normalised rate of bed change computed from $q = AU U ^2$ over one swash motion during $t = 503\text{-}508$ s and depth averaged velocity vectors for the reference case result.	176
8.2	Accumulated volume of the normalised value of B_t over one swash period ($t = 503\text{-}508$ s) computed from $q = AU U ^2$ of the reference case result.	177
8.3	Normalised rate of bed change computed from $q = AdU U ^2$ over one swash motion during $t = 503\text{-}508$ s and depth averaged velocity vectors for the reference case result.	179

8.4	Accumulated volume of the normalised value of B_t over one swash period ($t = 503-508$ s) computed from $q = AdU U ^2$ of the reference case result.	180
8.5	The idealised beach cusp topography created from the result of reference case.	181
8.6	The circulation pattern (vectors) averaged over preceeding wave period on the idealised beach cusp topography and the bed level (m) relative to the plane sloping beach (colours).	182
8.7	Accumulated volume of the normalised value of B_t over one swash period computed from a) $q = AU U ^2$, b) $q = AU U ^3$, c) $q = AdU U ^2$, d) $q = AdU U ^3$, e) $q = AU(U ^2 - U_{cr}^2)$, and f) $q = AdU(U ^2 - U_{cr}^2)$	185
8.8	Shoreface area topography of idealisation of beach cusp topography from data adaption equation.	189
8.9	Normalised rate of bed change computed from $q = AdU U ^2$ over one swash motion and depth averaged velocity vectors for the hydrodynamic on the idealised beach cusps.	191

List of Tables

4.1	Summary of results from the test cases	87
6.1	Summary of results of the morphodynamical simulations comparing with permeable beach results of Dodd et al. (2008).	130
6.2	Summary of the creation time from the plane slope beach results to create the initial curved beach profiles.	143
6.3	Summary of results of the morphodynamical simulations for the initial curved beach profiles	144
7.1	The alternatives of the K implementation.	163
8.1	Summary of the accumulated volume of the normalised value of B_t over one swash period in different area of beach cusps for the different sediment transport formulations.	187

CHAPTER 1

Introduction

The coastline, the boundary between land and sea, changes its shape and position continuously. Natural coastlines vary from the cohesive sediment coast (muddy beaches), sandy beaches, to the steep rocky cliff. Since the sandy beach is easily deformed by the action of wave and current compared with the rocky cliff, it is of particular interest to scientists and engineers.

This study focuses on modelling the changes of a coarse sand or gravel beach in the swash zone. On a typical beach, the swash is defined by Horikawa (1988) as the zone extending landward from the point of collision between backwash and the incoming waves to the wave uprush limit. This region is alternately wetted and dried from the incoming wave runup and rundown, which process is referred to as "*Swash motion*". Swash motions make the movement of water particles dynamic and complex, and strongly influence the sediment transport processes in this region. These sediment transport processes affect the beach

morphology leading to the creation of a typical swash zone profile, and also of alongshore features, including berms and beach cusps.

The major factor that makes the coastline change is wave and current action. This interaction between incoming waves and bed change in the swash zone is a complex process; however, it further is influenced by other factors such as the local groundwater table (Baird et al., 1998; Butt and Russell, 2000). Water moving up and down the beach during a swash motion has the potential to infiltrate into and to exfiltrate out of the beach face depending on the local position of the groundwater level. The infiltration (this study considers only infiltration) that occurs reduces the volume of water in the swash and thus also decreases the momentum of the swash. This infiltration action enhances the onshore sediment transport in the swash zone (Turner and Masselink, 1998).

Since the flow in the swash is complex and highly energetic, it has led to difficulties in measuring and obtaining data from field observation (Elfrink and Baldock, 2002). In the past, this led to an incomplete understanding of the processes in this zone, which in turn retarded the development of numerical models; however, measuring equipments and data collection techniques have been improved in very recent times. As a result, a better understanding of swash zone processes has helped to drive the development of numerical models for simulating beach change in the swash zone.

Early in the development of numerical models in the swash zone, the focus was on determining the motion of the water and shoreline moving up and down

the beach (Hibberd and Peregrine, 1979; Kobayashi et al., 1987, 1989). As swash zone processes (especially sediment transport) have become better understood, the focus of more recent numerical research has changed to determining sediment transport and morphology change (Hudson and Sweby, 2003; Pritchard and Hogg, 2005; Castro Diaz et al., 2008; Kelly, 2009). 2D or 3D morphodynamic models for determining the motion in the swash zone are becoming interesting topics for coastal research (Karambas and Koutitas, 2002; Zyserman and Johnson, 2002; Grunnet et al., 2004; Dodd et al., 2008).

Beach cusps are a particular feature of the swash that has a quasi-regular spacing. They are mostly observed in the swash zone on steeper beaches with coarse-grained sediment. Many scientists and engineers have attempted to explain how beach cusps form and develop. As a result of this work, two contrasting theories for their formation have gained acceptance: the subharmonic edge wave theory (a hydrodynamic explanation stemming from linear shallow water theory (Guza and Inman, 1975)) and the self-organisation theory (a morphodynamic explanation that has been illustrated using an abstracted model incorporating ballistic theory (Werner and Fink, 1993; Coco et al., 2000)).

Although many scientists and engineers tried to explain the formation of beach cusps by using the the subharmonic edge wave theory, self-organisation theory, or both of them, these previous studies either ignored the role of sediment or simplified the water motion. The physical mechanisms of beach change, which are depended on the hydrodynamic, are presented by Dodd et al. (2008) to de-

scribe the relationship between incoming wave conditions and beach cusp formation. In that study, the 2D process-based morphodynamic model, '*OTT2dm*', solving nonlinear shallow water equations with sediment conservation equation simultaneously is successful for simulating the beach cusps; however, they did not describe the evolution of beach cusps and the relationship between the beach cusp formation and sediment properties. Moreover, there still some limitations in the model; therefore, a numerical implementation is required to improve the accuracy of simulation.

Consequently, this study aims to improve understanding of the formation and long-term evolution of beach cusps by numerical simulation using 2D process-based morphodynamic model including infiltration. To achieve this aim, the objectives of this thesis are:

- Improving the accuracy of computation of a 2D process-based morphodynamic model used to simulate the beach cusps by implementing a numerical scheme.
- Improved understanding of the formation and long-term evolution of beach cusps under different incoming wave conditions, beach profiles, and sediment properties.
- A better understanding of the importance of the physical effects leading to sedimentation and erosion in the swash, in particular, to beach cusp formation.

The summary of the previous research prior to and motivating this study is described in Chapter 2. It contains the background knowledge of the swash zone processes including swash infiltration and swash sediment transport, theories about the occurrence of beach cusps, and numerical modelling in the swash zone.

Chapter 3 presents the governing equations used in this study and the numerical scheme of the Dodd et al. (2008) morphodynamic model. This chapter discusses the nonlinear shallow water equations and sediment conservation equation, which are the main equations in the model. The representations of bed diffusion and infiltration are also described. Moreover, Roe's scheme, used for capturing the shock behaviour in the computation, is explained there.

Chapter 4 explains the new numerical implementation for improving the accuracy of computation for the model. Entropy fixes, the Castro Diaz et al. (2008) numerical scheme, the time operator splitting scheme, and special numerical treatment of the shoreline boundary condition are illustrated. To assist in these developments, the cases of dambreak problems, the Shen and Meyer (1963) problem, and the Hibberd and Peregrine (1979) problem are used to test for the new implementations. The comparison between the model results and the previous solutions including analytical and numerical solutions is also demonstrated in this part.

After the new numerical scheme is tested, the 1D long-term beach change is simulated and shown in Chapter 5. This Chapter provides the sensitivity test

of important parameters which can be divided into two groups: numerical and physical parameters. The numerical parameter is minimum depth d_{tot} , and the physical parameters are bed friction coefficient f_w , hydraulic conductivity K , and sediment transport coefficient A .

In Chapter 6, the 2D formation and long-term evolution of beach cusps are investigated. Beach cusp parameters are defined in terms of physical formation, cusp spacing and swash excursion, and long-term evolution, and linear growth rate; 2D simulation results of beach cusps formation for the numerically improved model are also shown. With the complexity in the evolution of beach cusps, the global analysis is introduced by Garnier et al. (2006) for analysing the bed pattern data. Although the new numerical implementation gives the better calculation results, there are some cusp behaviours due to the physical properties that need more investigations. These are explained in the discussion part of this chapter.

The particular investigation of these physical properties is, respectively, shown in Chapter 7 and 8. In Chapter 7, the infiltration rate and volume of water that is lost in the beach over one swash period are discussed. Moreover, variation of the permeability conditions is implemented. Similarly in Chapter 8, the bed change over one swash cycle is discussed. Many sediment transport equations including Grass (1981) model, Pritchard and Hogg (2005) equations, and also the threshold sediment transport equation are tested to see the effect on beach change.

Finally, Chapter 9 contains the conclusion and discussion of the new findings from this thesis. Moreover, the recommendations for the future work are also stated in order to further understanding and investigation of the physics of swash zone morphodynamics.

CHAPTER 2

Literature Review

Beach cusps are an alongshore feature in the swash zone. The occurrence of a cusp pattern is the natural combination between the incoming waves and beach characteristics. To simulate this cusp pattern using a numerical model means that the model must incorporate the relevant physical processes of the swash zone. Therefore, the previous work on beach cusps and on numerical modelling in the swash zone are presented in this chapter.

2.1 Swash Zone Processes

The swash zone is the relatively steep upper part of the beach profile where the wave runs up and down the beach. The swash motion comprises a series of strong and unsteady flows of this run up and down, and it forms a continuously changing dynamic boundary between wet and dry zones of the beach, affecting

the large sediment transport and morphology changes at the shoreline (Elfrink and Baldock, 2002; Masselink et al., 2005).

Elfrink and Baldock (2002) classified the swash oscillations into two broadly different types: non-breaking standing waves (infragravity or edge waves) and broken short wave (bores). Edge waves are long-shore periodic wave motion that are trapped at the shoreline, and travel alongshore parallel to the beach (Guza and Inman, 1975; Horikawa, 1988; Butt and Russell, 2000). Cross-shore non-breaking standing wave oscillations are usually observed at low frequencies (infragravity range) corresponding to a wave period (T) between 30-300s or edge waves, T between 15-25s, whereas swash motions due to bores which collapse at the shoreline and propagate up the beach have T between 5-15s (Hughes, 1992). Both types of swash oscillation occur naturally at the same time, but one type dominates the motion behaviour depending on the site and to a large extent on the surf zone condition (Elfrink and Baldock, 2002).

Swash motion can be broken down into two phases: the uprush and the backwash. During the uprush, flow velocity at the tip increases very quickly from zero to its maximum after the arrival of the leading edge of the swash or the bore collapse; then the flow velocities decrease steadily to zero during the remainder of the uprush. On the other hand, during the backwash flow velocity increases gradually under gravity from zero to its maximum until it meets the next incoming wave (Hibberd and Peregrine, 1979; Hughes et al., 1997). One of the differences of the swash oscillation that is created from infragravity and

high frequency waves is the symmetry of the uprush and backwash velocities at a point. The flows of infragravity oscillations are approximately symmetrical; on the other hand, those created from bores are significantly asymmetrical (Butt and Russell, 1999; Elfrink and Baldock, 2002). Moreover, the duration of backwash is typically longer than the uprush (Hughes et al., 1997; Butt and Russell, 2000; Masselink and Hughes, 1998).

High free stream velocities are commonly found in swash motion. The uprush and backwash velocities in the field have been observed to exceed 2 m/s (Hughes et al., 1997; Butt and Russell, 1999; Elfrink and Baldock, 2002; Masselink et al., 2005), while the maximum velocities occur at the start of the uprush and at the end of backwash. With the high velocity flow and shallow water depths in the backwash phase, this combination may result in supercritical flow conditions and hydraulic jumps called "*backwash bores*" at the end of this phase, when the backwash water meets the next incoming wave (Hibberd and Peregrine, 1979; Masselink et al., 2005). This is one of the examples of turbulence in the swash zone. Other potential sources of turbulence are that advected from the inner surf zone, initial bore collapse at the shoreline, and turbulence due to bed friction (Elfrink and Baldock, 2002). This turbulence can affect the interaction between water and sediment and therefore sediment transport and morphology changes in the swash zone.

The roughness of the beach affects swash motion when the flow passes over it. Increased roughness slows the flow down as it passes over the beach and is of-

ten described in terms of a bed friction coefficient, f_w . From field observations, f_w varies with each phase of the swash cycle (Puleo and Holland, 2001; Masselink et al., 2005; Masselink and Puleo, 2006); however, there is still no exact conclusion about which phase of swash motion that has greater f_w .

2.1.1 Swash Infiltration

One of the important factors that influences the swash motion is the groundwater table. The position of the local groundwater table will determine the ability of the water in the swash to move vertically in/out of the beachface (infiltration/exfiltration). During the uprush phase, if the beach is dry (i.e. the groundwater table is low), the water will infiltrate into the beach; hence the volume and momentum is reduced in the backwash period decreasing the potential to move the sediment to the offshore. Moreover, the reduction of water volume and momentum from the infiltration is not only the main effect, but the effective weight and shear force on sediment particles are also the reason that the infiltration processes enhance the onshore sediment transport (see more details in Turner and Masselink (1998); Butt et al. (2001)).

In contrast, when groundwater table is high, the outflow of groundwater will exfiltrate to the beach to increase the volume of the swash; then the exfiltration will promote the offshore sediment transport. The process of exfiltration has been investigated in the past (Turner and Masselink, 1998; Butt et al., 2001; Li et al., 2002; Karambas, 2003), and it has been shown that infiltration-exfiltration

support the net upslope sediment transport during the uprush. The process of exfiltration will not be considered in this study.

The infiltration increases the asymmetry in the swash flow by weakening the backwash with respect to the uprush because most of the water that infiltrates will not participate in the backwash (Butt and Russell, 2000; Masselink and Li, 2001). The reduction in water volume due to infiltration decreases significantly the energy available for offshore sediment transport (Baird et al., 1998); therefore, the result is a net onshore sediment transport (Li et al., 2002).

Packwood (1983) used a numerical model based on the non-linear shallow water (NLSW) equations to simulate the runup due to a single bore incident on an initially dry beach. The infiltration rate was calculated using Darcy's law assumption that the flow will be predominantly vertical into the beach, driven by the time varying head of water above the bed, and used the model provided by Dicker (1969). This infiltration approach is simple and easy to implement; therefore, it is used in the model (see more detail in Section 3.4). It was also implemented in the numerical model of Karambas (2003).

However, the approach of Dicker (1969) and Packwood (1983) relies on Darcy's law, which depends on the laminar flow assumption. This is only valid where Reynolds number ($Re = wD_{50}/\nu$) is less than $O(1)$; thus, for example, for a grain diameter (D_{50}) ≤ 0.1 cm and kinematic viscosity $\nu = 0.01$ cm²/s, the assumption of laminar vertical flow is valid when flow velocity (w) < 0.1 cm/s (Turner and Masselink, 1998). On the other hand, the Packwood (1983) approach is also

implicitly limited in the case of a very coarse beach (gravel beach), because the permeability of a gravel beach is high and allows the faster flow percolation into the beach which is beyond the limit of laminar flow (Clarke et al., 2004).

An alternative approach for modelling the groundwater flow uses a 1D Boussinesq equation (Turner and Masselink, 1998; Baird et al., 1998). Turner and Masselink (1998) combined Darcy's law (2.1) with a continuity equation for mass within the bed on the assumption of homogeneous and isotropic sand beach to derive the 1D vertical flow Boussinesq equation (2.2);

$$w = -K \frac{\partial H_h}{\partial z} \quad (2.1)$$

$$\frac{\partial^2 H_h}{\partial x^2} = \frac{S_s}{K} \frac{\partial H_h}{\partial t} \quad (2.2)$$

where w is the vertical flow velocity in the porous media, K is the hydraulic conductivity, H_h is hydraulic head, x and z are horizontal (cross-shore) and vertical co-ordinates, t is time, and S_s is the specific yield, which is the capacity of an aquifer to release groundwater from storage. The numerical solution of (2.2) gives the change in head; then, it can be used in (2.1) to approximate w , and thus the infiltration rate.

The magnitude of the infiltration rate depends upon the position of the local groundwater corresponding to the hydraulic head and the beach material properties. The hydraulic head is the vertical distance between the swash oscillation surface elevation and the groundwater table. The greater hydraulic head has the greater pressure head to drive the water into the beach in order to increase the infiltration rate. With increasing volume of water in the beach, the ground-

water table rises up; then the infiltration stops when the beach becomes saturated. Two beach material properties affecting the infiltration are the porosity of the material and its hydraulic conductivity. The porosity of the beach is a measure how packed the beach material is. A larger porosity means the beach material is not well packed. The hydraulic conductivity is a measure of how fast the water moves in the beach. This factor depends on its grain size. The bigger grain size has the higher values of the hydraulic conductivity associated with a greater infiltration. Packwood and Peregrine (1980) provided values of hydraulic conductivity for each type of sand to gravel beach material.

2.1.2 Swash Sediment Transport

This section describes some important physical mechanisms affecting sediment transport in the swash zone. Initially, the sediment is moving in the same direction as the flow; therefore, sediment transport in the swash tends to be onshore during the uprush phase and offshore during the backwash phase. The asymmetry of the flow during the uprush and backwash leads to a corresponding net asymmetry in the sediment transport and so to change in the cross-shore bed profile and alongshore morphological features.

Although Horn and Mason (1994) found that bedload transport (defined as the sediment grains roll or slide along the bed) is more important in the swash zone than suspended load (defined as the sediment is put into suspension up above the bed, and carried by the current), the exact nature of the sediment

transport in the swash zone is still under discussion (Butt and Russell, 2000). Bedload transport generally dominates the backwash, whereas the combination of both bed load and suspended sediment is more important during the uprush phase (Horn and Mason, 1994; Masselink and Hughes, 1998; Masselink and Puleo, 2006). The sediment suspension is caused by the sudden change from offshore to onshore velocity (i.e. flow acceleration), and also by the turbulence in the swash-front, leading to onshore sediment advection by the uprush (Butt and Russell, 1999). Masselink et al. (2005) recorded that near-bed suspended sediment concentrations in the swash zone generally exceed 100 kg/m^3 at the start and the end of the backwash, and significant sediment concentrations ($> 20 \text{ kg/m}^3$) are often found more than 0.05 m from the bed.

From field observations and measurements, Hughes et al. (1997) and Masselink and Hughes (1998) measured the flow velocity associated sediment transport during both phases of swash motion. They found that the sediment load had a strong relationship with the velocity cubed, consistent with sediment transport equations for both bedload transport and total load transport. As a result of difficulty in separation of the transport modes it may be appropriate to consider the total load (Butt and Russell, 2000).

2.2 Beach Cusps

Many alongshore morphological features are created in the swash zone due to the complex and high energy flows of the swash motion. This study is focused

on only one rhythmic feature: "*beach cusps*". They are quasi-regularly spaced crescentic patterns in the alongshore, formed on the beachface, and mostly observed on steeper beaches with coarse-grained sediment. They consist of steep-gradient, seaward point horns and gentle sloping, seaward facing embayments (Masselink et al., 1997; Masselink and Pattiaratchi, 1998). Typically, the spacing of beach cusps at the coast can be found from a few metres (Longuet-Higgins and Parkin, 1962) up to around 40 m (Holland and Holman, 1996). Giant cusps with spacing greater than 75 m can be found; however, Inman and Guza (1982) claimed those giant cusps are formed by surf zone circulation and not by the swash motion (see also Calvete et al. (2005)).

Many previous studies confirmed that beach cusps are developed and maintained by a swash circulation pattern (Dean and Maurmeyer, 1980; Masselink et al., 1997; Masselink and Pattiaratchi, 1998; Dodd et al., 2008). Masselink and Pattiaratchi (1998) identified five swash flow patterns connected to the occurrence of beach cusps. These are oscillatory swash motion, horn divergent swash motion, horn convergent swash motion, sweeping swash motion, and swash jet as shown in Figure 2.1. The first three types are typical of fair-weather conditions, whereas the latter two types occur during storms. The most important of these swash flow patterns affecting the development of beach cusp is horn divergent flow (Masselink et al., 1997; Coco et al., 2000). Horn divergent patterns are characterised by the wave uprush diverging either side of the horn to the centre of the embayment, thus promoting onshore sediment transport and steep gradients on the cusp horns, and offshore sediment transport and gentle

gradients in the embayments (Dean and Maurmeyer, 1980; Masselink, 1999).

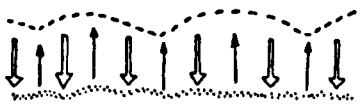



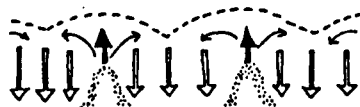
SWASH WATER CIRCULATION	DESCRIPTION
FAIR WEATHER CONDITIONS	
(a) 	OSCILLATORY <ul style="list-style-type: none"> • Predominantly two-dimensional flow up and down the beach • Weak flow divergence on cusp horns • Weak flow convergence in cusp embayments
(b) 	HORN DIVERGENT <ul style="list-style-type: none"> • Swash runup is diverted from cusp horn to embayment • In the embayment, flows meet to form a concentrated backwash • Mini rips form opposite cusp embayments
(c) 	HORN CONVERGENT <ul style="list-style-type: none"> • Swash runup enters the cusp embayment with the bore front aligned with the embayment contours • Uprush spreads laterally to the horns and forms backwash • Mini rips may form opposite cusp horns
STORM CONDITIONS	
(d) 	SWEEPING <ul style="list-style-type: none"> • Swash runup sweeps obliquely across the beachface • Backwash follows a parabolic arc • Littoral drift is pronounced
(e) 	SWASH JET <ul style="list-style-type: none"> • In the embayment, strong backwash retards incoming swash until it has sufficient head to overwhelm the backwash flow and rush up the beach as a narrow jet • Swash runup in the form of a swash jet fans out laterally as in (c)

Figure 2.1: Types of swash flow circulation associated with beach cusp morphology (Masselink and Pattiaratchi, 1998).

Although there is general agreement about the swash circulation conditions associated with cusp generation, there are still differing viewpoints on certain details of cusp formation process. Beach cusp morphology is usually associated with reflective wave conditions, relatively steep beach gradients, and normally incident waves, which can either be plunging or surging breakers, and it has also been noted that they occur on well-sorted coarser grained beach (see more further information in Longuet-Higgins and Parkin (1962); Sallenger

(1979); Dean and Maurmeyer (1980); Holland and Holman (1996); Masselink et al. (1997); Masselink and Pattiaratchi (1998); Coco et al. (2000)).

Historically, the views on the mechanisms leading to the beach cusp generation have been different, but two opposing theories have been generally accepted for describing the formation and behaviour of beach cusps: the standing edge wave model (Guza and Inman, 1975), and the self-organisation model originally proposed by Werner and Fink (1993). The field observation results are mixed. Longuet-Higgins and Parkin (1962); Dean and Maurmeyer (1980); Holland and Holman (1996); Masselink (1999); Masselink et al. (2004) found no statistical support for cusp generation by the edge wave mechanisms, but found a strong relationship between cusp spacing and swash excursion (the horizontal distance between the highest and lowest positions of the swash front on a beach), which supports the self-organisation theory. On the other hand Sallenger (1979) and Ciriano et al. (2005) recorded that cusp spacing has a correlation with edge waves.

2.2.1 Standing Edge Wave Theory

Edge waves are alongshore periodic wave motion trapped near to the shore by refraction, and their amplitudes decay exponentially in the offshore and vary sinusoidally alongshore (Sallenger, 1979). When a standing edge wave is superposed on a normally incident wave, it creates a systematic alongshore variation in swash height resulting in a regular erosional perturbation (Guza and

Inman, 1975) leading to the cusped pattern.

There is a possibility that more than one edge wave occurs on the beach; however, there are only two edge wave types that are generally proposed as being involved in the beach cusp formation. These are subharmonic edge waves and synchronous edge waves (Guza and Inman, 1975). Inman and Guza (1982) presented the relationship between the cusp spacing (λ_c) associated with zero mode subharmonic edge wave (2.3) and synchronous edge wave (2.4):

$$\lambda_c = \frac{g}{\pi} T^2 \tan \beta \quad ; \text{ for subharmonic edge wave} \quad (2.3)$$

$$\lambda_c = \frac{g}{2\pi} T^2 \tan \beta \quad ; \text{ for synchronous edge wave} \quad (2.4)$$

where T is the incident wave period, $\tan \beta$ is the beach gradient, and g is the gravity acceleration.

For subharmonic edge waves, horns correspond to edge wave nodes, where swash excursion is minimum, and embayments correspond to antinodes, where swash excursion is maximum. For synchronous edge waves, both horns and embayments are located at edge wave antinodes (Coco et al., 2003). The standing edge waves provide alongshore periodic perturbations in the bed form on an initially uniform beach. After the beach cusp formation is created, it reduces the subharmonic edge wave amplitude (Guza and Inman, 1975; Guza and Bowen, 1981), so this process is self-limiting. The further development of the cusps requires the positive feedback from the incident wave and the bed topography to maintain the cusped pattern (Inman and Guza, 1982).

2.2.2 Self-Organisation Theory

The self-organisation model was originally proposed by Werner and Fink (1993) and later developed by Coco et al. (2000, 2003). In this numerical model, the swash front is represented as water particles with an associated velocity and sediment carrying capacity. The movement of the water particles is described by ballistic theory on a slope, and the sediment transport flux is proportional to the cube of local particle velocity. Water particles deposit sediment when decelerating and erode when accelerating. A smoothing function is used for avoiding the formation of unrealistic deposits of sediment at individual local cells. The beach slope is limited to the angle of repose.

With this modelling, feedback between flow and morphology is continuously activated for every time step in such a way that every time a particle moves, the topography changes and can immediately affect the particle motion (Coco et al., 2000). The results from self-organisation models predict that

$$\lambda_c = f S_e \quad (2.5)$$

where λ_c is the cusp spacing, S_e is swash excursion, and f is a geometrical parameter in the range of 1-3 (Werner and Fink, 1993). Dean and Maurmeyer (1980) also confirmed this relation (2.5) using measured cusp data. Masselink (1999) and Coco et al. (2000) found the value of f to be 1.57 and 1.63 respectively.

2.2.3 Physical Mechanisms

Although both theories are accepted to explain the formation of beach cusps, they either ignored the role of sediment or simplified the water motion. Dodd et al. (2008) used the 2D process-based morphodynamic model solving NLSW equations and sediment conservation equations simultaneously to simulate the beach change in the swash zone. The infiltration effect was also included in their model in order to investigate the beach cusp formation under the various incoming wave conditions and beach permeabilities. In their work, the physical mechanisms of the depth-averaged sediment concentration gradient and the flow divergence at the horn are used to describe the processes leading to the development of beach cusps. Moreover, they found that the infiltration also enhances cusp formation by reducing further backwash.

2.3 Numerical Model in Swash Zone

The process-based morphodynamic model that is used in this study can be divided into two parts: hydrodynamic and bed update part. Non-linear shallow water (NLSW) equations are used to describe the hydrodynamic behaviour in the swash zone. This set of equations has been successfully applied to modelling wave transformations, wave reflection, swash motion, and wave overtopping. To complete the morphodynamic model, a sediment conservation equation is used (see Section 2.3.2).

2.3.1 Non-Linear Shallow Water Equations

The NLSW equations are well-known to particularly apply for the computation of shallow water flows (sometimes called long wave approximation) with a free surface under the influence of gravity; therefore, this study chooses the NLSW equations to comprise the hydrodynamic part in the model. The NLSW equations are the depth-averaged Navier-Stokes equations with the assumptions that the density of fluid is constant and the effect of external forces, i.e. coriolis force, surface tension force, viscous stresses, and turbulent stresses, are neglected. The pressure distribution is given as hydrostatics and results from assuming that the vertical acceleration of the water particles has a negligible effect on the pressure (see more details in Toro (1999, 2001)).

The 2D NLSW equations can be written in two forms: primitive variable form and flux conservation form. Toro (2001) showed that the primitive variable form is mathematically conservative but physically non-conservative; thus, this form might produce the wrong propagation speed of shock (discontinuity). However, he also found that error in the shock speed of the non-conservative formulation is small when the problem comprises with weak shock waves. The 2D NLSW equations including the bed friction effect the flux conservation form can be written as:

$$d_t + (dU)_x + (dV)_y = 0 \quad (2.6)$$

$$(dU)_t + \left(dU^2 + \frac{1}{2}gd^2 \right)_x + (dUV)_y = -gdB_x - \frac{f_w}{2} |\vec{U}| U \quad (2.7)$$

$$(dV)_t + (dUV)_x + \left(dV^2 + \frac{1}{2}gd^2 \right)_y = -gdB_y - \frac{f_w}{2} |\vec{U}| V \quad (2.8)$$

where $d(x, y, t)$ is the total water depth, $U(x, y, t)$ and $V(x, y, t)$ ($\vec{U} = (U, V)$) are, respectively, the cross- and alongshore depth-averaged velocity components, $B(x, y, t)$ is the bed level, t is time, x and y are the cross- and alongshore coordinates, and f_w is a dimensionless bed friction factor as shown in Figure 2.2. The depth-averaged velocity is the depth integration taken from the bed, $z = B$, to the free-surface, $z = B + d$, as:

$$U = \frac{1}{d} \int_B^{B+d} u dz, \quad V = \frac{1}{d} \int_B^{B+d} v dz \quad (2.9)$$

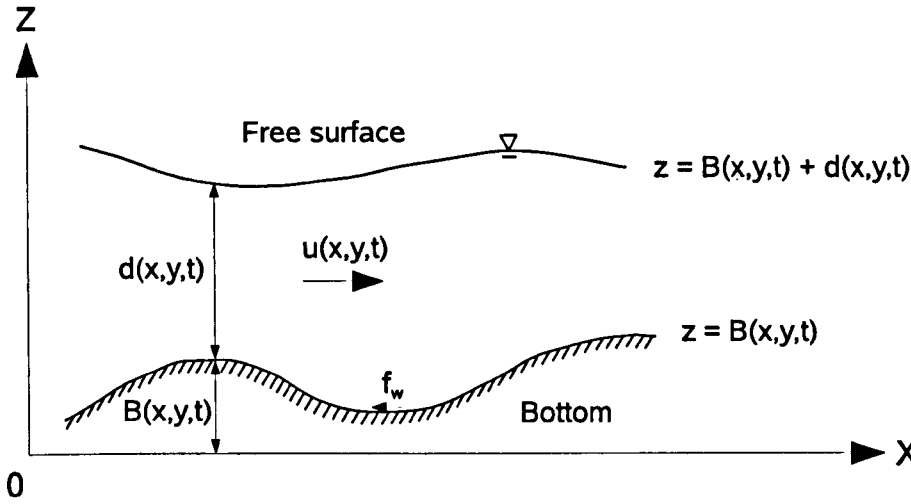


Figure 2.2: Shallow water flow with a surface under gravity in 1D.

where u and v are the velocity in the x and y directions respectively. The resulting equations (2.6) to (2.8) can be solved using the numerical techniques such as: finite difference or finite volume (Brocchini et al., 2001; Hubbard and Dodd, 2002).

Since the study emphasises the effects of swash motion created from short broken waves (bores) on the beach, here previous applications of NLSW equations

to the swash are discussed. Although the NLSW equations cannot model the details of the turbulence motion within the breaking wave front, they can describe the movement of the fluid and the overall changes of the water depth and velocity wherever it crosses bores with a reasonable approximation, especially in the swash zone (Hu et al., 2000).

Hibberd and Peregrine (1979) implemented the NLSW equations with the finite difference method based on a Lax-Wendroff type scheme to give a numerical solution for describing the behaviour of the swash motion during both runup and backwash phase when a uniform bore moves over a sloping beach. They also explained the formation of a landward-facing bore in the backwash (backwash bore).

Kobayashi et al. (1987) used an explicit dissipative Lax-Wendroff finite difference method to solve the 1D NLSW equations including the effects of bottom friction. This numerical model is created for prediction of the flow characteristics, including wave reflection and runup on rough slopes with a normally incident incoming wave. A slight modification of the offshore boundary condition in the model for improving the agreement between the computed and measured mean water levels on gentle slopes is presented by Kobayashi et al. (1989).

Titov and Synolakis (1995) developed a model solving the NLSW equations without artificial viscosity or friction factors using an explicit second-order finite difference scheme to simulate the 1D runup of solitary waves on a plane

beach. Their model had greatly improved the efficiency in term of the computations because of the usage of the variable grid in the calculation scheme. Then, Titov and Synolakis (1998) extended the usage of their model with a splitting method to simulate a 2D tsunami wave attacking a conical island.

Watson et al. (1992) introduced the weighted average flux (WAF) method which is one of the "*shock-capturing*" schemes where discontinuities are automatically treated without the need for a special tracking algorithm to solve the 1D NLSW equations. They reformulated the equations to include the bed slope source term within the local Riemann problem, which is simply the hyperbolic equation together with a piecewise constant data having a single discontinuity (LeVeque, 2002); then, the system of equations is solved by applying WAF method with a total variation diminishing (TVD) flux-limiter. A TVD flux-limiter reweights the average flux in order to eliminate spurious oscillations near the discontinuity, and makes the scheme somewhere between first and second-order to achieve a compromise between accuracy and stability (Watson et al., 1992). Later, Brocchini et al. (2001) implemented the WAF method to solve NLSW equations in a 2D domain, and applied their model to a dambreak and the run-up of a large tsunami wave.

Dodd (1998) used an upwind finite volume technique incorporating a Roe-type Riemann solver, which is another shock-capturing technique, to create a model solving the 1D NLSW equations for simulating the wave runup and overtopping of coastal structure and regeneration of waves beyond. Hubbard and

Dodd (2002) also used a Roe-type solver to create a 2D equivalent called "OTT-2d". It was tested with the 2D wave transformation, runup, and overtopping cases with good results. Hu et al. (2000) also developed an upwind finite volume model, but used an HLL approximate Riemann solver for shock-capturing scheme instead. Their model also receives a good agreement when they compare the model result with analytical solutions and laboratory data for the wave overtopping at a vertical seawall.

2.3.2 Morphodynamic Models

Morphodynamic models are useful tools for studying coastal evolution processes. Normally coastal behaviour is a 3D process but can be understood and predicted with modelling concepts based on fewer dimensions. Therefore, many forms of morphodynamic models have been created to simulate changes in the nearshore areas (surf zone and swash zone) for a variety of length and time scales.

The typical structure of the numerical morphodynamic model consists of 3 sub-models for calculating waves, nearshore currents, and sediment transport and beach change as shown in Figure 2.3 (see Horikawa (1988)). However, some models combine calculation of waves and currents together and solve them at the same time in a *Hydrodynamic model*, and then solve the sediment conservation equation (2.10), which calculates the change in the bed level depending on

the change in the sediment transport equation (see more details in Section 3.2):

$$\frac{\partial B}{\partial t} + \frac{1}{1-p} \left(\frac{\partial q_u}{\partial x} + \frac{\partial q_v}{\partial y} \right) = 0 \quad (2.10)$$

where B is the bed level, p is the porosity of the beach material, and q_u and q_v are the sediment transport rates in cross-shore and alongshore direction respectively. An advantage of this approach is the separation of the complexity of hydrodynamics from those of sediment transport, so the effects of reflection, refraction, diffusion of wave, or of sediment properties, like separation of suspended load and bed load are easier to add as additional modules to the model (Nicholson et al., 1997).

Other approaches, that use the Boussinesq type equations for a nonlinear breaking wave model (Karambas and Koutitas, 2002), the quasi three-dimensional approach in order to include vertical changes in water column (Zyserman and Johnson, 2002), or fully 3D process-based model (Grunnet et al., 2004) for computing in the hydrodynamic part, are quite complicated and require some computational expenses. Therefore, the morphodynamic model considered here uses the NLSW equations for the hydrodynamic part; thus the literature in this part emphasises in the previous studies that use the NLSW equations.

Li et al. (2002) used the uncoupled model to simulate the groundwater effect on sediment transport and beach profile changes in the swash; thus, their model has three major processes: wave motion, coastal groundwater flow, and cross-shore sediment transport. The wave motion model used the Lax-Wendroff finite difference scheme to solve the 1D NLSW equations, and the beach pro-

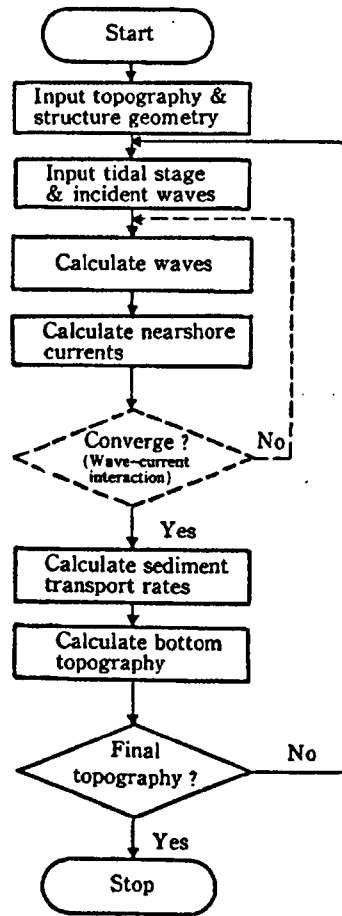


Figure 2.3: Flowchart of the morphodynamic model (from Horikawa (1988)).

file change was computed from the sediment conservation equation while the energetics-based model of Bagnold (1966) (threshold sediment transport equation) was used to calculate the sediment transport rate. In their groundwater flow model, Li et al. (2002) solved the Laplace equation for saturated flow in the aquifer. Their simulation results agreed qualitatively with the experimental observations of swash infiltration effects.

In the swash zone, the interaction of hydrodynamic and beach change is quite quick. A large amount of sediment transport occurs in the uprush, so that sig-

nificant changes occur in the bed configuration during half a wave cycle; similarly on the backwash (Butt and Russell, 1999; Masselink et al., 2005). It is necessary to consider instantaneous bed changes to correctly capture the morphodynamic behaviour; therefore, a fully coupled morphodynamic model is considered here, solving NLSW equations and sediment conservation equation simultaneously. Hudson et al. (2005) show that significant errors can occur when flow has the high Froude numbers, as is the case in the swash.

Hudson and Sweby (2003) compared the steady (or uncoupled) and unsteady (or coupled) approach in a 1D morphodynamic model. The steady approach had to compute the wave and current submodels until they reached a steady state, and then updated the bed, whereas, the unsteady approach solves all of three submodels simultaneously. In their study, they used the flux-limited version of Roe's scheme to discretise the equations. Then, Hudson and Sweby (2005) adapted the steady and unsteady approach to a 2D morphodynamic model. The main result from these two articles showed that in 1D, the steady approach was more accurate than the unsteady approach when the bed was interacting slowly with the water flow and for a small Froude number. However, in 2D the steady approach seemed to be producing inaccurate results.

Hudson et al. (2005) investigated and compared 1D morphodynamical systems that were decoupled and a coupled approach, using the Lax-Wendroff and the Roe schemes, applied with and without flux-limiting methods. There were some suggestions that the Lax-Wendroff scheme can produce spurious

oscillations, and therefore that a filtering method, such as that of Johnson and Zyserman (2002), should be applied; and a flux-limited approach was very important for long-term modelling. Nevertheless, for a small Froude number, the decoupled approach used less computational time than the coupled approach.

Dodd et al. (2008) combined the hydrodynamic model of Hubbard and Dodd (2002) with the bed update equation to create a coupled process-based morphodynamic model. This model solved the coupled 2D NLSW equations and sediment conservation equation simultaneously in the form of Hudson and Sweby (2005) including the effect of bed friction, bed diffusion, and infiltration, by using a Roe-approximated Riemann problem with a flux limiter scheme. This model was successful for the simulations of 1D mobile bed dam-break problem; then, it was used to simulate the beach change in the swash zone in order to explain the beach cusp formation and evolution (in term of linear growth rate).

Castro Diaz et al. (2008) created a 1D coupled morphodynamic model which also solved the non-conservative form of NLSW equation system simultaneously, and used the different numerical schemes for comparing the results of each scheme. The numerical schemes used in this study were Roe-solver finite volume scheme with and without flux limiters, and high order finite volume methods using WENO (weighted essentially non-oscillatory) reconstruction scheme, which is another numerical scheme to approximate the fluxes at cell boundaries to a high order accuracy and to avoid spurious oscillations near

shocks (Jiang and Shu, 1996). The model results agreed with the analytical solution and experimental data. Moreover, the variation of sediment transport equations compared with Grass (1981) model were also presented in their study.

CHAPTER 3

Morphodynamic Model

This study makes use of a process based morphodynamic model, *OTT2dm*, developed by Stoker (2005) and Dodd et al. (2008), to simulate the occurrence and formation of beach cusps. *OTT2dm* originates from the hydrodynamic model, *OTT-2d*, created for investigating swash zone wave behaviour: wave transformation, run-up and overtopping (see more detail in Hubbard and Dodd (2002)). Stoker (2005) and Dodd et al. (2008) combined the *OTT-2d* model with a sediment conservation equation, and used the numerical scheme of Hudson and Sweby (2003) to solve the non-linear shallow water (NLSW) equations and sediment conservation equation simultaneously.

This chapter gives a summary of a process based morphodynamic model including the governing equations, the calculation of sediment transport rate, bed diffusion and infiltration term. The Roe approximation used with the Hudson and Sweby (2003) scheme is explained in the last part.

3.1 Governing Equations

OTT2dm of Stoker (2005) is a fully coupled morphodynamic model, which comprises the NLSW and sediment conservation equation. As the model uses the Roe solver with flux limiter scheme, the coupled system of the original NLSW equations in flux conservative form, (2.6) to (2.8) and sediment conservation equation (2.10) has a problem in computation of Roe decomposition. Therefore, Hudson and Sweby (2005) presented the NLSW equation system to avoid the singular eigenvector matrices in Roe's method by substituting $dB_x = (dB)_x - d_x B$ and $dB_y = (dB)_y - d_y B$ into (2.7) and (2.8), respectively. As a result, the equations of fully coupled morphodynamic model are:

$$d_t + (dU)_x + (dV)_y = 0 \quad (3.1)$$

$$(dU)_t + \left(dU^2 + \frac{1}{2}gd^2 + gdB \right)_x + (dUV)_y = gd_x B - \frac{f_w}{2} |\vec{U}| U \quad (3.2)$$

$$(dV)_t + (dUV)_x + \left(dV^2 + \frac{1}{2}gd^2 + gdB \right)_y = gd_y B - \frac{f_w}{2} |\vec{U}| V \quad (3.3)$$

$$B_t + \xi (q_u)_x + \xi (q_v)_y = 0 \quad (3.4)$$

where $d(x, y, t)$ is the total water depth, $U(x, y, t)$ and $V(x, y, t)$ ($\vec{U} = (U, V)$) are, respectively, the cross- and alongshore depth-averaged velocity components where depth integration is taken from the bed to the free-surface as shown in (2.9), $B(x, y, t)$ is the bed level, t is time, x and y are the cross- and alongshore co-ordinates, f_w is a dimensionless bed friction factor, and $\xi = 1/(1 - p)$ where p is the porosity of the bed. The calculation of sediment transport rates, q_u and q_v , is explained in Section 3.2.

This set of equations is implemented upon a Cartesian grid, and the solution variables are stored at the centre of each cell, and the value assumed to be constant within the cell (the Roe-type scheme of Hudson and Sweby (2003) is then introduced to calculate the fluxes across the cell edges). With this numerical scheme, four solution variables are solved simultaneously. Nondimensional co-ordinates are introduced: $\hat{d} = d/h_0$, $\widehat{\vec{U}} = \vec{U}/\sqrt{gh_0}$, $\hat{x} = x/h_0$, $\hat{y} = y/h_0$, and $\hat{t} = t\sqrt{g/h_0}$, where $\hat{\cdot}$ denotes a nondimensional variable, and h_0 is a representative water depth which is the initial water depth at offshore boundary. Therefore, the equations are then rewritten in non-dimensional variables as:

$$d_t + (dU)_x + (dV)_y = 0 \quad (3.5)$$

$$(dU)_t + \left(dU^2 + \frac{1}{2}d^2 + dB \right)_x + (dUV)_y = d_x B - \frac{f_w}{2} |\vec{U}| U \quad (3.6)$$

$$(dV)_t + (dUV)_x + \left(dV^2 + \frac{1}{2}d^2 + gB \right)_y = d_y B - \frac{f_w}{2} |\vec{U}| V \quad (3.7)$$

$$B_t + \xi(q_u)_x + \xi(q_v)_y = 0 \quad (3.8)$$

where $\hat{\cdot}$ has now been dropped for convenience. The boundary conditions of the model are based on those of the *OTT-2d* model (Hubbard and Dodd, 2002), updated to include the bed level variable, B . Each boundary cell is adjacent to a double layer of dummy cells which are primed with information about the solution around the boundary. There are four types of external boundary used in the model:

- *Extrapolation* : dummy cells are overwritten with the solution values in the cells along the boundary, giving a very simple absorbing boundary suitable for outflow.

- *Reflection* : the normal velocity components of the flow in the dummy cells are taken to be a reflection in the domain boundary of the internal values, imitating a solid wall.
- *Periodic* : the solution at one end of the domain provides an input boundary at the opposite edge.
- *Absorbing/generating boundary* : the solution in the dummy cells at an offshore boundary is interpolated linearly from a time series of data, either synthetic or measured.

An extrapolation, reflection, or periodic boundary are applied at the lateral boundaries, while a simple absorbing/generating boundary is implemented at the offshore boundary as shown in Figure 3.1. To locate the shoreline position, there is no special tracking technique used; rather a wetting algorithm is used, and then these cells treated just like other cells, and then a drying algorithm applied.

3.2 Sediment Transport Rate

The model in this study uses Roe solver scheme to solve the coupled NLSW system. The sediment transport rate, \vec{q} , should be a simple formulae, because a more complex sediment transport equation, that accounts the bed load and the suspended load separately, such as van Rijn formulae (van Rijn (1984) and Soulsby (1997)), is considerably difficult to implement with Roe's method (the

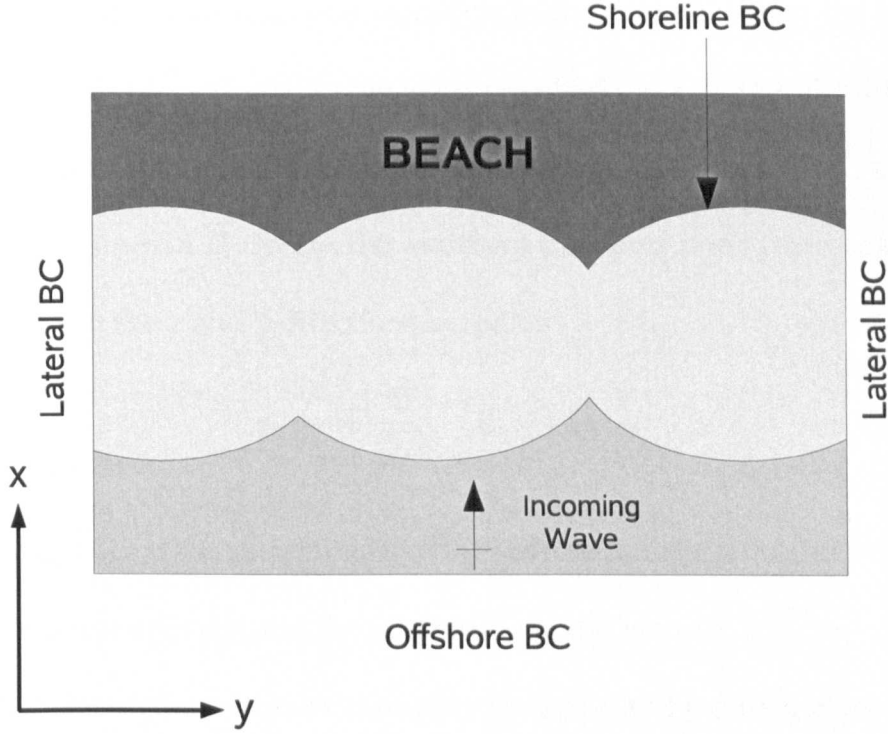


Figure 3.1: Computation domain and boundary conditions.

main numerical scheme used in the present model). Therefore, this study only considers the simple sediment transport rate of Grass (1981), based on a power law relationship as:

$$\vec{q}(\vec{U}) = A\vec{U}|\vec{U}|^{(m-1)} \quad (3.9)$$

where A is a dimensional constant related to the beach material and the flow regime. m is a constant in the range $1 \leq m \leq 4$. This approach was undertaken in order to use the Roe decomposition of Hudson and Sweby (2005). Castro Diaz et al. (2008) simplified the complex sediment transport equations of Meyer-Peter and Müller, Fernández Luque and Van Beek, van Rijn, and Nielsen to the particular form of Grass model. They found that only the van Rijn equation has $m = 3.4$, while the others have $m = 3$. Therefore, we use (3.9) with m

= 3 to be the sediment transport equation in the model. When the sediment transport rate is proportional to the velocity cubed ($m = 3$), this allows the sediment transport relationship to be differentiated with respect to \vec{U} , and to be valid for all values of \vec{U} . In 2D, the sediment transport rate is then split into its components in the x and y directions based on:

$$q_u = |\vec{q}| \frac{U}{|\vec{U}|}, \quad q_v = |\vec{q}| \frac{V}{|\vec{U}|} \quad (3.10)$$

where q_u and q_v are the components of the sediment transport rates in the x and y directions respectively, and the magnitude of the velocity is $|\vec{U}| = \sqrt{U^2 + V^2}$.

Hence, we obtain the sediment transport rates in x and y direction as:

$$\begin{aligned} q_u &= AU (U^2 + V^2) \\ q_v &= AV (U^2 + V^2) \\ \vec{q} &= (q_u, q_v) \end{aligned} \quad (3.11)$$

3.3 Bed Diffusion

The bed slope affects sediment transport rate, which is either enhanced or reduced also depending upon whether the sediment transport is down- or upslope (Horikawa, 1988). In order to account for this effect the sediment transport (3.11) is modified to include this downslope effect as follows:

$$\vec{q}^* = \vec{q} - C|\vec{q}||\vec{\nabla}b| \quad (3.12)$$

where \vec{q}^* is the modified sediment flux vector, and C is the dimensionless

diffusion coefficient related to the angle of repose of sediment, ϕ (where $C = 1/(\tan \phi)$). In this study, we set $\phi = 32^\circ$ such that $C = 1.6$. This approach allows sediment to move laterally down a slope; therefore the downslope sediment transport is increased, whereas the upslope sediment transport is decreased. Moreover, this downslope effect is only included with respect to the bed perturbation, b (changes from the starting bed). This means that when $|\vec{\nabla} b| = \tan \phi$, then $\vec{q}^* = 0$.

3.4 Infiltration

An important physical effect within the swash zone is infiltration into the beach face. Since infiltration reduces the effectiveness of the backwash to transport sediment offshore, it induces a change in net sediment transport in the swash zone, leading to enhanced deposition onshore. In order to model this process, Packwood (1983) proposed a method to calculate the volume of water that will flow into the beach, and the effect of this loss of water on the momentum equations. This approach is consistent with the assumption of Darcy's law. Packwood (1983) stated that the infiltration rate ($w(x, y, t)$) is related to the rate of change of the position of the free surface ($\zeta(x, y, t)$) in the porous media (as shown in Figure 3.2), and it is also related to head of water above the bed (the water depth, $d(x, y, t)$) and the hydraulic conductivity (K) as follows:

$$w = p\zeta_t = K \left(1 + \frac{d}{\zeta} \right) \quad (3.13)$$

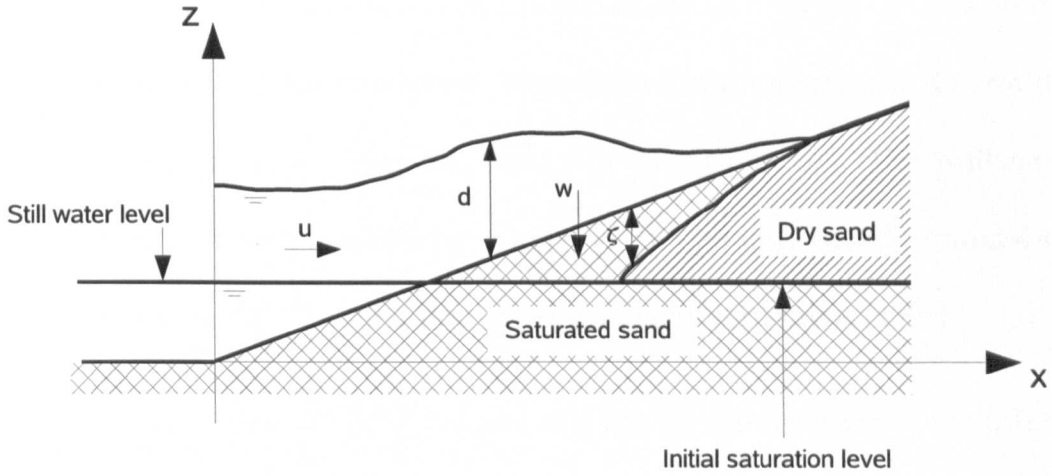


Figure 3.2: Run-up on initially dry beach.

where p is the porosity of the bed material, and K varies from 0.0001 m/s, 0.001 m/s, and 0.01 m/s for fine, medium, and coarse sands, respectively (Packwood and Peregrine, 1980). This is a reasonable assumption for coarse sands and gravels, having been verified by Turner and Masselink (1998). In the model, the differential equation (3.13) is solved using a fourth order Runge-Kutta scheme. Problems arise in the solution when water initially infiltrates the beach ($\zeta = 0$), because d/ζ in (3.13) is singular. In order to solve for the position of the free surface at the first time, an analytical solution (3.14) is used to determine ζ (Packwood, 1983) during the first computational time step. The solution is arrived at by assuming a linear variation of d during the time step Δt . The linear variation is from zero to d , where d has been determined by the solution of the system of modified NLSW equations prior to any infiltration. The analytical solution is:

$$\zeta = \frac{1}{2} \frac{K}{p} \left[1 + \left(1 + \frac{4pd}{\Delta t K} \right)^{\frac{1}{2}} \right] \Delta t \quad (3.14)$$

Once the initial infiltration has been calculated the solution to (3.13) is continued using the Runge-Kutta scheme. Then the infiltration rate w is determined based upon the current values for ζ and d in the current cell. This infiltration computation approach has also been applied in a process based groundwater model by Li et al. (2002), and a Boussineq model by Karambas (2003).

Because the equations are fully coupled and solved simultaneously, the infiltration rate and its effects are applied in a point-wise approach every time-step. They take into account the changing position of the bed level, and alter the hydrodynamics prior to the next simultaneous solution of the system.

Having calculated the volume of infiltrated water, this is extracted from the depth in the free flow region. In the momentum equations this effect applies in the form of a sink term acting to reduce the momentum to zero. The form of the momentum sink terms used in that suggested by Li et al. (2002) (see more detail in Dodd et al. (2008)). Equations (3.15) to (3.18) represent the final system of equations including the effects of infiltration and bed diffusion.

$$d_t + (dU)_x + (dV)_y = -w \quad (3.15)$$

$$(dU)_t + \left(dU^2 + \frac{1}{2}d^2 + dB \right)_x + (dUV)_y = d_x B - \frac{f_w}{2} |\vec{U}| U - U w \quad (3.16)$$

$$(dV)_t + (dUV)_x + \left(dV^2 + \frac{1}{2}d^2 + dB \right)_y = d_y B - \frac{f_w}{2} |\vec{U}| V - V w \quad (3.17)$$

$$B_t + \xi (q_u)_x + \xi (q_v)_y = \xi C |\vec{q}| |\vec{\nabla} b| \quad (3.18)$$

The additional source terms describing the infiltration, bed diffusion and bed friction are modelled using a point-wise approach with gradients expressed

using a central difference. Moreover, this set of equation can be also written in the vector form as:

$$\vec{W}_t + \vec{F}_x + \vec{G}_y = \vec{S} \quad (3.19)$$

where

$$\begin{aligned} \vec{W} &= [d, dU, dV, B]^T \\ \vec{F} &= \left[dU, dU^2 + \frac{1}{2}d^2 + dB, dUV, \xi q_u \right]^T \\ \vec{G} &= \left[dV, dUV, dV^2 + \frac{1}{2}d^2 + dB, \xi q_v \right]^T \\ \vec{S} &= \left[-w, d_x B - \frac{f_w}{2} |\vec{U}| U - Uw, d_y B - \frac{f_w}{2} |\vec{U}| V - Vw, \xi C |\vec{q}| |\vec{\nabla} b| \right]^T \end{aligned} \quad (3.20)$$

3.5 Roe's Scheme

The model in this study solved the system of NLSW equations and sediment balance equation in the non-dimensional vector form (3.19). This vector form of the system is discretised with an explicit upwind scheme. Applying a forward Euler timestep and central difference approximation to the spatial derivatives.

$$\vec{W}_{i,j}^{n+1} = \vec{W}_{i,j}^n - \frac{\Delta t}{\Delta x} \left(\vec{F}_{i+\frac{1}{2},j}^n - \vec{F}_{i-\frac{1}{2},j}^n \right) - \frac{\Delta t}{\Delta y} \left(\vec{G}_{i,j+\frac{1}{2}}^n - \vec{G}_{i,j-\frac{1}{2}}^n \right) + \Delta t \vec{S}_{i,j}^n \quad (3.21)$$

where $\vec{W}_{i,j}^n$ is the vector of conserved variables in cell (i, j) at the current timestep n , $\vec{F}_{i\pm\frac{1}{2},j}^n$ and $\vec{G}_{i,j\pm\frac{1}{2}}^n$ are numerical fluxes at interfaces, $\vec{S}_{i,j}^n$ is the source term vector, Δt is the timestep and $(\Delta x, \Delta y)$ is the grid spacing as illustrated in Figure 3.3. All the terms on the right hand side are evaluated using values at the current timestep (n) .

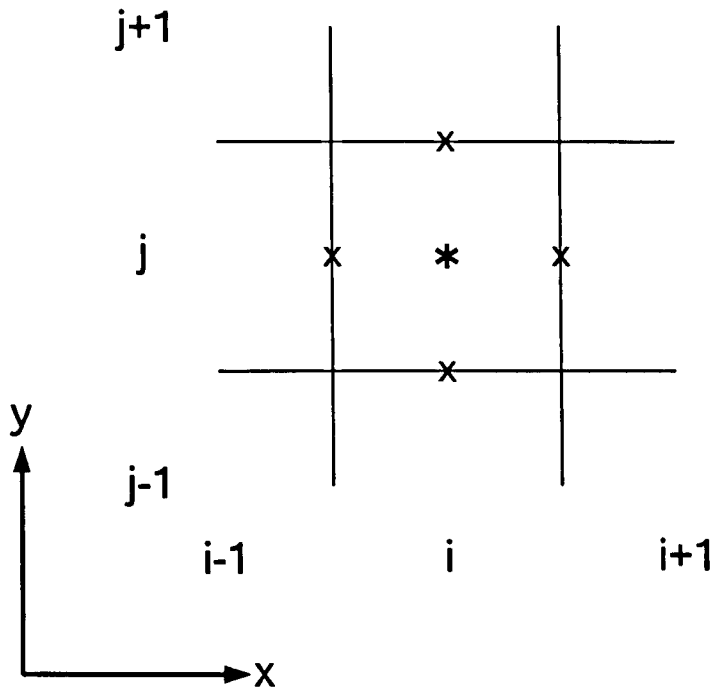


Figure 3.3: Grid system used to solve the numerical scheme within *OTT2dm*.

(*) is cell centre, (x) cell interface (edge).

The numerical fluxes at cell interfaces are evaluated using Roe's approximate Riemann solver. This scheme was proposed by Roe (1981); subsequently many researchers, such as Toro (1999, 2001), LeVeque (2002), Hubbard and Dodd (2002), and Hudson and Sweby (2003, 2005), used and developed this scheme to solve hyperbolic problems. Roe's scheme approximates each cell interface as a linearised Riemann problem. Each interface flux is expressed as four components ($k = 1, 2, 3, 4$) obtained by solving four equations simultaneously, then evaluated using the exact solution of the local Riemann problem. In order to obtain higher order accuracy and to avoid the spurious oscillation near the shocks, the Total Variational Diminishing (TVD) technique with flux-limited functions is implemented in the model to compromise between accuracy and stability.

Equations (3.22) introduces the Roe approximation of interface flux with the flux-limiters.

$$\vec{F}_{i+\frac{1}{2},j}^n = \frac{1}{2} \left(\vec{F}_{i+1,j}^n + \vec{F}_{i,j}^n \right) - \frac{1}{2} \left(\sum_{k=1}^4 \tilde{\alpha}_k [1 - \mathcal{B}(\tilde{r}_k) (1 - |\tilde{v}_k|)] |\tilde{\lambda}_k| \vec{\tilde{e}}_k \right)_{i+\frac{1}{2},j} \quad (3.22)$$

where $\tilde{\lambda}_k$ and $\vec{\tilde{e}}_k$ are the eigenvalues and right eigenvectors of the Roe averaged Jacobian matrix, $\tilde{\mathbf{A}} = \frac{\partial \vec{F}}{\partial \vec{W}}$ as shown in (3.24), $\tilde{\alpha}_k$ is the associated wave strength, $\tilde{v}_k = \tilde{\lambda}_k \Delta t / \Delta x$ is the Courant number associated with the k th wave, and $\mathcal{B}(\tilde{r}_k)$ is a nonlinear flux limiter function (see more details in Toro (1999) and LeVeque (2002)). The flux limiter function used in this study is a Minmod flux limiter as:

$$\mathcal{B}(\tilde{r}_k) = \max(0, \min(1, \tilde{r}_k)) \quad (3.23)$$

where \tilde{r}_k is a ratio of wave strengths of the upwind wave strength to the local wave strength. Similar expressions exist for $\vec{F}_{i-\frac{1}{2},j}^n$ and $\vec{G}_{i\pm\frac{1}{2},j}^n$. In the case of $\vec{G}_{i\pm\frac{1}{2},j}^n$ the eigenvalues and eigenvectors are associated with the matrix, $\tilde{\mathbf{B}} = \frac{\partial \vec{G}}{\partial \vec{W}}$ as shown in (3.25),

$$\tilde{\mathbf{A}} = \begin{bmatrix} 0 & 1 & 0 & 0 \\ (\tilde{d} + \tilde{B}) - \tilde{U}^2 & 2\tilde{U} & 0 & \tilde{d} \\ -\tilde{U}\tilde{V} & \tilde{V} & \tilde{U} & 0 \\ -\tilde{U}\tilde{D}^F - \tilde{V}\tilde{E}^F & \tilde{D}^F & \tilde{E}^F & 0 \end{bmatrix} \quad (3.24)$$

$$\tilde{\mathbf{B}} = \begin{bmatrix} 0 & 0 & 1 & 0 \\ -\tilde{U}\tilde{V} & \tilde{V} & \tilde{U} & 0 \\ (\tilde{d} + \tilde{B}) - \tilde{V}^2 & 0 & 2\tilde{V} & \tilde{d} \\ -\tilde{V}\tilde{D}^G - \tilde{U}\tilde{E}^G & \tilde{E}^G & \tilde{D}^G & 0 \end{bmatrix} \quad (3.25)$$

where the Roe-averaged values are

$$\begin{aligned} \tilde{d} &= \frac{1}{2}(d_R + d_L), \quad \tilde{B} = \frac{1}{2}(B_R + B_L), \\ \tilde{U} &= \frac{\sqrt{d_R}U_R + \sqrt{d_L}U_L}{\sqrt{d_R} + \sqrt{d_L}}, \quad \tilde{V} = \frac{\sqrt{d_R}V_R + \sqrt{d_L}V_L}{\sqrt{d_R} + \sqrt{d_L}}, \\ \tilde{D}^F &= \frac{\xi A (\sqrt{d_R} + \sqrt{d_L})}{\sqrt{d_R}d_L + \sqrt{d_L}d_R} (U_R^2 + U_RU_L + U_L^2 + \tilde{V}^2), \\ \tilde{D}^G &= \frac{\xi A (\sqrt{d_R} + \sqrt{d_L})}{\sqrt{d_R}d_L + \sqrt{d_L}d_R} (\tilde{U}^2 + V_R^2 + V_RV_L + V_L^2), \\ \tilde{E}^F &= \frac{\xi A [2\sqrt{d_R}\sqrt{d_L}(U_RV_R + U_LV_L) + (d_RU_L + d_LU_R)(V_R + V_L)]}{(\sqrt{d_R}d_L + \sqrt{d_L}d_R)(\sqrt{d_R} + \sqrt{d_L})}, \\ \tilde{E}^G &= \frac{\xi A [2\sqrt{d_R}\sqrt{d_L}(U_RV_R + U_LV_L) + (d_RV_L + d_LV_R)(U_R + U_L)]}{(\sqrt{d_R}d_L + \sqrt{d_L}d_R)(\sqrt{d_R} + \sqrt{d_L})} \end{aligned} \quad (3.26)$$

where \tilde{D} and \tilde{E} are the Roe-averaged terms corresponding to the sediment transport equation of Grass (1981), i.e. \tilde{D}^F , \tilde{E}^F , \tilde{D}^G , and \tilde{E}^G are respectively computed by $\frac{\partial(\xi\tilde{q}_u)}{\partial(\tilde{d}\tilde{U})}$, $\frac{\partial(\xi\tilde{q}_u)}{\partial(\tilde{d}\tilde{V})}$, $\frac{\partial(\xi\tilde{q}_v)}{\partial(\tilde{d}\tilde{V})}$, and $\frac{\partial(\xi\tilde{q}_v)}{\partial(\tilde{d}\tilde{U})}$. The superscript F and G denote that variables are associated with \vec{F} and \vec{G} , respectively.

3.5.1 Source Terms

For (3.15) - (3.18), the bed slope terms of the source vector are upwinded in the same way as the numerical fluxes in order to maintain the equilibrium that exists in the original NLSW equations (2.7) and (2.8) (Stoker, 2005). The other terms, bed friction, bed diffusion and infiltration terms, are evaluated pointwise using the values at the cell centre.

The implementation of the bed slope source terms are decomposed into characteristic components, similar to the flux difference shown in the discretised form at each cell edges:

$$\vec{S}_{i,j}^n = \vec{S}_{i+\frac{1}{2},j}^- + \vec{S}_{i-\frac{1}{2},j}^+ + \vec{S}_{i,j+\frac{1}{2}}^- + \vec{S}_{i,j-\frac{1}{2}}^+ \quad (3.27)$$

where superscripts refer to the direction of travel of the edge contribution and subscripts refer to the cell edge that is contributing to the source term. Each source term edge contribution takes the form

$$\vec{S}^\pm = \frac{1}{2} \sum_{k=1}^4 \left(1 \pm \text{sgn}(\tilde{\lambda}_k) \right) [1 - \mathcal{B}(\tilde{r}_k)(1 - |\tilde{v}_k|)] \tilde{\beta}_k \vec{e}_k \quad (3.28)$$

where $\tilde{\beta}_k$ are the coefficients of the decomposition of the source term onto the eigenvector \vec{e}_k of the appropriate flux Jacobian ($\tilde{\beta}_k = \tilde{\lambda}_k \tilde{\alpha}_k$ for $k = 1$ to 4).

CHAPTER 4

Model Development

This study aims to simulate the occurrence of beach cusps using a process-based morphodynamic model of the coupled NLSW and sediment conservation equations. The starting point is the model of Stoker (2005) and Dodd et al. (2008). This model was successfully used for simulating the early development of beach cusps, but there are limitations addressed in this chapter.

Here an entropy fix, an amended numerical scheme (Castro Diaz et al., 2008), a different method for dealing with source terms (Time Operator Splitting, TOS) (Toro (1999, 2001) and LeVeque (2002)), and the shoreline boundary condition (SBC) are addressed, to improve numerical stability and physical realism. After implementing the new numerical methods, the model is tested by simulating some idealised 1D cases, and compared with the analytical or numerical solutions from the previous studies.

4.1 Entropy Fix

Using a linearised Riemann problem solution like Roe's scheme can result in some problems that are due to the resulting approximate Riemann solution consisting only of discontinuities in the flow variables. On the other hand, rarefaction waves carry a continuous change in flow variables, and as time increases, they tend to spread. This means that the spatial gradient decays, and the characteristics diverge from the discontinuity. As a result, the linearised approximation via the kind of discontinuous jump is totally incorrect. In a practical computation, this problem shows up in the form of unphysical discontinuous waves (Toro, 1999); however, it is only significant when the rarefaction wave is *transonic* which its eigenvalue, representing the characteristic speed of that rarefaction wave, changes from negative to positive.

$$\lambda_k^L < 0 < \lambda_k^R \quad (4.1)$$

where $\lambda_k^{L,R}$ are the characteristic speeds of the left, L , and right, R , edges respectively of the rarefaction wave. To solve this problem, Harten and Hyman (1983) introduced the *Entropy fix* approach to split the single travelling rarefaction shock with Roe-averaged speed, $\tilde{\lambda}_k$, into two smaller jumps as shown in the example of an entropy fix approach applied to a left transonic rarefaction wave in Figure 4.1.

From the Roe's flux equation (3.22), the flux limiter term is neglected to simplify

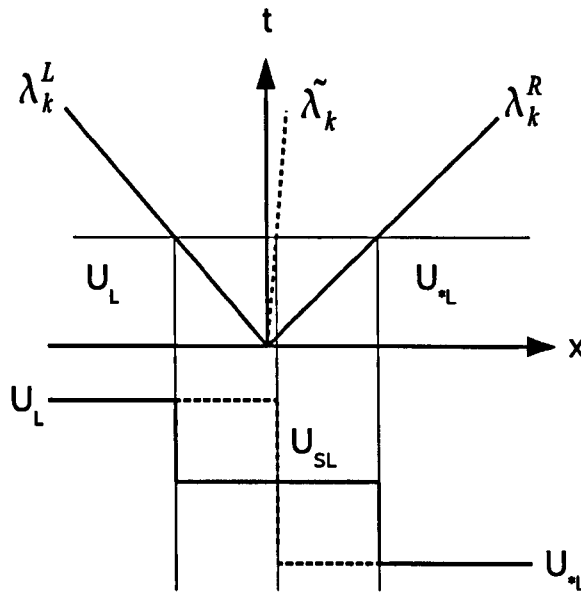


Figure 4.1: Entropy fix for left transonic rarefaction wave. The single jump $U_{*L} - U_L$ travelling with speed $\tilde{\lambda}_k$ is split into the two jumps $U_{SL} - U_L$ and $U_{*L} - U_{SL}$ travelling with speeds λ_k^L and λ_k^R , where U_{SL} is a transonic state.

the flux equation to:

$$\vec{F}_{i+\frac{1}{2},j}^n = \frac{1}{2} \left(\vec{F}_{i+1,j}^n + \vec{F}_{i,j}^n \right) - \frac{1}{2} \left(\sum_{k=1}^4 \tilde{\alpha}_k |\tilde{\lambda}_k| \vec{e}_k \right)_{i+\frac{1}{2},j} \quad (4.2)$$

To split the transonic wave into two smaller jumps, (4.2) is modified to so as to implement the entropy fix by changing $|\tilde{\lambda}_k|$ as follows:

$$|\tilde{\lambda}_k| = \tilde{\lambda}_k^+ - \tilde{\lambda}_k^- \quad (4.3)$$

where

$$\tilde{\lambda}_k^\pm \equiv \frac{1}{2} \left[\tilde{\lambda}_k \pm \frac{1}{2} \phi_\delta(\tilde{\lambda}_k) \right] \quad (4.4)$$

where $\phi_\delta(\tilde{\lambda}_k)$ is an absolute-value function for splitting the transonic rarefaction wave.

4.1.1 Harten and Hyman Entropy Fix

The widely used entropy fix approach proposed by Harten and Hyman (1983) introduced the absolute-value function, $\phi_\delta(\tilde{\lambda}_k)$, based on increasing the viscosity for recomputing the eigenvalues so that they are not too close to zero. Since there is a little difference in the splitting wave process between the model used in this study and the original implementation of Harten and Hyman (1983), we need to modify the Harten and Hyman entropy fix to be compatible with the equation (4.4):

$$\phi_\delta(\tilde{\lambda}_k) = \begin{cases} |\tilde{\lambda}_k| & \text{if } 2|\tilde{\lambda}_k| \geq \delta_k \\ \frac{\tilde{\lambda}_k^2 + \delta_k^2}{\delta_k} & \text{if } 2|\tilde{\lambda}_k| < \delta_k \end{cases} \quad (4.5)$$

where the parameter δ_k can be defined as;

$$\delta_k = \max \left[0, \tilde{\lambda}_k - \lambda_k^L, \lambda_k^R - \tilde{\lambda}_k \right] \quad (4.6)$$

4.1.2 Hubbard and Dodd Entropy Fix

The model of Dodd et al. (2008) was based on that of Hubbard and Dodd (2002). Although Hubbard and Dodd (2002) used the entropy fix approach to solve the transonic rarefaction wave problem, they used a different $\phi_\delta(\tilde{\lambda}_k)$ function

from that of the original approach (Harten and Hyman, 1983). Hubbard and Dodd (2002) constructed a smooth function by estimating it from the maximum spreading rate of the characteristic structure of a 1D dambreak problem, which is solved by Roe's method. The spreading rate across the rarefaction wave is limited to $3\tilde{c}$, where \tilde{c} is the Roe-averaged wave celerity. Therefore, this ϕ_δ is given by

$$\begin{aligned}\phi_\delta(\tilde{\lambda}_1) &= \frac{3\tilde{\alpha}_1}{2\tilde{c}} & \text{when } \tilde{\lambda}_1 \approx \tilde{U} + \tilde{c} \\ \phi_\delta(\tilde{\lambda}_2) &= -\frac{3\tilde{\alpha}_2}{2\tilde{c}} & \text{when } \tilde{\lambda}_2 \approx \tilde{U} - \tilde{c} \\ \phi_\delta(\tilde{\lambda}_3) &= \phi_\delta(\tilde{\lambda}_4) = 0\end{aligned}\tag{4.7}$$

where $\tilde{\lambda}_k$ is the characteristic wave speed, i.e. the k th eigenvalue of the Roe-averaged Jacobian matrix; \tilde{U} is the Roe-averaged horizontal speed, and $\tilde{\alpha}_k$ is the Roe-averaged wave strength. Only two extreme wave characteristic components are applied with this entropy fix, because this entropy fix is estimated from the wave characteristic structure of a 1D dambreak problem on nonerodible beach which has only two wave characteristics. Moreover, (4.7) is applied to (4.4) when

$$\phi_\delta(\tilde{\lambda}_k) > 2|\tilde{\lambda}_k|\tag{4.8}$$

4.2 Castro-Diaz Scheme

The model of Stoker (2005) and Dodd et al. (2008) used the Roe's method to solve the NLSW and sediment conservation equations simultaneously. For the

ideal of SBC, it is expected to be the wet/dry interface. However, the absolute wet/dry boundary condition could not be implemented by Roe's method because certain of the Roe-average become singular at a dry bed. Instead, an *artificial wetting dry bed* is introduced by setting the water depth to a small positive tolerance (minimum depth, d_{tol}) which this magnitude has to closed to zero. Although the usage of slight wetting gives a bore at the front, unlike the contact wave that should be there (Toro, 2001), this artificial wetting dry cell approach makes the Roe's scheme work well for the wet/dry boundary condition. Dodd et al. (2008) used $d_{tol} = 2$ cm in their simulations, because the smaller minimum depth found that numerical errors increased in their study.

For this reason the source of these numerical problems was investigated. It was found that there were two sources (i) the Shoreline Boundary Condition (SBC) (discussed in Section 4.4), and (ii) the system of equation that uses in the model. It was found a problem that the eigenvalues of (3.24) and (3.25) were functions of the bed elevation, B (see more details in Hudson (2001)). This either makes the wave move at an incorrect shock speed or creates a non-physical discontinuity when $B \neq 0$. For example, the Dodd et al. (2008) model is used to simulate the two cases of the classical dambreak problem (see more details of this problem in Section 4.5.1), which has the initial water depth is 1 m, for different bed levels. The results are shown in Figure 4.2.

For $B = 1$ m, the model results show that the effect of bed level which is included in the eigenvalue function creates the non-physical shock at $x = 0$,

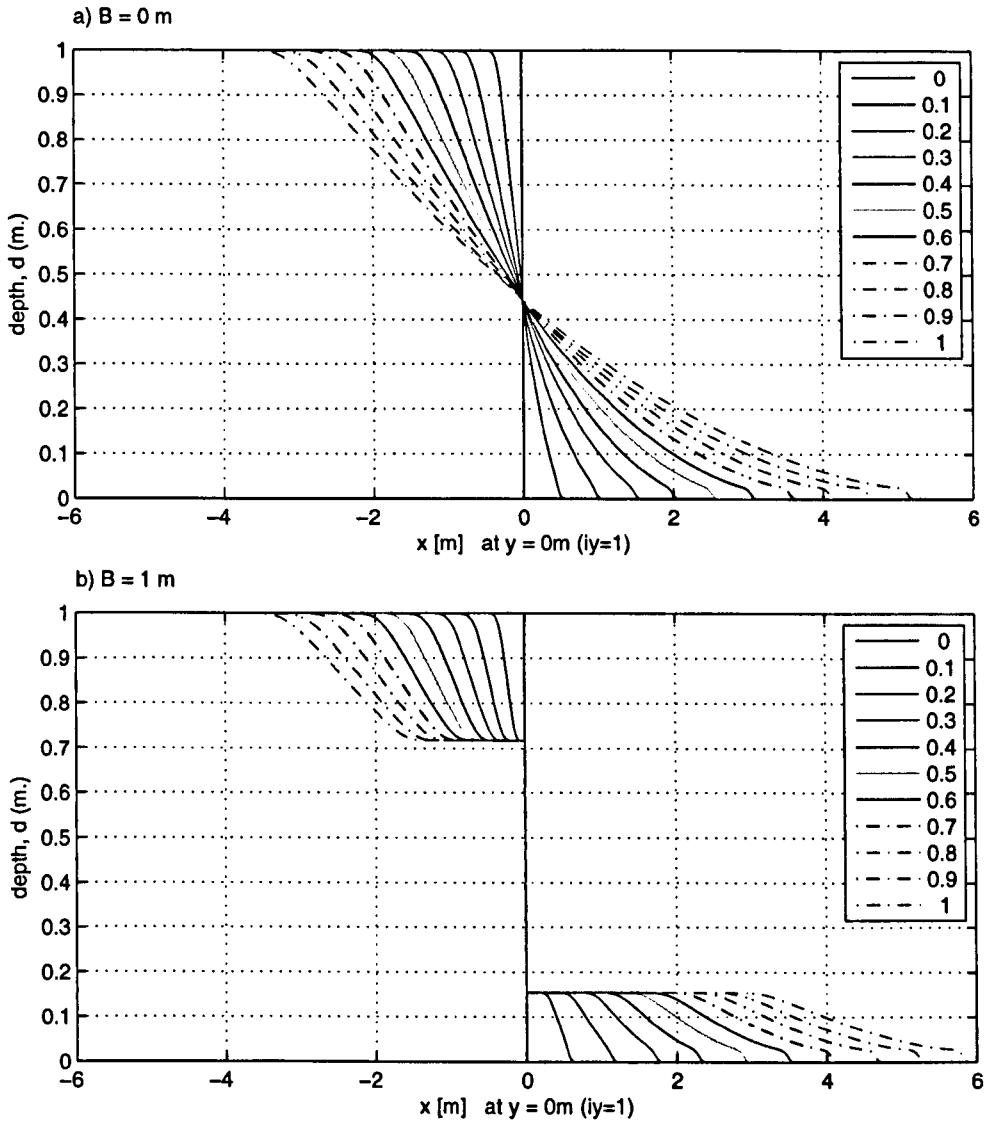


Figure 4.2: Water depth results of the classical dambreak problem simulated by Dodd et al. (2008) model where a) $B = 0$ m case and b) $B = 1$ m case.

whereas the simulation of the $B = 0$ m case has not that shock. Note that Dodd et al. (2008) took $B \approx 0$ in their modelling, so that this non-physical structure is very small.

To keep away from the non-physical shock resulted by the eigenvalues and to

avoid the singular eigenvector matrices in the Roe method, a non-conservative numerical scheme of Castro Diaz et al. (2008) with the Roe-approximation is introduced to implement in the model solving the original form of NLSW equations and sediment conservation equation, (3.1) to (3.4), which includes bed friction, bed diffusion, and infiltration effects in the non-dimensional form as:

$$d_t + (dU)_x + (dV)_y = -w \quad (4.9)$$

$$(dU)_t + \left(dU^2 + \frac{1}{2}d^2 \right)_x + (dUV)_y = -dB_x - \frac{f_w}{2} |\vec{U}| U - Uw \quad (4.10)$$

$$(dV)_t + (dUV)_x + \left(dV^2 + \frac{1}{2}d^2 \right)_y = -dB_y - \frac{f_w}{2} |\vec{U}| V - Vw \quad (4.11)$$

$$B_t + \xi (q_u)_x + \xi (q_v)_y = \xi C |\vec{q}| |\vec{\nabla} b| \quad (4.12)$$

Following Castro Diaz et al. (2008), equations (4.9) to (4.12) can be rewritten in the vector form of a non-conservative term and a source term.

$$\vec{W}_t + \vec{F}_x + \vec{G}_y = \mathbf{C}(\vec{W})\vec{W}_x + \mathbf{D}(\vec{W})\vec{W}_y + \vec{S} \quad (4.13)$$

where

$$\begin{aligned}
 \vec{W} &= \begin{bmatrix} d \\ dU \\ dV \\ B \end{bmatrix}, & \vec{F} &= \begin{bmatrix} dU \\ dU^2 + \frac{1}{2}d^2 \\ dUV \\ \xi q_u \end{bmatrix}, & \vec{G} &= \begin{bmatrix} dV \\ dUV \\ dV^2 + \frac{1}{2}d^2 \\ \xi q_v \end{bmatrix}, \\
 \mathbf{C}(\vec{W}) &= \begin{bmatrix} 0 & 0 & 0 & 0 \\ 0 & 0 & 0 & -d \\ 0 & 0 & 0 & 0 \\ 0 & 0 & 0 & 0 \end{bmatrix}, & \mathbf{D}(\vec{W}) &= \begin{bmatrix} 0 & 0 & 0 & 0 \\ 0 & 0 & 0 & 0 \\ 0 & 0 & 0 & -d \\ 0 & 0 & 0 & 0 \end{bmatrix}, \\
 \vec{S} &= \begin{bmatrix} -w \\ \frac{f_w}{2} |\vec{U}| U - Uw \\ \frac{f_w}{2} |\vec{U}| V - Vw \\ \xi C |\vec{q}| |\vec{\nabla} b| \end{bmatrix}
 \end{aligned} \tag{4.14}$$

When using the Roe-approximation to apply with the Castro-Diaz scheme, the system (4.13) can be written as a non-conservative hyperbolic system

$$\vec{W}_t + \mathcal{A}(\vec{W}) \vec{W}_x + \mathcal{B}(\vec{W}) \vec{W}_y = \vec{S} \tag{4.15}$$

where $\mathcal{A}(\vec{W}) = \tilde{\mathbf{A}}(\vec{W}) - \tilde{\mathbf{C}}(\vec{W})$ and $\mathcal{B}(\vec{W}) = \tilde{\mathbf{B}}(\vec{W}) - \tilde{\mathbf{D}}(\vec{W})$, and $\tilde{\mathbf{A}}(\vec{W})$ and $\tilde{\mathbf{B}}(\vec{W})$ are the Roe-averaged Jacobian matrix of \vec{F} and \vec{G} respectively. Therefore,

$$\tilde{\mathcal{A}}(\vec{W}) = \begin{bmatrix} 0 & 1 & 0 & 0 \\ \tilde{d} - \tilde{U}^2 & 2\tilde{U} & 0 & \tilde{d} \\ -\tilde{U}\tilde{V} & \tilde{V} & \tilde{U} & 0 \\ -\tilde{U}\tilde{D}^F - \tilde{V}\tilde{E}^F & \tilde{D}^F & \tilde{E}^F & 0 \end{bmatrix} \quad (4.16)$$

$$\tilde{\mathcal{B}}(\vec{W}) = \begin{bmatrix} 0 & 0 & 1 & 0 \\ -\tilde{U}\tilde{V} & \tilde{V} & \tilde{U} & 0 \\ \tilde{d} - \tilde{V}^2 & 0 & 2\tilde{V} & \tilde{d} \\ -\tilde{V}\tilde{D}^G - \tilde{U}\tilde{E}^G & \tilde{E}^G & \tilde{D}^G & 0 \end{bmatrix} \quad (4.17)$$

where the Roe approximate value is the same as that of the Dodd et al. (2008) model which is given by (3.26), and the superscript F and G denote that variables are associated with \vec{F} and \vec{G} , respectively. Roe's decomposition must be effected in each direction. Therefore, we start the calculation in the x direction. From equation (4.16), it is found that one of the eigenvalues of $\tilde{\mathcal{A}}$ is $\tilde{\lambda}_4^F = \tilde{U}$ and the others are obtained by solving the cubic

$$P(\tilde{\lambda}) = \tilde{\lambda}^3 - 2\tilde{U}\tilde{\lambda}^2 + \left[\tilde{U}^2 - (\tilde{d} + \tilde{d}\tilde{D}^F) \right] \tilde{\lambda} + \tilde{d}\tilde{D}^F\tilde{U} = 0 \quad (4.18)$$

The roots of $P(\tilde{\lambda})$ are determined by using formulae for roots of a cubic, see Hudson (2001). For a cubic equation,

$$P(x) = x^3 + a_1x^2 + a_2x + a_3 = 0$$

if we let $Q = \frac{1}{9}(3a_2 - a_1^2)$ and $R = \frac{1}{54}(9a_1a_2 - 27a_3 - 2a_1^3)$, then the *discriminant* is $D = Q^3 + R^2$ and if

1. $D > 0$ then one root is real and two are complex.
2. $D = 0$ then all roots are real and two are equal.
3. $D < 0$ then all roots are real and unequal.

If $D < 0$ then the roots of $P(x)$ are

$$\begin{aligned} x_1 &= 2\sqrt{-Q} \cos\left(\frac{1}{3}\theta\right) - \frac{1}{3}a_1 \\ x_2 &= 2\sqrt{-Q} \cos\left(\frac{1}{3}(\theta + 2\pi)\right) - \frac{1}{3}a_1 \\ x_3 &= 2\sqrt{-Q} \cos\left(\frac{1}{3}(\theta + 4\pi)\right) - \frac{1}{3}a_1 \end{aligned} \quad (4.19)$$

where $\cos \theta = \frac{R}{\sqrt{-Q^3}}$.

Once the eigenvalues have been obtained, they are used to determine the eigenvectors

$$\vec{e}_k^F = \begin{bmatrix} 1 \\ \tilde{\lambda}_k \\ \tilde{V} \\ \frac{\tilde{U}^2 - \tilde{d} + (\tilde{\lambda}_k - 2\tilde{U}) \tilde{\lambda}_k}{\tilde{d}} \end{bmatrix} \quad (4.20)$$

for $k = 1, 2, 3$ and $\tilde{E} \neq 0$ then

$$\vec{e}_4^F = \begin{bmatrix} 1 \\ \tilde{U} \\ \tilde{V} - \frac{\tilde{U}}{\tilde{E}} \\ -1 \end{bmatrix} \quad \text{otherwise} \quad \vec{e}_4^F = \begin{bmatrix} 0 \\ 0 \\ 1 \\ 0 \end{bmatrix} \quad (4.21)$$

After the eigenvectors are computed, the wave strengths $\vec{\alpha}_k$ are found from the right eigenvector matrix, $\vec{\alpha}_k = \mathcal{R}^{-1} \Delta \vec{W}$. From (4.21), the computation of $\vec{\alpha}_k$ can be divided into two conditions, (i) $\tilde{E} \neq 0$ and (ii) $\tilde{E} = 0$. The second condition occurs when the depth-averaged velocities from both sides (left and right) of the computational cell have the same magnitude, but their directions are opposite; for example, $V_L = -V_R$ while $d_L = d_R$ and $U_L = U_R$. Therefore, $\vec{\alpha}_k$ is computed by

- when $\tilde{E} \neq 0$ then

$$\tilde{\alpha}_k = -\frac{\tilde{E} \psi_k}{\tilde{U} (\tilde{\lambda}_k - \tilde{\lambda}_a) (\tilde{\lambda}_k - \tilde{\lambda}_b)} \quad (4.22)$$

where

$$\begin{aligned} \psi_k = & \left[(2\tilde{U} - \tilde{\lambda}_a - \tilde{\lambda}_b) \tilde{U} \tilde{V} - \tilde{d} \tilde{V} + (\tilde{\lambda}_a \tilde{\lambda}_b + \tilde{d} - \tilde{U}^2) \left(\tilde{V} - \frac{\tilde{U}}{\tilde{E}} \right) \right] \Delta d \\ & - \frac{\tilde{U}}{\tilde{E}} \left(2\tilde{U} - \tilde{\lambda}_a - \tilde{\lambda}_b \right) \Delta(dU) - (\tilde{U} - \tilde{\lambda}_a) (\tilde{U} - \tilde{\lambda}_b) \Delta(dV) + \tilde{d} \Delta B \end{aligned}$$

for $k, a, b \in \{1, 2, 3\}$ where $a \neq k \neq b$ and

$$\tilde{\alpha}_4 = \frac{\tilde{E} [\tilde{V} \Delta d - \Delta(dV)]}{\tilde{U}} \quad (4.23)$$

- when $\tilde{E} = 0$ then

$$\tilde{\alpha}_k = \frac{(\tilde{\lambda}_a \tilde{\lambda}_b + \tilde{d} - \tilde{U}^2) \Delta d + (2\tilde{U} - \tilde{\lambda}_a - \tilde{\lambda}_b) \Delta(dU) + \tilde{d} \Delta B}{(\tilde{\lambda}_k - \tilde{\lambda}_a) (\tilde{\lambda}_k - \tilde{\lambda}_b)} \quad (4.24)$$

for $k, a, b \in \{1, 2, 3\}$ where $a \neq k \neq b$ and

$$\tilde{\alpha}_4 = \frac{\tilde{E} [\tilde{V} \Delta d - \Delta(dV)]}{\tilde{U}} \quad (4.25)$$

For the bed slope decomposition term

$$\tilde{\beta}_k = -\frac{(2\tilde{U} - \tilde{\lambda}_a - \tilde{\lambda}_b) \tilde{d} \Delta B}{(\tilde{\lambda}_k - \tilde{\lambda}_a)(\tilde{\lambda}_k - \tilde{\lambda}_b)} \quad (4.26)$$

for $k, a, b \in \{1, 2, 3\}$ where $a \neq k \neq b$ and $\tilde{\beta}_4 = 0$.

The operator Δ is defined as $\Delta(\bullet) = \bullet_R - \bullet_L$; for example, $\Delta d = d_R - d_L$. The subscript L and R denote as left and right components of computational cell, and k, a , and b denote the component numbers of Roe-averaged Jacobian matrix.

Similarly for y direction. From (4.17), one of the eigenvalues of $\tilde{\mathcal{B}}$ is $\tilde{\lambda}_4^G = \tilde{V}$ and the other three are obtained by solving the cubic

$$P(\tilde{\lambda}) = \tilde{\lambda}^3 - 2\tilde{V}\tilde{\lambda}^2 + [\tilde{V}^2 - (\tilde{d} + \tilde{d}\tilde{D}^G)]\tilde{\lambda} + \tilde{d}\tilde{D}^G\tilde{V} = 0 \quad (4.27)$$

The roots of $P(\tilde{\lambda})$ are determined by using formulae for roots of a cubic. Eigenvectors are

$$\vec{\tilde{e}}_k^G = \begin{bmatrix} 1 \\ \tilde{U} \\ \tilde{\lambda}_k \\ \frac{\tilde{V}^2 - \tilde{d} + (\tilde{\lambda}_k - 2\tilde{V})\tilde{\lambda}_k}{\tilde{d}} \end{bmatrix} \quad (4.28)$$

for $k = 1, 2, 3$, and if $\tilde{E} \neq 0$ then

$$\vec{\tilde{e}}_4^G = \begin{bmatrix} 1 \\ \tilde{U} - \frac{\tilde{V}}{\tilde{E}} \\ \tilde{V} \\ -1 \end{bmatrix} \quad \text{otherwise} \quad \vec{\tilde{e}}_4^G = \begin{bmatrix} 0 \\ 1 \\ 0 \\ 0 \end{bmatrix} \quad (4.29)$$

Wave strengths $\vec{\alpha}_k$ are

- when $\tilde{E} \neq 0$ then

$$\tilde{\alpha}_k = -\frac{\tilde{E}\psi_k}{\tilde{V}(\tilde{\lambda}_k - \tilde{\lambda}_a)(\tilde{\lambda}_k - \tilde{\lambda}_b)} \quad (4.30)$$

where

$$\begin{aligned} \psi_k = & \left[(2\tilde{V} - \tilde{\lambda}_a - \tilde{\lambda}_b) \tilde{U}\tilde{V} - \tilde{d}\tilde{U} + (\tilde{\lambda}_a\tilde{\lambda}_b + \tilde{d} - \tilde{V}^2) \left(\tilde{U} - \frac{\tilde{V}}{\tilde{E}} \right) \right] \Delta d \\ & - (\tilde{V} - \tilde{\lambda}_a)(\tilde{V} - \tilde{\lambda}_b) \Delta(dU) - \frac{\tilde{V}}{\tilde{E}} (2\tilde{V} - \tilde{\lambda}_a - \tilde{\lambda}_b) \Delta(dV) + \tilde{d}\Delta B \end{aligned}$$

for $k, a, b \in \{1, 2, 3\}$ where $a \neq k \neq b$ and

$$\tilde{\alpha}_4 = \frac{\tilde{E} [\tilde{U}\Delta d - \Delta(dU)]}{\tilde{V}} \quad (4.31)$$

- when $\tilde{E} = 0$ then

$$\tilde{\alpha}_k = \frac{(\tilde{\lambda}_a\tilde{\lambda}_b + \tilde{d} - \tilde{V}^2) \Delta d + (2\tilde{V} - \tilde{\lambda}_a - \tilde{\lambda}_b) \Delta(dV) + \tilde{d}\Delta B}{(\tilde{\lambda}_k - \tilde{\lambda}_a)(\tilde{\lambda}_k - \tilde{\lambda}_b)} \quad (4.32)$$

for $k, a, b \in \{1, 2, 3\}$ where $a \neq k \neq b$ and

$$\tilde{\alpha}_4 = \frac{\tilde{E} [\tilde{U}\Delta d - \Delta(dU)]}{\tilde{V}} \quad (4.33)$$

For the bed slope decomposition term

$$\tilde{\beta}_k = -\frac{(2\tilde{V} - \tilde{\lambda}_a - \tilde{\lambda}_b) \tilde{d}\Delta B}{(\tilde{\lambda}_k - \tilde{\lambda}_a)(\tilde{\lambda}_k - \tilde{\lambda}_b)} \quad (4.34)$$

for $k, a, b \in \{1, 2, 3\}$ where $a \neq k \neq b$ and $\tilde{\beta}_4 = 0$.

The spatial discretisation used is the same as the usual Roe's scheme with a flux-limiter function as given by equations (3.21) and (3.22). The first order Euler method is applied for the time increment, and the source term is evaluated pointwise using the values at the cell centre.

4.3 Time Operator Splitting Scheme

Only the bed slope term is treated by the upwinding scheme of Roe's method in both models of Dodd et al. (2008) and new one which uses the Castro Diaz et al. (2008) scheme, whereas bed friction, bed diffusion, and infiltration effects are implemented by the pointwise method. This group of source terms (\vec{S} in (4.14)) is integrated by the first order Euler scheme. To achieve higher order accuracy when computing the source terms, modellers have proposed splitting schemes, fractional-step methods, and time operator splitting scheme (TOS) (see LeVeque (2002)). The TOS scheme divides the NLSW systems to two subproblems in space and time, and solves them independently. In the present study, the system of NLSW and sediment conservation equations is applied with TOS scheme by splitting the equation into the homogeneous partial differential equation (PDE) and ordinary differential equation (ODE) as shown in the vector form of (4.35) and (4.36), respectively.

$$\text{Problem A : } \quad \vec{W}_t + \vec{F}_x + \vec{G}_y = 0 \quad (4.35)$$

$$\text{Problem B : } \quad \vec{W}_t = \vec{S} \quad (4.36)$$

In each of these subproblems, there is therefore more a flexibility in choosing the solver: the high-resolution shock-capturing methods can be used directly for the homogeneous equation (4.35), whereas the higher accuracy scheme for the time increment can also be applied to ODE (4.36), such as the Runge-Kutta fourth order scheme. We discuss the application of the TOS method separately: first the homogeneous part (4.35), and then the inhomogeneous part (4.36).

Homogeneous Part

In equation (4.9) to (4.12), the source term, which appears on the right hands side (RHS) of those equations, comprises the bed slope, bed friction, bed diffusion, and infiltration terms consistent with the approach taken in this work, the homogeneous equation is solved with Roe's method.

However, using the Roe-approximation with the homogeneous equation without the bed slope term (solely the terms presented in the left hand side (LHS) of (4.9)-(4.12)), leads to a problem in calculating the wave strengths $\tilde{\alpha}_k$ when \tilde{U} or \tilde{V} equal to zero. This makes the right eigenvector matrix (\mathcal{R}^F and \mathcal{R}^G) of the Jacobian matrices, (4.37) and (4.38), of this homogeneous equation is singular; therefore, the wave strength components do not exist.

$$\mathcal{R}^F = \begin{bmatrix} 1 & 1 & 0 & 0 \\ \tilde{U} + \sqrt{\tilde{d}} & \tilde{U} - \sqrt{\tilde{d}} & 0 & 0 \\ \tilde{V} & \tilde{V} & 0 & \frac{\tilde{U}}{\tilde{E}^F} \\ \frac{\tilde{D}^F \sqrt{\tilde{d}}}{\tilde{U} + \sqrt{\tilde{d}}} & -\frac{\tilde{D}^F \sqrt{\tilde{d}}}{\tilde{U} - \sqrt{\tilde{d}}} & 1 & 1 \end{bmatrix} \quad (4.37)$$

$$\mathcal{R}^G = \begin{bmatrix} 1 & 1 & 0 & 0 \\ \tilde{U} & \tilde{U} & 0 & \frac{\tilde{V}}{\tilde{E}^G} \\ \tilde{V} + \sqrt{\tilde{d}} & \tilde{V} - \sqrt{\tilde{d}} & 0 & 0 \\ \frac{\tilde{D}^G \sqrt{\tilde{d}}}{\tilde{V} + \sqrt{\tilde{d}}} & -\frac{\tilde{D}^G \sqrt{\tilde{d}}}{\tilde{V} - \sqrt{\tilde{d}}} & 1 & 1 \end{bmatrix} \quad (4.38)$$

In order to avoid a singular matrix of right eigenvectors, the bed slope term is treated by the source term upwinding scheme of Roe's method and solved at

the same time as flux term in this homogeneous part. Then this amended homogeneous equation can be solved using the Roe-averaged Castro-Diaz scheme without the pointwise source term.

Inhomogeneous Part

The fourth order Runge-Kutta method is used to integrate (4.36) which now contains the effect of bed friction, bed diffusion and infiltration. To increase accuracy, reduce numerical oscillations, and minimise computational effort, the adaptive stepsize control for the Runge-Kutta method is used here (see Press et al. (1992)). This control method compares the error between one big step and two small steps between the same two times of the fourth order Runge-Kutta method, and adjusts the time stepsize on the next step, depending on the difference between the two estimates.

Second order accuracy in time for TOS scheme

A second order accurate TOS method is introduced by Toro (1999) and LeVeque (2002) and implemented in the model. This treatment has three steps as:

$$\begin{aligned}
 1) \text{ (ODE)} : \quad \vec{W}_{i,j}^* &= \vec{W}_{i,j}^n + \frac{\Delta t}{2} \vec{S}_{i,j}^n & : \vec{W}^n \xrightarrow{\Delta t/2} \vec{W}^* \\
 2) \text{ (PDE)} : \quad \vec{W}_{i,j}^{**} &= \vec{W}_{i,j}^* - \frac{\Delta t}{\Delta x} \left(\vec{F}_{i+\frac{1}{2},j}^* - \vec{F}_{i-\frac{1}{2},j}^* \right) - \frac{\Delta t}{\Delta y} \left(\vec{G}_{i,j+\frac{1}{2}}^* - \vec{G}_{i,j-\frac{1}{2}}^* \right) \\
 & & : \vec{W}^* \xrightarrow{\Delta t} \vec{W}^{**} \\
 3) \text{ (ODE)} : \quad \vec{W}_{i,j}^{n+1} &= \vec{W}_{i,j}^{**} + \frac{\Delta t}{2} \vec{S}_{i,j}^{**} & : \vec{W}^{**} \xrightarrow{\Delta t/2} \vec{W}^{n+1}
 \end{aligned}$$

where $\vec{W}_{i,j}^*$ and $\vec{W}_{i,j}^{**}$ are the intermediate solutions at the end of the first and second step respectively, $\vec{S}_{i,j}^{**}$ is the source term computed from the intermediate solutions of $\vec{W}_{i,j}^{**}$. The first and the third steps use the adaptive stepsize control Runge-Kutta method with the Roe-averaged Castro-Diaz scheme implemented in the second step. The comparison of results between the TOS method and the unsplit Roe-averaged Castro-Diaz scheme is shown in Section 4.6.2.

4.4 Shoreline Boundary Condition

In order to allow a moving boundary, a SBC must be included in the model. A SBC for Godunov-type models consists of a wetting and drying algorithm, and a method to estimate the fluxes at a wet/dry boundary (see Briganti and Dodd (2009)). In the following we state the wetting/drying algorithm and then present two methods for computing the wet-dry flux, the first being based on that of Hubbard and Dodd (2002), Stoker (2005), and Dodd et al. (2008) and the second being novel.

4.4.1 Wetting/Drying Algorithm

Stoker (2005) and Dodd et al. (2008) used the wetting and drying method of Hubbard and Dodd (2002). There is no special tracking procedure used in their method. The shoreline is constructed from the mesh interfaces between wet and dry cells. A cell is considered to be dry if the depth is below a minimum value,

d_{tol} . At the beginning of each integration of the numerical scheme in the model, there is a search routine to find cells which have the potential to be flooded. A cell is in a position to be flooded if the bed level is below the water level in an adjacent cell. After the completion of each integration step with cells updated, the drying procedure is implemented. The depth of water in certain cells may have dropped below d_{tol} . These cells are considered to be dry and their depth d is reset to zero.

4.4.2 Fluxes via Hubbard and Dodd Approach

Following Hubbard and Dodd (2002), the calculation of the fluxes at the shore-line cells can be divided into three different types of internal edge as shown in Figure 4.3, which are treated as follows:

- *wet/wet* use Roe's scheme as normal for both cells.
- *dry/dry* ignore completely, no contribution is made to either cell.
- *wet/dry* no update is made to either cell from this edge. This is done because it has already been decided that the dry cell will remain dry, so a zero flux condition is applied to this edge.

For the cell at the SBC, the wetting/drying algorithm is a tool for searching the flood potential cells; then the water depth of those cells is set to the minimum depth criterion ($d = d_{tol}$) and the depth averaged horizontal velocities, U and V , are zero. Therefore, these cells become to be the wet cells which have one

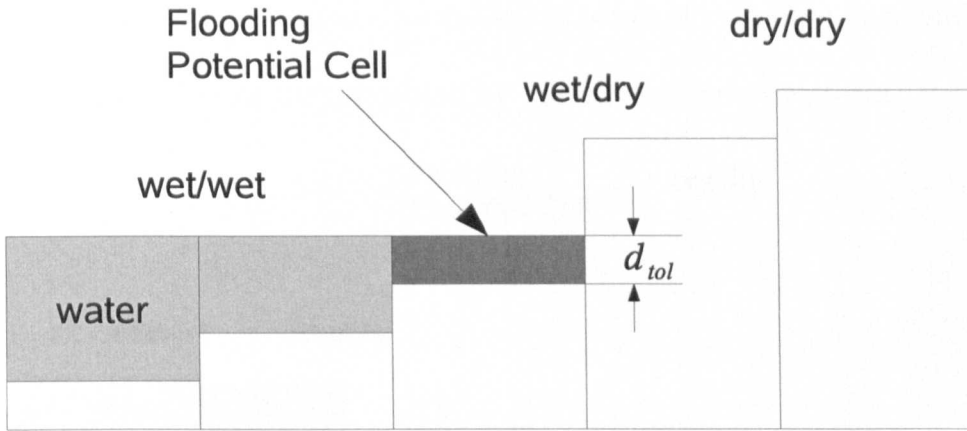


Figure 4.3: The wetting/drying procedure illustrated in 1D.

side is wet/wet boundary and another is wet/dry boundary when they are considered in 1D as shown in Figure 4.3. This allows the fluxes at the interfaces of the potentially flooded cells are computed by the Roe solver scheme on the wet/wet side, whereas the wet/dry side is applied with a zero flux condition. Hereafter, we called this type of SBC as HDA.

4.4.3 Primitive Form BC

Using the artificial wetting dry bed method in the model might cause the numerical problems in the simulation as discussed in Section 4.2. The real wet/dry interface is the ideal for the SBC. Therefore, the primitive variable form of the system equations is introduced to be another alternative for calculating fluxes only at the flooding potential cells instead of filling the water to those cells, because the Roe decompositions of the primitive variable form are valid at the dry cell ($d = 0$). With this boundary condition, fluxes of the flooding potential cells

is computed by Roe-averaged Castro-Diaz scheme of primitive variable form; whereas, the other cells are computed by the flux conservative form.

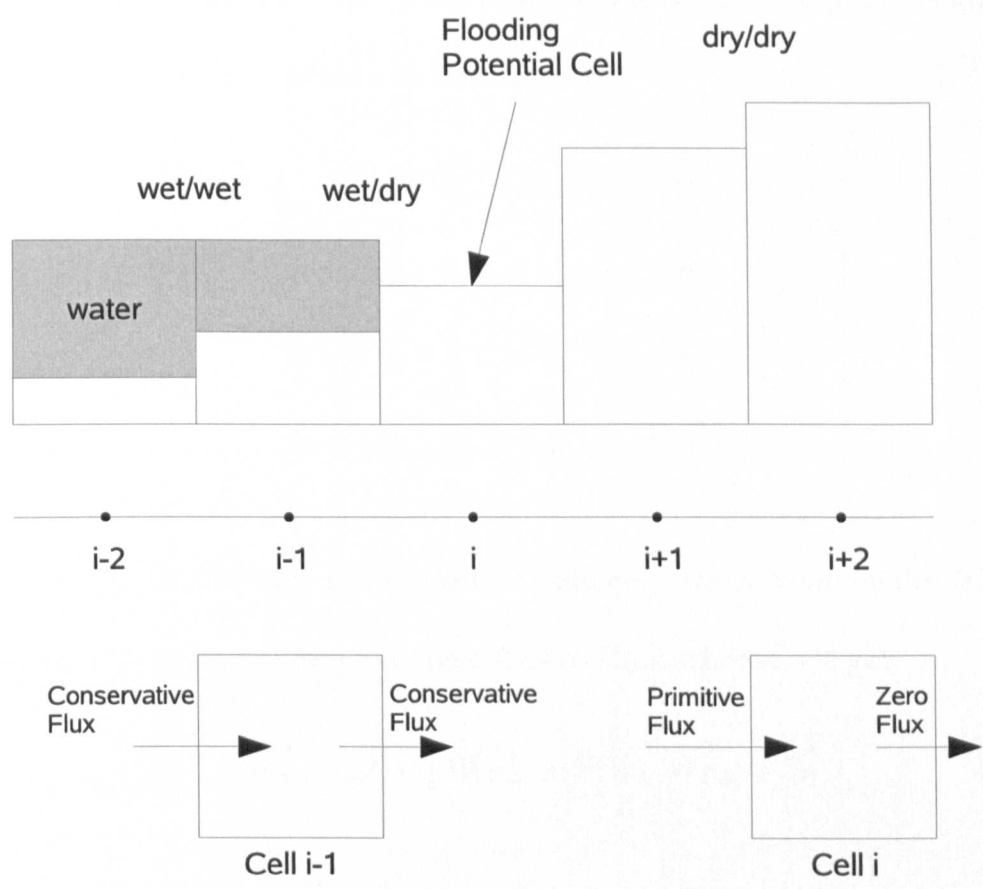


Figure 4.4: Applying the primitive and normal Roe-averaged fluxes to cells illustrated in 1D

Figure 4.4 illustrates the interface fluxes of the flooding potential cell and the neighbour cells. The cell i is the potentially flooded cell, in which dependent variables are updated by the primitive flux at the *wet/dry* edge and zero flux at the *dry/dry* edge. On the other hand the adjacent wet cell, cell $i-1$, is updated with the Roe-averaged conservative fluxes in both *wet/wet* and *wet/dry* edges. Below we present the full Roe decomposition used for the SBC.

Roe-averaged Castro-Diaz scheme of primitive variable form

The primitive variable form of the dimensionless NLSW equations and sediment conservation equation can be written as:

$$d_t + U d_x + d U_x + V d_y + d V_y = -w \quad (4.39)$$

$$U_t + U U_x + d_x + V U_y = -B_x - \frac{f_w}{2d} |\vec{U}| U \quad (4.40)$$

$$V_t + U V_x + V V_y + d_y = -B_y - \frac{f_w}{2d} |\vec{U}| V \quad (4.41)$$

$$B_t + \xi (q_u)_x + \xi (q_v)_y = \xi C |\vec{q}| |\vec{\nabla} b| \quad (4.42)$$

Linearising (4.39)-(4.42) at an interface between two constant states (right (R) and left (L)) using the Roe-averaged Castro-Diaz scheme, we get:

$$\vec{W}_{P,t} + \mathcal{A}(\vec{W}_P) \vec{W}_{P,x} + \mathcal{B}(\vec{W}_P) \vec{W}_{P,y} = \vec{S}_P \quad (4.43)$$

where $\vec{W}_P = [d, U, V, B]^T$ is the dependent variable vector, the source term vector $\vec{S}_P = \left[-w, \frac{f_w}{2d} |\vec{U}| U, \frac{f_w}{2d} |\vec{U}| V, \xi C |\vec{q}| |\vec{\nabla} b| \right]^T$, $\mathcal{A}(\vec{W}_P) = \tilde{\mathbf{A}}(\vec{W}_P) - \tilde{\mathbf{C}}(\vec{W}_P)$ and $\mathcal{B}(\vec{W}_P) = \tilde{\mathbf{B}}(\vec{W}_P) - \tilde{\mathbf{D}}(\vec{W}_P)$, $\tilde{\mathbf{A}}(\vec{W}_P)$ and $\tilde{\mathbf{B}}(\vec{W}_P)$ are the Roe-averaged Jacobian matrices of \vec{F}_P and \vec{G}_P respectively, $\tilde{\mathbf{C}}(\vec{W}_P)$ and $\tilde{\mathbf{D}}(\vec{W}_P)$ are the Roe-averaged Jacobian matrices of the bed slope terms in the x and y directions respectively, and subscript P refers to primitive form. Thus,

$$\widetilde{\mathcal{A}}(\overrightarrow{W_P}) = \begin{bmatrix} \tilde{U}_P & \tilde{d} & 0 & 0 \\ 1 & \tilde{U}_P & 0 & 1 \\ 0 & 0 & \tilde{U}_P & 0 \\ 0 & \tilde{D}_P^F & \tilde{E}_P & 0 \end{bmatrix} \quad (4.44)$$

$$\widetilde{\mathcal{B}}(\overrightarrow{W_P}) = \begin{bmatrix} \tilde{V}_P & 0 & \tilde{d} & 0 \\ 0 & \tilde{V}_P & 0 & 0 \\ 1 & 0 & \tilde{V}_P & 1 \\ 0 & \tilde{E}_P & \tilde{D}_P^G & 0 \end{bmatrix} \quad (4.45)$$

where the Roe-averaged variables of the primitive form are different from the flux conservative form as:

$$\begin{aligned} \tilde{d} &= \frac{1}{2}(d_R + d_L), \quad \tilde{U}_P = \frac{1}{2}(U_R + U_L), \quad \tilde{V}_P = \frac{1}{2}(V_R + V_L), \\ \tilde{D}_P^F &= \xi A \left(U_R^2 + U_R U_L + U_L^2 + \tilde{V}_P^2 \right), \\ \tilde{D}_P^G &= \xi A \left(\tilde{U}_P^2 + V_R^2 + V_R V_L + V_L^2 \right), \\ \tilde{E}_P &= \xi A \left[\tilde{U}_P \tilde{V}_P + \frac{1}{2}(U_R V_R + U_L V_L) \right] \end{aligned} \quad (4.46)$$

To calculate the Roe's decomposition in each direction, we start with the x direction equation (4.44). One of the eigenvalues of $\widetilde{\mathcal{A}}$ is $\tilde{\lambda}_{P,4}^F = \tilde{U}_P$ and the others are obtained by solving the cubic

$$P(\tilde{\lambda}_P) = \tilde{\lambda}_P^3 - 2\tilde{U}_P \tilde{\lambda}_P^2 + \left[\tilde{U}_P^2 - (\tilde{d} + \tilde{D}_P^F) \right] \tilde{\lambda}_P + \tilde{D}_P^F \tilde{U}_P = 0 \quad (4.47)$$

Note the difference between (4.47) and (4.18) come from that the terms of \tilde{D}_P^F , \tilde{D}_P^G , and \tilde{E}_P are not divided by the water depth, so \tilde{d} is no longer multiplied by

\tilde{D}_P^F in the third term of RHS of (4.47). For this reason, the Roe decompositions of the primitive form are valid in order to compute the real wet/dry condition without artificial wetting dry bed technique. Hence, the eigenvectors then become:

$$\vec{\tilde{e}}_{P,k}^F = \begin{bmatrix} 1 \\ \frac{\tilde{\lambda}_{P,k} - \tilde{U}_P}{\tilde{d}} \\ \frac{\tilde{\lambda}_{P,k} (\tilde{U}_P - \tilde{\lambda}_{P,k})^2 + \tilde{D}_P^F (\tilde{U}_P - \tilde{\lambda}_{P,k}) - \tilde{d} \tilde{E}_P}{\frac{\tilde{d} \tilde{\lambda}_{P,k}}{(\tilde{U}_P - \tilde{\lambda}_{P,k})^2 - \tilde{d}}} \end{bmatrix} \quad (4.48)$$

for $k = 1, 2, 3$ and $\tilde{E}_P \neq 0$, and when $\tilde{E}_P = 0$, we obtain

$$\vec{\tilde{e}}_{P,k}^F = \begin{bmatrix} 1 \\ \frac{\tilde{\lambda}_{P,k} - \tilde{U}_P}{\tilde{d}} \\ 0 \\ \frac{(\tilde{U}_P - \tilde{\lambda}_{P,k})^2 - \tilde{d}}{\tilde{d}} \end{bmatrix} \quad (4.49)$$

For $k = 4$ and $\tilde{E}_P \neq 0$,

$$\vec{\tilde{e}}_{P,4}^F = \begin{bmatrix} 1 \\ 0 \\ -\frac{\tilde{U}_P}{\tilde{E}_P} \\ -1 \end{bmatrix} \quad \text{otherwise} \quad \vec{\tilde{e}}_{P,4}^F = \begin{bmatrix} 0 \\ 0 \\ 1 \\ 0 \end{bmatrix} \quad (4.50)$$

Thus, the wave strengths $\vec{\alpha}_{P,k}$ are:

- when $\tilde{E}_P \neq 0$ then

$$\tilde{\alpha}_{P,k} = \frac{\psi_{P,k}}{(\tilde{U}_P - \tilde{\lambda}_{P,k}) (\tilde{\lambda}_{P,k} - \tilde{\lambda}_{P,a}) (\tilde{\lambda}_{P,k} - \tilde{\lambda}_{P,b})} \quad (4.51)$$

where

$$\begin{aligned} \psi_{P,k} = & (\tilde{\lambda}_{P,a} + \tilde{\lambda}_{P,b} - 2\tilde{U}_P) \tilde{d} \Delta d \\ & - \left[(\tilde{U}_P - \tilde{\lambda}_{P,a}) (\tilde{U}_P - \tilde{\lambda}_{P,b}) + (\tilde{d} + \tilde{D}_P^F) \right] \tilde{d} \Delta U \\ & - \tilde{d} \tilde{E}_P \Delta \tilde{V} + (\tilde{\lambda}_{P,a} + \tilde{\lambda}_{P,b} - \tilde{U}_P) \tilde{d} \Delta B \end{aligned}$$

for $k, a, b \in \{1, 2, 3\}$ where $a \neq k \neq b$; and

$$\tilde{\alpha}_{P,4} = \frac{\psi_{P,4}}{(\tilde{U}_P - \tilde{\lambda}_{P,1}) (\tilde{U}_P - \tilde{\lambda}_{P,2}) (\tilde{U}_P - \tilde{\lambda}_{P,3})}, \quad (4.52)$$

where

$$\begin{aligned} \psi_{P,4} = & \left[\tilde{d} (3\tilde{U}_P - \tilde{\lambda}_{P,1} - \tilde{\lambda}_{P,2} - \tilde{\lambda}_{P,3}) \right. \\ & \left. + (\tilde{U}_P - \tilde{\lambda}_{P,1}) (\tilde{U}_P - \tilde{\lambda}_{P,2}) (\tilde{U}_P - \tilde{\lambda}_{P,3}) \right] \Delta d \\ & + \left[3\tilde{U}_P^2 - 2\tilde{U}_P (\tilde{\lambda}_{P,1} + \tilde{\lambda}_{P,2} + \tilde{\lambda}_{P,3}) \right. \\ & \left. + (\tilde{\lambda}_{P,1}\tilde{\lambda}_{P,2} + \tilde{\lambda}_{P,1}\tilde{\lambda}_{P,3} + \tilde{\lambda}_{P,2}\tilde{\lambda}_{P,3}) + \tilde{d} + \tilde{D}_P^F \right] \tilde{d} \Delta U \\ & + \tilde{d} \tilde{E}_P \Delta V + (2\tilde{U}_P - \tilde{\lambda}_{P,1} - \tilde{\lambda}_{P,2} - \tilde{\lambda}_{P,3}) \tilde{d} \Delta B \end{aligned}$$

For the bed slope decomposition term

$$\tilde{\beta}_{P,k} = - \frac{\left[(\tilde{U}_P - \tilde{\lambda}_{P,a}) (\tilde{U}_P - \tilde{\lambda}_{P,b}) + \tilde{d} + \tilde{D}_P^F \right] \tilde{d} \Delta B}{(\tilde{\lambda}_{P,k} - \tilde{\lambda}_{P,a}) (\tilde{\lambda}_{P,k} - \tilde{\lambda}_{P,b}) (\tilde{U}_P - \tilde{\lambda}_{P,k})} \quad (4.53)$$

for $k, a, b \in \{1, 2, 3\}$ where $a \neq k \neq b$; and

$$\tilde{\beta}_{P,4} = \frac{\varphi_{P,4}}{(\tilde{U}_P - \tilde{\lambda}_{P,1}) (\tilde{U}_P - \tilde{\lambda}_{P,2}) (\tilde{U}_P - \tilde{\lambda}_{P,3})}, \quad (4.54)$$

where

$$\begin{aligned} \varphi_{P,4} = & - \left[3\tilde{U}_P^2 - 2\tilde{U}_P \left(\tilde{\lambda}_{P,1} + \tilde{\lambda}_{P,2} + \tilde{\lambda}_{P,3} \right) \right. \\ & \left. + \left(\tilde{\lambda}_{P,1}\tilde{\lambda}_{P,2} + \tilde{\lambda}_{P,1}\tilde{\lambda}_{P,3} + \tilde{\lambda}_{P,2}\tilde{\lambda}_{P,3} \right) + \tilde{d} + \tilde{D}_P^F \right] \tilde{d}\Delta B \end{aligned}$$

- when $\tilde{E}_P = 0$ then

$$\tilde{\alpha}_{P,k} = \frac{\psi_{P,k}}{\left(\tilde{\lambda}_{P,k} - \tilde{\lambda}_{P,a} \right) \left(\tilde{\lambda}_{P,k} - \tilde{\lambda}_{P,b} \right)} \quad (4.55)$$

where

$$\begin{aligned} \psi_{P,k} = & \left[\left(\tilde{U}_P - \tilde{\lambda}_{P,a} \right) \left(\tilde{U}_P - \tilde{\lambda}_{P,b} \right) + \tilde{d} \right] \Delta d \\ & + \left(2\tilde{U}_P - \tilde{\lambda}_{P,a} - \tilde{\lambda}_{P,b} \right) \tilde{d}\Delta U + \tilde{d}\Delta B \end{aligned}$$

for $k, a, b \in \{1, 2, 3\}$ where $a \neq k \neq b$; and

$$\tilde{\alpha}_{P,4} = \Delta V \quad (4.56)$$

For the bed slope decomposition term

$$\tilde{\beta}_{P,k} = \frac{\left(\tilde{\lambda}_{P,a} + \tilde{\lambda}_{P,b} - 2\tilde{U}_P \right) \tilde{d}\Delta B}{\left(\tilde{\lambda}_{P,k} - \tilde{\lambda}_{P,a} \right) \left(\tilde{\lambda}_{P,k} - \tilde{\lambda}_{P,b} \right)} \quad (4.57)$$

for $k, a, b \in \{1, 2, 3\}$ where $a \neq k \neq b$, and $\tilde{\beta}_{P,4} = 0$.

Similarly for y direction. From equation (4.45), one of the eigenvalues of $\tilde{\mathcal{B}}$ is

$\tilde{\lambda}_{P,4}^G = \tilde{V}_P$ and the other three are obtained by solving the cubic

$$P(\tilde{\lambda}_P) = \tilde{\lambda}_P^3 - 2\tilde{V}_P\tilde{\lambda}_P^2 + \left[\tilde{V}_P^2 - \left(\tilde{d} + \tilde{D}_P^G \right) \right] \tilde{\lambda}_P + \tilde{D}_P^G\tilde{V}_P = 0 \quad (4.58)$$

The roots of $P(\tilde{\lambda}_P)$ are determined by using formulae for roots of a cubic. Once the eigenvalues have been obtained, they are used to determine the eigenvectors

$$\vec{\tilde{e}}_{P,k}^G = \begin{bmatrix} 1 \\ \frac{\tilde{\lambda}_{P,k} \left(\tilde{V}_P - \tilde{\lambda}_{P,k} \right)^2 + \tilde{D}_P^G \left(\tilde{V}_P - \tilde{\lambda}_{P,k} \right) - \tilde{d} \tilde{\lambda}_{P,k}}{\frac{\tilde{d} \tilde{E}_P}{\tilde{\lambda}_{P,k} - \tilde{V}_P}} \\ \frac{\left(\tilde{V}_P - \tilde{\lambda}_{P,k} \right)^2 - \tilde{d}}{\tilde{d}} \end{bmatrix} \quad (4.59)$$

for $k = 1, 2, 3$ and $\tilde{E}_P \neq 0$. When $\tilde{E}_P = 0$, we obtain

$$\vec{\tilde{e}}_{P,k}^G = \begin{bmatrix} 1 \\ 0 \\ \frac{\tilde{\lambda}_{P,k} - \tilde{V}_P}{\frac{\tilde{d}}{\left(\tilde{V}_P - \tilde{\lambda}_{P,k} \right)^2 - \tilde{d}}} \end{bmatrix} \quad (4.60)$$

for $k = 4$ and $\tilde{E}_P \neq 0$,

$$\vec{\tilde{e}}_{P,4}^G = \begin{bmatrix} 1 \\ -\frac{\tilde{V}_P}{\tilde{E}_P} \\ 0 \\ -1 \end{bmatrix} \quad \text{otherwise} \quad \vec{\tilde{e}}_{P,4}^G = \begin{bmatrix} 0 \\ 1 \\ 0 \\ 0 \end{bmatrix} \quad (4.61)$$

After the eigenvectors are computed, the wave strengths $\vec{\alpha}_{P,k}$ are

- when $\tilde{E}_P \neq 0$ then

$$\tilde{\alpha}_{P,k} = \frac{\psi_{P,k}}{\left(\tilde{V}_P - \tilde{\lambda}_{P,k} \right) \left(\tilde{\lambda}_{P,k} - \tilde{\lambda}_{P,a} \right) \left(\tilde{\lambda}_{P,k} - \tilde{\lambda}_{P,b} \right)} \quad (4.62)$$

where

$$\begin{aligned}\psi_{P,k} = & \left(\tilde{\lambda}_{P,a} + \tilde{\lambda}_{P,b} - 2\tilde{V}_P \right) \tilde{d}\Delta d \\ & - \left[\left(\tilde{V}_P - \tilde{\lambda}_{P,a} \right) \left(\tilde{V}_P - \tilde{\lambda}_{P,b} \right) + \left(\tilde{d} + \tilde{D}_P^G \right) \right] \tilde{d}\Delta V \\ & - \tilde{d}\tilde{E}_P\Delta U + \left(\tilde{\lambda}_{P,a} + \tilde{\lambda}_{P,b} - \tilde{V}_P \right) \tilde{d}\Delta B\end{aligned}$$

for $k, a, b \in \{1, 2, 3\}$ where $a \neq k \neq b$ and

$$\tilde{\alpha}_{P,4} = \frac{\psi_{P,4}}{\left(\tilde{V}_P - \tilde{\lambda}_{P,1} \right) \left(\tilde{V}_P - \tilde{\lambda}_{P,2} \right) \left(\tilde{V}_P - \tilde{\lambda}_{P,3} \right)} \quad (4.63)$$

where

$$\begin{aligned}\psi_{P,4} = & \left[\tilde{d} \left(3\tilde{V}_P - \tilde{\lambda}_{P,1} - \tilde{\lambda}_{P,2} - \tilde{\lambda}_{P,3} \right) \right. \\ & \left. + \left(\tilde{V}_P - \tilde{\lambda}_{P,1} \right) \left(\tilde{V}_P - \tilde{\lambda}_{P,2} \right) \left(\tilde{V}_P - \tilde{\lambda}_{P,3} \right) \right] \Delta d \\ & \left[3\tilde{V}_P^2 - 2\tilde{V}_P \left(\tilde{\lambda}_{P,1} + \tilde{\lambda}_{P,2} + \tilde{\lambda}_{P,3} \right) \right. \\ & \left. + \left(\tilde{\lambda}_{P,1}\tilde{\lambda}_{P,2} + \tilde{\lambda}_{P,1}\tilde{\lambda}_{P,3} + \tilde{\lambda}_{P,2}\tilde{\lambda}_{P,3} \right) + \tilde{d} + \tilde{D}_P^G \right] \tilde{d}\Delta V \\ & + \tilde{d}\tilde{E}_P\Delta U + \left(2\tilde{V}_P - \tilde{\lambda}_{P,1} - \tilde{\lambda}_{P,2} - \tilde{\lambda}_{P,3} \right) \tilde{d}\Delta B\end{aligned}$$

For the bed slope decomposition term

$$\tilde{\beta}_{P,k} = - \frac{\left[\left(\tilde{V}_P - \tilde{\lambda}_{P,a} \right) \left(\tilde{V}_P - \tilde{\lambda}_{P,b} \right) + \tilde{d} + \tilde{D}_P^G \right] \tilde{d}\Delta B}{\left(\tilde{\lambda}_{P,k} - \tilde{\lambda}_{P,a} \right) \left(\tilde{\lambda}_{P,k} - \tilde{\lambda}_{P,b} \right) \left(\tilde{V}_P - \tilde{\lambda}_{P,k} \right)} \quad (4.64)$$

for $k, a, b \in \{1, 2, 3\}$ where $a \neq k \neq b$ and

$$\tilde{\beta}_{P,4} = \frac{\varphi_{P,4}}{\left(\tilde{V}_P - \tilde{\lambda}_{P,1} \right) \left(\tilde{V}_P - \tilde{\lambda}_{P,2} \right) \left(\tilde{V}_P - \tilde{\lambda}_{P,3} \right)} \quad (4.65)$$

where

$$\begin{aligned} \varphi_{P,4} = & - \left[3\tilde{V}_P^2 - 2\tilde{V}_P \left(\tilde{\lambda}_{P,1} + \tilde{\lambda}_{P,2} + \tilde{\lambda}_{P,3} \right) \right. \\ & \left. + \left(\tilde{\lambda}_{P,1}\tilde{\lambda}_{P,2} + \tilde{\lambda}_{P,1}\tilde{\lambda}_{P,3} + \tilde{\lambda}_{P,2}\tilde{\lambda}_{P,3} \right) + \tilde{d} + \tilde{D}_P^G \right] \tilde{d}\Delta B \end{aligned}$$

- when $\tilde{E}_P = 0$ then

$$\tilde{\alpha}_{P,k} = \frac{\psi_{P,k}}{\left(\tilde{\lambda}_{P,k} - \tilde{\lambda}_{P,a} \right) \left(\tilde{\lambda}_{P,k} - \tilde{\lambda}_{P,b} \right)} \quad (4.66)$$

where

$$\begin{aligned} \psi_{P,k} = & \left[\left(\tilde{V}_P - \tilde{\lambda}_{P,a} \right) \left(\tilde{V}_P - \tilde{\lambda}_{P,b} \right) + \tilde{d} \right] \Delta d \\ & + \left(2\tilde{V}_P - \tilde{\lambda}_{P,a} - \tilde{\lambda}_{P,b} \right) \tilde{d}\Delta V + \tilde{d}\Delta B \end{aligned}$$

for $k, a, b \in \{1, 2, 3\}$ where $a \neq k \neq b$ and

$$\tilde{\alpha}_{P,4} = \Delta U \quad (4.67)$$

For the bed slope decomposition term

$$\tilde{\beta}_{P,k} = \frac{\left(\tilde{\lambda}_{P,a} + \tilde{\lambda}_{P,b} - 2\tilde{V}_P \right) \tilde{d}\Delta B}{\left(\tilde{\lambda}_{P,k} - \tilde{\lambda}_{P,a} \right) \left(\tilde{\lambda}_{P,k} - \tilde{\lambda}_{P,b} \right)} \quad (4.68)$$

for $k, a, b \in \{1, 2, 3\}$ where $a \neq k \neq b$, and $\tilde{\beta}_{P,4} = 0$.

4.5 Test Cases

In this section we present test cases for one-dimensional (1D) simulations which are used to evaluate the effects of the various numerical developments described earlier. These chosen test cases are useful for either (a) being analytical solutions of the NLSW equations; (b) being quasi-analytical solutions of the

NLSW morphodynamic system; and (c) being useful numerical cases to compare with the previous works.

In the following the results from the rigid bed cases by taking a small value of $A = 1 \times 10^{-8} \text{ s}^2/\text{m}$ and the mobile bed cases ($A = 0.004 \text{ s}^2/\text{m}$) can be compared with those of previous studies; however the model cannot use $A = 0 \text{ s}^2/\text{m}$, because this value make the $\tilde{D}^{F,G}$ and $\tilde{E}^{F,G} = 0$, corresponding to the singular matrix of the eigenvectors; then this leads to the invalid Roe decomposition. Secondly, d_{tol} is an important numerical parameter for the wet/dry boundary condition. Although this parameter should be close to zero, it could make the model crash. Therefore, we test two values of d_{tol} : $d_{tol} = 1 \times 10^{-4} \text{ m}$ and $1 \times 10^{-8} \text{ m}$. Lastly, we also use either (i) use a purely first order *Upwind* scheme, or (ii) the simple *Minmod* flux-limiter function (Hudson, 2001; LeVeque, 2002) for comparing the result between the first order scheme which is less accurate but more stable, and higher order accuracy by TVD scheme which might create the spurious oscillation near the shock.

4.5.1 Dam-break Problem

The dambreak is a *classical* benchmark problem for shallow water theory. This is an instantaneous failure of a dam on a dry bed downstream (*wet/dry* dambreak) with no friction. Many researchers have derived exact or approximate solutions to this problem, on both rigid and mobile beds. Kelly and Dodd (2009) compared their numerical results with Ritter's (1892) analytical solution for a

fixed bed dambreak problem ($A = 1 \times 10^{-8} \text{ s}^2/\text{m}$). Kelly and Dodd (2009) also provided numerical prediction using the method of characteristics, which then compared with the results from an exact Riemann solver for a dambreak on a mobile bed ($A = 0.004 \text{ s}^2/\text{m}$). The present model has also been tested for this dambreak problem, Figure 4.5 shows the initial conditions, which are given by:

$$d(x, 0) = \begin{cases} d_0 & \text{if } x < 0 \\ 0 & \text{if } x > 0 \end{cases} \quad (4.69)$$

where the initial still water depth, $d_0 = 1 \text{ m}$ with $U(x, 0) = 0 \text{ m/s}$, and $B(x, 0) = 0 \text{ m}$

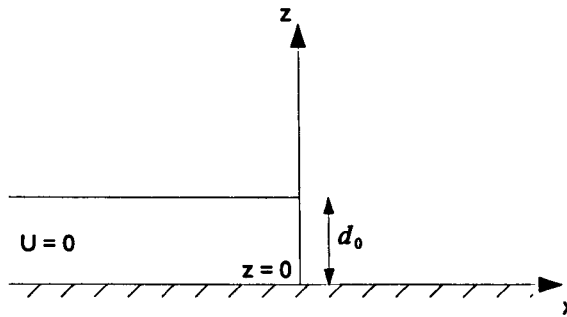


Figure 4.5: Initial conditions of dambreak test case

4.5.2 Shen and Meyer Solution

An interesting test for shallow water theory is the dambreak onto a slope. This dambreak on slope situation is quite similar to a uniform bore travelling over still water with zero velocity meeting the shoreline, described by Shen and

Meyer (1963), so we called this testing case as SM63. Figure 4.6 shows initial conditions and definition of variables of SM63 test case.

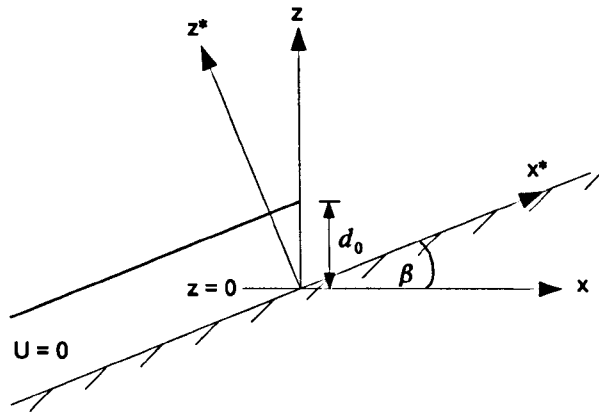


Figure 4.6: Initial conditions of SM63 test case

where the initial water depth $d_0 = 1$ m and depth-averaged velocity $U_0 = 0$ m/s with plane beach slope of 0.1. The analytical solution of the water depth when the bore reaches the shoreline for rigid bed SM63 case was originally derived by Shen and Meyer (1963), then Peregrine and Williams (2001) (hereafter, PW01) who undertook further analysis and stated the explicit formulations for the shoreline position $x_s^*(t)$, water depth $d^*(x^*, t)$ and depth averaged velocity $U^*(x^*, t)$ in $x^* - z^*$ plane as shown in Figure 4.6 with dimensional form as:

$$x_s^*(t) = 2U_b^*t - \frac{1}{2}gt^2 \tan \beta \quad (4.70)$$

$$d^*(x^*, t) = \frac{(U_b^*t - \frac{1}{2}gt^2 \tan \beta - x^*)^2}{9gt^2} \quad (4.71)$$

$$U^*(x^*, t) = \frac{U_b^*t - 2gt^2 \tan \beta + 2x^*}{3t} \quad (4.72)$$

where U_b^* is the bore velocity at the initial shoreline position, $g = 9.81 \text{ m/s}^2$ is gravitational acceleration, and $\tan \beta$ is beach slope. Although the Shen and

Meyer solution of PW01 is on the x^* and z^* co-ordinates, it could be converted to $x - z$ plane which the results are approximately the same when the bed slope is small ($\tan \beta \approx \sin \beta$) as assigned in the present test.

4.5.3 Hibberd and Peregrine Solution

The simplest physically realisable bore for investigating the swash motion is the so-called "*uniform bore*" for which height and velocity everywhere behind the bore front remain constant. The uniform bore over a sloping beach is an idealised problem including most of the features which can occur in the bore region and also the swash motion (Hibberd and Peregrine (1979), hereafter HP79); therefore, this problem is another test case used for investigating the stability of the new schemes that are implemented in the model.

In this study, the wet/wet dambreak problem (Stoker, 1957) is used to initiate the uniform bore approaching a sloping beach; thus, the dambreak is located at 5 m ($x = -5$ m) before the toe of the sloping beach ($x = 0$ m). A definition of the variables used for this test is illustrated in Figure 4.7.

This study sets the initial water depth of the dambreak $d_0 = 2.3$ m for creating the uniform bore height $h_b \approx 0.6$ m moving into undisturbed water with $d_i = 1.0$ m toward a plane beach of slope $\tan \beta = 0.1$.

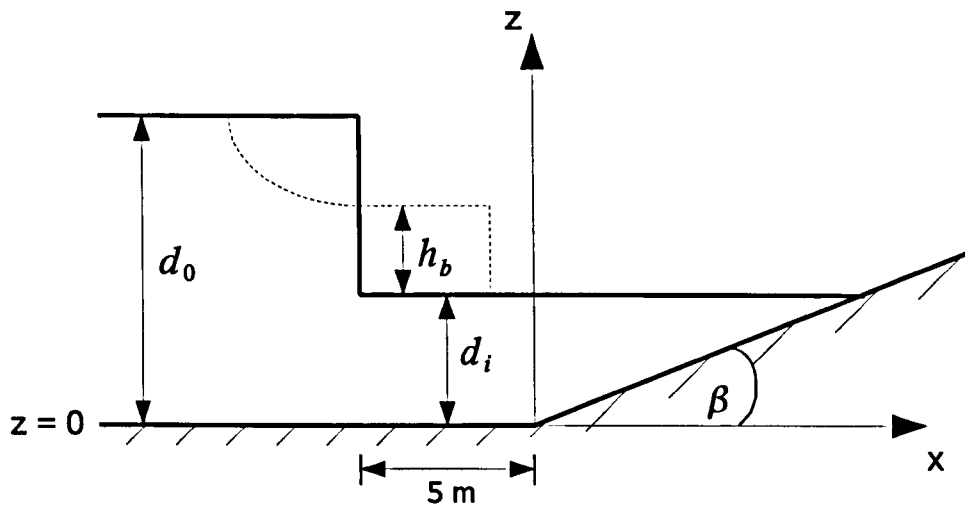


Figure 4.7: Notation and initial bathymetry for a uniform bore approaching a plane sloping beach

4.6 Test Results

New developments of the model are tested and presented in this section. With many changes in the model, this section is separated into three parts. The first part shows a comparison between two entropy fixes; then the results from the different numerical schemes (Castro-Diaz and TOS scheme) and the SBC are examined by using the test cases. Finally, comparisons between the selected numerical scheme in this study and the previous analytical or numerical solutions are shown.

Before presenting the test results from the new development of the model, the first order upwind Castro-Diaz scheme with Hubbard and Dodd entropy fix is simulated for the dambreak problem when $B = 0$ and 1 m as shown in Figure 4.8.

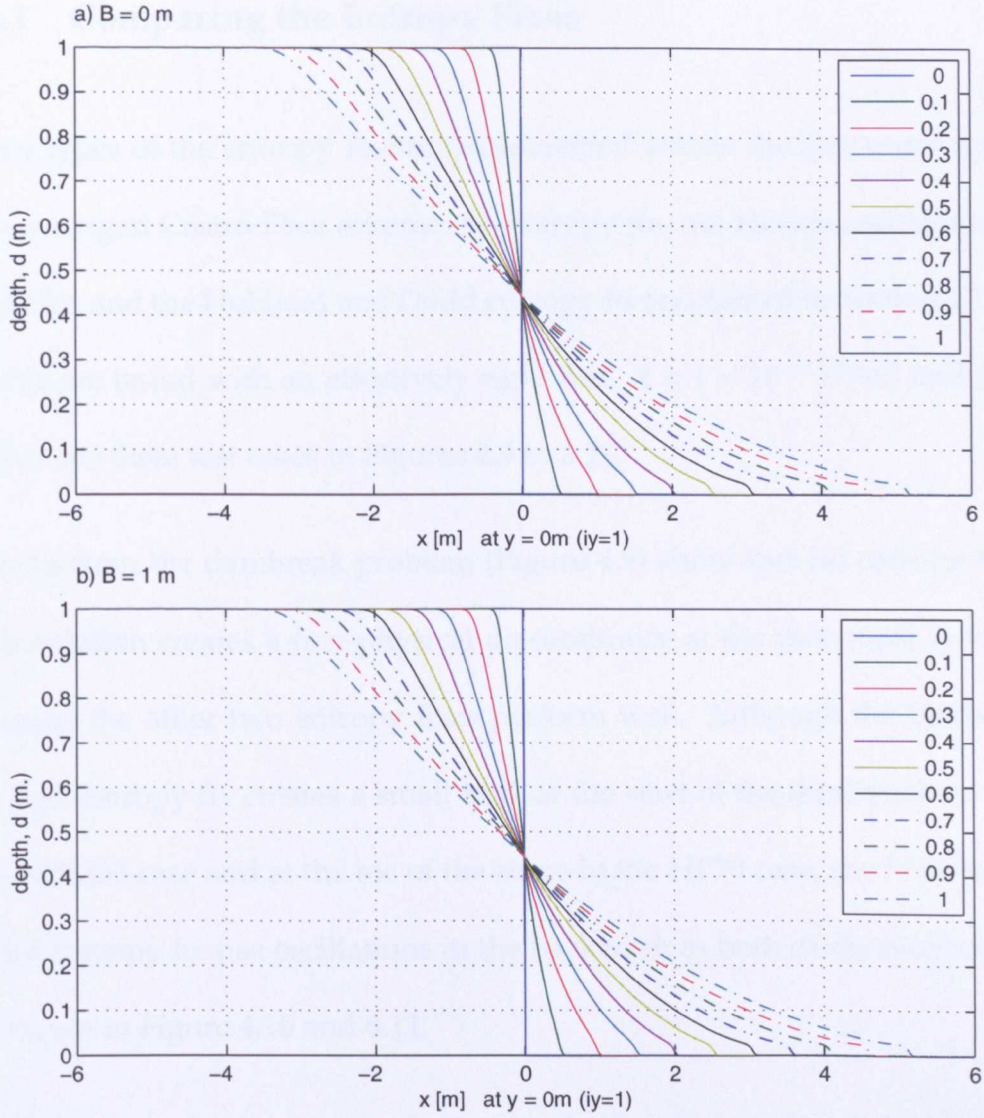


Figure 4.8: Water depth results of the dambreak problem simulated by first order upwind Castro-Diaz scheme where a) $B = 0$ m case and b) $B = 1$ m case.

From Figure 4.8, it can be seen that the previous non-physical shock no longer exists (see Figure 4.2 b)). Therefore, the *OTT2dm* of Dodd et al. (2008) will be not compared with the other schemes in this section.

4.6.1 Comparing the Entropy Fixes

Three types of the entropy fix are implemented within the first order upwind Roe-averaged Castro-Diaz scheme: no entropy fix, the Harten and Hyman entropy fix, and the Hubbard and Dodd entropy fix (explained in Section 4.1). The results are tested with an effectively rigid bed, $A = 1 \times 10^{-8} \text{ s}^2/\text{m}$, and results shown for three test cases in Figures 4.9 to 4.11.

Results from the dambreak problem (Figure 4.9) show that no entropy fix implementation creates a non-physical discontinuity at the dambreak ($x = 0 \text{ m}$), whereas the other two entropy fixes perform well. Although the Harten and Hyman entropy fix creates a small kink at the start of the dambreak ($x = 0 \text{ m}$) in the SM63 case and at the toe of the slope in the HP79 case, the Hubbard and Dodd entropy fix has oscillations in the backwash in both of the two test cases as shown in Figure 4.10 and 4.11.

The reason for the backwash oscillations for the Hubbard and Dodd entropy fix could stem from the criterion used to apply the fix (4.8) and the overestimate of the spreading rate that is used in this method. In the backwash, these oscillation occur when the depth-averaged velocity reaches the wave celerity, $\tilde{U} \approx -\tilde{c}$ (transonic condition). The Hubbard entropy fix is applied to induce the splitting shock for the $\tilde{U} + \tilde{c}$ characteristic which it does not need to split, as we compare with the smooth results of no entropy fix implementation during the backwash of SM63 and HP79 test cases. On the other hand, the Harten and Hyman entropy fix does not meet the entropy fix criterion (4.6) in this situation;

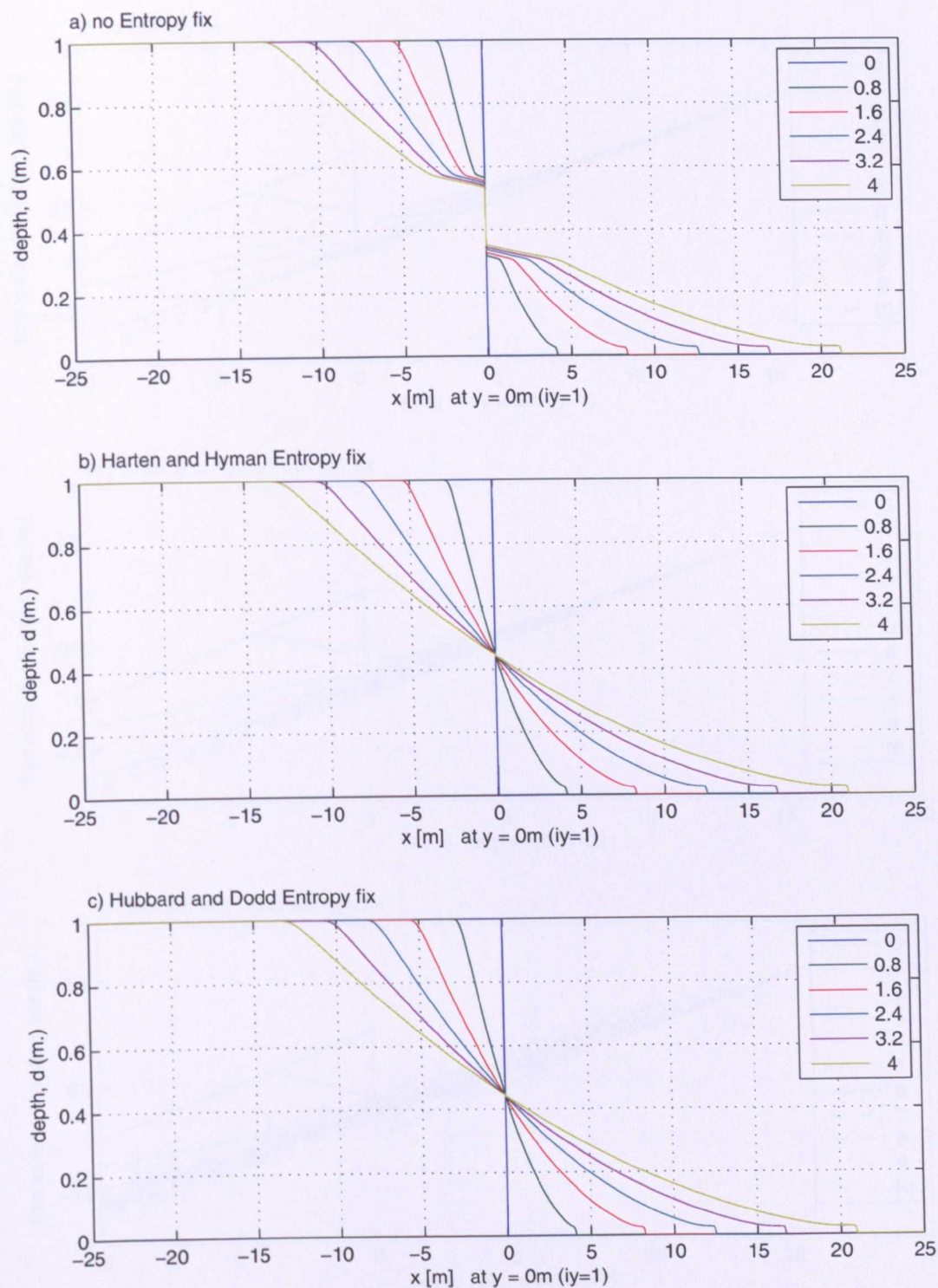


Figure 4.9: Results of dambreak problem using a) no entropy fix, b) Harten and Hyman entropy fix, and c) Hubbard and Dodd entropy fix.

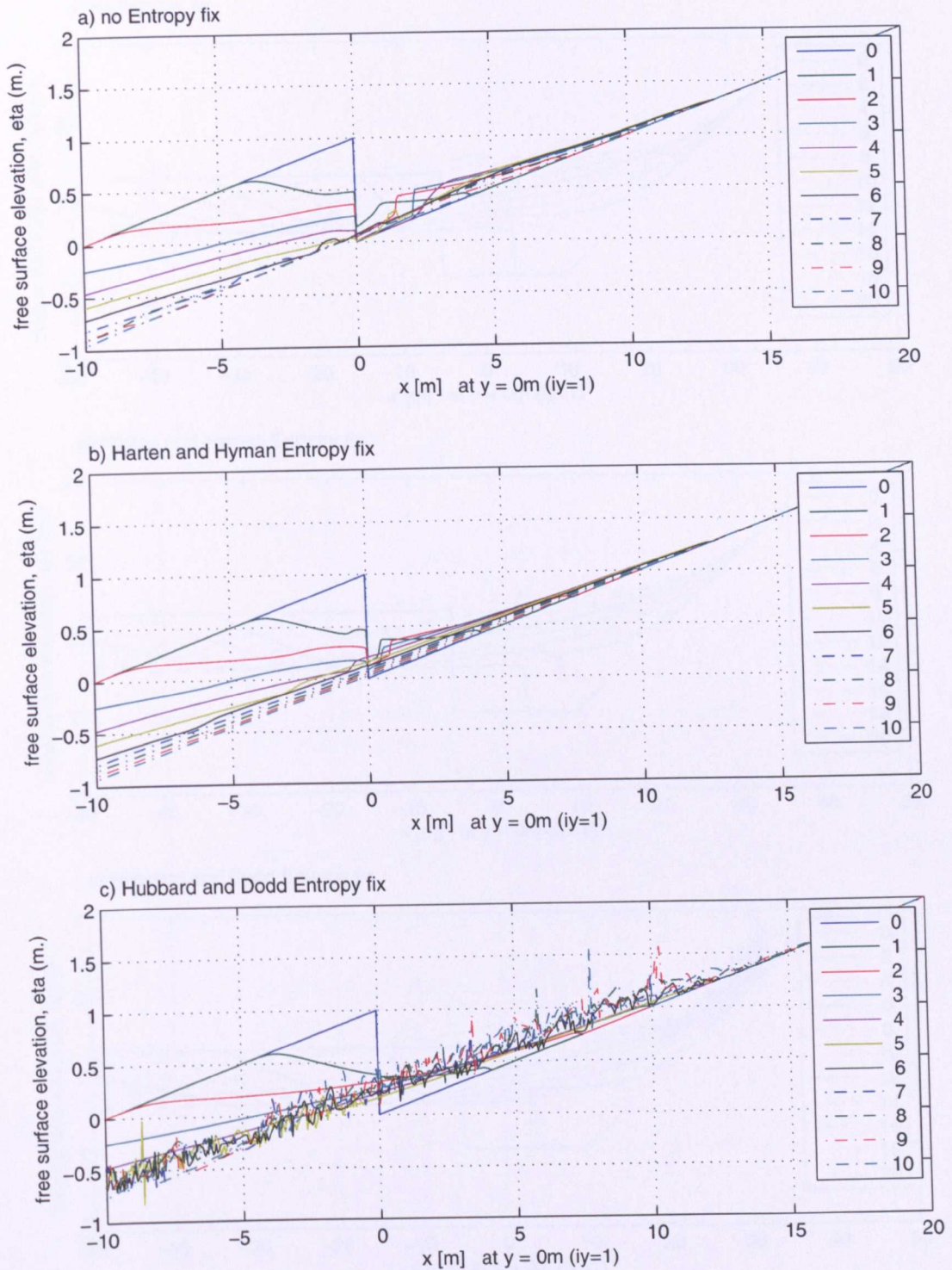


Figure 4.10: Results of SM63 problem using a) no entropy fix, b) Harten and Hyman entropy fix, and c) Hubbard and Dodd entropy fix.

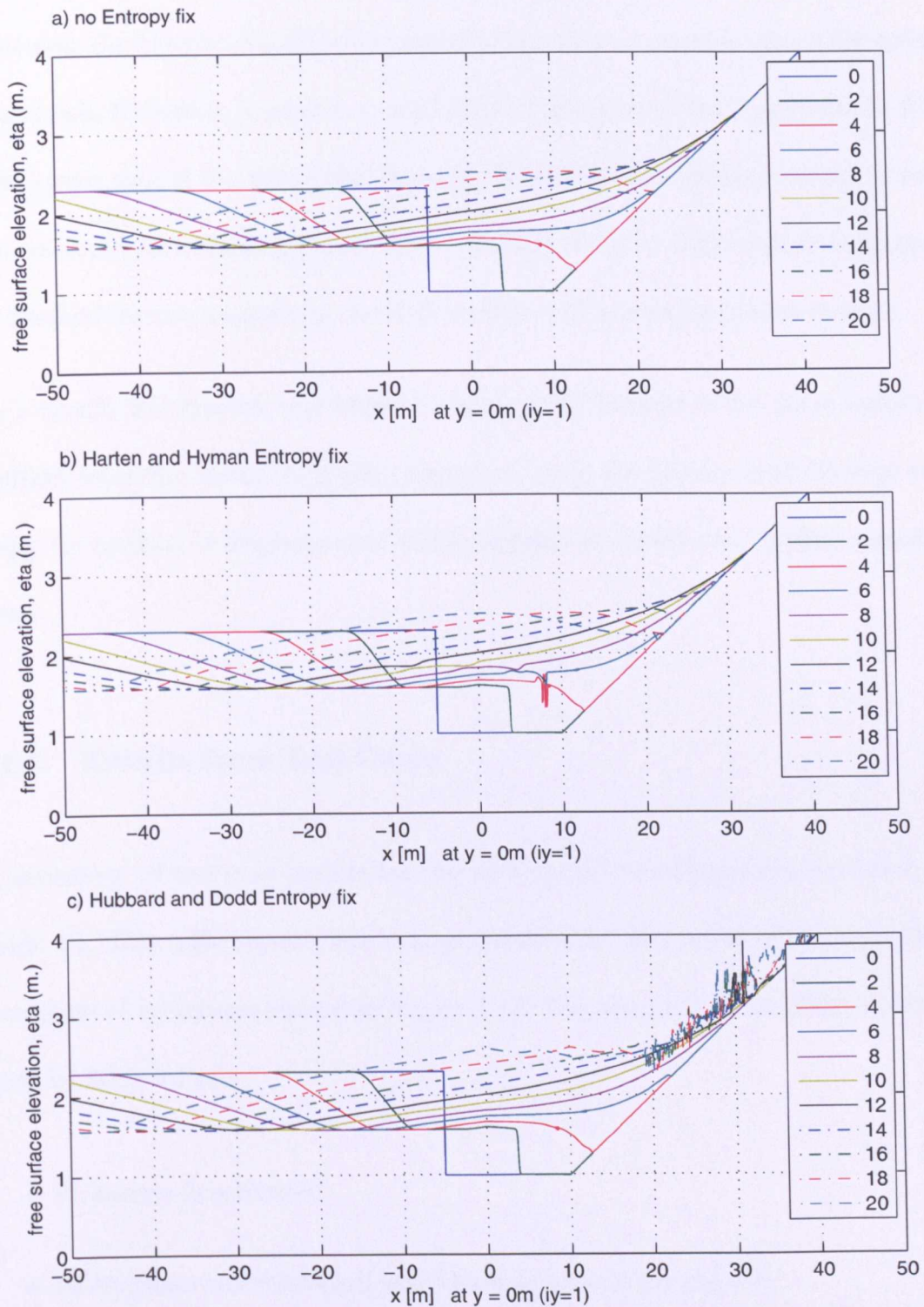


Figure 4.11: Results of HP79 problem using a) no entropy fix, b) Harten and Hyman entropy fix, and c) Hubbard and Dodd entropy fix.

therefore, no splitting shock occurs for this method, leading to no oscillation. However the Harten and Hyman entropy fix covers a smaller range for splitting shock; therefore, it creates a small kink at the start of the dambreak in the SM63 case, and at the toe of the slope in the HP79 case, corresponding to the transonic rarefaction condition of the $\tilde{U} - \tilde{c}$ characteristic. Although this entropy fix method creates a spurious oscillation, this oscillation disappears in time.

As a result, the Harten and Hyman entropy fix method is the most suitable method from the tested methods; therefore, only the Harten and Hyman entropy fix method is implemented in the numerical scheme for further simulations.

4.6.2 Results from Test Cases

A summary of test case results for the new model developments is shown in Table 4.1. This table reports the strange behaviours that occur in the test cases, examples of which are shown in Figure 4.12. The meaning of the abbreviations used in Table 4.1 are:

- FL means flux limiter.
- HDA means the Hubbard and Dodd approach for the SBC.
- "-" means the results are "*acceptable*" with no inappropriate shock, kink, or oscillation.

- Crashed means the model did not run until completion. There is a numerical crash during the simulation.
- xS means that there is a shock near the tip when x is the size of shock
 - SS means small shock
 - LS means large shock
- xK means that there is a kink at starting of the dambreak in dambreak and SM63 cases and at the toe of the slope in HP79 case, when x is the size of kink
 - SK means small kink
 - LK means large kink
- xO means that there are oscillations in the results excluding the oscillations after tip when x is the size of amplitude of oscillation
 - SO means small amplitude oscillation
 - LO means large amplitude oscillation
- The other abbreviations are the specific types of errors
 - PO means that there is a jump at the tip
 - POA means that there are point jump at the tip and oscillations after tip

Table 4.1: Summary of results from the test cases

Scheme	FL	SBC	d_{tol} (m)	Rigid bed, $A = 1 \times 10^{-8} \text{ s}^2/\text{m}$			Mobile bed, $A = 0.004 \text{ s}^2/\text{m}$		
				Dambreak	SM63	HP79	Dambreak	SM63	HP79
Roe averaged Castro-Diaz scheme	1 st -order Upwind	HDA	1×10^{-8}	-	LK,PO	LK,PO	-	Crashed	Crashed
			1×10^{-4}	SS	LK,POA	LK,LO,POA	-	SK	SS
	Minmod FL	Primitive	1×10^{-8}	-	LK	LK,LO,POA	-	SK,PO	Crashed
			1×10^{-4}	SS	LK	LK,LO,PO	LK,LO	SK,PO	SS,NO
TOS with Castro-Diaz scheme	1 st -order Upwind	HDA	1×10^{-8}	-	SK,POA	SS,SO,PO	SK	Crashed	Crashed
			1×10^{-4}	LS	SK,PO	SS,POA	SS	SK,PO	SS,SK,POA
	Minmod FL	Primitive	1×10^{-8}	SS	SK	SO,POA	Crashed	Crashed	Crashed
			1×10^{-4}	LS	SK	SO	Crashed	Crashed	Crashed
TOS with Castro-Diaz scheme	1 st -order Upwind	HDA	1×10^{-8}	-	SK,PO	PO	-	SK,PO	Crashed
			1×10^{-4}	SS	SK,PO	PO	-	SK,POA	SS,SO
	Minmod FL	Primitive	1×10^{-8}	-	SK,PO	PO	LK,LO	LK	SS,SK,POA
			1×10^{-4}	SS	SK	PO	LK,LO	LK	SS,SK
TOS with Castro-Diaz scheme	1 st -order Upwind	HDA	1×10^{-8}	-	Crashed	Crashed	SK,SO	Crashed	Crashed
			1×10^{-4}	LS	SK,PO	SS,POA	SS	SK,POA	Crashed
	Minmod FL	Primitive	1×10^{-8}	SS,SO	SK,PO	PO	LK,SO	Crashed	Crashed
			1×10^{-4}	LS	SK	SS,PO	LK,LO	Crashed	SS,SK,SO

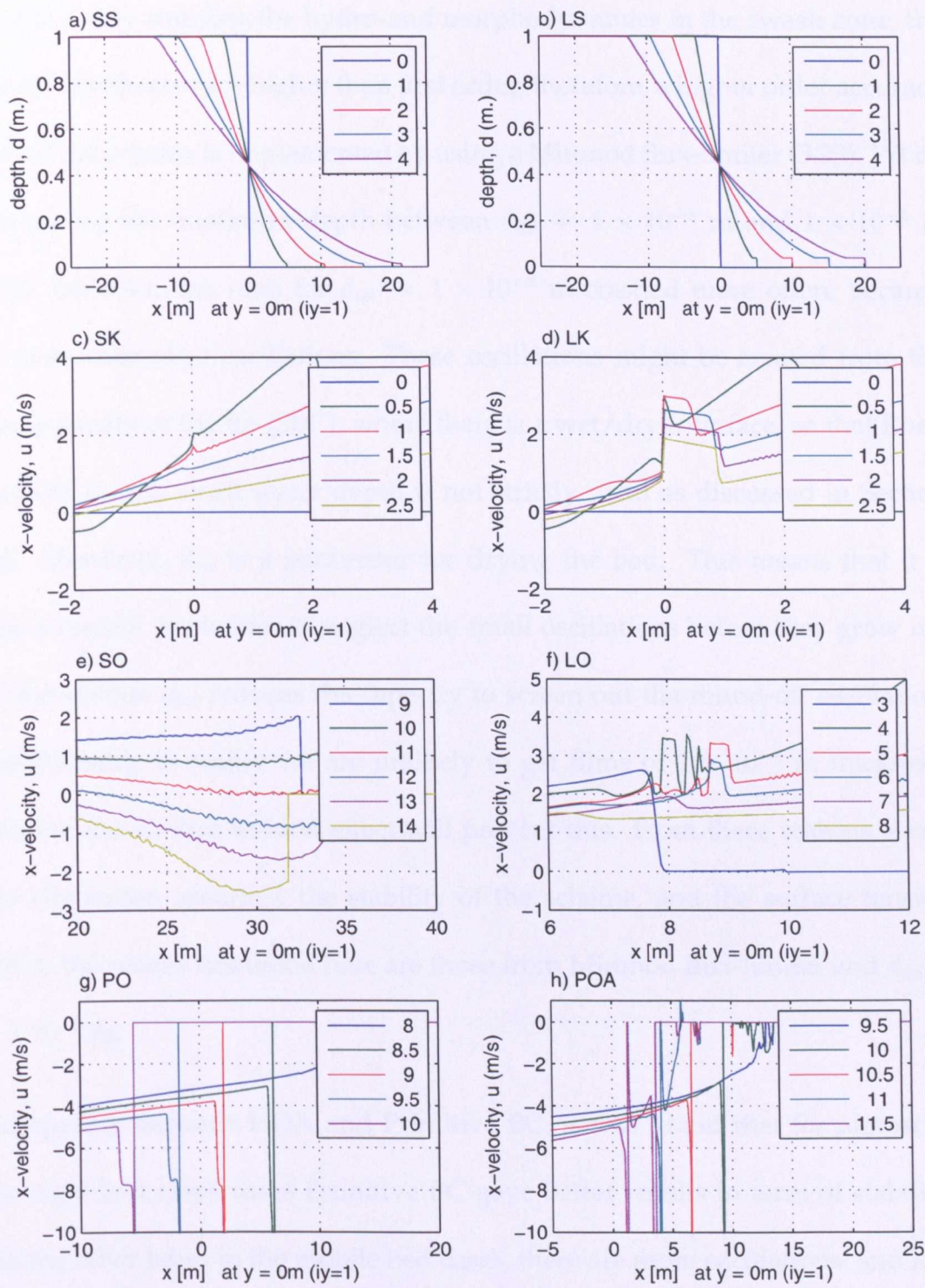


Figure 4.12: Examples of strange behaviours that occur in the test cases.

To accurately simulate the hydro-and morphodynamics in the swash zone, the model needs accuracy higher than first order; therefore, a higher order accuracy numerical scheme is implemented by using a Minmod flux-limiter (3.23). When comparing the minimum depth between $d_{tol} = 1 \times 10^{-8}$ m and 1×10^{-4} m from Table 4.1, the runs for $d_{tol} = 1 \times 10^{-8}$ m crashed more often, because of more numerical oscillations. These oscillations might be created from the discontinuity at the tip (SBC), where there is a wet/dry interface, so that Roe's method for the small water depth is not strictly valid as discussed in Section 4.2. Moreover, d_{tol} is a parameter for drying the bed. This means that it is also a control parameter to neglect the small oscillations before they grow up, so the smaller d_{tol} reduces the capacity to screen out the round-off oscillation. Additionally, in reality we are unlikely to get films of 1×10^{-8} m thickness, because the surface tension effect will prevent this. From these reasons about the simulation accuracy, the stability of the scheme, and the surface tension effect, the results discussed here are those from Minmod flux-limiter and $d_{tol} = 1 \times 10^{-4}$ m.

Comparing between HDA and Primitive BC, it was found that for almost of the rigid bed slope cases Primitive BC gave better results in term of stability. On the other hand in the mobile bed cases, there are more oscillations, and less stability when using the Primitive BC (see Table 4.1).

About the numerical schemes, there is not much difference between Roe averaged Castro-Diaz scheme and TOS with Castro-Diaz scheme for the rigid bed

cases; however, in the mobile bed cases the TOS with Castro-Diaz scheme produces more numerical oscillation than the other scheme. Since the aim of this study is to simulate the occurrence of beach cusps on a mobile bed, the Roe-averaged Castro-Diaz scheme with Minmod flux-limiter using the HDA for SBC is selected to be the model for further simulations.

4.6.3 Comparing Testing Case Results with Previous Works

To verify the new implementation of the model, it needs to be compared with analytical or alternative numerical solutions from previous works. Only the rigid and mobile bed dambreak problems and the rigid bed of SM63 could be compared with the previous works, while the other test cases (mobile bed of SM63 case, rigid and mobile bed of HP79 cases) do not have valid analytical or numerical solutions for the same initial condition that can be compared with the present test cases. However, these test cases are good for testing the stability of the new implementation schemes as discussed in Section 4.6.2.

As all test cases have to deal with the wet/dry boundary condition, causing the numerical problem there, the evolution of a sand bar in steady unidirectional channel flow, as considered by Hudson and Sweby (2003), is also another good test for the morphodynamic model without the wet/dry boundary condition. Therefore, this study provides the result from this test case in the last part of this section.

Rigid Bed Dambreak Problem

For the rigid bed dambreak problem, the Ritter (1892) solution is a well-known analytical solution. Figure 4.13 illustrates the model result compared with Ritter solution in the dashed black line. The model result corresponds well with the Ritter solution except at the tip. At the tip region, there is a shock caused by using the high d_{tot} value, and the Minmod flux-limiter makes this shock bigger, as can be seen when comparing the results for rigid dambreak problem in Table 4.1. This shock at the tip limits the tip speed at ≈ 5 m/s, whereas the analytical solution shown that the tip speed $= 2c_0$ ($= 6.26$ m/s for this test case) where $c_0 = \sqrt{gd_0}$ is the wave celerity .

Mobile Bed Dambreak Problem

For the mobile bed case, there is a numerical solution for mobile bed dambreak problem presented by Kelly and Dodd (2009). Their solution is computed from the same parameters as we set for the mobile bed dambreak test case, therefore the comparison between the model result and Kelly and Dodd (2009) numerical solution is illustrated in Figure 4.14.

Although the model produced a good overall result, the tip speed from the model (4.5 m/s) is still slower than the Kelly and Dodd (2009) tip speed (5.0 m/s) with the same reason, the shock at the tip, which is discussed in rigid bed dambreak problem comparison. Moreover, another difference is in the constant region (around $x = -2$ to 2 m), which could be linked with the incorrect tip

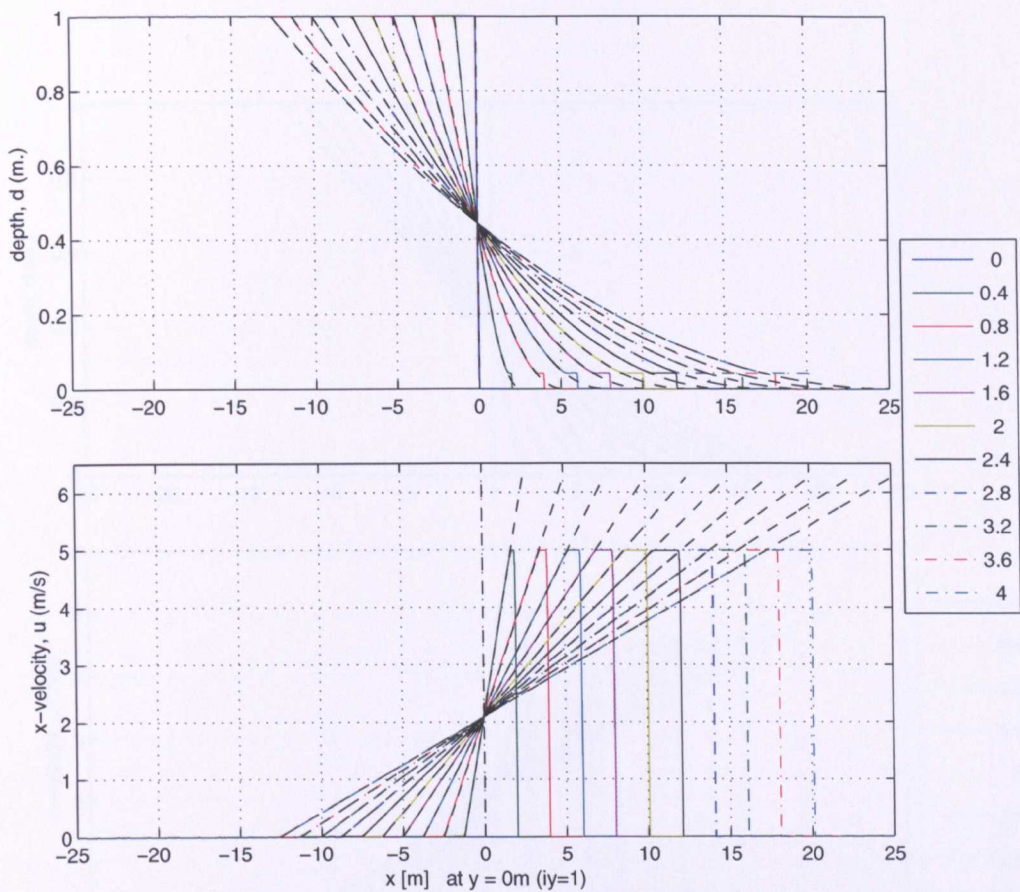


Figure 4.13: Comparing the model result (colour lines) with Ritter solution (dashed black lines) for rigid bed dambreak problem when $f_w = 0$, $d_{tol} = 0.0001$ m, $A = 1 \times 10^{-8}$ s²/m.

speed.

SM63 Case

The results from the model for the (rigid bed) SM63 test case are plotted and compared with this analytical solution, including comparisons for the tip re-
gion, in Figure 4.15 and 4.16.

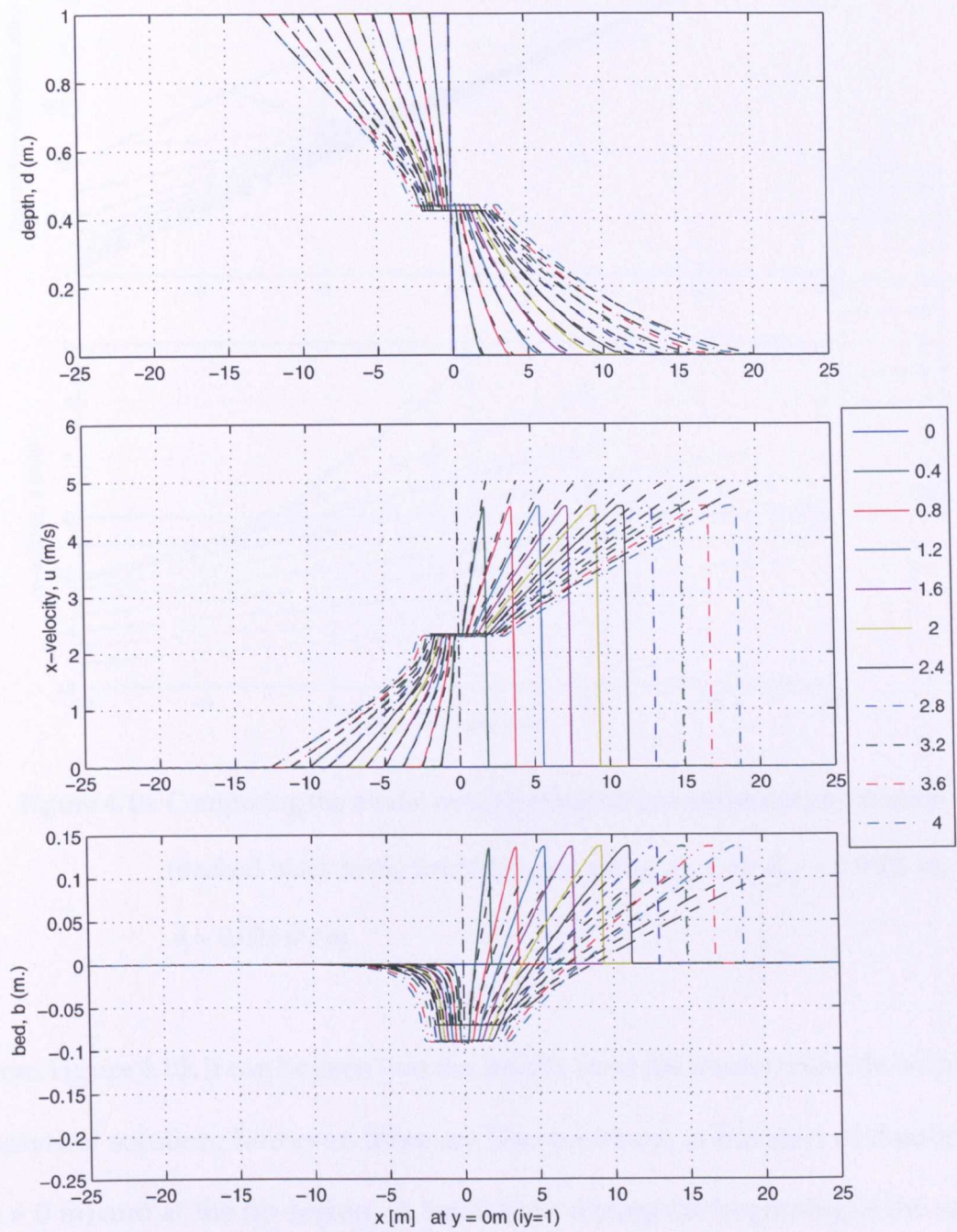


Figure 4.14: Comparing the model result (colour lines) with numerical solution of Kelly and Dodd (2009) (dashed black lines) for mobile bed dambreak problem when $f_w = 0$, $d_{tol} = 0.0001$ m, $A = 0.004$ s²/m.

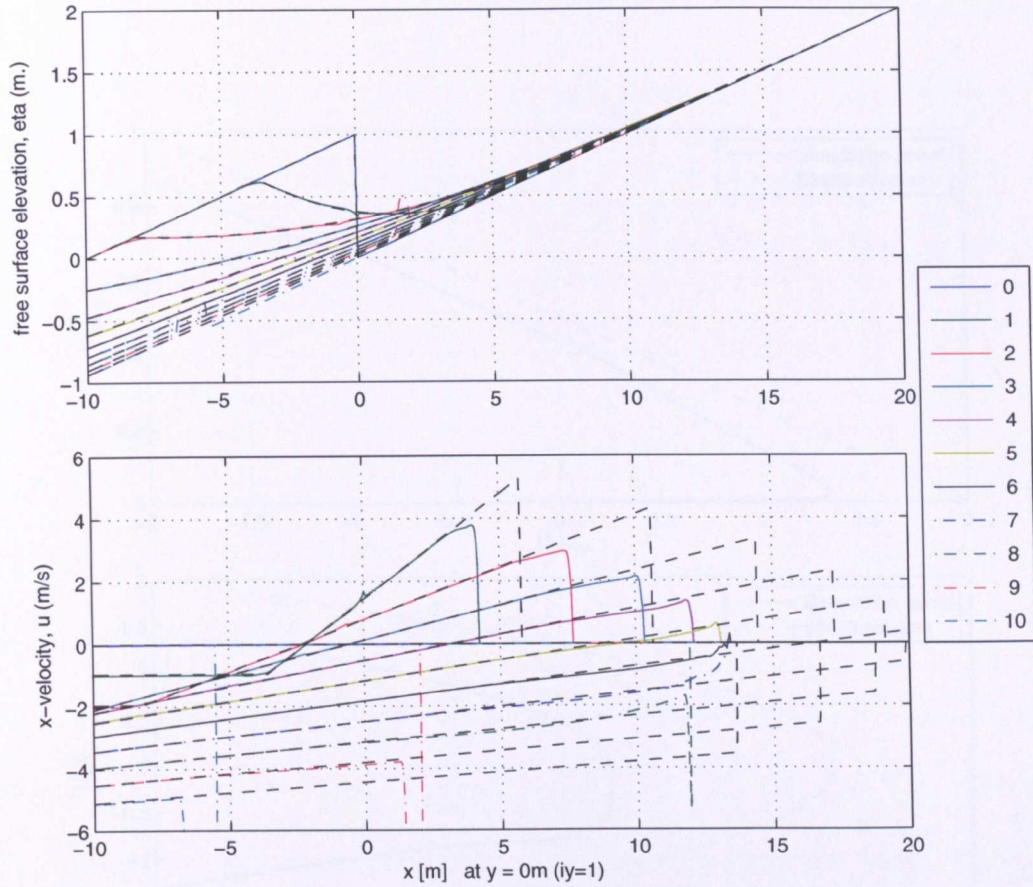


Figure 4.15: Comparing the model result (colour lines) with analytical solution (dashed black lines) for SM63 case when $f_w = 0$, $d_{tol} = 0.0001$ m, $A = 0.004 \text{ s}^2/\text{m}$.

From Figure 4.15, it can be seen that the results from the model coincide with the analytical solution; however, there are also problems at the start of dambreak ($x = 0$ m) and at the tip region. A small kink during the beginning is the same problem with the method of entropy fix used in the model, as discussed in Section 4.6.1.

In the tip region, there are the physical and numerical problems, which are discussed here. Firstly, we start with the physical behaviour of the tip: the tip

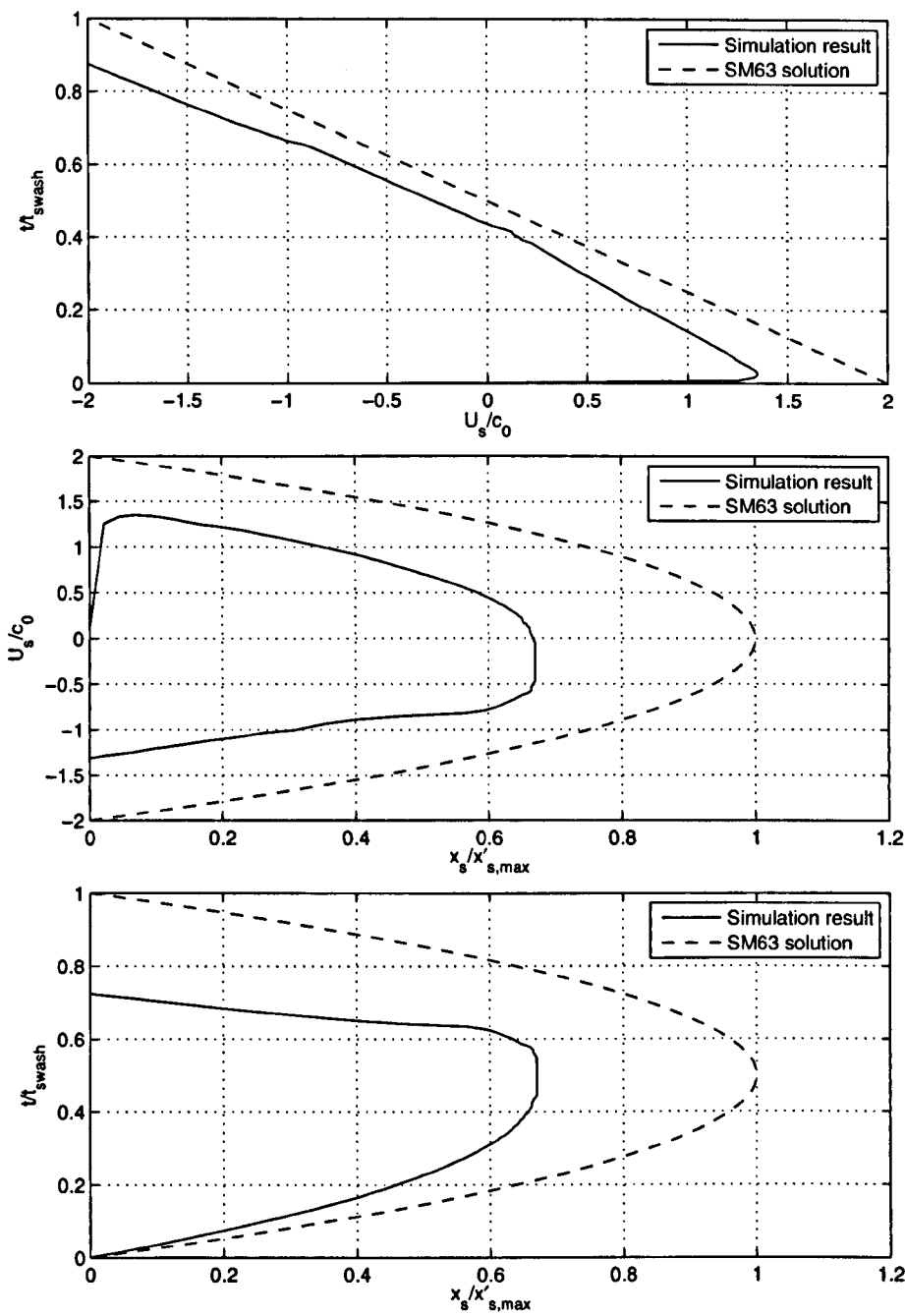


Figure 4.16: Comparing tip result of SM63 case between analytical solution and the model result.

speed (U_s) and tip position (x_s). These variables are investigated in the terms of non-dimensional parameters that are $x_s/x'_{s,max}$, U_s/c_0 , and t/t_{swash} , where $x'_{s,max}$ is the maximum of the tip position of SM63 analytical solution, t is time, and t_{swash} is swash period. Figure 4.16 shows that the starting value of the tip speed from the model result and analytical solution are different. The tip speed of the analytical solution starts at $2c_0$, and then it decreases due to the slope. On the other hand, the model tip speed starts from zero; then it increases immediately before dropping down. For this reason, the $x_{s,max}$ from the model result is less than the one from the analytical solution. The error of both $x_{s,max}$ and U_s of this case are around 35% as shown in Figure 4.16. Secondly, there is a numerical problem shown in the form of big jump at the tip during only the backwash phase, which is also the same as PO error type in Table 4.1. This numerical problem might be caused from SBC corresponding to the use of Roe's method for the wet/dry condition.

Sand Bar in Channel Flow Case

So far, the present model is verified with the test cases including the SBC. It is found that there is a numerical problem due to the very shallow water depth; therefore, the channel test problem is considered here to investigate the evolution of a sand bar in steady unidirectional channel flow without the wet/dry boundary condition. Hudson and Sweby (2003) introduced the initial condition

of this test case as a channel of length 1,000 m with

$$d(x, 0) = d_0 - B(x, 0) \quad \text{and} \quad U(x, 0) = \frac{Q_c}{d(x, 0)} \quad (4.73)$$

where Q_c is a constant discharge in the channel flow, d_0 is the initial background water depth, and the initial bathymetry is

$$B(x, 0) = \begin{cases} \sin^2 \left(\frac{\pi (x - 300)}{200} \right) & \text{if } 300 \leq x \leq 500 \\ 0 & \text{otherwise} \end{cases} \quad (4.74)$$

Moreover, Hudson and Sweby (2003) also presented an approximate solution of the channel test problem by assuming that the water level and the discharge is constant throughout the whole domain. These assumptions are only valid when the bed is interacting slowly the water flow ($A < 0.01 \text{ s}^2/\text{m}$) with the discharge, $|Q_c| \leq 10 \text{ m}^2/\text{s}$. By making these assumptions, an approximate solution for $B(x, t)$ is

$$B(x, t) = \begin{cases} \sin^2 \left(\frac{\pi (x_0 - 300)}{200} \right) & \text{if } 300 \leq x_0 \leq 500 \\ 0 & \text{otherwise} \end{cases} \quad (4.75)$$

where x_0 is the initial co-ordinate, and the value of x is determined by substituting values of x_0 and t into

$$x = x_0 + \xi A m Q_c^m t \begin{cases} \left(d_0 - \sin^2 \left(\frac{\pi (x_0 - 300)}{200} \right) \right)^{-(m+1)} & \text{if } 300 \leq x_0 \leq 500 \\ d_0^{-(m+1)} & \text{otherwise} \end{cases} \quad (4.76)$$

To test the present model with this test case, the values of $A = 0.001 \text{ s}^2/\text{m}$, $Q_c = 10 \text{ m}^2/\text{s}$, $d_0 = 10 \text{ m}$, are set for the initial condition. Figure 4.17 illustrates

the comparison of the model result and the approximate solution at $t = 230,000$ s. It can be seen that the present model can produce an acceptable numerical result without spurious oscillations, which is similar to the results of Hudson and Sweby (2003). The diffusive behaviour in the result might be caused by the small time step that is used in the simulation.

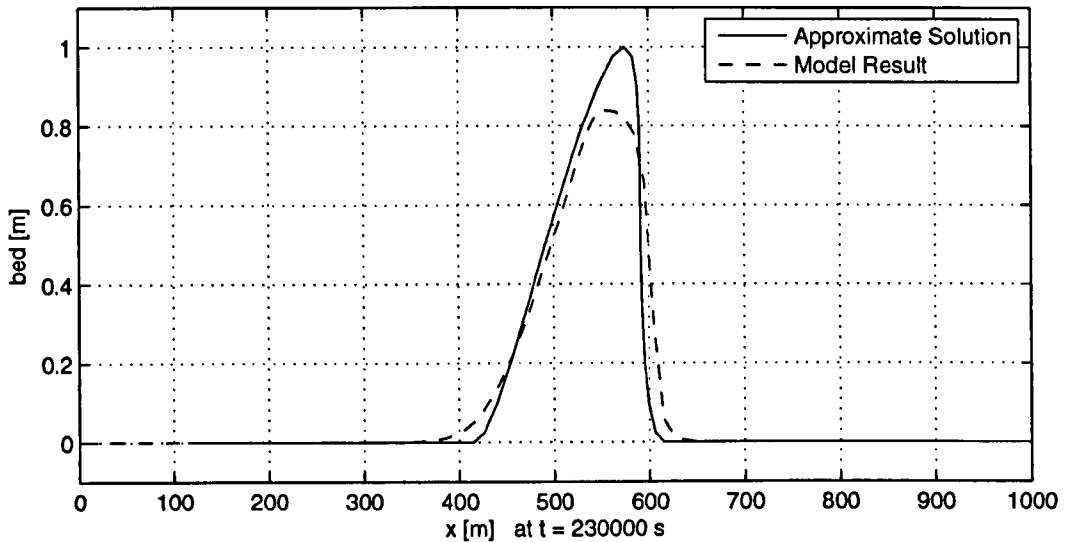


Figure 4.17: Comparing the model result with approximate solution for HS03 case at $t = 230,000$ s.

As a result, the selected modelling scheme produces overall acceptable results when compared with analytical or numerical solutions from previous works. The only significant problem with this scheme is the calculation of the tip position and speed corresponding to the SBC; this is still a problem for engineers and scientists at the present day (see Briganti and Dodd (2009)).

CHAPTER 5

1D Swash Zone Simulation

So far, the discussion of various numerical schemes for improving the accuracy and stability of the morphodynamic model in swash zone is presented. The test cases considered in Chapter 4 involve single swash events and simple dambreaks. Chapter 5 investigates the long term evolution of the swash zone of a 1D (initially plane) beach subjected to continuous incoming waves. Sensitivity tests are conducted to examine the influence of numerical and physical parameters. Two types of regular wave are considered: sine and sawtooth profiles.

5.1 1D Long-term Evolution of Beach Profile

The Roe-averaged Castro-Diaz scheme with Minmod flux-limiter using Hubbard and Dodd approach for SBC is used here.

1D Simulation Setup

The test cases in this chapter start from the 8° plane beach slope with continuous incoming sine waves of period $T = 5$ s, height $H = 0.25$ m, and offshore initial still water depth = 1 m (see Figure 5.1). To investigate the 1D long-term evolution of beach profile, each simulation lasts 20,000s (4,000 wave periods).

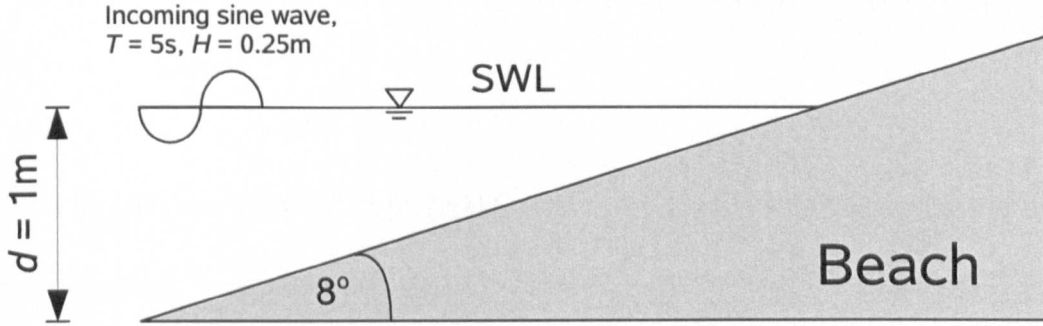


Figure 5.1: 1D simulation initial condition.

To compare the results with those of Dodd et al. (2008), the reference case parameters are set as follows: $f_w = 0.05$, $K = 0.01$ m/s, and $A = 0.004$ s²/m. In the present improved model $d_{tol} = 1$ mm, unlike the value of 2 cm used by Dodd et al. (2008).

The simulation result of the reference case is illustrated in Figure 5.2. The evolution of 1D beach profile of this reference case starts to develop a long-shore bar around $x = 1.5 - 3$ m and swash berm, due to deposition in the upper swash region ($x = 8-9$ m), while there is an erosion at the lower swash ($x = 6-7$ m). Then, the long-shore broadens and moves to the offshore, whereas the erosion at the upper swash area is found. This behaviour is different from the 1D per-

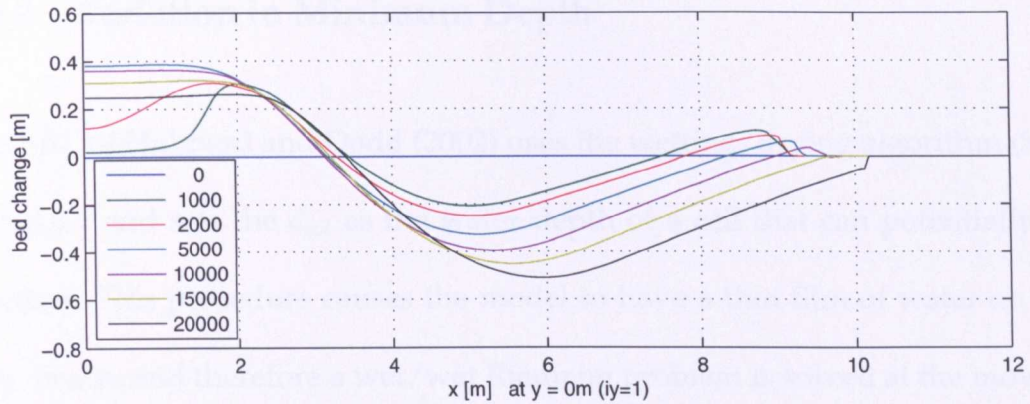


Figure 5.2: Bed change result of 1D beach profile evolution for the reference case.

meable beach case of Dodd et al. (2008) where the long-shore bar is smaller and the swash berm has more deposition. However, the present simulation uses a smaller d_{tol} which caused more erosion in the upper swash region as discussed in Section 5.2.1.

5.2 Sensitivity Test of Numerical Parameters

An important numerical parameter, that relates to the SBC and the stability of the model, is the minimum depth d_{tol} . The sensitivity test of this parameter is presented.

5.2.1 Variation in Minimum Depth

The SBC of Hubbard and Dodd (2002) uses the wetting/drying algorithm (Section 4.4.1 and sets the d_{tol} as the water depth of a cell that can potentially be flooded. This procedure causes the model to have a thin film of water on the 'dry' beach, and therefore a wet/wet Riemann problem is solved at the moving shoreline instead of the real wet/dry boundary, because the Roe-approximation variables are not valid for the wet/dry problem as discussed in Section 4.2. As a result, d_{tol} is an important numerical parameter in the model.

Dodd et al. (2008) use $d_{tol} = 2$ cm for simulating 2D beach cusps to stabilise the numerical scheme. But, this magnitude of d_{tol} is quite a high value comparing with the ideal wet/dry SBC. Therefore, the sensitivity of d_{tol} is tested for investigating the effect of d_{tol} to the beach change by varying this variable between 0.5, 1, 2, and 5 mm. The results are shown in Figure 5.3

Since the new numerical scheme is implemented in the model, the sensitivity of d_{tol} is tested for investigating the effect of d_{tol} to the beach change by varying this variable between 0.5, 1, 2, and 5 mm. The results are shown in Figure 5.3

Figure 5.3 shows the relationship between d_{tol} and beach profile shape. When d_{tol} is bigger, there is more deposition at the upper swash ($x = 8-10$ m) and the long-shore bar ($x = 0-3$ m). On the other hand the maximum of tip position ($x_{s,max}$) is farther onshore, and there is more erosion in the tip region, when d_{tol} is smaller.

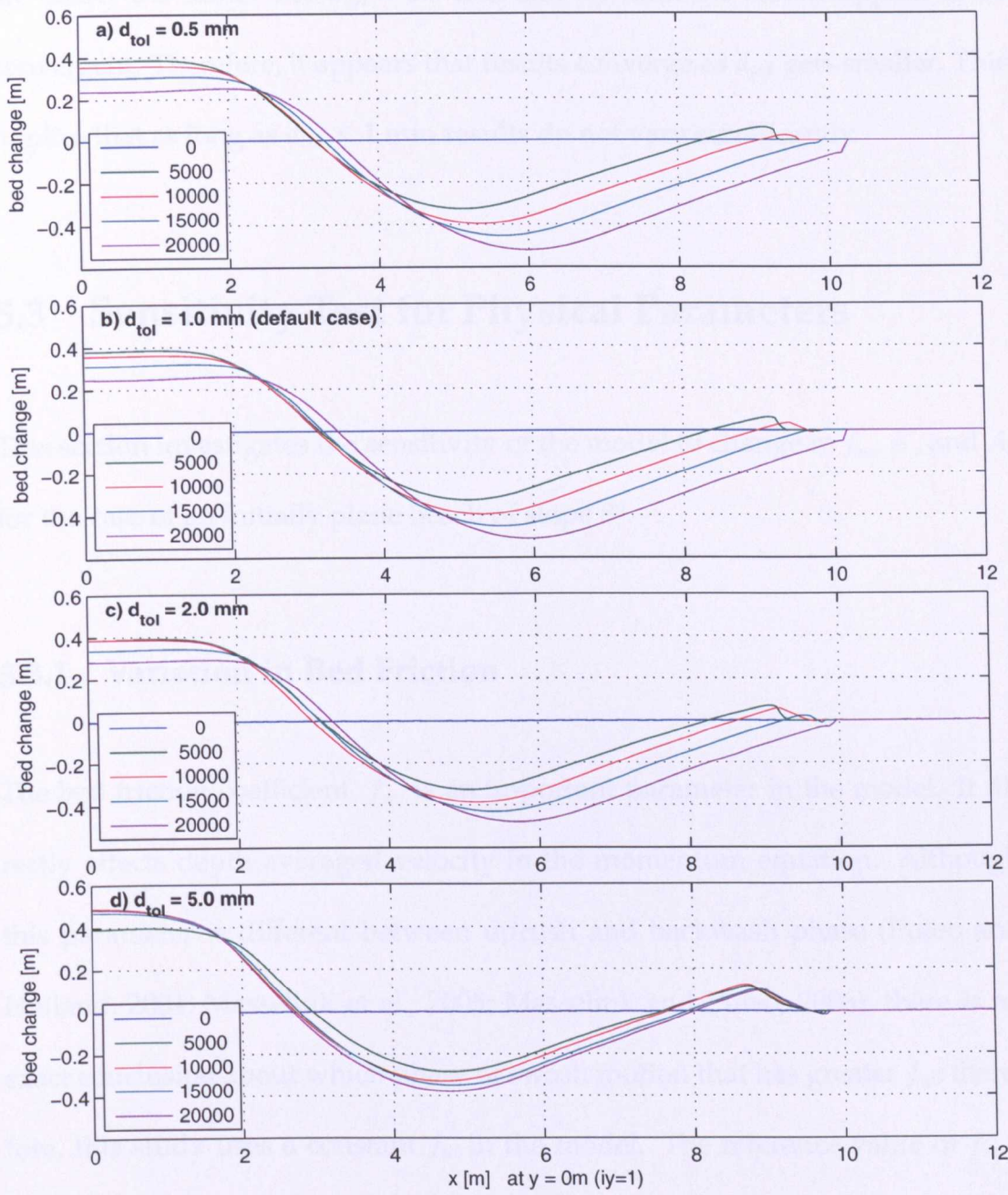


Figure 5.3: Bed change results of sensitivity test of minimum depth, d_{tol} , from

$t = 0 - 20,000$ s. a) $d_{tol} = 0.5$ mm, b) $d_{tol} = 1.0$ mm, c) $d_{tol} = 2.0$ mm, d) $d_{tol} = 5.0$ mm.

From Figure 5.3 a), b), and c), it can be seen that the patterns of bed change are nearly the same. For $d_{tol} = 0.5$ mm and 1.0 mm, the results appear to be convergent. Therefore, it appears that results converge as d_{tol} gets smaller. This implies that as long as $d_{tol} \leq 1$ mm results do not vary significantly.

5.3 Sensitivity Test for Physical Parameters

This section investigates the sensitivity of the model to change in f_w , K , and A , for the case of an initially plane beach of slope 8° .

5.3.1 Variation in Bed Friction

The bed friction coefficient, f_w , is an important parameter in the model. It directly affects depth averaged velocity in the momentum equation. Although this parameter is different between uprush and backwash phase (Puleo and Holland, 2001; Masselink et al., 2005; Masselink and Puleo, 2006), there is no exact conclusion about which phase of swash motion that has greater f_w ; therefore, this study uses a constant f_w in the model. The reference value of $f_w = 0.05$; the sensitivity test considers $f_w = 0.005, 0.02, 0.05$, and 0.1 . The results are illustrated in Figure 5.4.

The results are consistent with what we expect: $x_{s,max}$ increases as f_w gets smaller as shown in Figure 5.4 b), c), and d). It is the same conclusion as Stoker (2005). However, the $f_w = 0.005$ case has a different result from the other cases

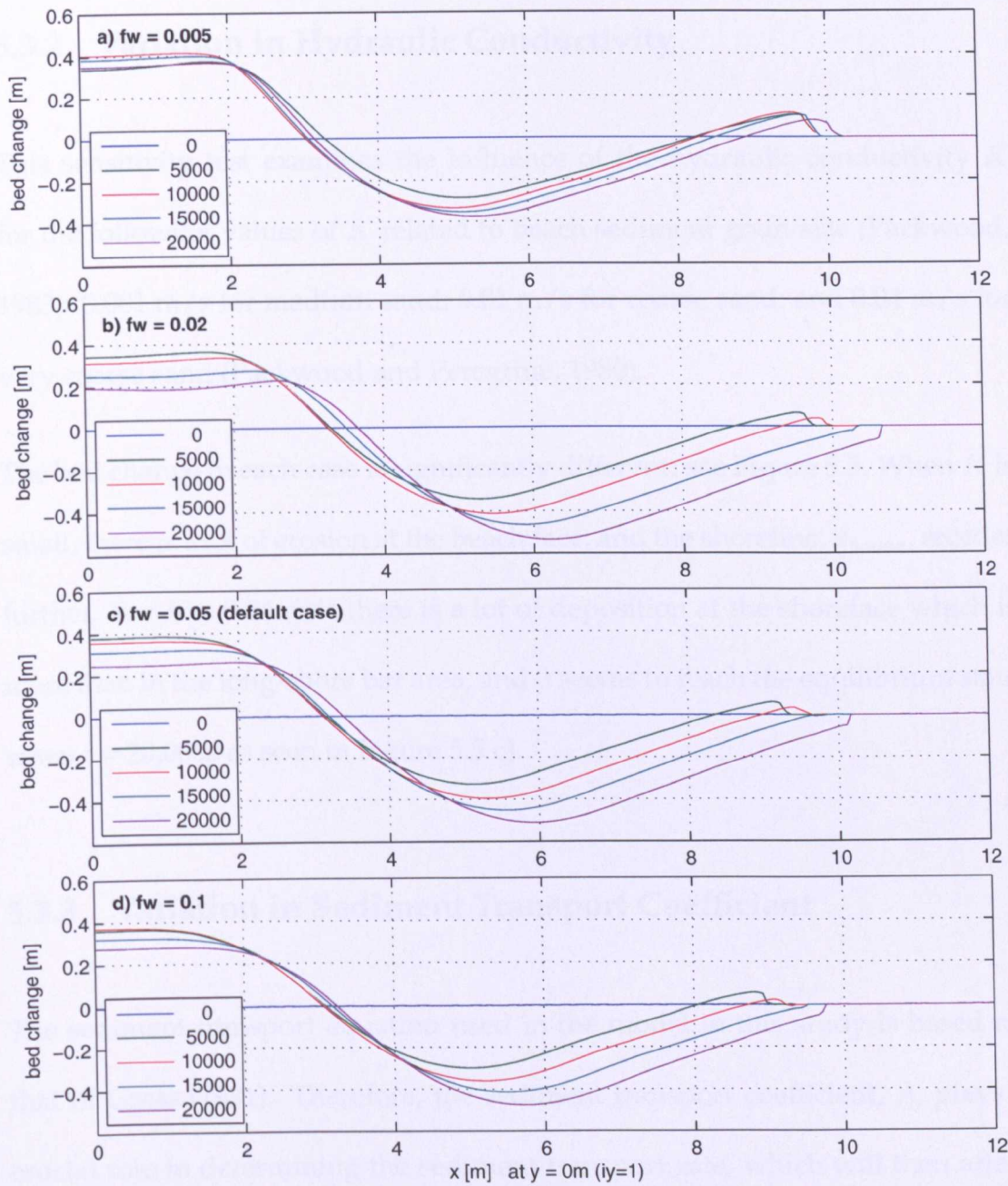


Figure 5.4: Bed change results of sensitivity test of bed friction, f_w from $t = 0 - 20,000$ s. a) $f_w = 0.005$, b) $f_w = 0.02$, c) $f_w = 0.05$, d) $f_w = 0.1$.

which will be discussed in Section 5.5.

5.3.2 Variation in Hydraulic Conductivity

This sensitivity test examines the influence of the hydraulic conductivity K for the following values of K related to beach sediment grain size (Packwood, 1983): 0.001 m/s for medium sand; 0.01 m/s for coarse sand; and 0.04 m/s for very coarse sand (Packwood and Peregrine, 1980).

The bed change in each case is significantly different: see Figure 5.5. When K is small, there is a lot of erosion at the beach face, and the shoreline, $x_{s,max}$, recedes further. For $K = 0.04$ m/s there is a lot of deposition at the shoreface which is more than in the long-shore bar area, and it seems to reach the equilibrium state when $t = 20,000$ s as seen in Figure 5.5 c).

5.3.3 Variation in Sediment Transport Coefficient

The sediment transport equation used in the model in this study is based on that of Grass (1981). Therefore, the sediment transport coefficient, A , plays a crucial role in determining the sediment transport rate, which will then affect the bed change. This parameter is related to sediment properties and bed profile: such as grain size (e.g. D_{50}), sediment specific gravity ($\gamma_s = \rho_s/\rho$ where ρ_s and ρ are density of sediment and water, respectively), and the bed slope (see more detail in Grass (1981), Hudson (2001), and Castro Diaz et al. (2008)).

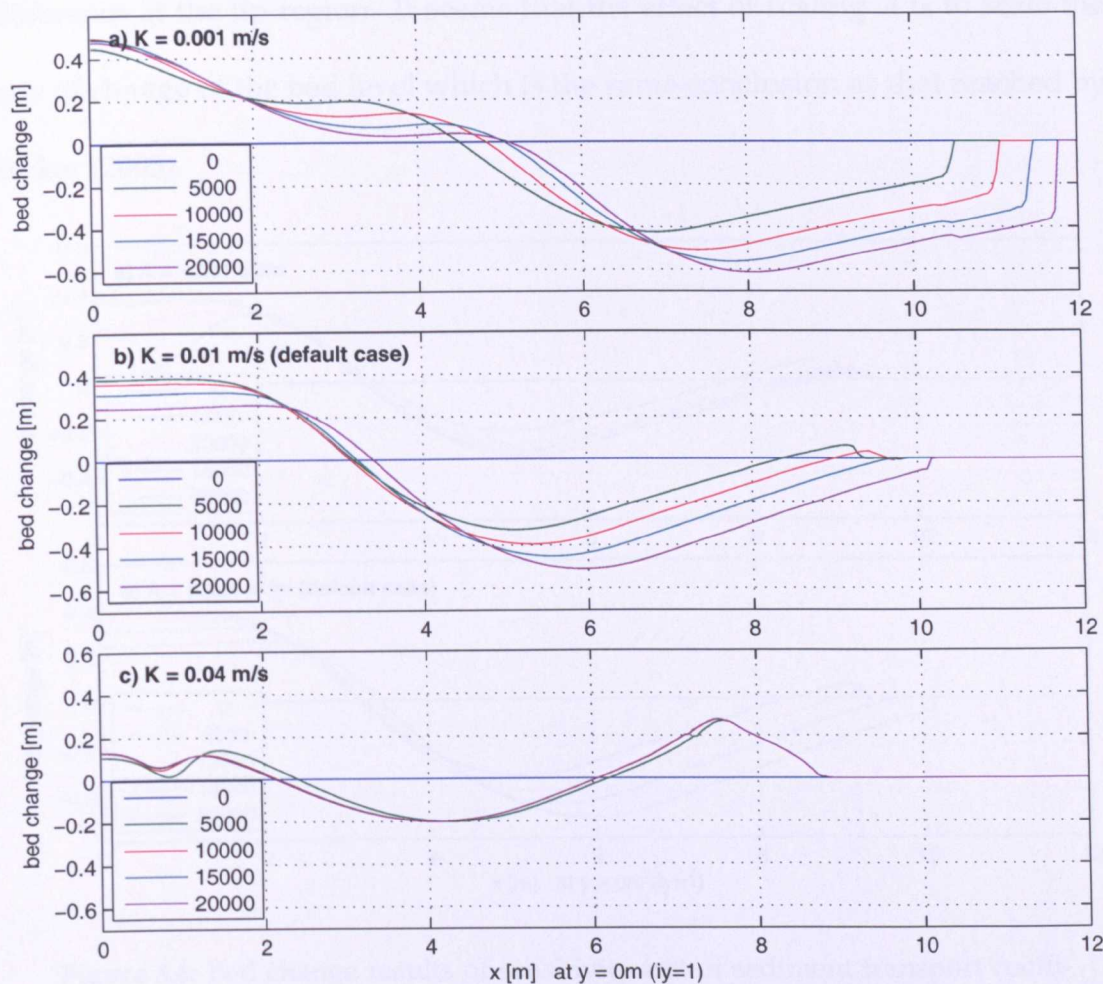


Figure 5.5: Bed change results of sensitivity test of hydraulic conductivity, K from $t = 0 - 20,000$ s. a) $K = 0.001$ m/s, b) $K = 0.01$ m/s, c) $K = 0.04$ m/s.

Bed Change by Incoming Wave Types

Following Stoker (2005), the sensitivity test for A uses $A = 0.001, 0.004$, and 0.04 s^2/m . However, for $A = 0.04$ s^2/m , the model crashed for reasons discussed in Section 5.5. Figure 5.6 represents results for $A = 0.001$ and 0.004 s^2/m . It can be seen that the bed changes are similar, but occur at different rates. For examples, the $A = 0.004$ s^2/m case at $t = 5,000$ s and the $A = 0.001$ s^2/m case at $t = 20,000$ s have approximately similar bed changes, although there is a more pronounced

difference at the tip region. It seems that the effect of scaling A is to scale the rate of change of the bed level which is the same conclusion as that reached by Stoker (2005).

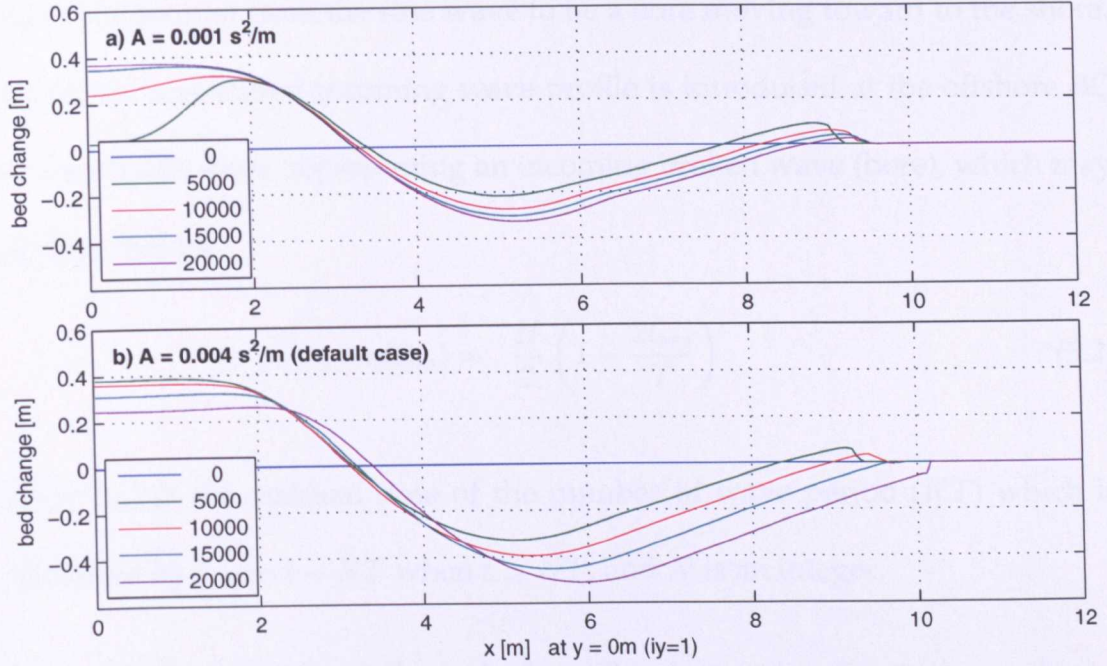


Figure 5.6: Bed change results of sensitivity test of sediment transport coefficient, A from $t = 0 - 20,000$ s. a) $A = 0.001 \text{ s}^2/\text{m}$, b) $A = 0.004 \text{ s}^2/\text{m}$.

5.4 Variation in Incoming Wave Types

So far, the incoming wave used in the model has been a sine wave, which is applied as the time variation of the surface elevation ($\eta(t)$) at the offshore BC:

$$\eta(t) = \frac{H}{2} \sin\left(\frac{2\pi t}{T}\right), \quad (5.1)$$

where H is the incoming wave height, and T is the incoming wave period. This

type of incoming wave always breaks when it moves on to the sloped beach. When the wave is breaking, it initiates sediment movement and creates the long-shore bar at the location where the wave is broken. The shape of breaking wave is reformed from the sine wave to be a bore moving toward to the shore. Therefore, a modified incoming wave profile is introduced at the offshore BC as a sawtooth wave, representing an incoming broken wave (bore), which may be describes by:

$$\eta(t_{res}) = \frac{H}{2} \left(1 - \frac{2t_{res}}{T} \right) \quad (5.2)$$

where t_{res} is the residual time of the number of wave period (NT) which is calculated by $t_{res} = t - NT$ when $t > NT$, and N is an integer.

Figure 5.7 illustrates the different bed profiles that evolve due to sine and sawtooth incoming waves. The sawtooth wave causes considerable deposition at the upper swash region, and continuously enlarge the swash berm. The sine wave initially creates a small swash berm that is then eroded (disappearing at $t = 15,000$ s), before erosion occurs at the bed in the upper swash region by $t = 20,000$ s. With the different behaviour in the upper swash region, it also affects to the whole beach profile behaviour. The long-shore bar of the sawtooth wave case moves offshore corresponding to more deposition at the upper swash, whereas the sine waves broaden the long-shore bar in time and it moves onshore due to the movement of the shoreline.

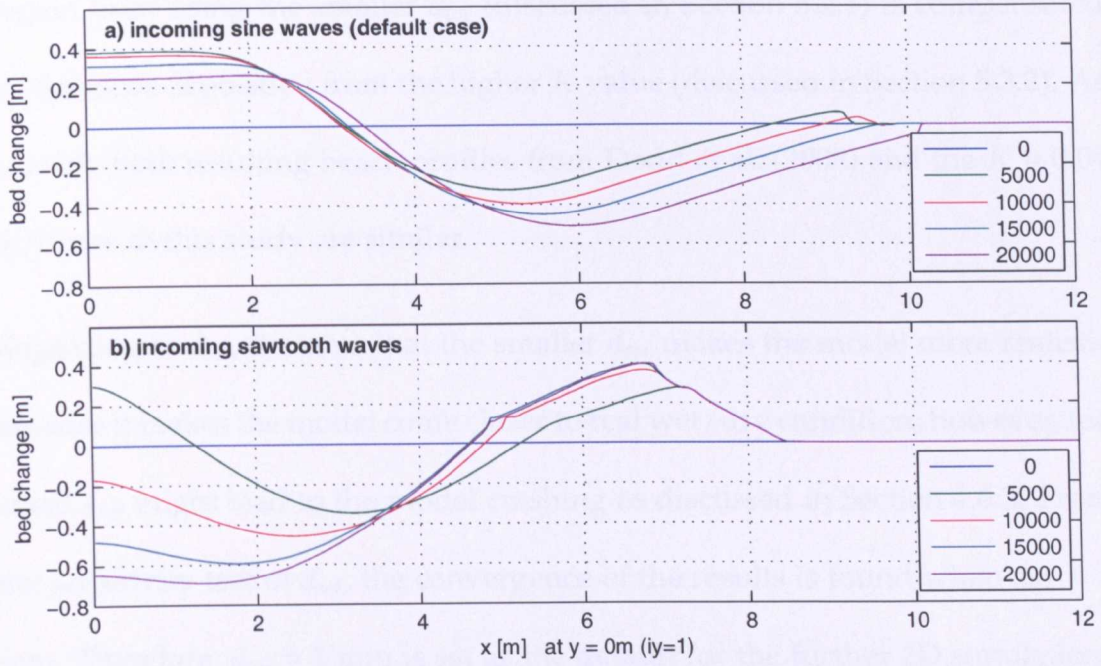


Figure 5.7: Bed change results of sensitivity test of sediment transport coefficient, A from $t = 0 - 20,000$ s. a) $A = 0.001 \text{ s}^2/\text{m}$, b) $A = 0.004 \text{ s}^2/\text{m}$.

5.5 Discussion

The evolution of 1D beach profile with the infiltration effect starts from creating the long-shore bar at location of wave breaking and the deposition in the upper swash region. Then, the beach evolves according to the numerical and physical parameters which are tested for their sensitivity as illustrated in Section 5.2 and 5.3. Most of the test cases do not reach the equilibrium state except the $K = 0.04 \text{ m/s}$ case which can be compared with a cross-shore equilibrium profile from the 1D cross-shore permeable beach simulation of Dodd et al. (2008). The $K = 0.04 \text{ m/s}$ case uses $d_{tol} = 1 \text{ mm}$ which is smaller than Dodd et al. (2008) cases ($d_{tol} = 2 \text{ cm}$ and $K = 0.01 \text{ m/s}$). It seems that the more erosion at the upper swash

region from using the smaller d_{tol} (discussed in Section 5.2.1) is compensated by the more deposition from the higher K value (discussed in Section 5.3.2). As a result, both resulting beach profiles from Dodd et al. (2008) and the $K = 0.04$ m/s case in this study are similar.

Regarding to d_{tol} , it seems that the smaller d_{tol} makes the model more realistic because it makes the model come closer to real wet/dry condition; however, too small d_{tol} might lead to the model crashing as discussed in Section 4.6.2. From the sensitivity test of d_{tol} , the convergence of the results is found when $d_{tol} \leq 1$ mm. Therefore, $d_{tol} = 1$ mm is set as the default for the further 2D simulations in this study.

The choice of value for f_w mainly affects the shoreline position, with higher $f_w \rightarrow$ shorter $x_{s,max}$ and shifting the beach profile as shown in Figure 5.4. Although the beach profile results of $f_w = 0.02-0.1$ cases have the same shapes, the shifting effect leads to different net volume of the bed change (V_b) which can be calculated by

$$V_b = \Delta x \int_{x_{offshore}}^{x_{s,max}} b(x, y, t) dx \quad (5.3)$$

where Δx is the cross-shore dimension of a calculation cell, $x_{offshore}$ is the off-shore position, and $b(x, y, t)$ is bed change related from the plane sloping beach. The V_b of $f_w = 0.02, 0.05$, and 0.1 cases are $-0.319, -0.266$, and -0.221 m³/m, respectively, where the minus sign of V_b means the net volume is the erosion.

However, the $f_w = 0.005$ case led to qualitatively different beach evolution the other cases. It has shorter $x_{s,max}$ and $V_b = -0.059$ m³/m. The reason why this

case is unique is not clear. Nevertheless, the beach profile development during the first 5,000 s is developed in the same ways as the other cases do except the more deposition at the upper swash. Therefore, this bigger swash berm might affect the flow and sediment movement resulting the different evolution.

As shown by the results in Section 5.3.2, increasing K led to greater deposition at the upper swash region, a phenomenon also observed by Masselink and Li (2001). The higher K takes more infiltration which directly affects to the water depth and depth-averaged velocity; then, the swash berm (upper swash deposition) is created, and deposition continuously occurs until equilibrium is reached. On the other hand when K is small, there is less momentum and reduced infiltration, so that surface water can move farther up the beach leading to more erosion at the upper swash.

From the sensitivity test of sediment transport coefficient, it appears that bed change is the same for all A values except that for small (large) A development is slower (faster). Therefore, the size of A appears not to lead to qualitative differences. However, the model crashed at the highest value of A considered ($A = 0.04 \text{ s}^2/\text{m}$).

This problem arises because the smaller d_{tol} used in the present model creates a higher difference in sediment fluxes at SBC, causing the bed level to change rapidly when the previous rundown and the new runup meet together. During this event, the sign of depth averaged velocity is switched resulting in sudden deposition and erosion, because the sediment transport equation in the model

depends on the depth averaged velocity. Selection of the highest A value led to accelerated occurrence of a discontinuity in the bed level, followed by spurious oscillation and model break down. In the case of $A = 0.04 \text{ s}^2/\text{m}$, the abnormal discontinuity at the maximum rundown of the swash motion ($x = 6.5 \text{ m}$) was found at $t = 63 \text{ s}$ before the model crashed as shown in Figure 5.8.

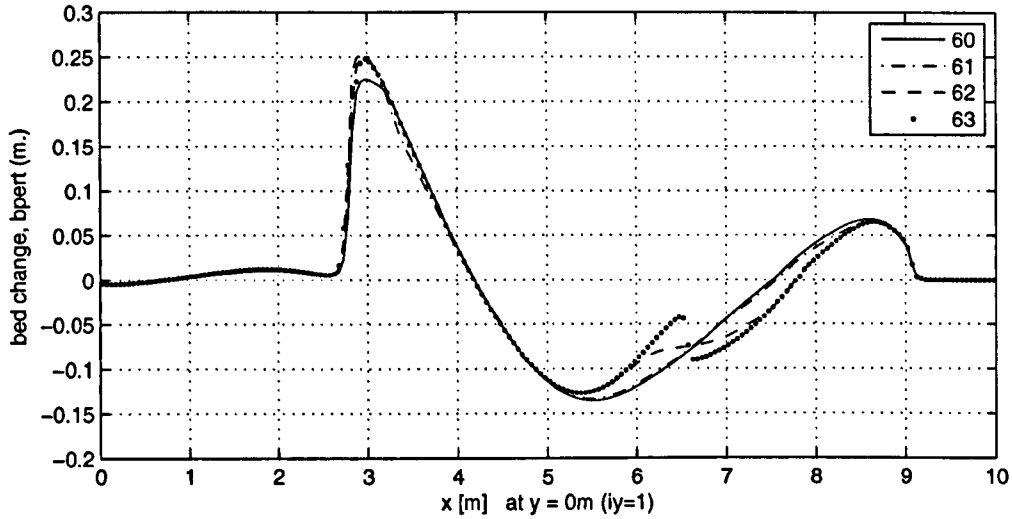


Figure 5.8: Bed change results of $A = 0.04 \text{ s}^2/\text{m}$ during $t = 60\text{--}63 \text{ s}$.

The different incoming wave profiles led to very different evolved beach profiles. The sine wave has an erosion at $t = 20,000 \text{ s}$, whereas the sawtooth wave results in a large deposition at the upper swash. The reason is not clear, but the dissimilarity may be due to differences in deposition that occur at the beginning of the simulation. Since the sine wave is breaking after it moves on the sloping beach, it transports less onshore sediment transport than the sawtooth wave which has already broken at the offshore BC. As the small amount of deposition occurs for the sine wave case at the beginning, the later incoming waves can spill over that swash berm and cause erosion. On the other hand, the

sawtooth wave transports a considerable amount of sediment from the onset of the simulation, resulting in the creation of a large swash berm. Later waves cannot pass that bar, leading to continuous deposition in the upper swash zone and the final beach profile shown in Figure 5.7.

The sine wave produces a beach profile having the same components, i.e. long-shore bar, trough, and swash berm, as the beach profile of Masselink and Li (2001), whereas the sawtooth wave creates a wider equivalent region, with the wave simply breaking further offshore. As a result, the sine wave is used for the further 2D simulations in this study.

CHAPTER 6

Formation and Evolution of Beach Cusps

Here, the method is used to investigate the formation and long-term evolution of beach cusps. The incoming wave variables and beach properties for the simulations are presented in the first part of this chapter; then, the cusp parameters that are used to explain the physical evolution of beach cusps are discussed. Next, the results of beach cusp formation and long-term evolution simulations are presented and compared with previous works. A recently developed method to investigate bed changes over the time called "*Global Analysis*" is presented; here this method is used to investigate the change from 1D to 2D dynamic. The results from the simulations are discussed in the final part.

6.1 2D Cusp Simulation

This study aims to investigate the formation and long-term evolution of beach cusps due to various incoming waves for a given initial beach profile. This study considers incoming waves of period 3, 4, 5, 6, 7, and 8 s at the offshore boundary where the still water depth of 1 m. Two types of initial beach profiles are considered: a plane 8° sloping beach and an initial curved beach which is created from the evolution of the plane beach (see the details of the curved beach creation in Section 6.6) before significant 2D evolution has taken place. For studying the long-term evolution, all cases are simulated for 400 wave periods (e.g., the $T = 6$ s case the simulation starts at $t = 0$ s, and ends at $t = 2,400$ s).

Since the model used in this study is an improvement of Dodd et al. (2008) model, the parameters of the reference case are selected to be the same as those used by Dodd et al. (2008) for their permeable beach case: incoming wave height (H) = 0.25 m, wave period (T) = 5 s, bed friction factor (f_w) = 0.05, sediment porosity (p) = 0.4, hydraulic conductivity (K) = 0.01 m/s, sediment transport coefficient (A) = 0.004 s²/m, bed diffusion coefficient (C) = 0.16, but the minimum depth (d_{tot}) decreases to 1 mm because of the new numerical implementation. Cell sizes are $\Delta x = \Delta y = 0.1$ m, which are a reasonable compromise between the model resolution and computational efficiency. The cross-shore profile of the initially planed beach used in the 2D simulation is the same as that used in 1D test which is shown in Figure 5.1.

6.1.1 Perturbations in the model

In Dodd et al. (2008) perturbations are imposed on an initially alongshore uniform state by adding a random perturbation on the offshore wave height. Here we repeat this approach but also investigate a perturbation to the bed. This perturbation is applied once at the initial state, and hence, does not have later effects on beach cusp evolution after the initial transient.

Wave Perturbation

Following Dodd et al. (2008), random perturbations chosen from a normal distribution in the range of ± 2 cm are added to the underlying incoming wave height at each alongshore cell of the offshore BC, so that:

$$\eta(y, t) = \eta_0(t) + \epsilon_p(y, t) \quad (6.1)$$

where η is the surface elevation, η_0 is the unperturbed surface elevation, and ϵ_p is the perturbed elevation. These values are subsequently smoothed in space and time in order to avoid the formation of unrealistic shocks. A spatial 5-point weighted average function is used, while a simple average method between the new perturbation and the previously applied perturbation is applied for time smoothing function (see Stoker (2005) for more details).

Bed Perturbation

The bed perturbation is introduced to avoid the continuously perturbed signal every computational time step. Since the bed perturbation also only affects the simulation once at the initial state, it is significantly different from that of Dodd et al. (2008). Nonetheless, we should expect cusp development to be similar, and so we can make sure that the cusp results from model are not coming from the perturbations.

In order to avoid that the initial beach topography dominates the final beach cusp formation, the bed perturbation function should provide uniformly distributed spectral energy at the initial state (Garnier et al., 2006). Therefore, the bed perturbation in this study uses a Dirac delta function, which adds a perturbed elevation (ϵ_p) to the beach profile at one point in the computational domain once before the simulation starts. To investigate the effect of bed perturbation elevation and position, this study considers perturbed elevations of 1 and 5 mm, and the chosen points of bed perturbation are varied in cross-shore direction (x -direction) between 3, 5, and 7 m. In the alongshore direction the positions are fixed at $y = 25$ m, which is the middle point of the domain. Because the periodic boundary condition is used for the alongshore boundary in the model, the different alongshore positions (y -direction) affect only the positions of horns and embayments.

6.1.2 Comparison of Wave Perturbation and Bed Perturbation

The bed perturbation has more advantage than the wave perturbation by avoiding the continuous perturbation. This can be confirmed that the final beach cusp formation is not directly created by the perturbation. However, Dodd et al. (2008) used the wave perturbation in their study, and that previous work is the reference for this study. Therefore, this section provides the comparison results between wave and bed perturbation cases in order to sensitivity test between both two perturbations. The parameters in these simulations are those of the reference case, and results are shown in the terms of change in bed level relative to the initial plane beach, with velocity vectors averaged over the preceeding period to illustrate the circulation pattern as shown in Figures 6.1 and 6.2. The velocity vectors in all of the figures in this study are plotted in form of $(U - \langle U \rangle, V)$ to exclude the purely 1D effect of cross-shore which is typically much than alongshore velocity component, and $\langle U \rangle$ is the average of the cross-shore velocity over the alongshore section as:

$$\langle U(x) \rangle = \frac{1}{L_y} \int_0^{L_y} U(x, y) dy \quad (6.2)$$

where L_y is length of computation domain in the alongshore direction.

Figures 6.1 and 6.2 illustrate the bed change for the wave and bed perturbation at position $x = 5$ m, $y = 25$ m, (5,25), with $\epsilon_p = 1$ mm. As these figures are used for comparison of wave and bed perturbation, the details of the formation and long-term evolution of these results will be discussed in Sections 6.3 and 6.4, respectively. It can be seen that the formation of beach cusps, the circulation

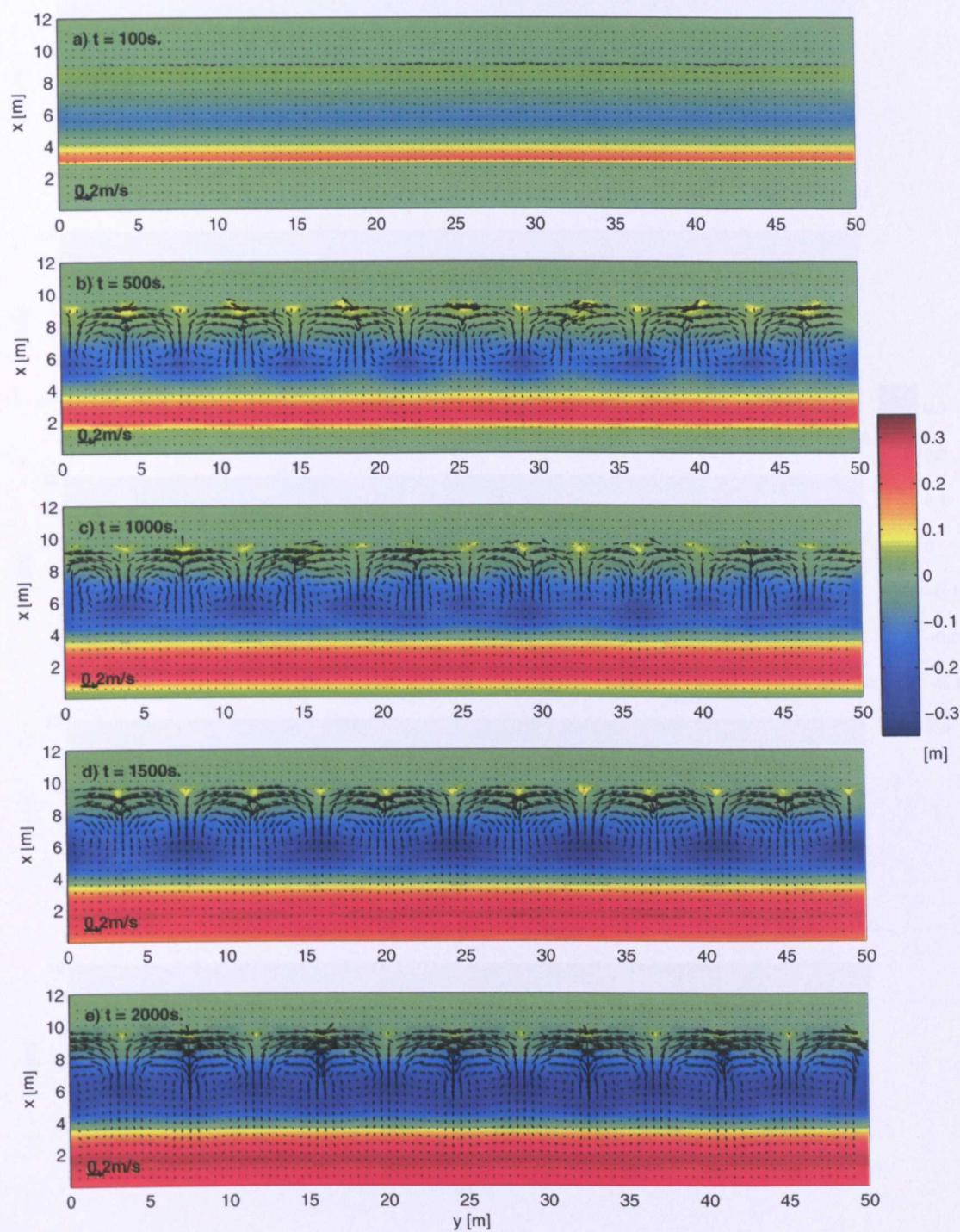


Figure 6.1: Change in bed level (m) relative to a plane beach (colours) after 20, 100, 200, 300, and 400 periods, and velocity vectors averaged over preceeding period for the wave perturbation reference case.

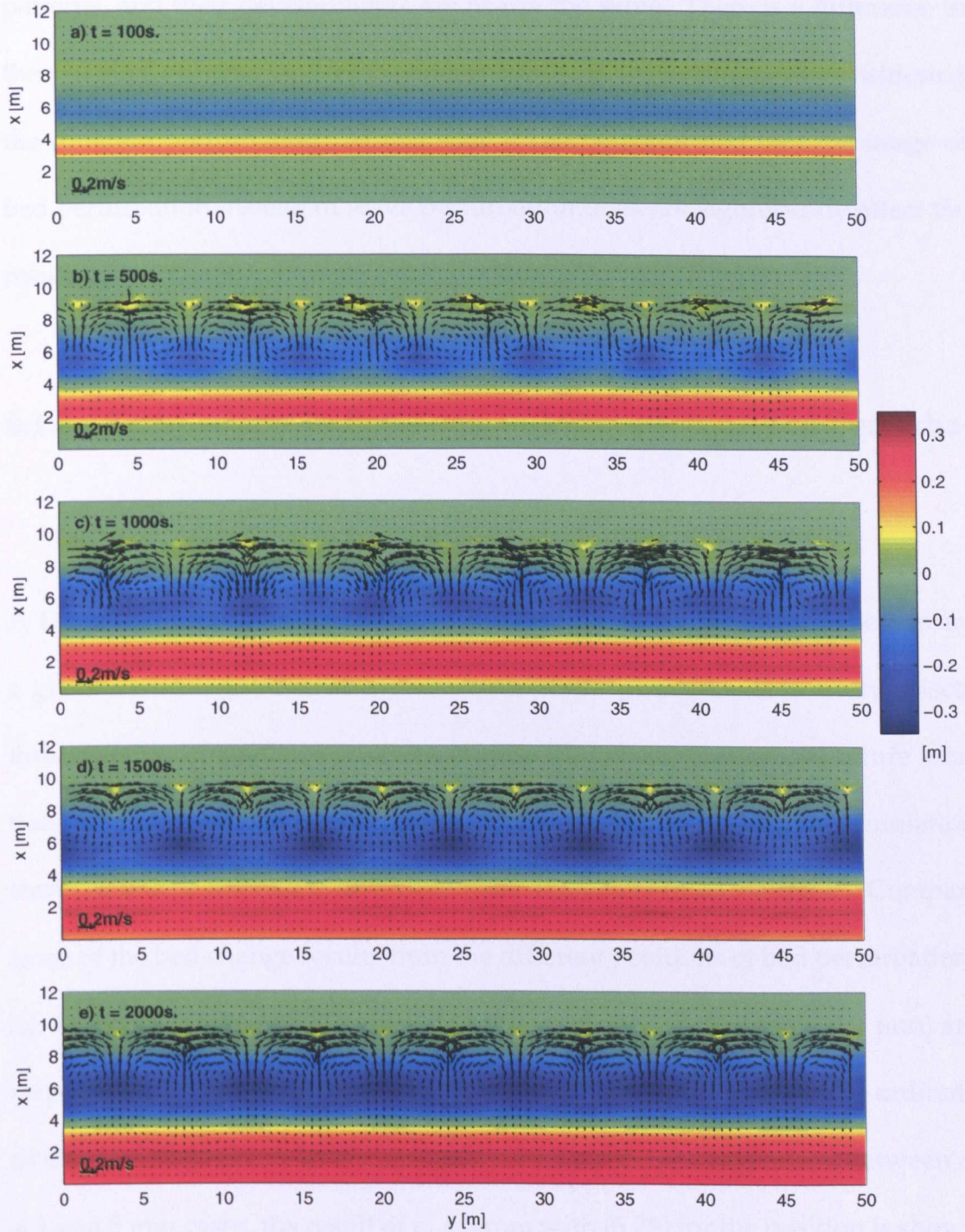


Figure 6.2: Change in bed level (m) relative to a plane beach (colours) after 20, 100, 200, 300, and 400 periods, and velocity vectors averaged over preceeding period for the bed perturbation at (5,25) with $\epsilon_p = 1$ mm, and other parameters as same as reference case.

patterns, and their developments are nearly the same. There is a difference in the position of horns and embayments which is understandable considering the different perturbation. At this state it can be confirmed that the usage of bed perturbation instead of wave perturbation does not significantly affect the results.

6.1.3 Comparison in Positions and Elevation of Bed Perturbation

A Dirac delta function is applied in the present study to perturb the bed by a given vertical distance at a given cross-shore position. This study selects three different cross-shore positions representing the approximated future locations of long-shore bar, trough region, and shoreface region after the simulation starts. These positions are estimated from 1D results (see Chapter 5). Comparisons of the bed change results from the different positions of bed perturbation, i.e. (3,25), (5,25), and (7,25), with the same perturbed elevation ($\epsilon_p = 1$ mm) are respectively shown in Figure 6.3 a), b), and c), where (x,y) are the co-ordinate of the perturbed point. In terms of perturbed elevation comparison between $\epsilon_p = 1$ and 5 mm cases, the result of $\epsilon_p = 5$ mm with (5,25) for the position is shown in Figure 6.3 d).

From Figure 6.3, there is no significant difference in bed change characteristic and circulation pattern when comparing both different positions and perturbation elevations. The specific difference again is in the position of horns and

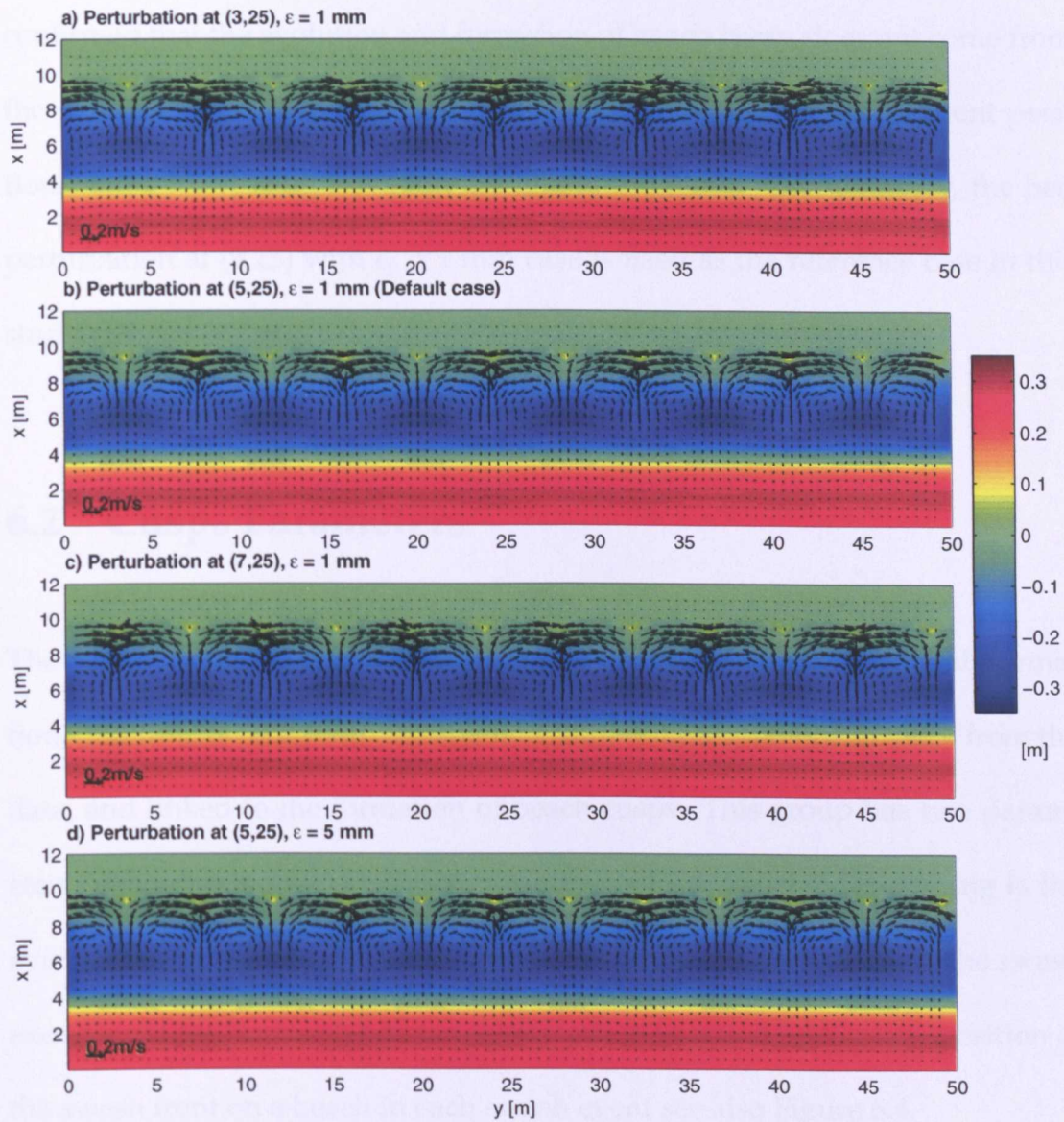


Figure 6.3: Change in bed level (m) relative to a plane beach (colours) after 400 periods, and velocity vectors averaged over preceeding period for the bed perturbation at a) (3,25) with $\epsilon_p = 1$ mm, b) (5,25) with $\epsilon_p = 1$ mm, c) (7,25) with $\epsilon_p = 1$ mm, and d) (5,25) with $\epsilon_p = 5$ mm.

embayments. As discussed before, bed perturbation has an advantage over wave perturbation in terms of avoiding the continuous perturbation. It can be confirmed that the evolution and formation of beach cusps does not come from the perturbations. Moreover, the results of simulations for the different positions and perturbation elevation are nearly the same. Consequently, the bed perturbation at (5,25) with $\epsilon_p = 1$ mm case is used as the reference case in this study.

6.2 Cusps Parameters

The cusp parameters can be divided into two groups in terms of spatial (formation) and time (evolution). The spatial group can be observed directly from the data, and linked to the formation of beach cusps. This group has two parameters: cusp spacing (λ_c) and swash excursion (S_e). Beach cusp spacing is the average distance from adjacent horn to horn as shown in Figure 6.4. The swash excursion is the horizontal distance between the highest and lowest position of the swash front on a beach in each swash event see also Figure 6.4.

6.2.1 Growth rate

An important parameter representing the initial development of beach cusps is the growth rate. Growth rate is one indicator to show how fast beach cusps initially develop (see Dodd et al. (2008)). In this study, the growth rate is computed

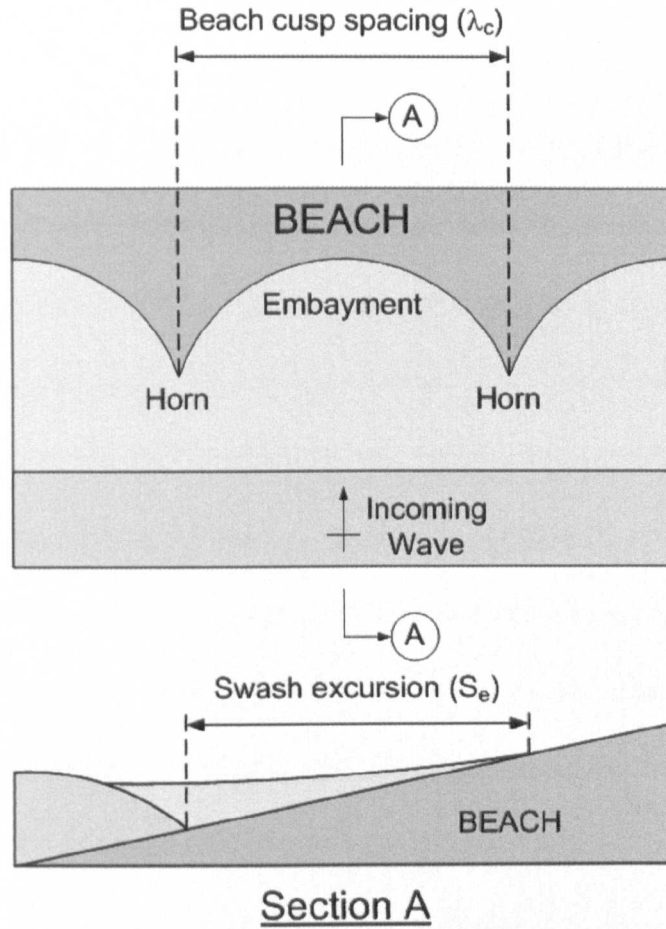


Figure 6.4: Definition of beach cusp spacing and swash excursion.

based on the assumption of that the perturbations are expected to grow initially exponentially in time, during the cusp development from 1D beach profile to 2D beach cusps, consistent with the linear stability theory (Dodd et al., 2003), and called this growth rate the "*linear growth rate*", σ . The computation of the linear growth rate needs the discrete Fourier transform to extract the significant bed signal.

Fourier analysis

This study uses the Fast Fourier Transform (FFT) to find the dominant wavelength (λ_m) of the cusp patterns from the bed patterns created from the simulations. The FFT method can be applied only one section at each time; therefore, an alongshore section between the upper swash and lower swash is chosen for this analysis. After the FFT is applied, the dominant wavelength is the wavelength corresponding to the Fourier maximum coefficient $\mathcal{H}(\lambda_m, t)$. From the assumption that the beach change grows exponentially in time at the initial state of the simulation, $\mathcal{H}(\lambda_m, t) \approx \mathcal{H}(\lambda_m, 0) \exp(\sigma t)$. Therefore, the linear growth rate (σ) can be computed from the gradient of the logarithm value of the amplitude of the dominant wavelength as:

$$\sigma = \frac{\ln \mathcal{H}(\lambda_m, t_2) - \ln \mathcal{H}(\lambda_m, t_1)}{t_2 - t_1} \quad (6.3)$$

Here, the comparison of the Fourier analysis between the section in the upper swash ($x = 7.2$ m) and that in the lower swash ($x = 5.1$ m) is considered. The bed development, the Fourier coefficient, and the logarithmic value of the amplitude of the dominant wavelength of section $x = 7.2$ m are respectively shown in Figure 6.5 a), b), and c), while those variables of section $x = 5.1$ m are also illustrated in Figure 6.5 d), e), and f). The σ can be also computed from the gradient of Figure 6.5 c) and f). When comparing the results, there are some differences in the bed development and the Fourier coefficient; however, the λ_m and σ from both sections are the same. As a result, it could be implied that the Fourier analysis of any section from the upper and lower swash zones provides

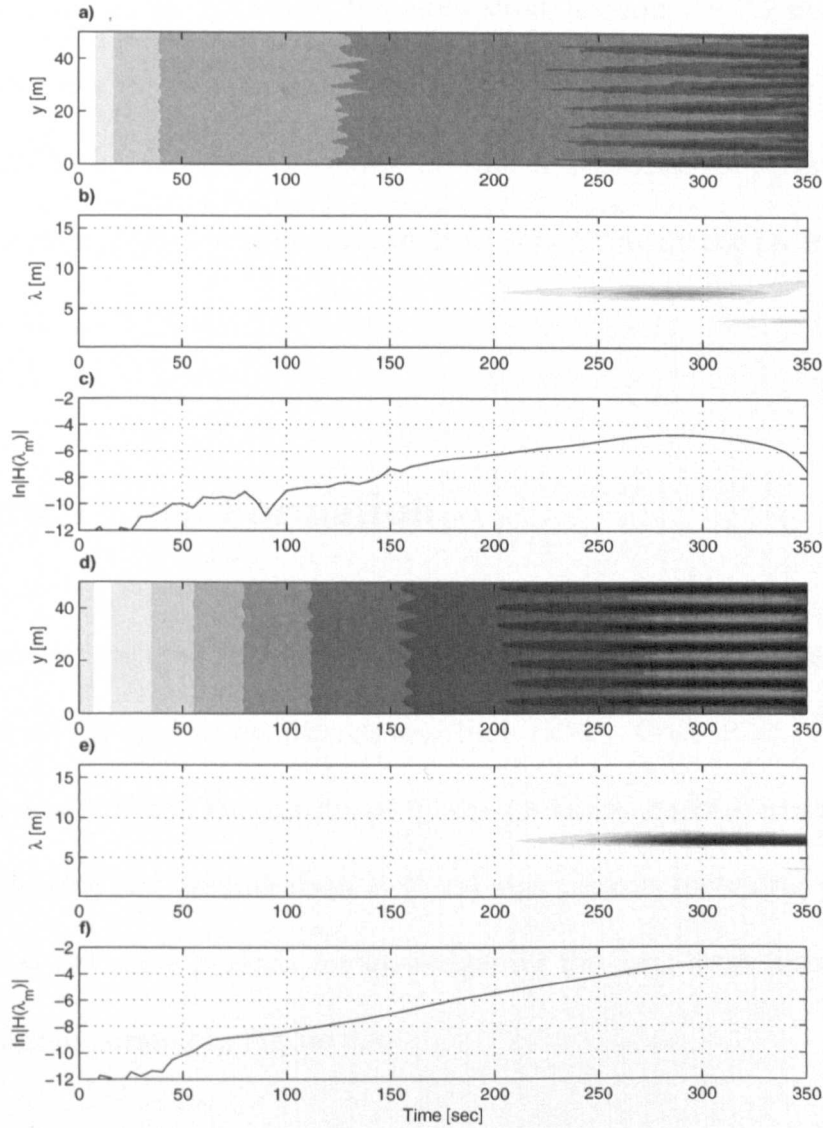


Figure 6.5: Linear growth rate computation using discrete Fourier analysis for the reference case ($T = 5$ s) at section $x = 7.2$ and 5.1 m. a) Series of the $x = 7.2$ m section in time, b) Discrete Fourier analysis of the section $x = 7.2$ m, c) Logarithmic value of the amplitude of the dominant wavelength for section $x = 7.2$ m, d) Series of the $x = 5.1$ m section in time, e) Discrete Fourier analysis of the section $x = 5.1$ m, f) Logarithmic value of the amplitude of the dominant wavelength for section $x = 5.1$ m.

the same λ_m and σ . In this study, the alongshore section $x = 7.2$ m is selected to do the Fourier analysis because this section coincides with the still water level and the beach cusps start to form around this section for all simulations, while the section at the lower swash is varied depending on the incoming wave condition.

6.3 Beach Cusp Formation

This section looks at cusp formation, and the compares of the simulation results with the previous studies by Werner and Fink (1993), Coco et al. (1999, 2000), and Dodd et al. (2008). The results of the beach cusps starting from the plane slope beach with bed perturbation at (5,25) and various incoming wave periods after $t = 400$ wave periods for investigating the long-term formation and evolution are illustrated in Figure 6.6.

As shown in Figure 6.6, λ_c increases for increasing T . Although λ_c can be measured directly from the plots, in certain cases it was not easy to identify the positions of the cusp horns and embayments. From the Fourier analysis, the dominant wave length (λ_m) can also represent beach cusp spacing (λ_c); therefore, the λ_c for all simulations in this study is given by the λ_m .

The cusp formation results are represented in terms of cusp spacing (λ_c) and swash excursion (S_e). In order to compare with previous works, the geometrical parameter (f) from self-organisation theory is computed using (2.5). Since

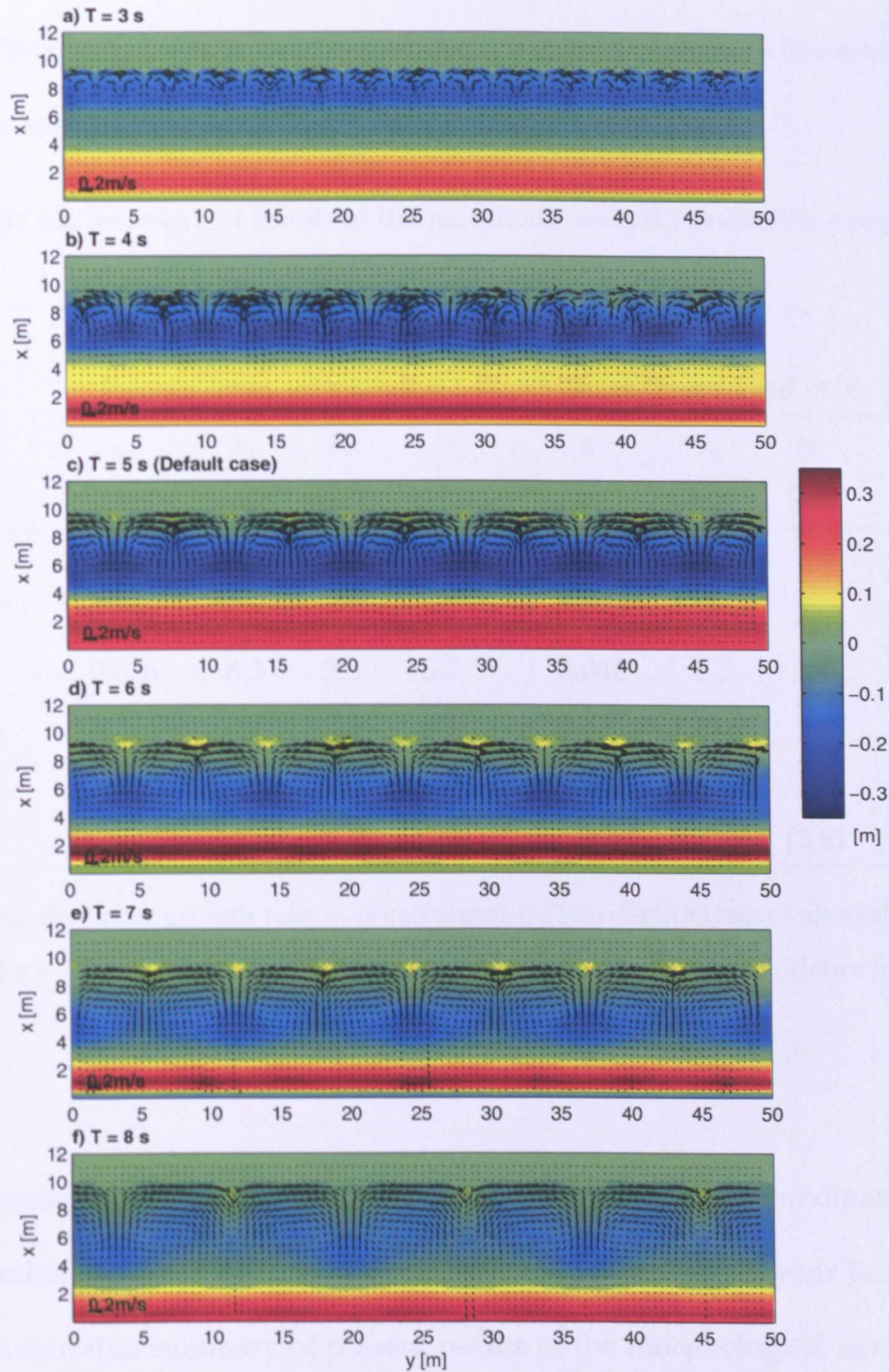


Figure 6.6: Changing in bed level (m) relative to a plane beach (colours), and velocity vectors averaged over preceding period after 400 periods of $T = 3, 4, 5, 6, 7$, and 8 s cases.

the cases of this study are similar to those for the permeable beach of Dodd et al. (2008), Table 6.1 provides the comparison of the results between this study simulations and the permeable beach results of Dodd et al. (2008).

Table 6.1: Summary of results of the morphodynamical simulations comparing with permeable beach results of Dodd et al. (2008).

T [s]	Results from simulations				Results from Dodd et al. (2008)			
	σ [s ⁻¹]	λ_c [m]	S_e [m]	f	σ [s ⁻¹]	λ_c [m]	S_e [m]	f
3	0.041	3.6	1.1	3.3	0.057	4.2	1.4	3.1
4	0.032	6.2	2.0	3.1	0.064	5.3	2.0	2.7
5	0.026	8.3	2.5	3.3	0.048	8.3	2.4	3.4
6	0.024	10.0	2.9	3.4	0.025	10.0	2.9	3.4
7	0.014	12.5	3.2	3.9	0.017	12.5	3.4	3.7
8	(0.0056)	(16.6)	(3.3)	(5.0)	(0.0064)	(13.8)	(3.8)	(3.6)

Note that the linear growth rate, σ , is calculated by Fourier analysis of alongshore sections at $x = 7.2$ m, and the figures in parentheses denote only weak evidence for cusps.

The results show that λ_c and S_e increase with T , with an approximately constant value of the self-organisation geometrical parameter, f . From Table 6.1, it can be seen that summary of present results of the morphological simulations with those of Dodd et al. (2008) for a permeable beach. However, f from both simulations and Dodd et al. (2008) are still high when compared with Werner and Fink (1993) ($1 < f < 3$), and Masselink (1999) and Coco et al. (2000) ($f \approx 1.6$). This might be caused from the depositions at the embayments which have not

been observed in the field (Coco et al., 2003) as shown in Figure 6.6. Actually, the S_e is determined at the embayment, because the longest horizontal distance between the highest and lowest position of the swash front is found there. As there is deposition in the embayment, it causes S_e to reduce and hence f to increase, while λ_c does not change. However, the occurrence of these depositions will be discussed in Section 6.7.

6.4 Beach Cusp Evolution

In Figures 6.7 to 6.10 show cusp development over 400 wave periods for the reference case. The evolution of the cusps starts from the creation of a long-shore bar and deposition at the upper swash. Up to this point only 1D behaviour in the cross-shore profile is observed with no appearance of 2D behaviour, as shown in Figure 6.7 a); then, a 2D circulation pattern starts to develop at the upper swash (around $x = 9$ m) at $t = 200$ s (Figure 6.7 b)). During this 1D development stage most of sediment is moved from the trough area (around $x = 6$ m) to the long-shore bar at $x = 3$ m (depositions); however, some of sediment is deposited at the upper swash.

Thereafter 2D circulation starts at the upper swash; this circulation pattern is expanded to the trough area to create the beach cusps as seen in Figure 6.7 c). Not only are horns and embayments created from this 2D circulation, but also the cusp-like patterns are in anti-phase in the trough area. Sediment continues to move from the shoreface and trough area to the long-shore bar. During this

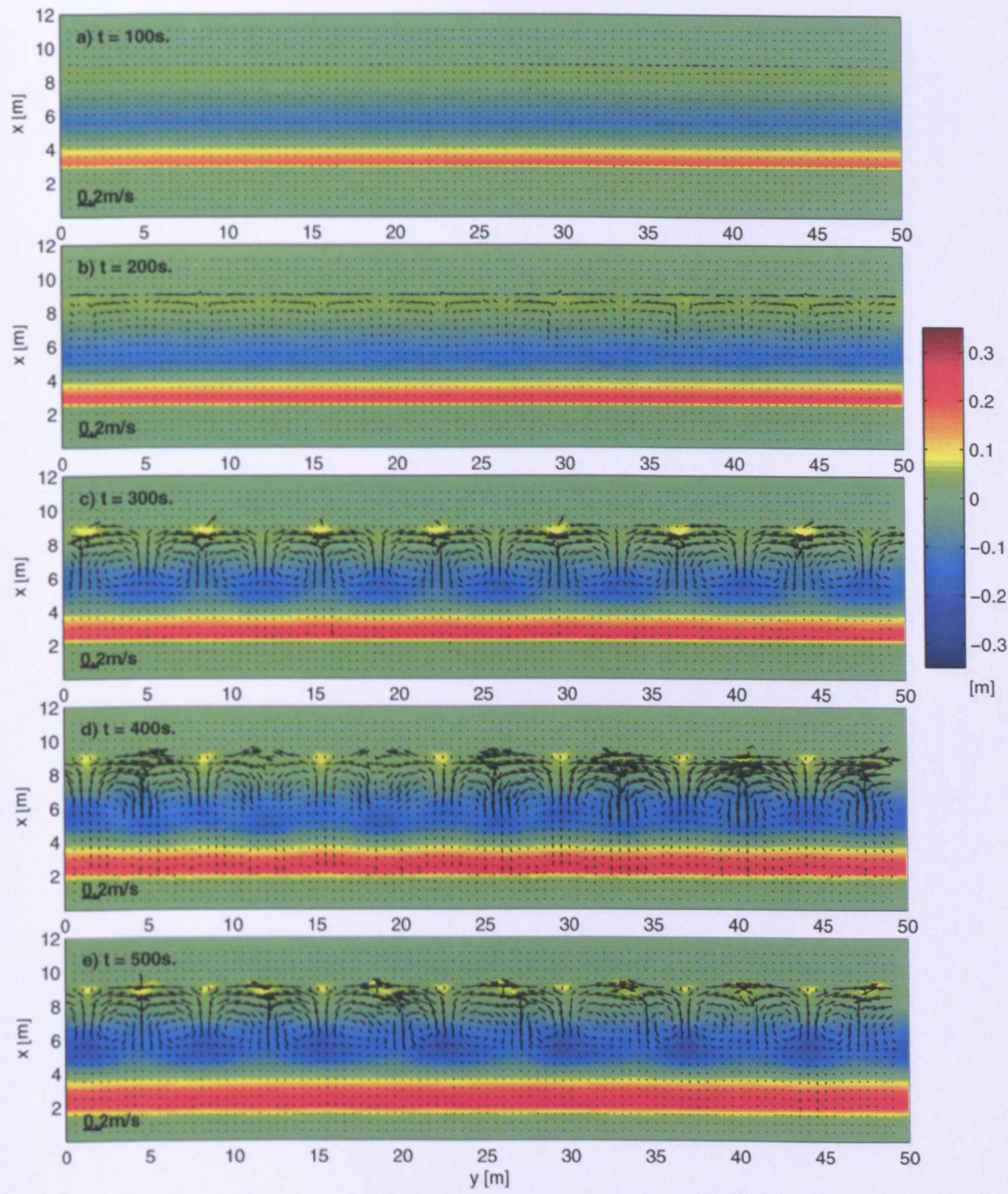


Figure 6.7: Change in bed level (m) relative to a plane beach (colours) and velocity vectors averaged over preceeding period for the reference case from $t = 100$ -500 s.

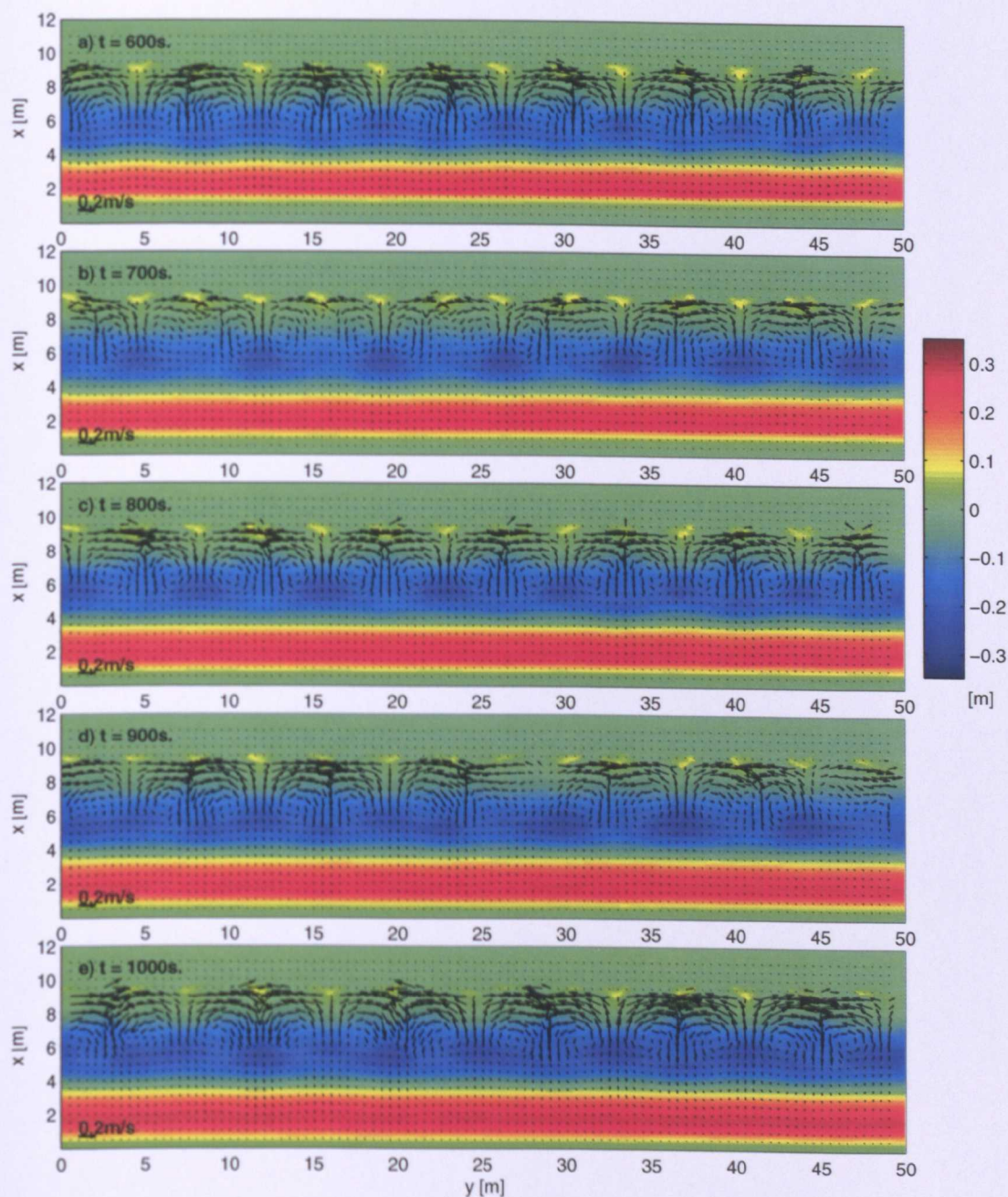


Figure 6.8: Change in bed level (m) relative to a plane beach (colours) and velocity vectors averaged over preceding period for the reference case from $t = 600\text{-}1,000 \text{ s}$.

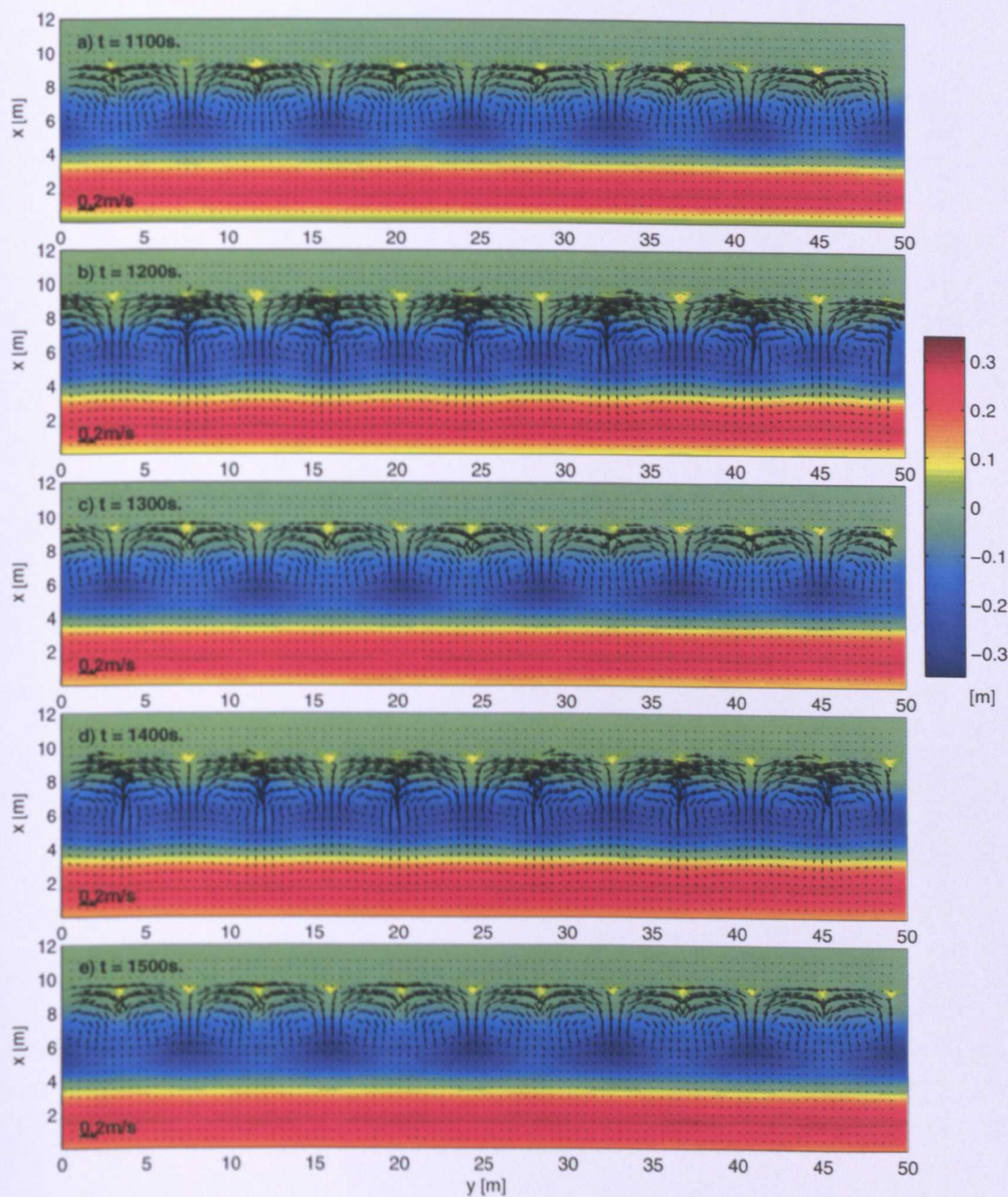


Figure 6.9: Change in bed level (m) relative to a plane beach (colours) and velocity vectors averaged over preceding period for the reference case from $t = 1,100\text{-}1,500 \text{ s}$.

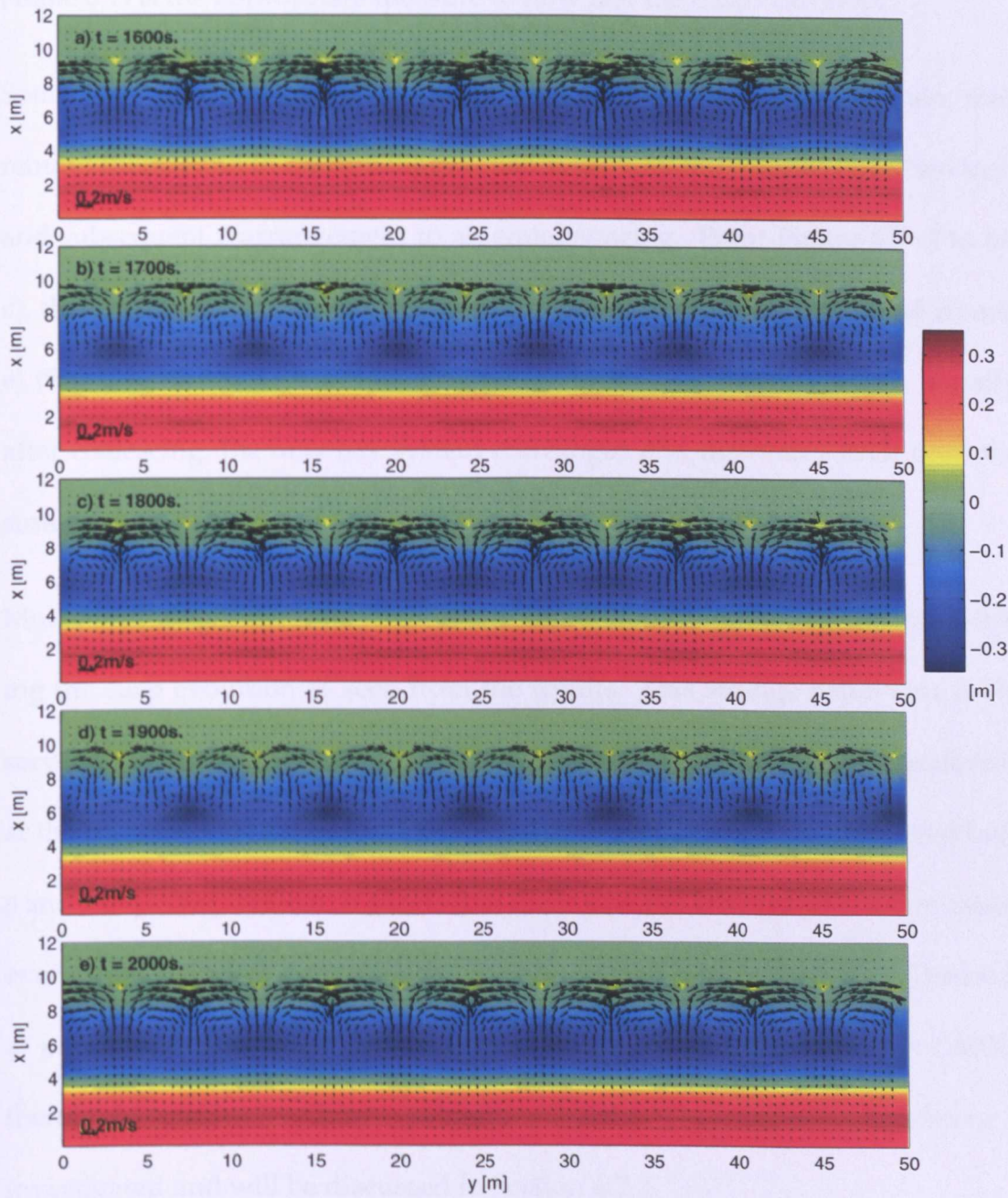


Figure 6.10: Change in bed level (m) relative to a plane beach (colours) and velocity vectors averaged over preceding period for the reference case from $t = 1,600\text{-}2,000\text{ s}$.

transition period from 1D to 2D of the cusp evolution, the linear growth rate (Table 6.1) is the appropriate measure to how fast the cusps develop.

Some beach cusps are initially created with a "*small*" cusp spacing; then, they rebuild themselves to create a bigger cusp system by the coalescing of two bays and subsequent rearrangement to an equal spacing. From Figure 6.7 c) to 6.8 c), there are 7 embayments in the computational domain; in Figure 6.8 d) and e) (900-1,000 s), there is a transition period from 7 to 6 embayments. Finally, after coalescing, the new bay system rearranges and maintains itself until the simulation is as shown in Figure 6.9 and 6.10.

More surprising is the reversing behaviour between horn and embayment during the cusp evolution as seen from the results. This strange behaviour is observed after horns and embayments are already created from the 2D circulation at the shoreface. In this reference cases, the reversing behaviour occurred both 6 and 7 bays cusp system. It seems that the horns and embayments are reversed every 200 s (40 wave periods) by observing from Figure 6.10 a) to e). The horn at $y = 12$ m when $t = 1,600$ s changes to be the embayment when $t = 1,800$ s; then it changes back to horn again at $t = 2,000$ s. This reversible behaviour is investigated and will be discussed in Section 6.7.2.

6.5 Global Analysis

As the simulation results of beach cusp development are very dynamic each time step and widely changeable in shape pattern, global analysis is introduced to investigate and explain the dynamic process of cusp evolution, by considering all the bed changes relative to the initial beach in the computational domain. Garnier et al. (2006) used the concept of global analysis to define the time dependent variable of bed change, $||b||$, as:

$$||b|| = \left(\frac{1}{L_x L_y} \int_0^{L_y} \int_0^{L_x} b^2 dx dy \right)^{1/2} \quad (6.4)$$

where b is bed change related to the initial plane sloping beach, L_x and L_y are lengths of the computational domain in the cross- and alongshore directions, respectively. However, it found that more bed change occurs in the cross-shore direction than in the alongshore direction; thus, the results from (6.4) primarily reflect the cross-shore behaviour. To remove purely on-offshore effect and to investigate the beach cusp which is a 2D pattern, the average of bed change in alongshore direction is subtracted by $\langle b \rangle$:

$$||b - \langle b \rangle|| = \left(\frac{1}{L_x L_y} \int_0^{L_y} \int_0^{L_x} (b - \langle b \rangle)^2 dx dy \right)^{1/2} \quad (6.5)$$

The $\langle b \rangle$ is computed by the same method as shown in (6.2). The comparison of $||b||$ and $||b - \langle b \rangle||$ of the reference case is shown in Figure 6.11 a) and b), respectively. The value of $||b||$ is much higher than that of $||b - \langle b \rangle||$. This confirms that $||b - \langle b \rangle||$ is more suitable for investigating the evolution of 2D beach cusps,

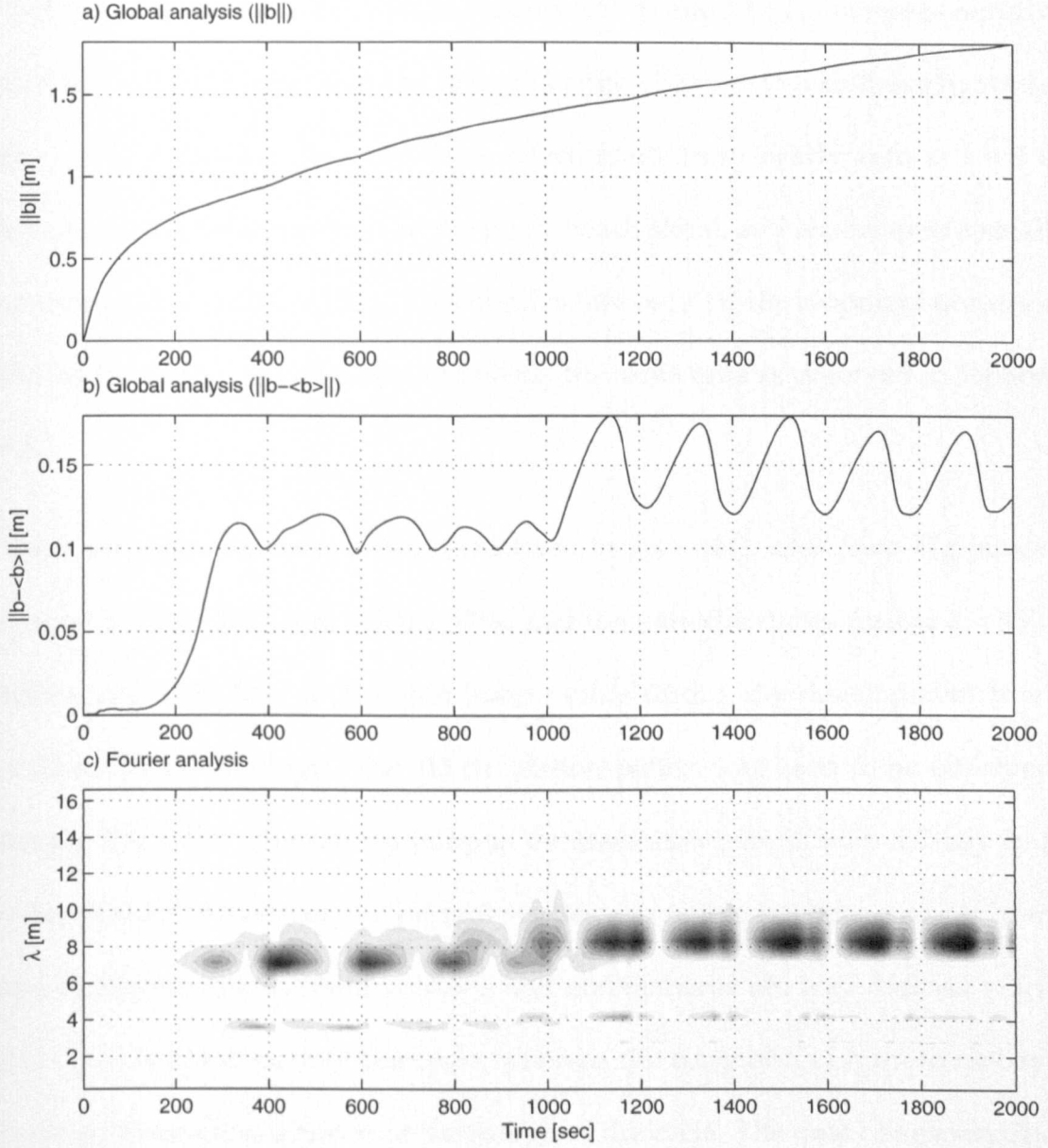


Figure 6.11: Comparison of a) the global bed change ($\|b\|$), b) the global bed change with alongshore averaged subtraction ($\|b - \langle b \rangle\|$), and c) the Fourier analysis of section $x = 7.2$ m for the reference case.

because the $\|b\|$ value mainly reflects the cross-shore evolution; therefore, here-
after the global bed change parameter is taken to be $\|b - \langle b \rangle\|$.

The global analysis plot can be compared with the behaviour of cusp evolution

shown in Figures 6.7 to 6.10. From Figures 6.11 a) and b), $||b||$ increases rapidly during $t = 0-150$ s, after that the rate of change of $||b||$ increases linearly, while $||b - \langle b \rangle||$, extracting the cross-shore effect, starts from nearly zero at $t = 0$ s because of the Dirac function on the plane beach slope, and increases to a small constant value until $t \approx 150$ s. This implies that only 1D development occurred during $t = 0-150$ s, which is approximately the same time as observed in Section 6.4.

There are still two main different features in $||b - \langle b \rangle||$ plot: two big jumps around $t = 150-300$ s and 1,000-1,150s, and the periodic cycles during $t = 300-1000$ s and 1150-2000 s. The first jump occurs during the development from a 1D to 2D morphology. The 2D circulation pattern can start to be observed during this time. The second jump is the transition period from a 7 bay to a 6 bay system. Moreover, the periodic cycles can reflect the behaviour of horn and embayment reversibility. Horns and embayments are well defined when $||b - \langle b \rangle||$ is at the peak of the cycle, whereas the transition of horn to embayment and vice versa appears at the trough of the cycle. The time corresponding to the peak of the cycle in the plot of $||b - \langle b \rangle||$ is similar to the time when the Fourier analysis of the section $x = 7.2$ m has a peak, while the trough of that cycle occurs at the same time as when the Fourier coefficient is approximately uniformly distributed (Figure 6.11 c)). Consequently, the global analysis plot can describe the long-term evolution of beach cusps, and the period of reversal is approximately 200 s for the reference case which is the same period as found in Section 6.4. However, the reversible behaviour of the beach cusps is

not found in the field, so the period of reversal is simply a number without reference to any physics. The reason of the reversible behaviour will be discussed in Section 6.7.2.

6.6 Simulation of Initial Curved beach

So far in this study, all simulations have started from a plane sloping beach. In these simulations see also Dodd et al. (2008), cusp evolution is initially 1D; then, 2D beach cusps and circulation patterns appear. Therefore, since we primarily focus on beach cusps it makes sense to start from a beach from which cusps develop immediately. Global analysis is used as a tool for determining the end of the 1D development time, and the averaged cross-shore profile at that time will be expanded to create the alongshore uniform curved beach profile. The global analysis results for comparing the d_{tol} between 0.5, 1, 2, and 5 mm of $T = 3-8$ cases are shown in Figure 6.12.

From Figure 6.12, the $\|b - \langle b \rangle\|$ value of $d_{tol} = 0.5, 1$, and 2 mm cases have the same cusp development, whereas the $d_{tol} = 5$ mm cases are totally different. This confirms the earlier conclusion from 1D simulations that the simulation results have converged for $d_{tol} \leq 1.0$ mm, as discussed in Section 5.2.1. Moreover, the convergence in the results makes more confidence in using the present model to simulate and investigate the beach cusp evolution.

The lagging in time of the 1D to 2D development (as discussed for analysing

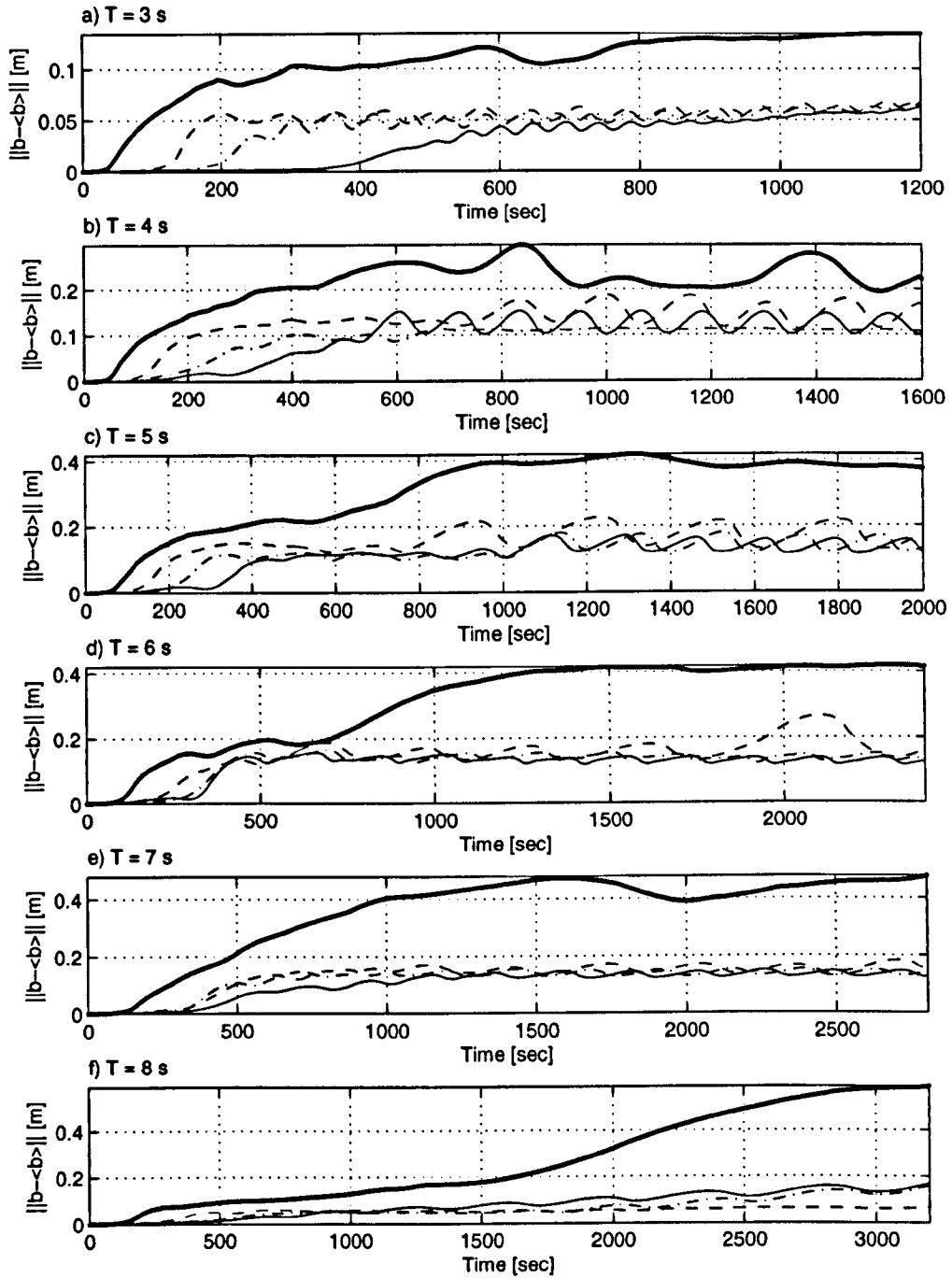


Figure 6.12: Comparison of the global bed change with alongshore averaged subtraction in time for different d_{tol} values of the $T = 3, 4, 5, 6, 7$, and 8 s case. Solid line: $d_{tol} = 0.5$ mm; dot-dashed line: $d_{tol} = 1$ mm; dashed line: $d_{tol} = 2$ mm; thick solid line: $d_{tol} = 5$ mm.

the global analysis curve in Section 6.5) for $d_{tol} = 0.5$ and 1.0 mm cases can be observed. The bigger d_{tol} case can develop 2D behaviour faster than the smaller one. With this configuration and the convergence in simulation results from $d_{tol} = 0.5$ and 1 mm case, we make the assumption that the break apart point between $d_{tol} = 0.5$ and 1.0 mm cases is the end of the 1D development of $d_{tol} = 1.0$ mm case, while $d_{tol} = 0.5$ mm case continues the 1D process. Therefore, the selected time to pick up the averaged cross-shore profile in order to create a 2D initial curved beach is assigned at the break apart point.

Finally, the time steps to create the initial curved beach are determined case by case from the first point that differences of $||b - \langle b \rangle||$ between $d_{tol} = 0.5$ and 1 mm over h_0 exceed $\pm 1 \times 10^{-3}$ as shown in Figure 6.13. The reason for choosing 1×10^{-3} to be the divergence/convergence decision value comes from the fact that the bed perturbed elevation used for the initial condition is 1 mm ($\epsilon_p/h_0 = 1 \times 10^{-3}$), which can disturb the global bed change. The summary of the selected time to create the initial curved beach profile using averaged profile of the plane slope beach results is shown in Table 6.2. Each initial curved beach profile has to add the 1 mm Dirac delta function at (5,25) as the bed perturbation to be the initial beach condition before starting the initial curved beach simulation.

6.6.1 Cusp Formation of Initial Curved beach

New initial curved beach profiles with bed perturbations for each incoming wave conditions are simulated, and the results presented in Table 6.3. The cusp

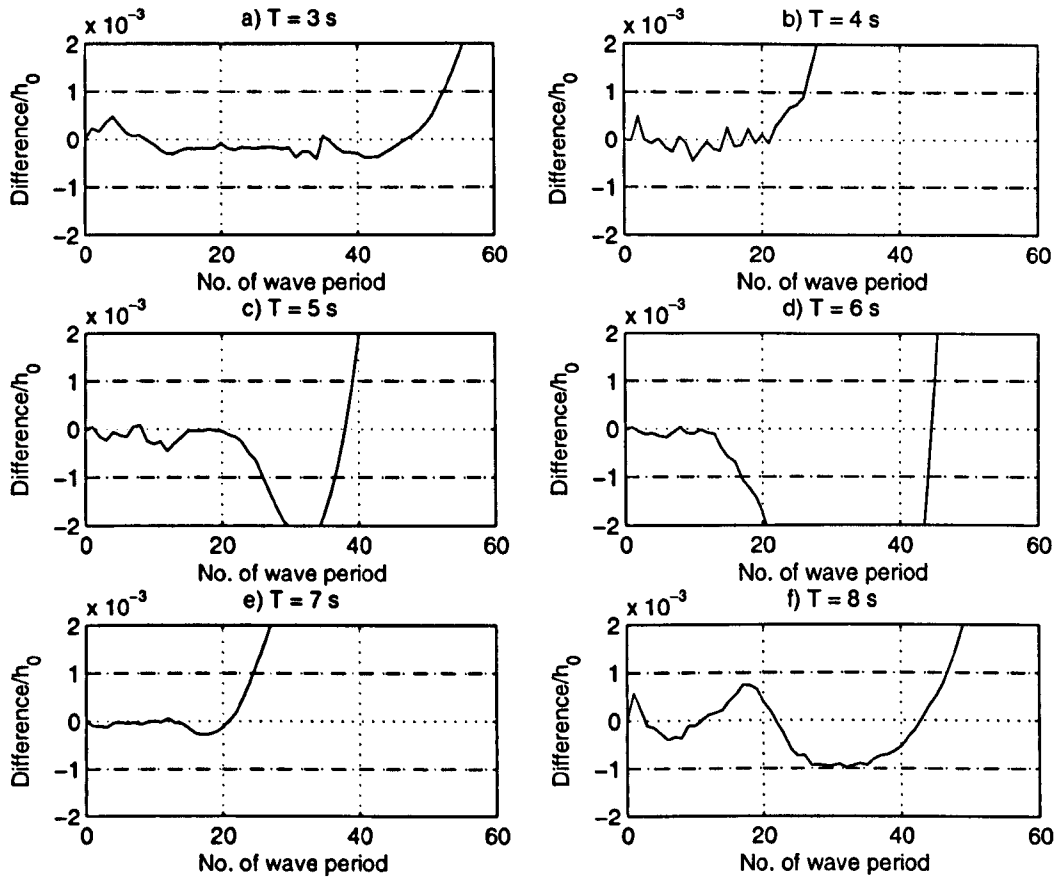


Figure 6.13: Differences of $\|b - \langle b \rangle\|$ between $d_{tot} = 0.5$ and 1.0 mm over h_0 of $T = 3, 4, 5, 6, 7$, and 8 s cases.

Table 6.2: Summary of the creation time from the plane slope beach results to create the initial curved beach profiles.

wave period, T [s]	3	4	5	6	7	8
time, t [s]	156	104	130	102	168	368

parameters (λ_c , S_e , and σ) are found by the same method as used for plane slope beach initial condition.

The beach cusp formations obtained from the two initial beach profiles are sim-

Table 6.3: Summary of results of the morphodynamical simulations for the initial curved beach profiles

T [s]	σ [s ⁻¹]	λ_c [m]	S_e [m]	f
3	0.038	3.8	1.5	2.5
4	0.034	6.2	2.2	2.8
5	0.021	8.3	2.7	3.1
6	0.021	10.0	3.2	3.1
7	0.021	12.5	3.2	3.9
8	(0.0062)	(16.6)	(3.3)	(5.0)

ilar. However, the main difference between these two initial profile results can be recognised for the shorter incoming wave period cases ($T = 3-6$ s). In these cases, the swash excursions from the initial curved beach profiles are higher, while the cusp spacings remain the same. This reduces the self-organisation geometrical parameter, f , and makes the f values become close to the range of those provided by Werner and Fink (1993).

The reason S_e is longer in the initially curved beach cases is due to the initial deposition of sediment in the upper swash; then, the sediment in the lower swash tends to move offshore which is the same behaviour as the 1D case do when there is a lot of deposition at the upper swash during the beginning of the simulation as discussed in Chapter 5. Therefore, the position of the trough of beach cusps is farther offshore, while the maximum runup position is not changed, resulting in longer S_e . For example, the comparison of averaged beach

profile between the initial plane sloping beach and curved beach for $T = 4$ s cases at $t = 400$ periods indicates that the trough of beach cusp in the initial plane sloping beach is at $x \approx 6$ m, while that of initial cusp beach is at $x \approx 5$ m as shown in Figure 6.14.

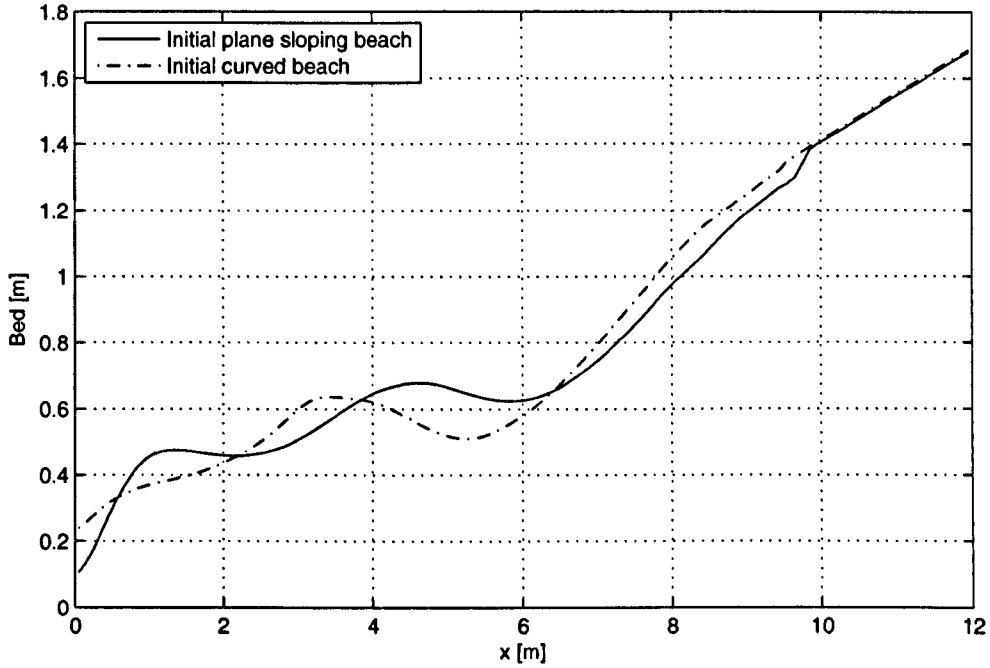


Figure 6.14: Comparison of averaged beach profile between the initial plane sloping beach and the initial curved beach for $T = 4$ s cases at $t = 400$ periods.

6.6.2 Evolution of Initial Curved beach

The investigation of long-term evolution of beach cusps for the initial curved beach profile for $T = 5$ s case is shown in terms of the global analysis, and the results compared with those of the reference case in Figure 6.15.

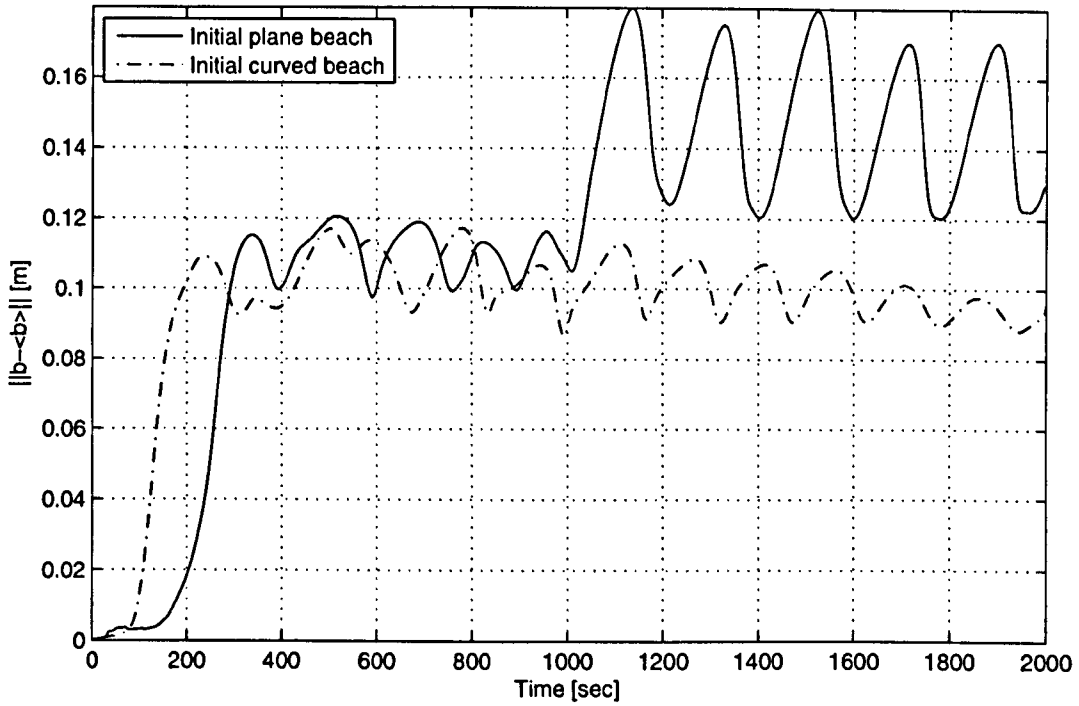


Figure 6.15: The global bed change with alongshore averaged subtraction in time of initial curved beach, $T = 5$ s case.

From the comparison, the pattern of cusp evolution is the same as the reference case which starts from the 1D development, then a system of small cusp is created before the system of larger cusps develops. However, the difference of cusp development between these two cases is the usage time in each phase. The 1D development of the initial curved beach starts before the reference case as we expect; then, the small cusp system phase is shorter ($t = 200$ – 400 s). Afterwards, the cusp pattern evolve to a system of large cusps, with reversible behaviour occurring during this evolutionary stage. The period of reversal for the initial curved beach profile case is around 160 s which is faster than the initial plane sloping beach case. The shorter period of small cusp system with no

big jump during the transition between small and big cusp system of the initial curved beach case, and the faster period of reversal might be a reason why the beach profile already has deposition in the upper swash zone; thus, the deposited sediment can easily move alongshore to create a system of large cusps faster than the reference case without the big change in the $||b - \langle b \rangle||$ value.

6.7 Discussion

The simulations of the formation and long-term evolution of beach cusps provide an improved understanding of the development of cusped system. The results for beach cusp formation are very similar to those obtained by Dodd et al. (2008). Global analysis is more efficient than Fourier analysis at evaluating the evolution of cusps, because the global method includes all of the computational points in calculation domain, whereas the Fourier analysis accounts solely for the selected section. Even so, Fourier analysis is required in order to identify the cusp spacing, which global analysis cannot.

6.7.1 Sensitivity Test of Bed Diffusion Coefficient

The bed diffusion coefficient, C , is the parameter for including the downslope effect in the sediment transport equations. In 2D simulations, we use $C = 1.6$, corresponding to the angle of repose of sediment of 32° (see more details in Section 3.3). Therefore, the sensitivity test of this parameter varies C between

1.0 and 2.0, and the results of bed changes are shown in Figure 6.16.

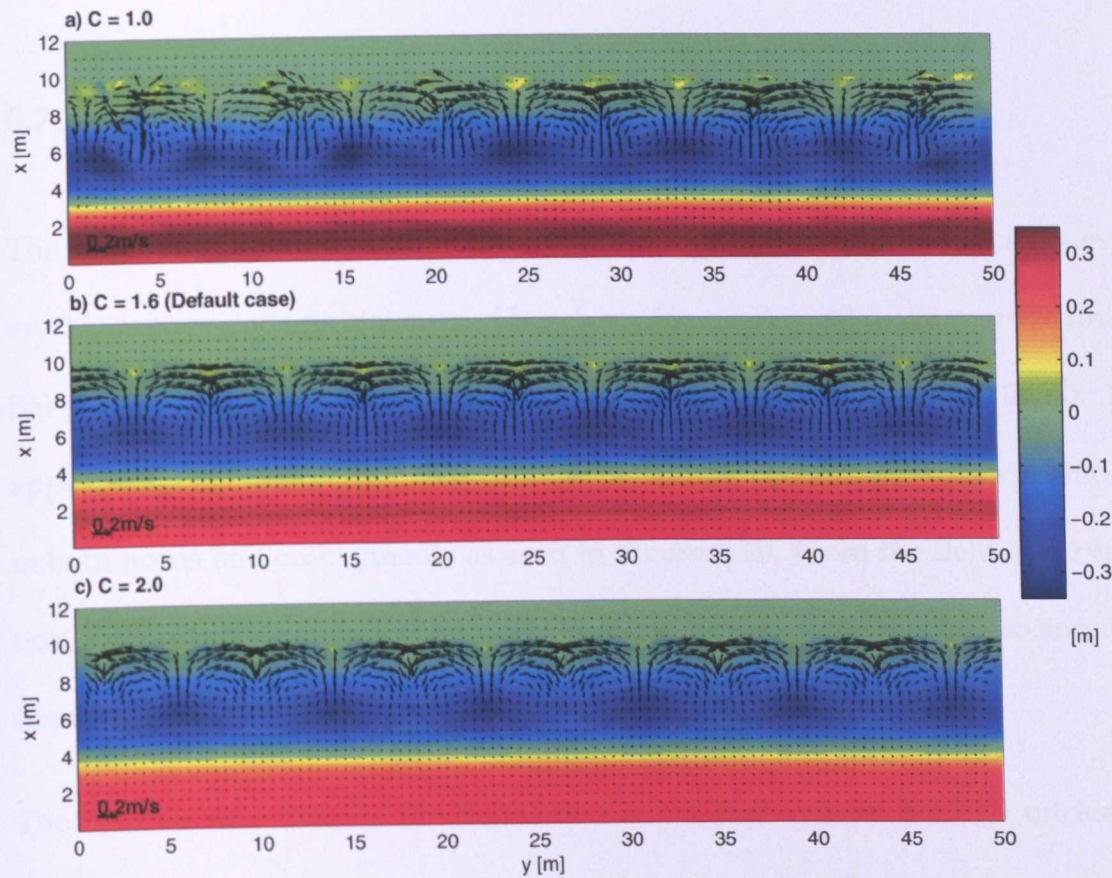


Figure 6.16: Change in bed level (m) relative to a plane beach (colours) after 20, 100, 200, 300, and 400 periods, and velocity vectors averaged over preceeding period for sensitivity test of bed diffusion, $C = 2.0$, when other parameters as same as reference.

Beach cusp formation and evolution are similar to the reference case ($C = 1.6$). The effect of bed diffusion coefficient can be observed at the long-shore bar and also at the upper swash region. The height of long-shore bar is higher, but its width is narrower when C is smaller. This behaviour is also reflected in that the higher C moves the sediment downslope and reduces the berm slope. In conclusion, the variation of bed diffusion coefficient does not have any significant

effect to λ_c , but affects directly the long-shore bar.

6.7.2 Reversible Behaviour

The reversible behaviour of the horns and embayments in the beach cusps every 32 wave periods (initial curved beach profile case) or 40 wave periods (initial plane slope beach case) is not observed in the field (Coco et al., 2003). It appears that the reason for this reversible behaviour comes from the deposition in both horns and embayments as seen in Figure 6.10. From the field observation, the deposition is found only at the horns, whereas there is no erosion or deposition at the embayments.

The reasons why there is the deposition at the embayment are still unclear. There could possibly be two sources. Firstly, the permeability used herein had a constant value here. This parameter is found to have a large effect on the profile and deposition at the shoreface in Chapter 5, and more investigation of the permeability pattern in one swash period will be presented in Chapter 7.

Secondly, the simple sediment transport equation is used for this study, because the implementation of a complex sediment transport equation is limited with the Roe approximation scheme. This simple sediment transport equation is only a function of depth averaged velocity, and the way to approximate the depth averaged alongshore velocity in the Roe approximation solver could create the zero velocity at the embayment when two alongshore velocities which have the same magnitude but the difference direction meet together; thus, it

causes the sediment deposition at the embayment. The behaviour of the zero velocity in the Roe approximation could be found in the model using any sediment transport equations; however, the sediment transport rate formulation used now in the model makes the result worse, because it induces the rapid bed change when the zero velocity occurs. Therefore, the variation of the sediment transport equations will be tested and discussed in Chapter 8.

6.7.3 The Effect of Domain size

The cusp simulations use a periodic boundary condition for lateral boundaries. This allows us to shorten the domain length for a simulation that has exactly repeating behaviour along the domain lateral boundaries. However, with the lateral feedback signal too short a domain length (in the longshore direction) could affect the formation and evolution of beach cusps. Therefore, the domain length is increased in the alongshore direction (y -direction) from 50 to 60 m with the other parameters kept as reference.

For this simulation, the cusp parameters are: $\lambda_c = 8.6$ m, $S_e = 2.6$ m, $f = 3.4$, $\sigma = 0.026$ s⁻¹, which are approximately the same as the reference case. By the global analysis, the cusp evolution behaviour has the same three phases as the reference case. The evolution starts from 1D development, then a small cusp system phase can be observed before the bigger cusp system occurs. The main difference in cusp evolution is the duration of each development phase. This case has longer duration for the small cusp system than the reference case, while

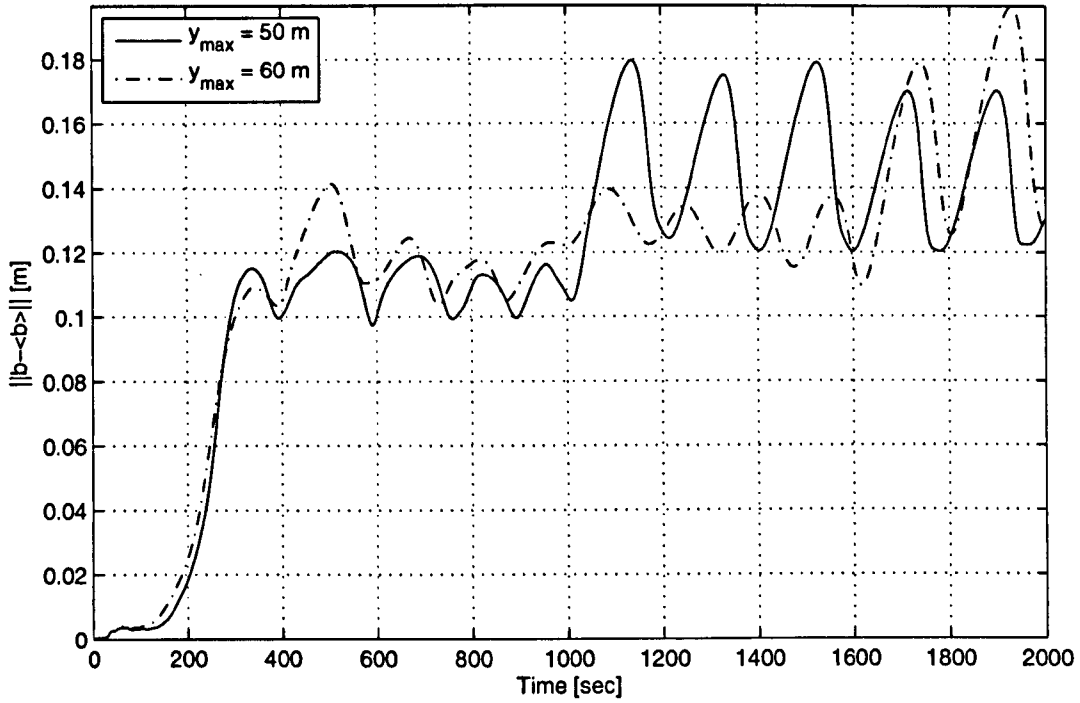


Figure 6.17: The global bed change with alongshore averaged subtraction in time for expansion in y -direction to 60 m case when other parameters as same as reference.

the other behaviours are similar as shown in Figure 6.17. In conclusion, there is no significant effect of the domain size used in this study on the beach cusp formation and evolution.

6.7.4 Grid Convergence

The size of spatial grid, Δx and Δy , is one of the important parameters for the numerical model. A smaller number of the computation cells (bigger Δx , Δy) produces a bigger error; therefore, the variation of the grid size is tested in this section for investigating the convergence of the error on $\Delta x, \Delta y \rightarrow 0$.

In this study, the grid convergence test varies the number of computation cells (number of cells in cross-shore direction (N_x) \times number of cell in alongshore direction (N_y)) between 120×500 , 96×400 , 72×300 , 60×250 , and 48×200 , while the domain size remains the same ($12 \text{ m} \times 50 \text{ m}$). This means that the grid sizes are varied between $\Delta x = \Delta y = 0.1$ (reference case), 0.125 , 0.167 , 0.2 , and 0.25 m , respectively. After $t = 500 \text{ s}$ of simulation, the root mean square error (ϵ_{rms}) of all computation cells and equations in each case is computed by

$$\epsilon_{rms} = \sqrt{\frac{\sum_i^{N_x} \sum_j^{N_y} \sum_n^4 \epsilon_{i,j,n}^2}{4N_x N_y}} \quad (6.6)$$

where $\epsilon_{i,j,n}$ is the computation error in each cell and equation, which is computed by substituting the resulting value into central discretisation of (4.9) to (4.12). The i and j denote the cell number in cross- and alongshore direction, and n denotes the number of equation. Figure 6.18 shows the relationship of ϵ_{rms} and the total number of computational cells. The ϵ_{rms} value reduces when the number of cells increases. The best fit line has a gradient of -0.52 , although one would expect a value nearer -2.00 for a fully second order code. A smaller cell size than that used in the reference case ($\Delta x = \Delta y = 0.1 \text{ m}$) could have less errors, however the finer cell size, such as $\Delta x = \Delta y = 0.05 \text{ m}$, causes the model crash. Therefore, the reference case has the most reasonable cell size to simulate the beach cusps in this study.

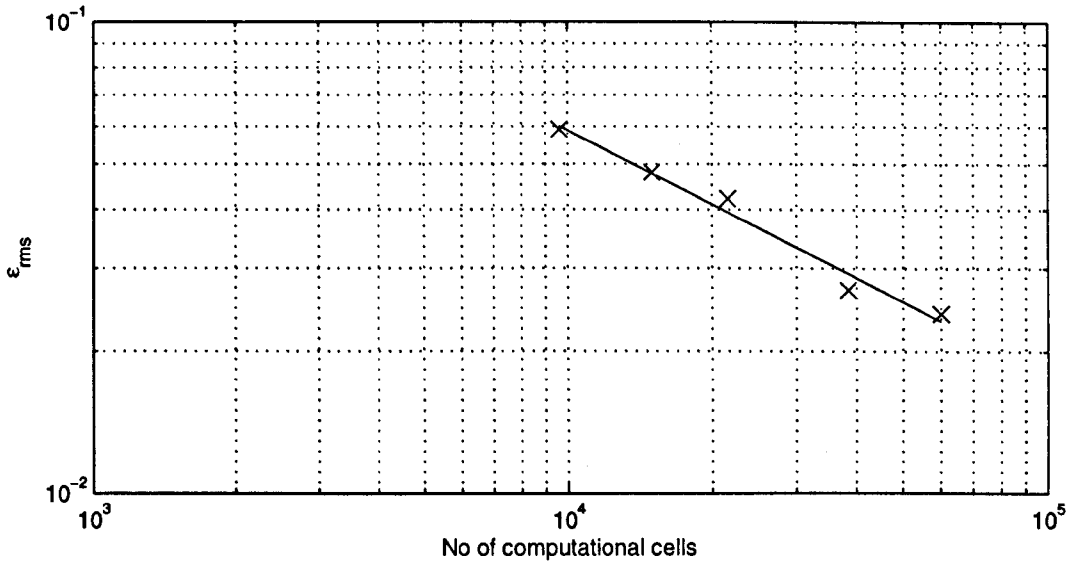


Figure 6.18: Grid convergence test result.

6.7.5 Numerical Problems in the model

The presently implemented numerical scheme mostly reproduces the results of Dodd et al. (2008), but it still needs some improvement in the stability of the calculation and the special treatment of the shoreline boundary condition. The model experiences numerical instability in certain cases, such as: the $f_w < 0.05$, the higher hydraulic conductivity ($K = 0.04$), and the finer resolution ($\Delta x = \Delta y = 0.05$ m) cases. All of the crashes in the model occur near the shoreface area which has a shallow water depth. It is recommended that further research be carried out with the aim of resolving the numerical difficulties that arise at the shoreline due to the very small depths encountered.

CHAPTER 7

Beach Permeability

The model predictions show reversible behaviour between the cusp horns and embayments, unlike nature where this does not occur. It is possible that the numerical reversings are due to the treatment of infiltration in the model. Beach permeability plays an important role in 1D cross-shore beach profile change as discussed in Chapter 5. In the present chapter, the sensitivity of cusp formation and evolution to infiltration is tested. The infiltration velocity, w , at each time step and the accumulated water volume of infiltration over one swash motion are also presented to identify the reversal mechanism. The influence of the particular numerical implementation selected to represent the infiltration term is also examined.

7.1 Sensitivity Test of Hydraulic Conductivity in 2D Simulations

Chapter 5 has presented sensitivity tests of hydraulic conductivity, K , in 1D simulations. That test varies $K = 0.001, 0.01$, and 0.04 m/s corresponding to medium sand, coarse sand and gravel beach (Packwood and Peregrine, 1980). The same K sensitivity tests for 2D simulations, caused the model to crash for the $K = 0.04$ m/s case. Therefore, the values of K that are used in this 2D sensitivity cases are $0.001, 0.005$ and 0.02 m/s. Figures 7.1 to 7.3 display the results in the form of bed level change over time along with the averaged velocity vector field over the preceding period.

To compare these results, refer to the reference case ($K = 0.01$ m/s), which is shown in Figure 6.2. It can be seen that the important effect causing by large K is deposition at the upper swash. When K is small, there are double circulation velocity patterns at the swash and long-shore bar, and an anti-phase cusp like pattern at the long-shore bar is observed instead of the deposition at the upper swash as shown in Figure 7.1, and 7.2. However, this double circulation and rhythmic pattern at the long-shore bar have not been found for the higher K cases.

For $K = 0.02$ m/s, there is more deposition at the upper swash than for the reference case. The evolution of beach cusp starts from 1D development; then the circulation pattern is observed at the upper swash, and the flow diverges

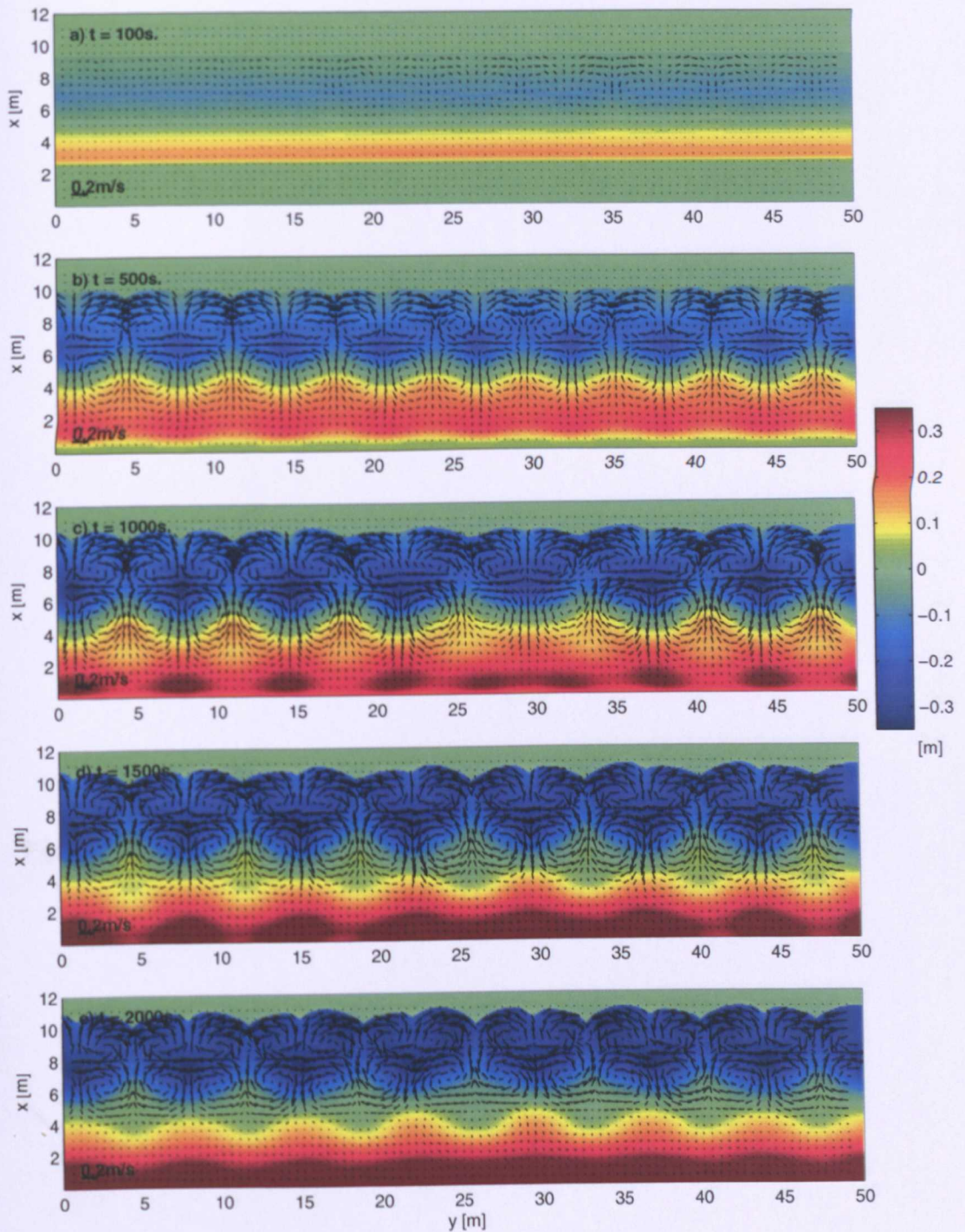


Figure 7.1: Change in bed level (m) relative to a plane beach (colours) after 20, 100, 200, 300, and 400 periods, and velocity vectors averaged over preceding period for $K = 0.001\text{ m/s}$, and other parameters as same as reference.

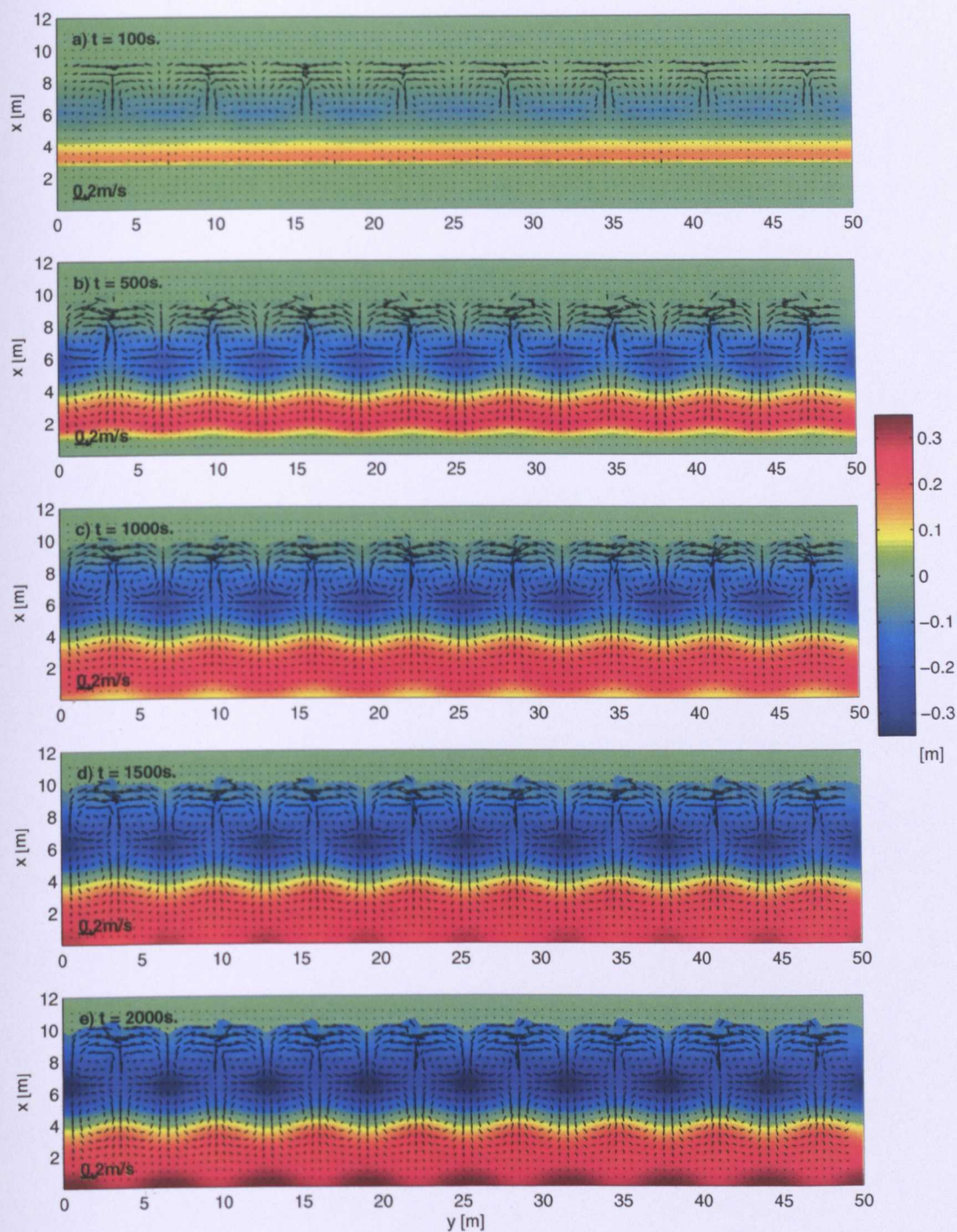


Figure 7.2: Change in bed level (m) relative to a plane beach (colours) after 20, 100, 200, 300, and 400 periods, and velocity vectors averaged over preceding period for $K = 0.005$ m/s, and other parameters as same as reference.

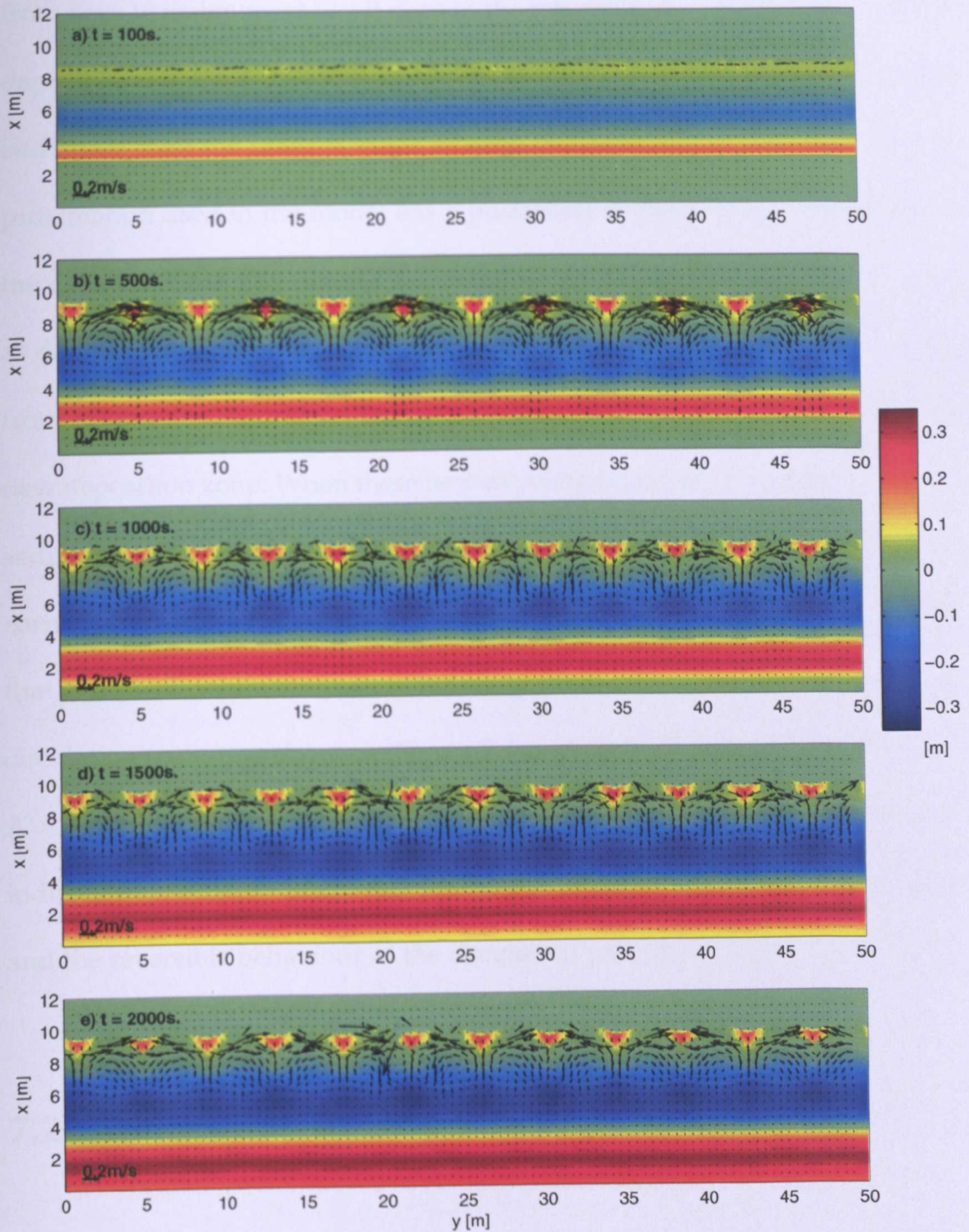


Figure 7.3: Change in bed level (m) relative to a plane beach (colours) after 20, 100, 200, 300, and 400 periods, and velocity vectors averaged over preceding period for $K = 0.02$ m/s, and other parameters as same as reference.

from horn to embayment like it does in the reference case. With more sediment deposited at the upper swash, the horns in the $K = 0.02$ m/s case have higher bed levels than the other K cases as seen in Figure 7.3 b). Since the Roe approximation used in the model has a possibility to create a stagnation zone at the embayment and the simple sediment transport equation used in the model as discussed in Section 6.7.2, the diverged flow moves the deposited sediment from 1D development along the cusps to the embayment in order to create the new deposition zone. When these new deposition zones have enough height of sediment, it acts like horns; thus, the small scale circulation pattern is created corresponding to the small cusp system as seen in Figure 7.3 c) and d). After that, the small circulation pattern is broken down, and it tries to form the bigger circulation pattern as shown in Figure 7.3 e). As a result, the beach evolution of $K = 0.02$ m/s case is similar to the reversibility of horns and embayments in an indirect way, because it also creates the deposition at the head of embayment and the reversible behaviour of the circulation pattern.

7.2 Infiltration in One Swash Period

So far the overall relationship between K and the beach cusp formation is presented, but not the detail of the infiltration pattern over one swash motion. This section describes the water loss into the beach in terms of instantaneous infiltration velocity, w , at each time step for the reference case ($T = 5$ s) during $t = 503$ - 508 s as shown in Figure 7.4.

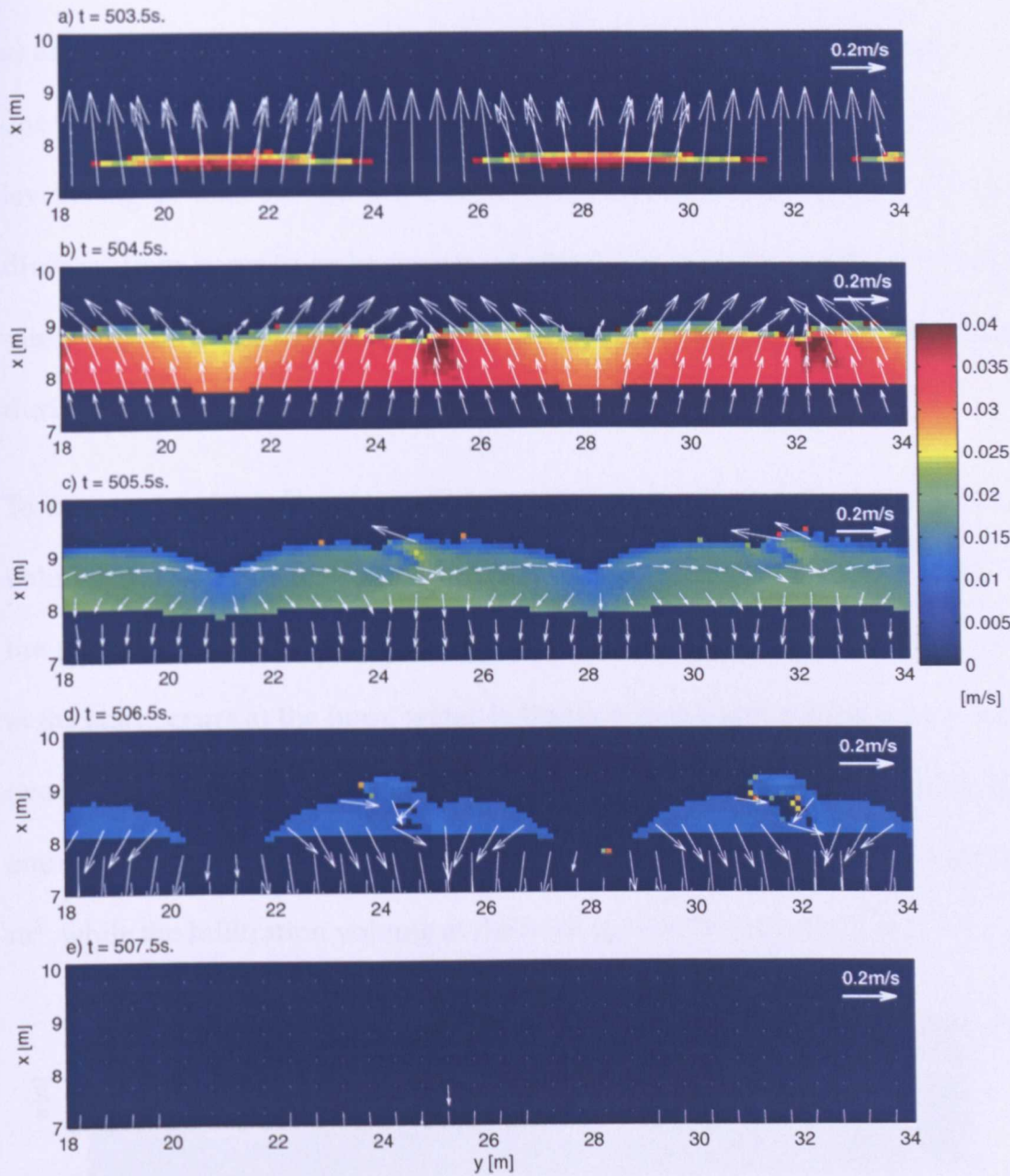


Figure 7.4: Instantaneous infiltration velocity, w , (m/s) and depth averaged velocity vectors over one wave period ($t = 503-508$ s) for the reference case.

Figure 7.4 illustrates the instantaneous infiltration velocity corresponding to the infiltration rate during the uprush phase of the swash motion (Figure 7.4 a) and b)), while the backwash phase is shown in Figure 7.4 c), d), and e). In one swash period, infiltration occurs first at the horns at the time that the water level is higher than the still water level (SWL) around $x = 7.2$ m; then, the flow diverges from horns to embayments causing infiltration there. The infiltration rate is high during the uprush and reduces in time with the smaller water depth during the backwash.

To summarise the infiltration volume over a swash period, the accumulated volume of infiltration over one swash period along two bays of beach cusps of the reference case is presented in Figure 7.5. Although a high infiltration rate at the start occurs at the horn, water infiltration in the embayment area occurs over a longer period. As a result, the volume of infiltrated water lost at the embayment ($y = 22.5$ -26 m) during $t = 503$ -508 s for the reference case is 0.24 m^3 , while the infiltration volume at the horn ($y = 26$ -29.5 m) is 0.21 m^3 .

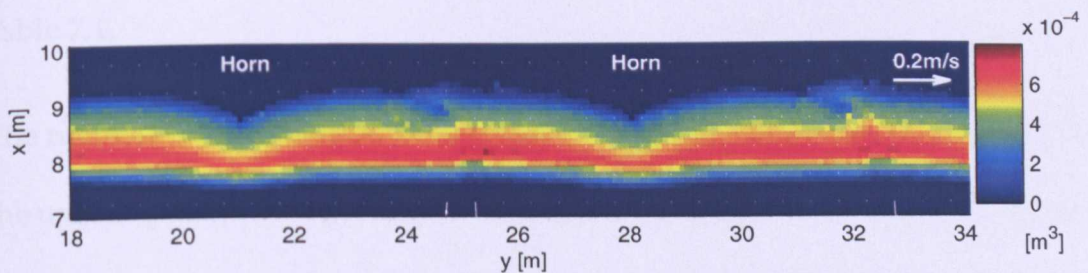


Figure 7.5: Accumulated infiltration volume (m^3) over one swash period ($t = 503$ -508 s) and average velocity vectors at $t = 508$ s for the reference case.

Not only is water lost, but so is momentum. These losses limit the potential of backwash to remove the sediment causing deposition in the upper swash zone (Stoker, 2005). From the result of the accumulated infiltration volume, the more infiltration is found at the embayment than at the horn; thus, this results in deposition at the embayment leading to the reversible behaviour as discussed in Section 6.7.2.

7.3 Variation in Infiltration Calculation

In the present model, the groundwater level and exfiltration are not included. Only a simple Darcy's law using a constant hydraulic conductivity is implemented in the model (see more detail in Section 3.4); therefore, the hydraulic conductivity is the most crucial parameter in the calculation of infiltration. Here we examine different ways of including Darcian infiltration. The alternatives for implementing the infiltration velocity calculation in the model are shown in Table 7.1.

The rationale of the Alternative 3) is that most infiltration might be expected on the uprush phase when groundwater level is lowest. The reason for the Alternative 4) is that finer particles with lower hydraulic conductivity are often found in the lower swash, whereas coarser sediments with higher hydraulic conductivity, are found near the shoreline (Masselink et al., 1997) as shown the difference of the grain size along the beach cusps in Figure 7.6. However, the present tests aim to investigate solely the behaviour of beach change corresponding to

Table 7.1: The alternatives of the K implementation.

Alternative	Description
1) No infiltration	K is set to zero
2) Constant K	K is constant for every calculation cell
3) Only uprush phase	K is applied when $U > 0$.
4) Linear interpolation	K varies linearly from zero at still water level (SWL) to $K = 0.01$ m/s at bed level 0.3 m above SWL.

Note that, Alternative 1) is the same as the impermeable beach case of Dodd et al. (2008); Alternative 2) is the reference case.

the different infiltration calculation; therefore, the maximum bed level ($= 0.3$ m) for K variation in Alternative 4) is estimated from the Figure 7.6. The results of Alternative 1), 3), and 4) are shown in Figures 7.7, 7.8, and 7.9, respectively. The Alternative 2) is the reference case, so the result is illustrated in Figure 6.2.

From the alternative criteria and the results, we can reorder the alternatives from the least to the most infiltration in volume occurring on the beach as: Alternative 1) no infiltration, 3) only uprush phase, 4) linear interpolation, and 2) constant K . When comparing the results, we found two main differences in beach shapes. For less infiltration (Alternatives 1) and 3)), there is no deposition at the upper swash, but a double circulation pattern is created from the upper swash and the rhythmic broad long-shore bar with no reversible behaviour during the cusp evolution. On the other hand in Alternatives 2) and 4), the deposition at the upper swash is created from the infiltration effect, and only one circulation pattern occurs: the shoreface rhythmic pattern; however,



Figure 7.6: Difference in sediment sizes along the beach cusps at Barton on Sea, UK provided by Guthrie, J.G.L.

these alternatives show reversible behaviour between horns and embayments during the beach cusp development. Moreover, when compared the results only the alternatives that has the infiltration effect (Alternative 2), 3), and 4)), the more infiltration caused the larger cusp spacing than the less one, which is the same conclusion from Dodd et al. (2008).

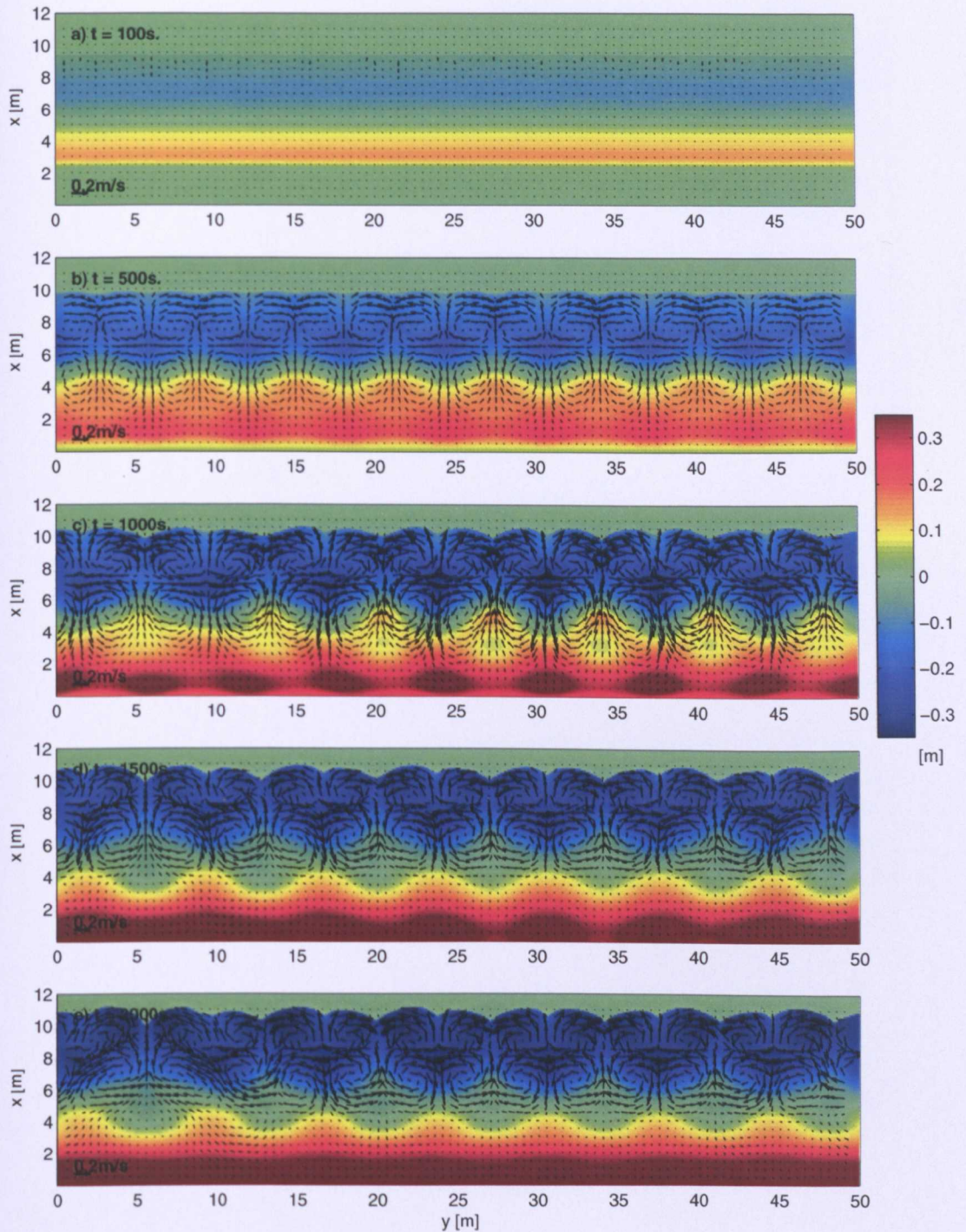


Figure 7.7: Change in bed level (m) relative to a plane beach (colours) after 20, 100, 200, 300, and 400 periods, and velocity vectors averaged over preceding period for Alternative 1).

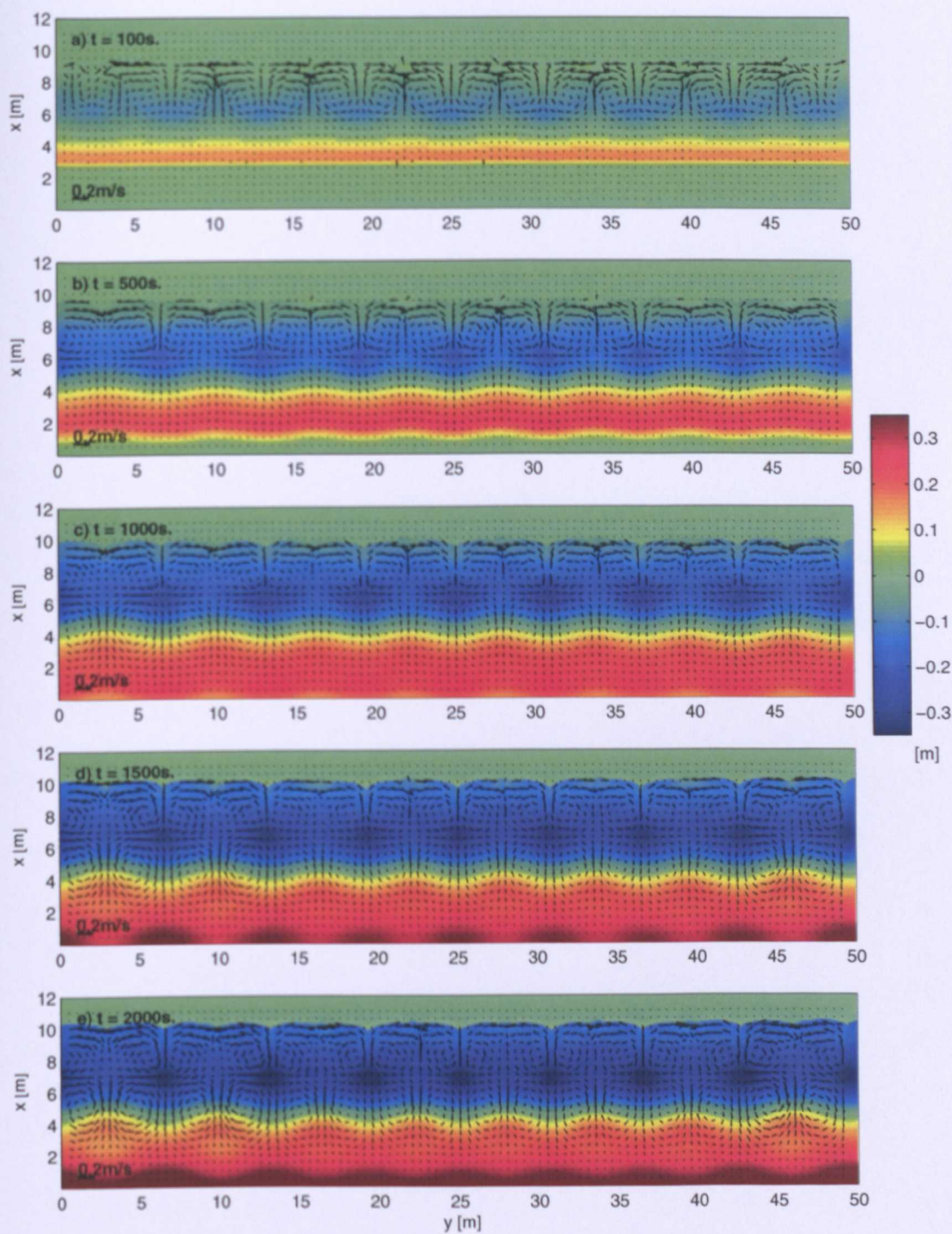


Figure 7.8: Change in bed level (m) relative to a plane beach (colours) after 20, 100, 200, 300, and 400 periods, and velocity vectors averaged over preceding period for Alternative 3).

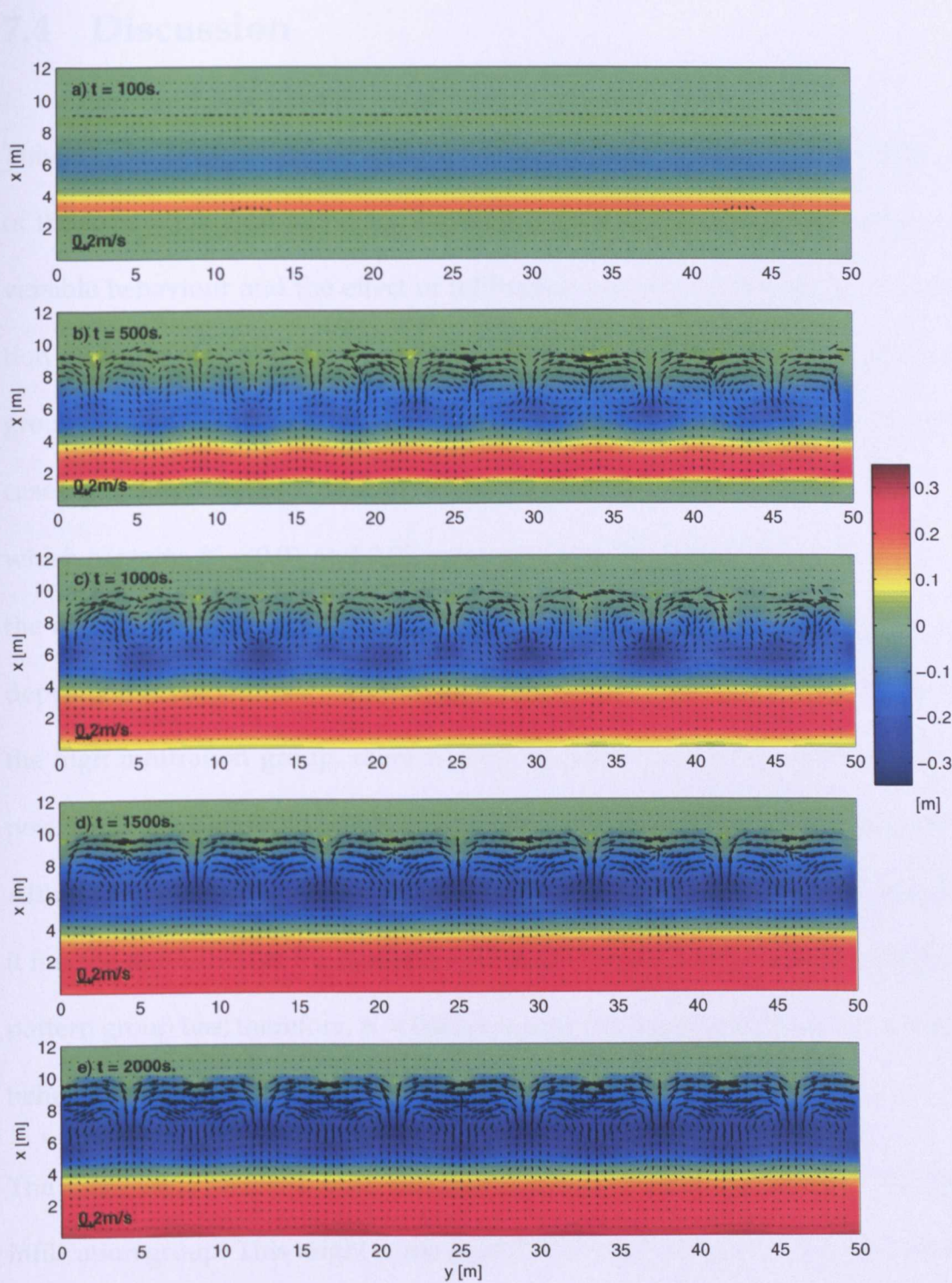


Figure 7.9: Change in bed level (m) relative to a plane beach (colours) after 20, 100, 200, 300, and 400 periods, and velocity vectors averaged over preceding period for Alternative 4).

7.4 Discussion

This chapter presents the sensitivity test of K and alters the implementation of the infiltration calculation for investigating especially the causes of the reversible behaviour and the effect of infiltration on cusp formation. The variation in values of K and the ways to implement K can be summarised into two groups. The first group is low infiltration, including $K = 0.001$ and 0.005 m/s cases and Alternatives 1) and 3); while the second group is high infiltration, which contains $K = 0.01$ and 0.02 m/s cases and Alternatives 2) and 4). From the results, the lower infiltration group has double circulation pattern, but no deposition at the shoreface and no reversible behaviour. On the other hand for the high infiltration group, there is only the one circulation pattern with deposition at the shoreface, but the reversible behaviour is found in this group. Although the $K = 0.02$ m/s case is not found the direct reversible behaviour, it has the deposition at the embayment which also the the same as the reversal pattern group has; therefore, $K = 0.02$ m/s case can be included in the reversible behaviour group.

The occurrence of the double circulation pattern is observed only in the low infiltration group. This might come from either small amount of the deposition or the erosion at the upper swash area during the 1D development of beach cusps, because of the small value of K ; thus, there will be more erosion at the upper swash in time which leads to the beach moving onshore as discussed in Section 5.3.2. For the 2D beach cusps of small K cases, there is more erosion

and $x_{s,max}$ occurs further onshore at the embayment than at the horn as shown in Figures 7.7 and 7.8. The difference of the shoreline position at the horn and embayment relates to the difference of the cross-shore position of the long-shore bar, leading to create the rhythmic long-shore bar and the double circulation.

Another investigation in this chapter is to identify the relationship between the infiltration and reversible behaviour. The reversible behaviour is found only in the high infiltration group, which has the high deposition at the embayments. Therefore, the detail of the infiltration velocity at each time steps of Alternative 2), Alternative 4) (high infiltration group), and Alternative 3) (low infiltration group) are used as an example for investigating the infiltration effect.

Comparing the instantaneous infiltration velocity at each time steps of the reference case (Figure 7.4), Alternative 3) case (Figure 7.10), and Alternative 4) case (Figure 7.11), it can be seen that they have the same pattern which starts with a high infiltration rate at the beginning, then the infiltration spreads along the cusps by the horn divergent flow and decreases in time. However, the main difference of Alternative 3) from the other cases is the shorter duration for the infiltration because its criteria are limited only to the uprush phase.

The shorter duration infiltration causes the total infiltrated volume over one swash period to be different from the other cases. From Figure 7.12, the accumulated infiltration volume of Alternative 3) has more or less the same amount of loss water along the cusps (horns ($y = 29.5-32.5$ m) = 0.14 m³ and embayment ($y = 26.5-29.5$ m) = 0.13 m³); however in Alternatives 2) and 4), the total

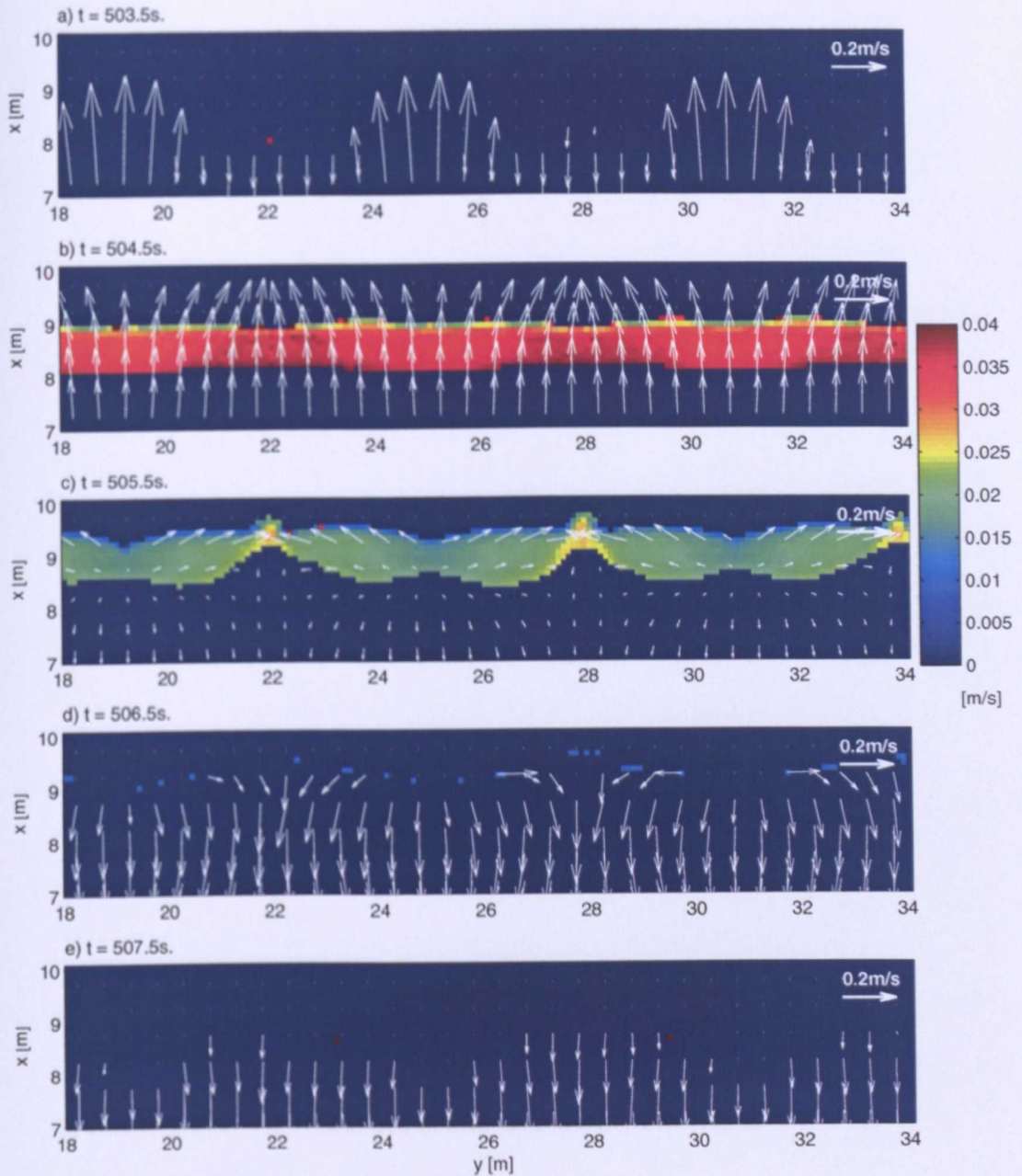


Figure 7.10: Instantaneous infiltration velocity, w , (m/s) and depth averaged velocity vectors over one wave period ($t = 503-508$ s) for Alternative 3).

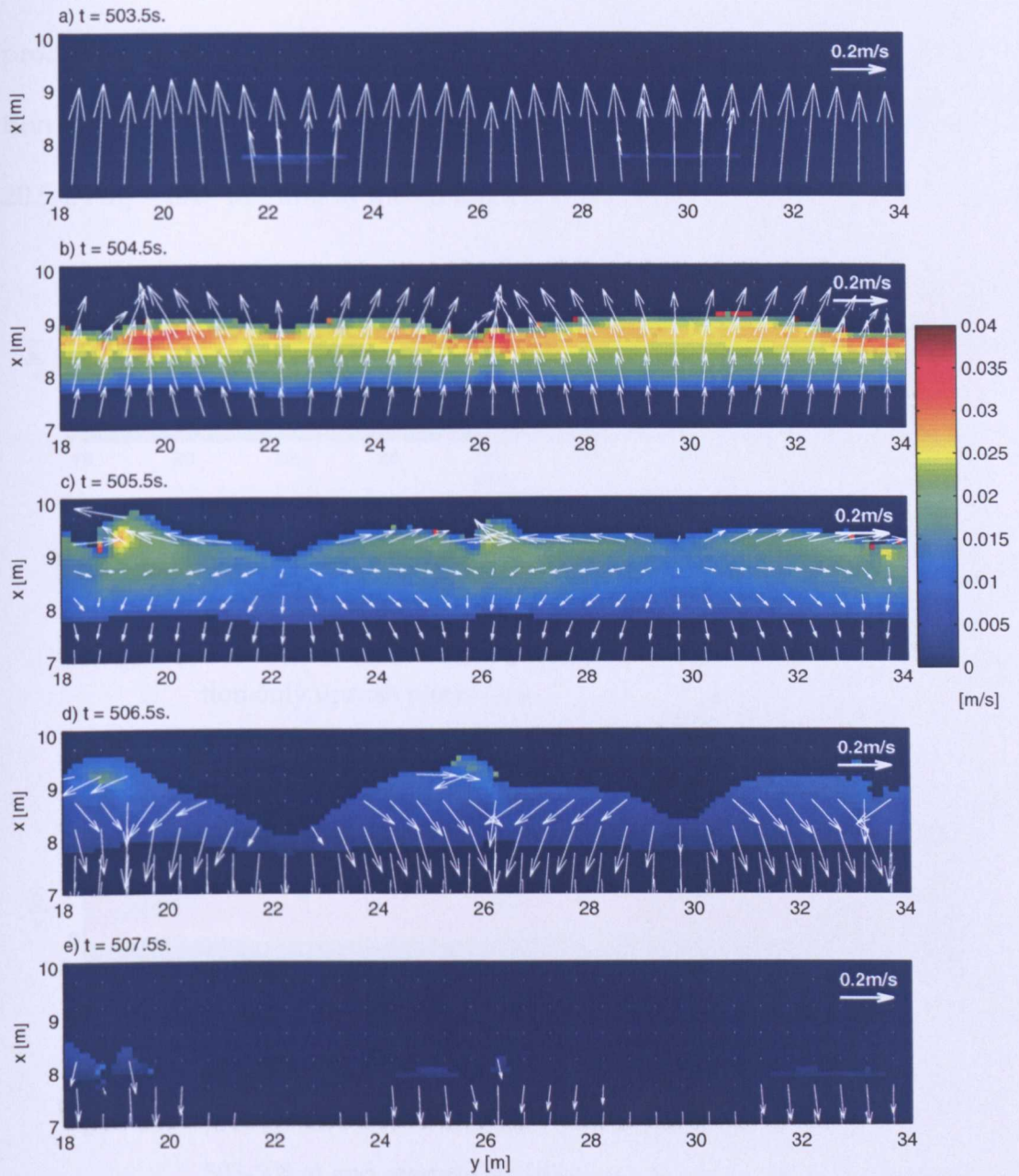


Figure 7.11: Instantaneous infiltration velocity, w , (m/s) and depth averaged velocity vectors over one wave period ($t = 503\text{--}508\text{ s}$) for Alternative 4).

of infiltrated water over one swash period in the embayment area is more than in the horn area as shown, respectively, in Figure 7.5 and 7.13. Alternative 2) produced the total infiltrated volume at the horn and embayment given in Section 7.2, whereas the total infiltrated volume of Alternative 4) at the horn ($y = 20.5-24 \text{ m}$) = 0.17 m^3 , and at the embayment ($y = 24-27.5 \text{ m}$) = 0.20 m^3 .

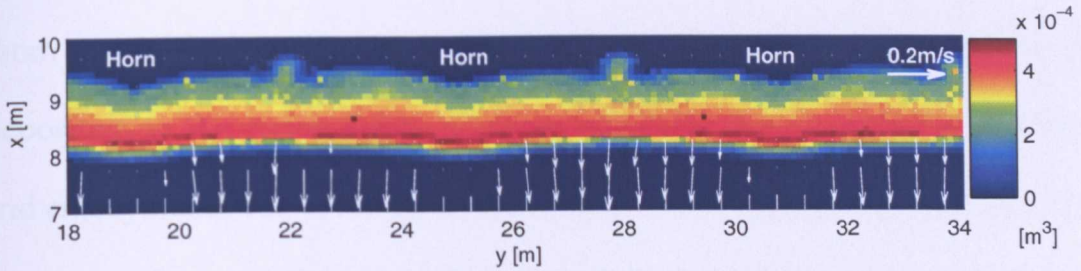


Figure 7.12: Accumulated infiltration volume (m^3) over one swash period ($t = 503-508 \text{ s}$) and average velocity vectors at $t = 508 \text{ s}$ for the infiltration only uprush phase case.

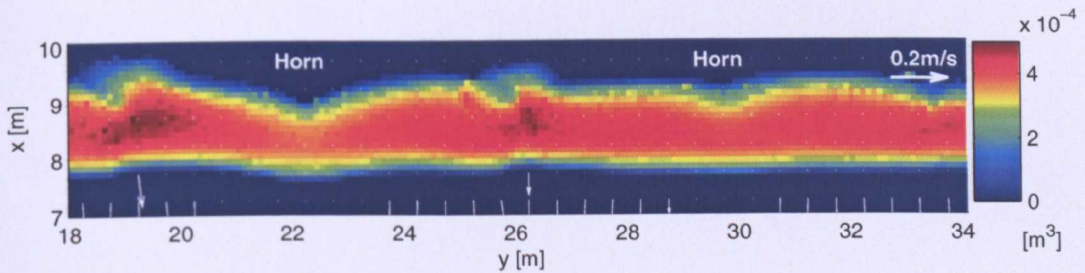


Figure 7.13: Accumulated infiltration volume (m^3) over one swash period ($t = 503-508 \text{ s}$) and average velocity vectors at $t = 508 \text{ s}$ for the linear variation of K case.

Increased infiltration directly affects the water volume and momentum of the backwash leading to less capability of containing the sediment transport; therefore, the sediment will deposit at the area where has higher infiltration. The

high infiltration group has more accumulated infiltration volume at the embayment than that at the horn, so deposition occurs at the embayment leading to reversible behaviour. On the other hand, no difference in accumulated infiltration volume along the cusps for the low infiltration group, causes no excessive deposition in the embayment area, and so there is no reversal.

From this evidence, it can be concluded that high infiltration directly causes deposition in the embayments, creating reversible behaviour between horns and embayments. However the results of low infiltration cases do not look like beach cusps, because there is no deposition at the upper swash, and they have a double circulation pattern; but they do not exhibit reversible behaviour, which is realistic.

CHAPTER 8

Testing Sediment Transport Equations

Chapter 7 showed the details of the infiltration effect that could be one of the reasons causing the reversible behaviour in the simulation results. Another source that might be the cause of this strange behaviour is the simple form of sediment transport equation used in the model. This chapter starts with the investigation of sediment movement over one swash period calculated from 2D morphodynamical simulation results (the same as shown in Chapter 6); then, the variation of sediment transport equations is tested to investigate the relationship between the sediment transport equation and reversible behaviour in the simulation using the idealisation of beach cusp topography adapted from the Dean and Maurmeyer (1980) equation.

8.1 Sediment Transport in One Swash Period

The sediment transport equation used here is a simple formulation (3.9) of that of Grass (1981), where $m = 3$, as discussed in Section 3.2. The behaviour of sediment over one swash period governed by (3.9) is investigated by recomputing the rate of bed change ($B_t = \partial B / \partial t$) in the central discretisation form of sediment conservation equation (3.4) at each time step, while the bed diffusion term is neglected as:

$$\frac{\partial B}{\partial t} = -\xi \left(\frac{q_{u_{i+1,j}} - q_{u_{i-1,j}}}{2\Delta x} + \frac{q_{v_{i,j+1}} - q_{v_{i,j-1}}}{2\Delta y} \right) \quad (8.1)$$

where $q_{u_{i,j}}$ and $q_{v_{i,j}}$ are cross- and alongshore sediment transport rate in a computational cell (i,j) , i and j are cell numbers in cross- and alongshore direction, respectively, and $\xi = 1 / (1 - p)$ where p is the porosity of the bed. The recomputed result of the reference case from $t = 503$ - 508 s is illustrated in Figure 8.1. Although the central difference method has less stability than the upwind discretisation, it provides the acceptable results with less computation for investigating the sediment movement over one swash period. Because this section aims to investigate the pattern of erosion/deposition, not the magnitude of the bed change rate, all the plotted data are expressed as normalised value of rate of bed change, $B_{t,norm} = B_t / |B_{t,max}|$, where $|B_{t,max}|$ is the maximum absolute value of rate of bed change in the upper swash area ($x = 7$ - 10 m) over the considered wave period.

Figure 8.1 shows two bays of beach cusps ($y = 18$ - 34 m), focusing on the upper

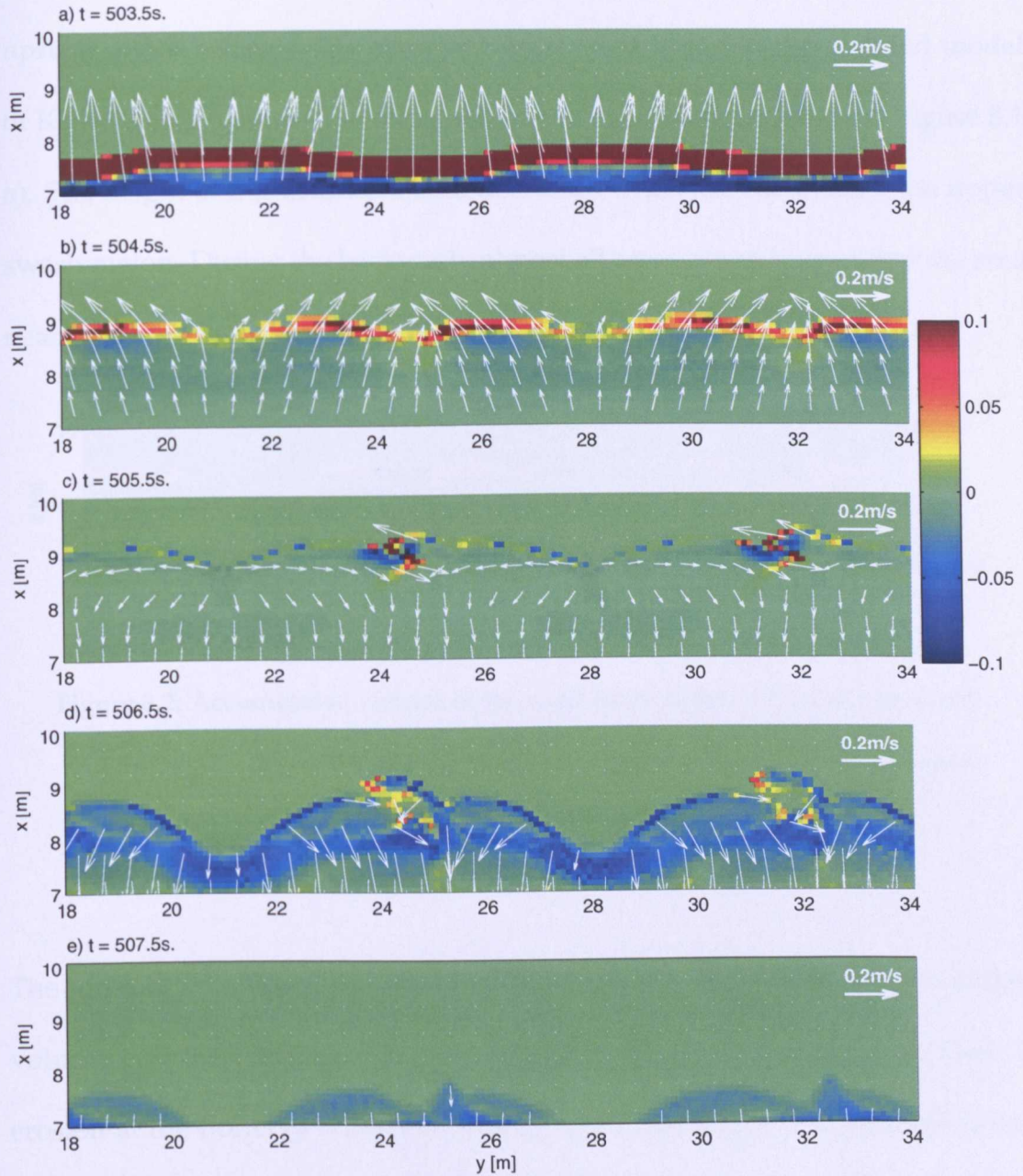


Figure 8.1: Normalised rate of bed change computed from $q = AU|U|^2$ over one swash motion during $t = 503\text{--}508\text{ s}$ and depth averaged velocity vectors for the reference case result.

swash area, to investigate the bed change at horns and embayments over one swash period. There is a sediment bore coming with the wave front during the uprush phase, which is the same behaviour that found in the coupled model of Kelly (2009), whereas the other area tends to erosion as shown in Figure 8.1 a). The height of this sediment bore decreases when the wave reach the upper swash region. During the backwash, almost all areas are erosive except the area near the shoreline of the embayments which has deposition.

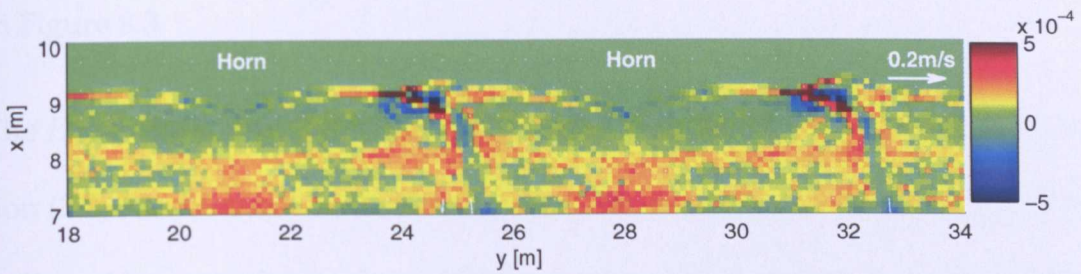


Figure 8.2: Accumulated volume of the normalised value of B_t over one swash period ($t = 503-508$ s) computed from $q = AU|U|^2$ of the reference case result.

The summary of the bed change over one swash period in terms of accumulated volume is shown in Figure 8.2. At the upper swash ($x = 8.5-9.5$ m), there is erosion at the horns ($y = 20-22$ and $27-29$ m), whereas the deposition is found around the embayments ($y = 24-26$ and $30.5-32.5$ m). On the other hand, there is more deposition at the horn than at the embayment in the lower swash ($x = 7-8$ m).

As part of an investigation into different generic sediment transport formulations, Pritchard and Hogg (2005) introduced the coupled depth and velocity

sediment transport rate \vec{q} as:

$$\vec{q}(d, \vec{U}) = Ad\vec{U} |\vec{U}|^{(m-1)} \quad (8.2)$$

where A is the dimensional sediment transport coefficient, and m is a constant. For comparison, we use the result of the depth averaged velocity from the reference case to calculate the sediment transport rate and rate of bed change by using (8.2) when $m = 3$ for each time step. The rate of bed change is illustrated in Figure 8.3.

The B_t pattern computed from (8.2) and the reference sediment transport equation (3.9) are different. The reference equation produces the erosion next to the sediment bore moving onshore during uprush phase, whereas no erosion is observed from the result computed by (8.2). During the backwash phase, (8.2) produces the approximate zero of B_t at the embayments in the upper swash as shown in Figure 8.3. As a result, there is no deposition at the head of the embayments in the plot of bed change accumulation in volume over one swash period; most of the sedimentation is found at the horns in the lower swash area as shown in Figure 8.4.

From the comparison of these two difference sediment transport equations, it may be observed that the choice of the simple sediment transport formula is a factor influencing the reversible behaviour in the simulation; however, the variables (d , U and V) that are used to compute the sediment transport rates and bed change in this investigation could be biased because they come from a simulation that exhibits reversible behaviour.

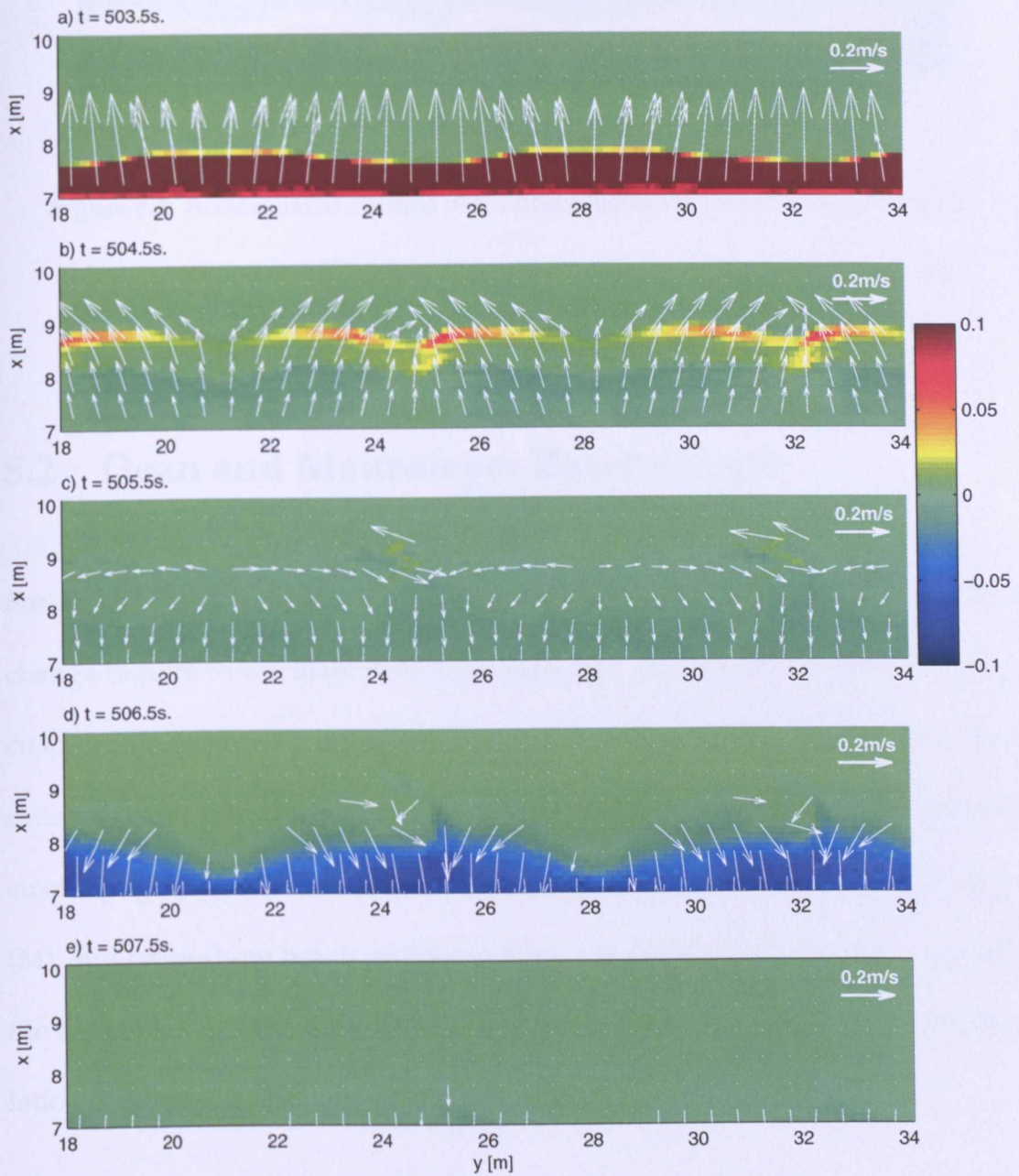


Figure 8.3: Normalised rate of bed change computed from $q = AdU|U|^2$ over one swash motion during $t = 503\text{-}508\text{ s}$ and depth averaged velocity vectors for the reference case result.

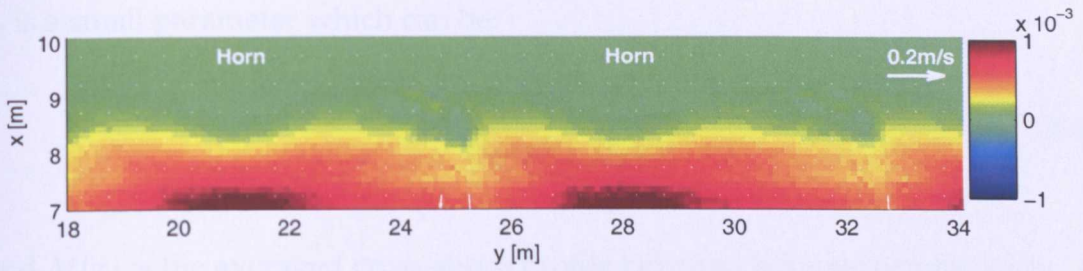


Figure 8.4: Accumulated volume of the normalised value of B_t over one swash period ($t = 503\text{--}508$ s) computed from $q = AdU|U|^2$ of the reference case result.

8.2 Dean and Maurmeyer Beach Cusps

For an unbiased comparison, the sediment transport rate and theoretical bed change require to calculate from hydrodynamic data for an equilibrium beach cusp profile (where by definition there is no beach change). Dean and Maurmeyer (1980) introduced the formulation to create the idealisation of beach cusp topography which requires the cusp spacing (λ_c), the average beach slope (M), and cross-shore beach profiles at horn and embayment. As the beach profile data is taken from the simulation, the Dean and Maurmeyer (1980) formulation is adapted to be compatible with the previous results as:

$$B(x, y) = M(x) \left[1 + \epsilon_c \sin \left(\frac{2\pi}{\lambda_c} \left(y + \frac{\lambda_c}{4} \right) \right) \right] \quad (8.3)$$

where $B(x, y)$ is the elevation of bed level above a datum, x and y represent the horizontal distances in the cross-shore and alongshore direction, respectively,

ϵ_c is a small parameter which can be:

$$\epsilon_c = \frac{B_H(x) - B_B(x)}{B_H(x) + B_B(x)} \quad (8.4)$$

and $M(x)$ is the averaged cross-shore profile between horn and embayment. It is assigned by:

$$M(x) = \frac{1}{2} (B_H(x) + B_B(x)) \quad (8.5)$$

where $B_H(x)$ and $B_B(x)$ are the cross-shore profile of the horn and embayment, respectively, from the simulation result. We apply the result of the reference case to (8.3) for creating the idealised beach cusp topography as shown in Figure 8.5.

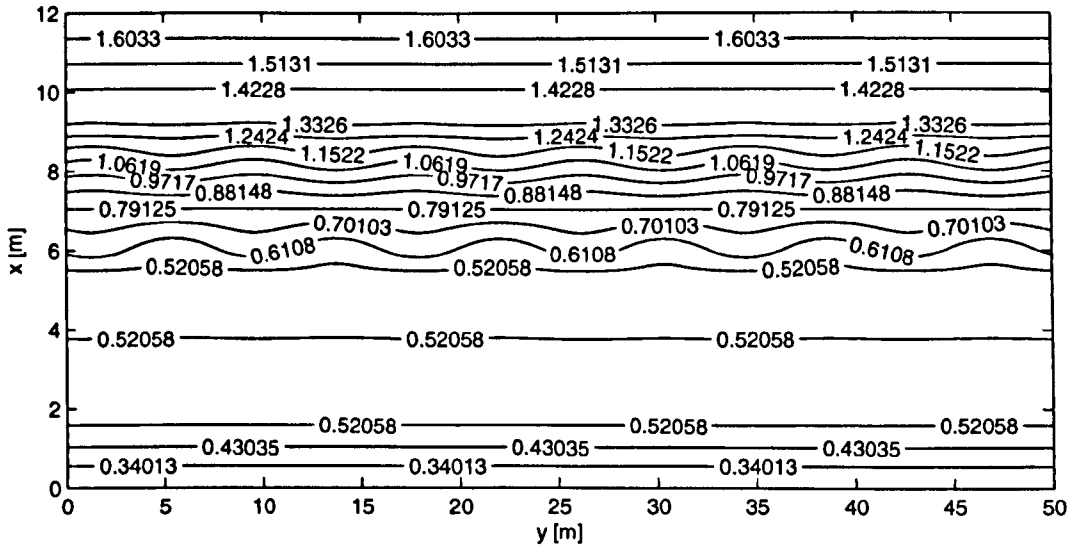


Figure 8.5: The idealised beach cusp topography created from the result of reference case.

After we got the idealised beach cusps profile, the *OTT-2d* model of Hubbard and Dodd (2002) is altered to include the infiltration effect by using the Pack-

wood (1983) equations (3.13) and (3.14); then, it is used to simulate 2D hydrodynamic behaviour on the idealised beach cusp profile of Figure 8.5 without sediment movement, in order to provide the hydrodynamic variables (d , U , and V) for testing the variation of sediment transport equations in the next section. The hydrodynamic result of the idealised beach cusps is illustrated in Figure 8.6.

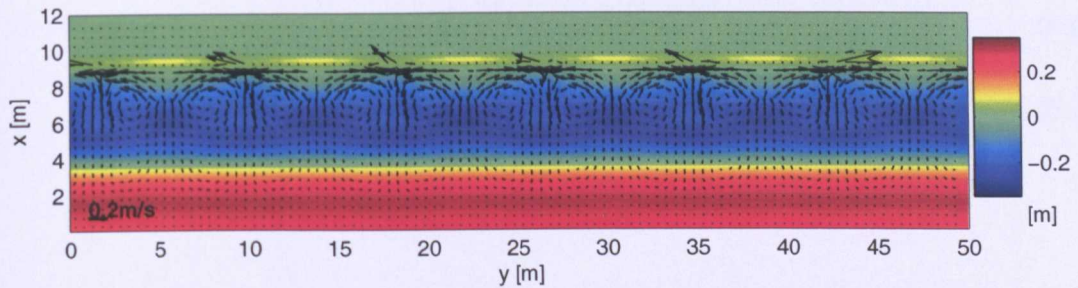


Figure 8.6: The circulation pattern (vectors) averaged over preceding wave period on the idealised beach cusp topography and the bed level (m) relative to the plane sloping beach (colours).

8.3 Variation in Sediment Transport Equations

The investigation of sediment movement prediction over one swash period computed by the various sediment transport equations is observed and presented in this section. The sediment transport rate and rate of bed change, as predicted by the different formulas, are computed using the same hydrodynamic data as calculated by the model of Hubbard and Dodd (2002), but including an infiltration term identical to (3.13), solved on the idealisation of

beach cusp topography as shown in Figure 8.5. The sediment transport equations that are used in this test come or are adapted from Pritchard and Hogg (2005); they can be divided into 3 groups:

- *Velocity-only group*: $\vec{q} = \vec{q}(\vec{U})$ only. This originates from the Grass (1981) equation. The m value in (3.9) is varied between 3 and 4 in this test as:

$$\vec{q}(\vec{U}) = A\vec{U} |\vec{U}|^2 \quad (8.6)$$

$$\vec{q}(\vec{U}) = A\vec{U} |\vec{U}|^3 \quad (8.7)$$

where A is sediment transport coefficient.

- *Coupled depth and velocity group*: $\vec{q} = \vec{q}(d, \vec{U})$, as in (8.2). In this test,

$$\vec{q}(d, \vec{U}) = Ad\vec{U} |\vec{U}|^2 \quad (8.8)$$

$$\vec{q}(d, \vec{U}) = Ad\vec{U} |\vec{U}|^3 \quad (8.9)$$

where $q(d, \vec{U})$ is the sediment transport rate, d is water depth.

- *Threshold group* is a group of sediment transport equations that contain a critical velocity corresponding to a critical bed shear stress as the criterion for sediment movement. In this test, we use

$$\vec{q}(\vec{U}) = A\vec{U} \left(|\vec{U}|^2 - U_{cr}^2 \right) \quad \text{when } |\vec{U}|^2 > U_{cr}^2 \quad (8.10)$$

$$\vec{q}(d, \vec{U}) = Ad\vec{U} \left(|\vec{U}|^2 - U_{cr}^2 \right) \quad \text{when } |\vec{U}|^2 > U_{cr}^2 \quad (8.11)$$

If $|\vec{U}|^2 \leq U_{cr}^2$, $q(\vec{U})$ and $q(d, \vec{U})$ in (8.10) and (8.11), respectively, are zero, where U_{cr} is the critical velocity, which is set to 1 m/s in this test (0.25-2 m/s is recommended in Pritchard and Hogg (2005)).

The comparison of various sediment transport equations is presented in the form of accumulated bed change volume over one swash period, as shown in Figure 8.7. Since this test aims to investigate only the bed change pattern that results from the various equations, the magnitude of bed change is not considered important; therefore, the values in the plot are the accumulated volume of the normalised value of B_t over one swash period and the sediment transport coefficient, A , in these equations could be not the same dimensions.

From Figure 8.7, we can arrange groups of sediment transport equations into two main groups, velocity-only and coupled depth and velocity groups, while those in the threshold group are divided between the two main groups: (8.10) is merged into the velocity-only group, and (8.11) with the coupled depth and velocity group.

When we start to investigate the results at the lower swash ($x = 7-8$ m), there is erosion at the horns ($y = 21-23$ and $29-31$ m) and deposition at the embayments ($y = 18-19$, $25-27$, and $33-34$ m) for both two main groups; however, the coupled depth and velocity group has more relative deposition than the velocity-only group. At the upper swash ($x = 8-10$ m), there is some erosion near the horns and depositions at the embayment centre for the velocity-only group, as shown in Figure 8.7 a), b), and e). Moreover the flow at the upper swash diverges from horns to embayments, as shown in Figure 8.5. This flow and bed change behaviour could imply that the velocity-only groups of sediment transport equations induce the sediment to move from horns and to deposit at the embayment

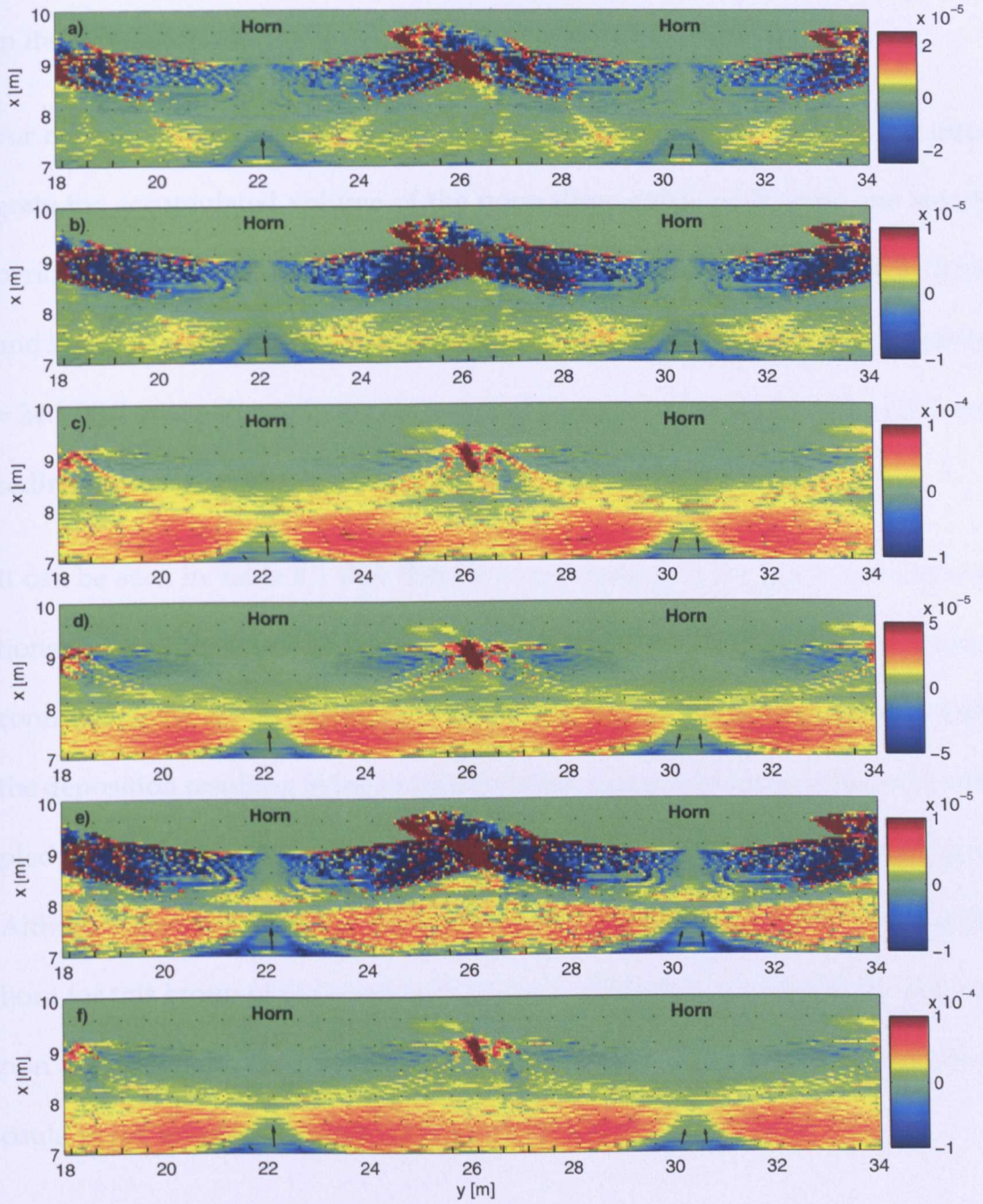


Figure 8.7: Accumulated volume of the normalised value of B_t over one swash period computed from a) $q = AU|U|^2$, b) $q = AU|U|^3$, c) $q = AdU|U|^2$, d) $q = AdU|U|^3$, e) $q = AU(|U|^2 - U_{cr}^2)$, and f) $q = AdU(|U|^2 - U_{cr}^2)$.

head (i.e. centre of embayment) and thereby to create the reversible behaviour in the simulation.

For more investigation in detail of the net beach change in one cusp, we integrate the accumulated volume of the normalised value of B_t over one swash period by dividing one beach cusp into four subareas: at the upper ($x = 8\text{-}10\text{ m}$) and lower ($x = 7\text{-}8\text{ m}$) swash of the horn ($y = 28.2\text{-}32.3\text{ m}$) and the embayment ($y = 24.1\text{-}28.2\text{ m}$), as shown in the summary of these calculations from the different sediment transport formulations in Table 8.1.

It can be seen in Table 8.1 that there is some erosion at the horn, and depositions at the embayment in the upper swash area for the velocity-only group, confirming that the sediment moves from the horn to the embayment to create the deposition resulting in the reversible behaviour. On the other hand, the coupled depth and velocity group creates deposition at both horn and embayment. Although the net volume of the deposition at embayment is more than at the horn for this group of sediment transport equations, it is found that the deposition at embayment head is one spot of high deposition. This spot of deposition could occur for other reasons, which will be discussed in Section 8.4.

8.4 Discussion

The testing of different sediment transport equations in Sections 8.1 and 8.3 shows that the sediment transport equations that are functions solely of depth

Table 8.1: Summary of the accumulated volume of the normalised value of B_t over one swash period in different area of beach cusps for the different sediment transport formulations.

		Velocity-only			Coupled depth and velocity		
		$m = 3$	$m = 4$	Threshold	$m = 3$	$m = 4$	Threshold
		(8.6)	(8.7)	(8.10)	(8.8)	(8.9)	(8.11)
Horn	US	-0.0042	-0.0030	-0.0038	0.0196	0.0040	0.0089
	LS	0.0016	0.0009	0.0018	0.0561	0.0217	0.0436
	Total	-0.0026	-0.0021	-0.0020	0.0757	0.0257	0.0525
Embayment	US	0.0118	0.0058	0.0100	0.0425	0.0154	0.0283
	LS	0.0034	0.0020	0.0047	0.0559	0.0263	0.0599
	Total	0.0152	0.0078	0.0147	0.0984	0.0417	0.0882
Beach Cusp	US	0.0076	0.0028	0.0062	0.0621	0.0194	0.0372
	LS	0.0050	0.0029	0.0065	0.1120	0.0480	0.1035
	Total	0.0126	0.0057	0.0127	0.1741	0.0674	0.1407

Note that: US means the upper swash area ($x = 8-10$ m); LS means the lower swash area ($x = 7-8$ m); the horn is accumulated between section $y = 28.2-32.3$ m; the embayments is accumulated between section $y = 24.1-28.2$ m

averaged velocity moves the sediment from horns to deposit at the embayment head. This causes the reversible behaviour in the simulation because the sediment at the embayments is deposited, whereas it is eroded at the horns until the sediment height at the embayment is higher than that at the horns. Therefore,

the flow will start to reverse back from the old embayments to the horns, and the old embayment will become the new horn. The reversal between horns and embayments occurs here.

In the case of sediment transport equations that couple water depth and depth averaged velocity, the bed change at the upper swash is less than at the lower swash; whereas the bed changes at the upper and lower swash are more or less the same for the velocity-only group as shown in Table 8.1. Although there is a spot of deposition at the embayment head for the coupled depth and velocity group as shown in Section 8.3, it might be caused from the channel at the embayment found from the close up contour plot of the idealisation of beach cusp topography as shown in Figure 8.8. This channel results from the selected result profiles, and these horn and embayment cross-shore profiles are the best from the big beach cusp system result of the reference case that we can find.

The channel is found between two small berms at horn locations ($y = 20\text{-}24$ and $28.5\text{-}32.5$ m). When the wave runs up, the flow can breach through this channel and move to the back of the berms as shown in Figure 8.9, during the transition period between uprush and backwash phase. This inundated flow causes the deposition spot in the channel at the embayments as shown in the results. From the results of using (8.8) on the reference beach case as shown in Figure 8.4, there is no channel at the embayment; thus, there is no flooding and no deposition spot at that location. This implies that the deposition spot is caused by breaching at the channel. Therefore, the coupled depth and velocity

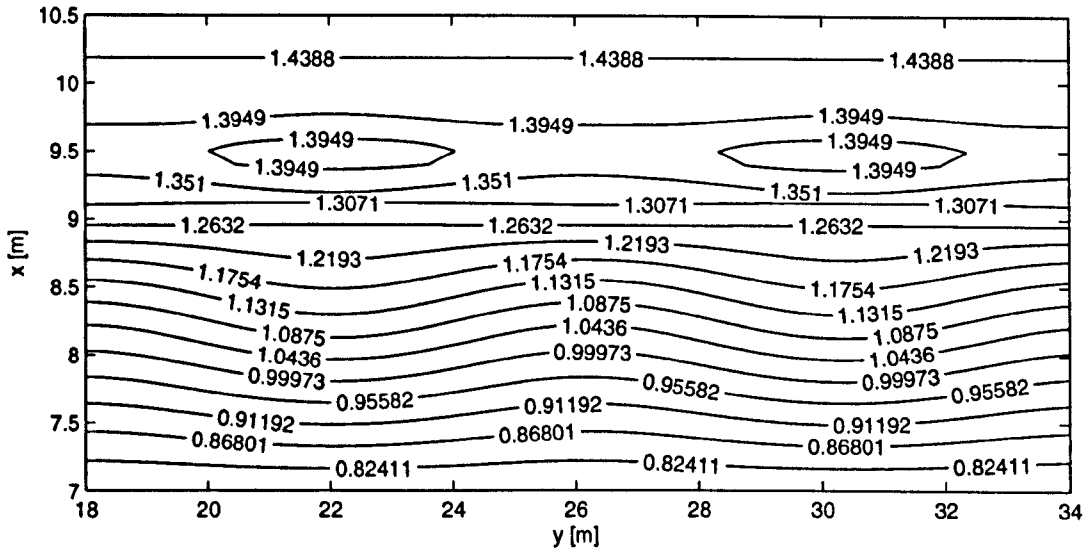


Figure 8.8: Shoreface area topography of idealisation of beach cusp topography from data adaption equation.

group of sediment transport equations might not create the deposition at the embayment that causes the reversible behaviour in the simulation, if there is no channel on the beach.

The deposition caused by breaching at the channel is also found in the results calculated by the velocity-only group. However, the percentage of the deposition at the upper swash of the embayment for the velocity-only group (68.0-77.6%) is higher than that for the coupled depth and velocity group (32.1-43.2%). Thus, if we assume that all deposition at the upper swash of the embayment for the coupled depth and velocity group is caused by the channel effect, and then, exclude this deposition by the same percentage from the velocity-only group, there still remains deposition occurring at the embayment head for the velocity-only group.

In conclusion, the velocity-only group of sediment transport equations is one of the reasons that the reversible behaviour is created in the simulation. However, we cannot confirm that the usage of the coupled depth and velocity group in the model will produce the non-reversible behaviour in the simulation.

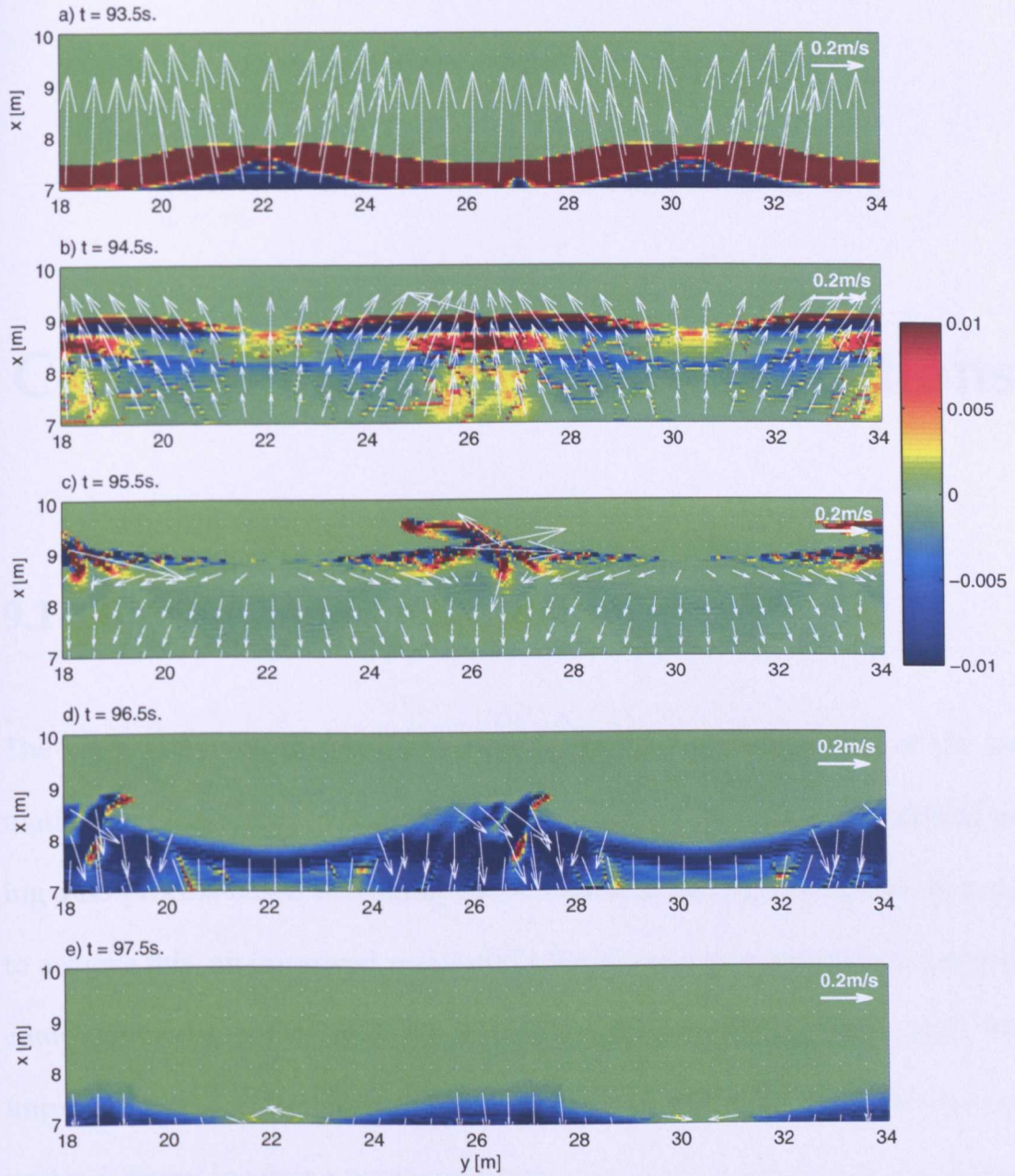


Figure 8.9: Normalised rate of bed change computed from $q = AdU|U|^2$ over one swash motion and depth averaged velocity vectors for the hydrodynamic on the idealised beach cusps.

CHAPTER 9

Conclusions and Recommendations

9.1 Review and Conclusions

The work presented in this thesis aims to improve understanding of the formation and long-term evolution of beach cusps by numerical simulation using a 2D process-based morphodynamic model including infiltration. In order to achieve this, an improved numerical scheme is implemented for improving computational accuracy of a 2D process-based morphodynamic model. The improved model is used to simulate the long-term development of beach cusps under different incoming wave conditions, initial beach profiles, and sediment properties, for investigating the evolution behaviour and the physical effects leading to sedimentation and erosion in the swash, in particular, to beach cusp formation.

A successful 2D process-based morphodynamic model for simulating the beach

cusps is presented by Dodd et al. (2008). The governing equations of that model, which includes the NLSW equations, sediment conservation equation, bed diffusion effect, and infiltration term, are described in Chapter 3. Moreover, the numerical scheme, the Roe's method, used for capturing the shock behaviour in the computation of Dodd et al. (2008) model is also explained there.

Although the Dodd et al. (2008) model is successful in simulating the occurrence of beach cusps, it still needs to improve the stability and the accuracy of the computation in very shallow water. Therefore, the new implementation including the entropy fixes, the Castro Diaz et al. (2008) numerical scheme, the time operator splitting scheme, and the special numerical treatment of the shoreline boundary condition are illustrated in Chapter 4. These new implementations are tested with the dambreak problem, the Shen and Meyer (1963) problem, and the Hibberd and Peregrine (1979) problem to compare the model results in terms of stability between each numerical scheme. From the comparison, the most suitable numerical scheme is the Roe-averaged scheme of Castro Diaz et al. (2008) with Minmod flux-limiter using the Harten and Hyman (1983) entropy fix method and the Hubbard and Dodd (2002) approach for the shoreline boundary condition. In terms of accuracy, this selected numerical scheme produces overall acceptable results, compared with the analytical and numerical solutions from previous works for both rigid and mobile bed cases. Although this successful numerical scheme has been proved that it makes the present model more stable than Dodd et al. (2008) model, it still has the signifi-

cant problem in the calculation of the tip position and speed, corresponding to the shoreline boundary condition.

In Chapter 5, the selected numerical scheme is tested for 1D long-term beach change. It also provides model sensitivity test for variations in minimum depth d_{tol} , bed friction coefficient f_w , hydraulic conductivity K , and sediment transport coefficient A . In addition, simulations of two types of incoming waves, the sine wave and the sawtooth wave, are used to investigate their effect on the 1D long-term beach profile. In all cases, the long-term beach profile is similar, consisting of a long-shore bar, a trough (erosion at the lower swash area), and a swash berm (deposition at the upper swash area) in accordance with the established profile (Masselink and Li, 2001). For the parameter sensitivity test, the convergence of the results is found when $d_{tol} \leq 1$ mm. The relationship between the bed profile and both numerical and physical parameters of beach cusps is that a greater maximum tip position $x_{s,max}$ is achieved, and more erosion in the tip region occurs, when d_{tol} , f_w , and K are smaller. The bigger K , such as $K = 0.04$ m/s, can initiate the deposition at the upper swash during the beginning of the simulation, and the deposition can continuously occur until it reaches an equilibrium state. On the other hand, the effect of scaling A is to scale the rate of change of the bed level, which is the same conclusion as Stoker (2005); therefore, the size of A appears not to lead to qualitative differences. However, very high A , such as $A = 0.04$ s²/m, can create the unexpected numerical bed shock in the model, which can lead to a model crash. Regarding the different types of incoming wave, the sine wave produces a beach profile having the

three components identified by Masselink and Li (2001), whereas the sawtooth wave creates a wider equivalent region, with the wave simply breaking farther offshore.

In Chapter 6, the 2D formation and long-term evolution of beach cusps under the different incoming wave conditions (vary wave period T), and initial beach profiles (a plane 8° sloping beach and initial curved beach) are discussed. The bed perturbation with the Dirac delta function is used instead of the wave perturbation in the simulation to make sure that the cusp results from the model are not coming from the perturbation. Beach cusp parameters are defined in terms of cusp spacing and swash excursion, and linear growth rate. We also use the Fourier analysis and the global analysis, introduced by Garnier et al. (2006), for analysing the bed pattern data and investigating the evolution of beach cusps. The 2D beach cusp formation results from both initial beach profiles, simulated by the new model, are approximately the same as those of Dodd et al. (2008); however, the geometrical parameters (f) from the self-organisation theory are still high ($f = 2.7\text{-}3.7$) when compared with the previous works (Werner and Fink (1993) ($f = 1\text{-}3$), Masselink (1999) ($f = 1.57$), and Coco et al. (2000) ($f = 1.63$)). The evolution of the beach cusp is investigated by both Fourier and global analysis, from which it can be concluded that there are three steps of the evolution. It starts with development a 1D cross-shore profile including a long-shore bar, a trough, a the swash berm. Then, 2D circulation commences in the upper swash region in order to create the cusp-like pattern with a small cusp spacing. Finally, the cusps reconstruct themselves by the coalescing of

two small bays and subsequent rearrangement to an equal spacing to form the bigger cusp system. More surprising is the reversing behaviour between horn and embayment during the cusp evolution, which is caused by the deposition in the embayment head. The reason of the deposition occurring in the embayment head could possibly be come from either the infiltration effect or the simple sediment transport equation used in the model.

The occurrence of deposition at the embayment head could perhaps be due to infiltration or the use of the simple sediment transport equation in the model. The detail of the infiltration and the pattern of sediment movement over one swash period are discussed in Chapters 7 and 8, respectively. In Chapter 7, the sensitivity of K in 2D simulations is tested, and the variation of the K implementation, i.e. no infiltration, constant K , applied K only uprush phase, and linear interpolation of K , is applied to the model. Moreover, the detail of the infiltration rate and the loss of volume of water into the beach over one swash period are observed. As a result, we can conclude that the high infiltration directly causes the deposition at the embayment head; whereas, the low infiltration cases produce the normal cusp evolution without non-reversible behaviour. However, the beach topography results from the low infiltration cases do not look like beach cusps, because there is no deposition at the upper swash, and the double circulation pattern is found in these beaches.

In Chapter 8, the sediment movement prediction over one swash cycle is observed by using the water depth and depth averaged velocity results from the

simulation to recompute the sediment transport rate and rate of beach change for the reference case beach profile and the idealised beach cusp topography, created by the adapted topography equation of Dean and Maurmeyer (1980). The sediment transport rate formulations in this observation can be divided into two main groups: the "*velocity-only*" group and the "*coupled depth and velocity*" group. The sediment transport equation used in the recent model is in the velocity-only group. In conclusion, the result of this investigation shows that the velocity-only group of sediment transport equations is one of the reasons to create the deposition at the embayment head, leading to the reversible behaviour. However, the usage of the couples depth and velocity group in the model cannot confirm that it will produce the non-reversible behaviour in the simulation.

9.2 Recommendations for future research

There is a considerable amount of future work that is required for improving this process-based morphodynamic model and for better understanding of the formation and long-term evolution of beach cusps. Here, we can divide the recommendations into numerical and physical issues.

Although this model can simulate the occurrence of beach cusps with the numerical improvements from Dodd et al. (2008), some numerical issues remain that could be improved:

- *Entropy fix*: although the Harten and Hyman (1983) entropy fix is a suitable method for computing the transonic situation, there is still a kink that can be observed in the result. While the Hubbard and Dodd (2002) entropy fix method is a better method to deal with the transonic rarefaction, it is not suitable for the normal backwash condition. Therefore, the best way forward is to alter the usage of the Hubbard and Dodd (2002) entropy fix method in the model by providing special criteria for applying this entropy fix method only for the transonic rarefaction fan, which requires the determination of the morphodynamic Riemann structure.
- *Shoreline boundary condition*: from the comparison of the model result with the analytical and numerical solutions from the previous works in the dambreak and the Shen and Meyer (1963) test cases, it can be seen that there is a significant error in the computation of the tip position and speed. To improve the calculation in the tip region, it requires the special treatment of the shoreline boundary condition.
- *Numerical scheme*: this is a continuous issue from the shoreline boundary condition. Since the Roe's method has a difficulty to solve the real wet/dry boundary condition, a new shock capturing scheme, such as the HLLC method and the WAF method, which can be implemented with the real wet/dry boundary, would be a better alternative to improve the accuracy and stability of the model.

With regard to the physical issues, a crucial next step would be the implemen-

tation of the other types of sediment transport equation instead of the velocity-only group, which cause the deposition at the embayment head, leading to the reversible behaviour between horn and embayment. The coupled depth and velocity type of sediment transport formulation is a good alternative for the new implementation. Additionally, the groundwater modelling for increasing the accuracy of the computation of the infiltration term, and the exfiltration effect should be included into the model. Moreover, the physical property of sediment, such as the sediment lagging and the water-sediment mixture, are also interesting effects to include in the model, along with investigating the relationship between these effects and the beach cusp formation and evolution.

So far, the recommendations above mostly discuss the improvement of the model used in this study. Future research also needs to examine other issues: the effect of introduction of a small amount of wave obliquity and randomness into the incoming waves on the formation and evolution of beach cusps; the application to natural beaches, by using field observation data; and the connection between the present model (swash zone model) and the surf zone by using results from a surf zone model to drive the present model. This latter topic will be particularly important for inputting sediment from the surf zone.

References

- Bagnold, R. A. (1966). An approach to the sediment transport problem from general physics. Professional Paper 422-I, U.S. Geophysical Survey, Washington, DC.
- Baird, A. J., Mason, T., and Horn, D. P. (1998). Validation of a boussinesq model of beach ground water behaviour. *Mar. Geol.*, 148:55–69.
- Briganti, R. and Dodd, N. (2009). Shoreline motion in nonlinear shallow water coastal models. *Coastal Eng.*, 56(5-6):495–505.
- Brocchini, M., Bernetti, R., Mancinelli, A., and Albertini, G. (2001). An efficient solver for nearshore flows based on the WAF method. *Coastal Eng.*, 43:105–129.
- Butt, T. and Russell, P. (1999). Suspended sediment transport mechanisms in high-energy swash. *Mar. Geol.*, 161:361–375.
- Butt, T. and Russell, P. (2000). Hydrodynamics and cross-shore sediment transport in the swash zone of natural beaches: a review. *J. Coastal Res.*, 16:255–268.
- Butt, T., Russell, P., and Turner, I. (2001). The influence of swash infiltration-

- exfiltration on beach face sediment transport: onshore or offshore? *Coastal Eng.*, 42:35–52.
- Calvete, D., Dodd, N., Falques, A., and Van Leeuwen, S. M. (2005). Morphological development of rip channel systems: normal and near normal wave incidence. *J. Geophys. Res.*, 110(C10):C10007, doi:10.1029/2004JC002803.
- Castro Diaz, M. J., Fernandez-Niteo, E. D., and Ferreiro, A. M. (2008). Sediment transport models in shallow water equations and numerical approach by higher order finite volume methods. *Computers and fluids*, 37:299–316.
- Ciriano, Y., Coco, G., Bryan, K., and Elgar, S. (2005). Field observations of swash zone infragravity motions and beach cusp evolution. *J. Geophys. Res.*, 110(C02018):doi:10.1029/2004JC002485.
- Clarke, S., Dodd, N., and Damgaard, J. S. (2004). Modelling flow in and above a porous beach. *ASCE J. Water. Port Coast. Ocean Eng.*, 130(5):223–233.
- Coco, G., Burnet, T. K., Werner, B. T., and Elgar, S. (2003). Test of self-organization in beach cusp formation. *J. Geophys. Res.*, 108 (C3)(3101).
- Coco, G., Huntley, D. A., and O'Hare, T. J. (2000). Investigation into a self-organization model for beach cusp formation. *J. Geophys. Res.*, 105(C9):21991–22002.
- Coco, G., O'Hare, T. J., and Huntley, D. (1999). Beach cusps: A comparison of data and theories for their formation. *J. Coastal Res.*, 15:741–749.

- Dean, R. G. and Maurmeyer, E. M. (1980). Beach cusps at Point Reyes and Drakes Bay beaches, California. In *Proc. 17th International Conference of Coastal Engineering*, pages 863–884. ASCE.
- Dicker, D. (1969). Transient free surface flow in porous media. In DeWiest, R. J. M., editor, *Flow through porous media*, pages 293–330. Academic Press.
- Dodd, N. (1998). A numerical model of wave run-up, overtopping and regeneration. *ASCE J. Water. Port Coast. Ocean Eng.*, 124(2):73–81.
- Dodd, N., Blondeaux, P., Calvete, D., De Swart, H. E., Falqués, A., Hulscher, S. J. M. H., Różyński, G., and Vittori, G. (2003). Understanding coastal morphodynamics using stability methods. *J. Coastal Res.*, 19(4):849–865.
- Dodd, N., Stoker, A., Calvete, D., and Sriariyawat, A. (2008). On the evolution of beach cusps. *J. Fluid Mech.*, 597:145–169.
- Elfrink, B. and Baldock, T. (2002). Hydrodynamics and sediment transport in the swash zone: a review and perspectives. *Coastal Eng.*, 45:149–167.
- Garnier, R., Calvete, D., Falqués, A., and Caballeria, M. (2006). Generation and nonlinear evolution of shore-oblique / transverse bars. *J. Fluid Mech.*, 567(doi:10.1017/S0022112006002126):327–360.
- Grass, A. (1981). Sediment transport by waves and currents. Report FL29, Ma. Tecnol., SERC London Cent.
- Grunnet, N. M., Walstra, D., and Ruessink, B. G. (2004). Process-based modelling of a shoreface nourishment. *Coastal Eng.*, 51:581–607.

- Guza, R. T. and Bowen, A. J. (1981). On the amplitude of beach cusps. *J. Geophys. Res.*, 86:4125–4132.
- Guza, R. T. and Inman, D. L. (1975). Edge waves and beach cusps. *J. Geophys. Res.*, 80:2997–3012.
- Harten, A. and Hyman, J. M. (1983). Self adjusting grid methods for one-dimensional hyperbolic conservation laws. *J. Comput. Phys.*, 50(2):235–269.
- Hibberd, S. and Peregrine, D. H. (1979). Surf and run-up on a beach: A uniform bore. *J. Fluid Mech.*, 95:323–345.
- Holland, K. T. and Holman, R. A. (1996). Field observations of beach cusps and swash motions. *Mar. Geol.*, 134:77–93.
- Horikawa, K., editor (1988). *Nearshore dynamics and coastal processes: Theory, Measurement and Predictive Models*. University of Tokyo Press.
- Horn, D. P. and Mason, T. (1994). Swash zone sediment transport modes. *Mar. Geol.*, 120:309–325.
- Hu, K., Mingham, C. G., and Causon, D. M. (2000). Numerical simulation of wave overtopping of coastal structures using the non-linear shallow water equations. *Coastal Eng.*, 41:433–465.
- Hubbard, M. E. and Dodd, N. (2002). A 2-d numerical model of wave run-up and overtopping. *Coastal Eng.*, 47(1):1–26.
- Hudson, J. (2001). *Numerical Techniques for Morphodynamic Modelling*. Ph.d. thesis, University of Reading, Department of Mathematics.

- Hudson, J., Damgaard, J. S., Dodd, N., Cooper, A. J., and Chesher, T. J. (2005). Approaches to 1d morphodynamical modelling in coastal engineering. *Coastal Eng.*, 52(8):691–707.
- Hudson, J. and Sweby, P. K. (2003). Formulations for numerically approximating hyperbolic systems governing sediment transport. *J. Sci. Comp.*, 19:225–252.
- Hudson, J. and Sweby, P. K. (2005). A high-resolution scheme for the equations governing 2d bed-load sediment transport. *Int. J. Numerical Meth. Fluids*, 47:1085–1091.
- Hughes, M. (1992). Application of a nonlinear shallow water theory to swash following bore collapse on a sandy beach. *J. Coastal Res.*, 8(3):562–578.
- Hughes, M. G., Masselink, G., and Brander, R. W. (1997). Flow velocity and sediment transport in the swash zone of a steep beach. *Mar. Geol.*, 138:91–103.
- Inman, D. L. and Guza, R. T. (1982). The origin of swash cusps on beaches. *Mar. Geol.*, 49:133–148.
- Jiang, G. S. and Shu, C. W. (1996). Efficient implementation of weighted eno schemes. *J. Comput. Phys.*, 126:202–228.
- Johnson, H. K. and Zyserman, J. A. (2002). Controlling spatial oscillations in bed level update schemes. *Coastal Eng.*, 46(2):109–126.

- Karambas, T. V. (2003). Modelling of infiltration-exfiltration effects of cross-shore sediment transport in the swash zone. *Coastal Engineering Journal*, 45(1):63–82.
- Karambas, T. V. and Koutitas, C. (2002). Surf and swash zone morphology evolution induced by nonlinear waves. *ASCE J. Water. Port Coast. Ocean Eng.*, 128(3):102–113.
- Kelly, D. M. (2009). *Bore-driven swash on a mobile beach*. PhD thesis, School of Civil Engineering, University of Nottingham, Nottingham, UK.
- Kelly, D. M. and Dodd, N. (2009). Floating grid characteristics method for unsteady flow over a mobile bed. *Computers and Fluids*, 38:899–909.
- Kobayashi, N., De Silva, G., and Watson, K. (1989). Wave transformation and swash oscillations on gentle and steep slopes. *J. Geophys. Res.*, 94:951–966.
- Kobayashi, N., Otta, A. K., and Roy, I. (1987). Wave reflection and run-up on rough slopes. *ASCE J. Water. Port Coast. Ocean Eng.*, 113(3):282–298.
- LeVeque, R. J. (2002). *Finite volume methods for hyperbolic problems*. Cambridge University Press, Cambridge.
- Li, L., Barry, D. A., Pattiaratchi, C. B., and Masselink, G. (2002). BeachWin: modelling groundwater effects on swash sediment transport and beach profile changes. *Environmental Modelling & Software*, 17:313–320.
- Longuet-Higgins, M. and Parkin, D. (1962). Sea waves and beach cusps. *Geogr. J.*, 128:194–201.

- Masselink, G. (1999). Alongshore variation in beach cusp morphology in a coastal embayment. *Earth Surface Processes and Landforms*, 24:335–347.
- Masselink, G., Evans, D., Hughes, M. G., and Russell, P. (2005). Suspended sediment transport in the swash zone of a dissipative beach. *Mar. Geol.*, 216:169–189.
- Masselink, G., Hegge, B. J., and Pattiaratchi, C. (1997). Beach cusp morphodynamics. *Earth Surface Processes and Landforms*, 22:1139–1155.
- Masselink, G. and Hughes, M. (1998). Field investigation of sediment transport in the swash zone. *Cont. Shelf Res.*, 18:1179–1199.
- Masselink, G. and Li, L. (2001). The role of swash infiltration in determining the beachface gradient: a numerical study. *Mar. Geol.*, 176:139–156.
- Masselink, G. and Pattiaratchi, C. B. (1998). Morphological evolution of beach cusps and associated swash circulation. *Mar. Geol.*, 146:93–113.
- Masselink, G. and Puleo, J. A. (2006). Swash zone morphodynamics. *Cont. Shelf Res.*, 26:661–680.
- Masselink, G., Russell, P., Coco, G., and Huntley, D. (2004). Test of edge wave forcing during formation of rhythmic beach morphology. *J. Geophys. Res.*, 109(C06003):doi:10.1029/2004JC002339.
- Nicholson, J., Broker, I., Roelvink, J. A., Price, D., Tanguy, J. M., and Moreno, L. (1997). Intercomparison of coastal area morphodynamic models. *Coastal Eng.*, 31:97–123.

- Packwood, A. R. (1983). The influence of beach porosity on wave uprush and backwash. *Coastal Eng.*, 7(1):29–40.
- Packwood, A. R. and Peregrine, D. H. (1980). The propagation of solitary waves and bores over a porous bed. *Coastal Eng.*, 3:221–242.
- Peregrine, D. and Williams, S. M. (2001). Swash overtopping a truncated beach. *J. Fluid Mech.*, 440:391–399.
- Press, W. H., Teulowsky, S. A., Vetterling, W. T., and Flannery, B. P. (1992). *Numerical Recipes in FORTRAN, The Art of Scientific Computing*. Cambridge University Press.
- Pritchard, D. and Hogg, A. J. (2005). On the transport of suspended sediment by a swash event on a plane beach. *Coastal Eng.*, 52:1–23.
- Puleo, J. A. and Holland, K. T. (2001). Estimating swash zone friction coefficients on a sandy beach. *Coastal Eng.*, 43(1):25–40.
- Roe, P. L. (1981). Approximate Riemann solvers, parameter vectors and difference schemes. *J. Comput. Phys.*, 43:357–372.
- Sallenger, A. (1979). Beach-cusp formation. *Mar. Geol.*, 29:23–37.
- Shen, M. C. and Meyer, R. E. (1963). Climb of a bore on a beach. Part 3. Run-up. *J. Fluid Mech.*, 16:113–125.
- Soulsby, R. L. (1997). *Dynamics of Marine Sands*. Thomas Telford, London.

- Stoker, A. M. (2005). *Process-based morphodynamic modelling of beach cusps*. PhD thesis, School of Civil Engineering, University of Nottingham, Nottingham, UK.
- Stoker, J. (1957). *Water Waves*. Interscience, New York, N.Y.
- Titov, V. V. and Synolakis, C. E. (1995). Modeling of breaking and nonbreaking long-wave evolution and runup using VTCS-2. *ASCE J. Water. Port Coast. Ocean Eng.*, 121(6):308–316.
- Titov, V. V. and Synolakis, C. E. (1998). Numerical modeling of tidal wave run-up. *ASCE J. Water. Port Coast. Ocean Eng.*, 124(4):157–171.
- Toro, E. F. (1999). *Riemann solvers and numerical methods for fluid dynamics*. Springer, Berlin, 2nd edition.
- Toro, E. F. (2001). *Shock-capturing methods for free-surface shallow flows*. Wiley, New York, NY.
- Turner, I. L. and Masselink, G. (1998). Swash infiltration-exfiltration and sediment transport. *J. Geophys. Res.*, 103(C13):30813–30824.
- van Rijn, L. (1984). Sediment transport, part i: Bed load transport; part ii: Suspended load transport; part iii: Bed forms and alluvial roughness. *ASCE J. Hydraulic Eng.*, 110:(HY10), 1431–1456; (HY11), 1631–1641; (HY12), 1733–1754.
- Watson, G., Peregrine, D. H., and Toro, E. (1992). Numerical solution of the

shallow water equations on a beach using the weighted average flux method.

In Hirsch, C., editor, *Computational Fluid Dynamics*, volume 1. Elsevier.

Werner, B. T. and Fink, T. M. (1993). Beach cusps as self-organized patterns. *Science*, 260:968–971.

Zyserman, J. A. and Johnson, H. K. (2002). Modelling morphological processes in the vicinity of shore-parallel breakwaters. *Coastal Eng.*, 45(3-4):261–284.